

NASA CONTRACTOR REPORT



NASA CR

0099653



TECH LIBRARY KAFB, NM

NASA CR-195

BRAYTON CYCLE SOLAR COLLECTOR DESIGN STUDY

by D. E. Stewart

Prepared under Contract No. NAS 3-2782 *by*

ELECTRO-OPTICAL SYSTEMS, INC.

Pasadena, Calif.

for

NATIONAL AERONAUTICS AND SPACE ADMINISTRATION • WASHINGTON, D. C. • APRIL 1965



0099653

NASA CR-195

BRAYTON CYCLE SOLAR COLLECTOR DESIGN STUDY

By D. E. Stewart

Distribution of this report is provided in the interest of information exchange. Responsibility for the contents resides in the author or organization that prepared it.

Prepared under Contract No. NAS 3-2782 by
ELECTRO-OPTICAL SYSTEMS, INC.
Pasadena, Calif.

for

NATIONAL AERONAUTICS AND SPACE ADMINISTRATION

For sale by the Office of Technical Services, Department of Commerce,
Washington, D.C. 20230 -- Price \$6.00

CONTENTS

	<u>Page</u>
SUMMARY	1
1. INTRODUCTION	2
2. PROGRAM COMPENDIUM	4
2.1 Collector Design	4
2.2 Manufacturing, Testing, Handling, and Transportation	7
2.2.1 Master Design and Fabrication	7
2.2.2 Mirror Fabrication	9
2.2.3 Testing, Handling, and Storage	10
2.2.4 Transportation	10
2.3 Efficiency	11
2.3.1 Collector Obscuration	11
2.3.2 Reflective Coating: Reflectance and Durability	11
2.3.3 Absorber Assumptions	12
2.3.4 Surface Errors	12
2.3.5 Misorientation	12
2.3.6 Alignment and Focus	13
2.3.7 Thermal Errors	13
2.3.8 Centrifugal Acceleration Effects	14
2.4 Structural Integrity	15
2.4.1 Static Acceleration Effects	15
2.4.2 Dynamic Characteristics	15
2.4.3 Thermal Effects	16
2.5 Reliability	17
2.6 Recommendations	18
3. COLLECTOR DESIGN	19
3.1 Material	19
3.2 Reflective Coating	21
3.3 Weight	21
3.4 Performance Characteristics	21
3.5 Alternate Structural Design	22
3.5.1 One-Piece Monocoque Structures	22
3.5.2 One-Piece Reflective Skin with Segmented Monocoque Backing Structure	22
3.5.3 Honeycomb Structures	25

	<u>Page</u>
4. MANUFACTURING, TESTING, HANDLING, AND TRANSPORTATION	27
4.1 Master Design and Fabrication	28
4.1.1 Template Machining	29
4.1.2 Blade Grinding	37
4.1.3 Plastic Overlay Process	46
4.1.4 Spin Casting	55
4.1.5 Comparative Evaluation and Recommendations	59
4.2 Mirror Plating Equipment	65
4.2.1 Plating Tank	65
4.2.2 Fluid Storage and Treatment	67
4.2.3 Power Supply	67
4.2.4 Anodes	69
4.3 Mirror Fabrication	69
4.3.1 Torus Fabrication	69
4.3.2 Master Preparation	70
4.3.3 Plating of Mirror Skin	73
4.3.4 Torus Attachment	75
4.3.5 Parting of Mirror from Master	76
4.3.6 Coatings	77
4.4 Testing	78
4.5 Handling and Storage	78
4.6 Transportation	79
4.6.1 Helicopter	80
4.6.2 Ship or Barge	80
4.6.3 Air Ship	80
4.6.4 Airplane	81
5. EFFICIENCY	82
5.1 Collector Obscuration	82
5.2 Reflective Coating	84
5.3 Optimum Collector Rim Angle	87
5.4 Computer Analysis Program	94
5.4.1 Collector Grid	95
5.4.2 Limb Darkening Effects	96
5.4.3 Representation of Surface Errors	96
5.5 Collector Surface Errors	97
5.5.1 Microscopic Errors	103
5.5.2 Macroscopic Errors	103
5.5.3 Long Wave Errors	103
5.5.4 Surface Error Analysis	104
5.6 Misorientation	104

	<u>Page</u>
5.7 Cavity Absorber Assumptions	111
5.8 Alignment and Focus	114
5.8.1 Axial Misfocus	114
5.8.2 Radial Misalignment	117
5.9 Thermal Errors	117
5.9.1 Ambient Temperature Effects	129
5.9.2 Collector Shell Thermal Gradient	129
5.9.3 Differential Thermal Expansion Effects	131
5.10 Effect of Centrifugal Acceleration	131
 6. STRUCTURAL INTEGRITY	 135
6.1 Structural Materials	136
6.2 Design	137
6.3 Axial Acceleration Effects	137
6.3.1 Membrane Analysis	137
6.3.2 Compressive Buckling Stress	141
6.4 Lateral Acceleration Effects	147
6.5 Centrifugal Acceleration Effects	149
6.5.1 Collector Shell	149
6.5.2 Strut Deflections	154
6.6 Vibration	154
6.6.1 Shell Frequencies	154
6.6.2 Torus	157
6.6.3 Torus-Shell	159
6.6.4 Vibration Effects	160
6.7 Shock	165
6.8 Acoustical Noise	166
6.9 Thermal Effects	168
 7. RELIABILITY	 172
7.1 Ground Testing and Handling	172
7.1.1 Coating Adhesion	172
7.1.2 Silver Diffusion	173
7.1.3 Prelaunch Protection	173
7.2 Launch Conditions	174
7.3 Orbit Conditions	174
7.3.1 Temperature Effects	175
7.3.2 Micrometeorites	175
7.3.3 Charged Particles	176
7.3.4 Ultraviolet	176
7.3.5 Miscellaneous	177
 8. WEIGHT CONSIDERATIONS	 179

	<u>Page</u>
8.1 Importance of Weight as an Optimization Parameter	179
8.1.1 Relationship to Competitive Systems	179
8.1.2 Booster Capability	181
8.1.3 Summary	181
8.2 Weight of Collector	182
9. CONCLUSIONS	185
9.1 Power	185
9.2 Reliability	185
9.3 Weight and Volume Collector	187
9.4 Cost	188
10. RECOMMENDATIONS	189
10.1 Structural Testing	189
10.1.1 Model Types	189
10.1.2 Experimental Tests	189
10.1.3 Analytical Correlation	190
10.2 Space Testing of Collector Surface Reflectance	191
APPENDIX A SOLAR BRAYTON CYCLE SPACE POWER SYSTEM ENVIRONMENTAL SPECIFICATION	192
APPENDIX B REFLECTANCE MEASUREMENTS AND SIMULATED MICROMETEORITE TESTS	196
APPENDIX C MASTER GRINDING, POLISHING, AND TESTING	212

NOMENCLATURE

Letters

a	plate width; ellipse diameter
A	area; amplification factor; earth albedo factor
b	radius of spherical cap; ellipse diameter
c	velocity of sound; heat capacity
C	dampening factor
d	cavity aperture diameter
D	diameter: mirror, torus, strut; rigidity
e	vector; master surface error angle
E	Young's modulus
f	focal length; frequency
F	function of; form factor; varies with; Farenheit
h	collector sagitta (without subscript); height (with appropriate subscript)
H	thermal flux
I	moment of inertia
K	thermal conductivity; constant
ℓ	length
L	length
m	mass
n	number: "g's", modes
p	pressure
q	unit load
r	radius: torus, from vehicle axis
R	collector radius: projected, curvature; Rankine (temperature)
s	yield stress; coordinate measured along parabolic curve
S	shear force per lineal inch
t	thickness
T	force per lineal inch; temperature
w	deflection
W	weight
x,y,z	coordinate axis

() Subscripts

1	meridional; sub-one
2	hoop; sub-two
12	shear
a	absorber, air
al	aluminum
b	back
c	collector; curvature; contact line between blade and master
c-a	collector-absorber
cl	classical
cr	critical
d	radiator
e	earth radiation
g	gray, gravity
i	inside
m	material; mirror
m()	mirror
n	natural frequency
ni	nickel
o	outside
p	power system, pressure
()'	prime
r	torus (ring), radiator, earth albedo radiation, radial, resonant
s	shell; strut; solar; spherical cap
x	variable; coordinate axis
y	variable; coordinate axis
z	variable; coordinate axis

Greek Letters

α	thermal expansion coefficient, angle between collector point and collector-vehicle axes; absorptivity; proportional to
β	misorientation angle; cavity form factor
γ	ratio of air heat capacities
δ	difference in reflected cone foci; blade tilt angle
$\Delta()$	difference (without parantheses) difference between ideal and actual parabola
ϵ	emmissivity
ζ	rim angle
Z	variable
η	efficiency; intercepted reflected energy; dissipation factor
θ	angle between radius of curvature and collector axis
λ	wavelength; spherical cap structural factor
ν	Poisson's ratio
ξ	dampening ratio
ρ	density
σ	Stefan-Boltzmann constant; standard deviation, stress
ϕ	collector plan view reference angle, orbit angle
Φ	variable
χ	variable
ω	frequency

Miscellaneous

\perp	perpendicular
$=$	same plane as
$()^{\circ}$	degrees of arc; temperature

SUMMARY

The Brayton Cycle Solar Collector Design Study has developed: parametric analysis of 20- and 30-foot one-piece electroformed mirrors, conceptual designs and manufacturing methods for these concentrators, predicted concentrator performance, analysis of structural integrity, and experimental studies of master fabrication techniques and reflectance samples subjected to simulated micrometeorite damage.

Based on this collector design study a one-piece toroidally supported electroformed nickel collector shell is proposed as the recommended Brayton cycle collector design. A 30-foot diameter, 55 degree rim angle collector of this design would consist of a 0.0107-inch electroformed nickel shell; a chemically deposited, protected silver reflective coating; and a torus of titanium or nickel, 0.030 inch thick. This structure would weigh a maximum of 614 pounds or a specific weight of 0.87 pound per foot² of projected collector area. The efficiency of this collector would be about 80.5 percent for a 0.267 degree misorientation, a radial surface error of 6 minutes standard deviation, 6 percent total obscuration, and 91 percent average surface reflectivity.

Experimental studies have demonstrated that either blade grinding or plastic overlay master fabrication techniques are amenable to the fabrication of high accuracy, highly specular collector masters.

Reflectance samples have been made, tested, and supplied to NASA-Lewis. These were exposed to simulated micrometeorite fluxes and were returned to EOS for retesting to determine reflectance loss.

1. INTRODUCTION

The availability of reliable, long-life, economical space power systems in the multikilowatt range will be essential for meeting the national space exploration goals during the next few years. The manned space stations now being planned are examples of applications for such power systems. At the present time, only solar energy and nuclear energy appear to be capable of supplying sizeable quantities of electrical energy necessary for long-term space missions. For output power levels up to approximately 40 kilowatts, solar energy power systems will probably be lighter, safer, less expensive, and available sooner than nuclear energy systems. Specifically, the solar Brayton cycle system now appears to offer the best promise of any multikilowatt system of being developed to a reliable operational status at an early date.

The feasibility of a practical solar Brayton cycle space electric power system is dependent on the fabrication of a suitable solar concentrator and other components. The highest accuracy, lightweight concentrator mirrors developed to date have been fabricated by one-piece electroforming construction methods. The Saturn-4B and S-2 stages permit maximum mirror diameters of 20 and 30 feet, respectively. Since one-piece electroformed mirrors of this size have not been fabricated previously, specific design and manufacturing problems required further study to demonstrate feasibility of a Brayton cycle solar collector mirror.

The objectives of this Brayton Cycle Solar Collector Design Study Program were to:

1. Conduct parametric analysis of specified variables that influence the performance and efficiency of 20- to 30-foot one-piece, fixed solar collectors.

2. Establish a concentrator design using electroformed nickel construction.
3. Predict concentrator performance under both ground test conditions and orbital use up to 10,000 hours duration.
4. Perform experimental studies on master fabrication techniques, including the construction of two electroformed mirrors, and take reflectance measurements on typical coating samples both before and after simulated micro-meteorite damage.

The Brayton Cycle Solar Collector Design Study is summarized in Section 2 and discussed in detail in Sections 3 through 11.

The emphasis in this program has been to demonstrate feasibility. In certain cases where more than one feasible approach has been found, a premature selection from the available alternatives has been avoided, pending more detailed technical and economic considerations.

The design study indicates that a 30-foot diameter single-piece electroformed nickel toroidally rim supported collector is a feasible concept with a potential of high performance and reliability.

2. PROGRAM COMPENDIUM

The proposed Brayton Cycle Power System offers the advantages of an efficient, reliable solar power system, available on a relatively short time schedule. In evaluating either the Brayton cycle system or the Brayton cycle solar collector designs the following criteria, used either singularly or in various combinations are most important.

1. Performance
2. Reliability
3. Weight
4. Volume
5. Cost

The collector design proposed by Electro-Optical Systems maximizes power output, has good ground test, launch, and orbit capability; satisfies the system packaging volume requirements, and is made by a high accuracy manufacturing process highly amenable to low-cost production techniques. Weight is comparable to that obtained by other known methods.

2.1 Collector Design

The basic Brayton cycle collector design is shown in Fig. 2-1, stowed in the launch position. The proposed collector is a single shell paraboloid, toroidally supported at the rim, with a 55-degree rim angle for the 30-foot diameter size and either a 38-degree or 55-degree rim angle for the 20-foot diameter collector. The nickel shell and nickel or titanium torus thicknesses are 0.0107 and 0.030 inch, respectively. Collector launch support will be by either eight mounting points or a continuous ring attached to the radiator. During orbit the collector will be attached to the cavity absorber by a tripod or quadrapod.

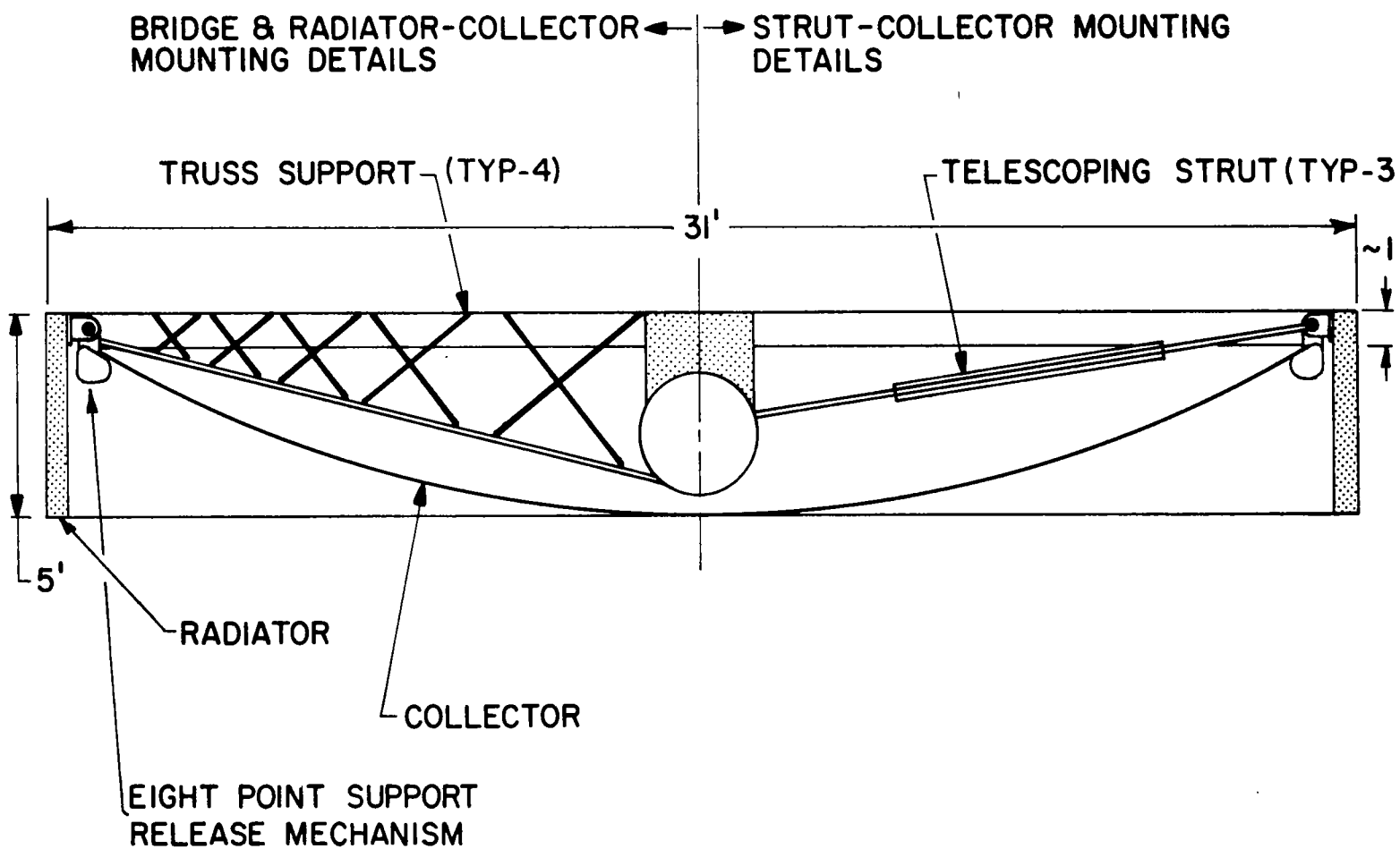


FIG. 2-1 COLLECTOR-RADIATOR MOUNTING DETAILS

The structure will be made either of all nickel or nickel and titanium. The nickel collector shell and the shell torus joint will be electroformed. The nickel torus will be electroformed whereas the titanium torus, proposed as an alternate design would be fabricated.

A collector-absorber efficiency of 80 percent can be expected for the following conditions:*

Maximum surface error - 6 minutes standard deviation

Misorientation - 0.276 degrees

Obscuration 6 percent

Reflectance 91 percent

Cavity absorber - blackbody at 2110°R operating temperature

Cavity aperture - 8 inches diameter

The weight of the proposed collector will be approximately 510 pounds (or 0.7 lbs per ft²) for the nickel-titanium collector and 614 pounds (or 0.87 lbs per ft²) for an all nickel collector.

The EOS collector design advantages include:

1. High power output and collector-absorber efficiency
2. High accuracy, specular surface
3. High reflectance, low cost, reflective coating
4. Low stressed, uniform, highly efficient paraboloidal shell
5. Single structural joint
6. All-metal construction
7. No closed gas pockets
8. High reliability capability - earth, launch and orbit
9. High manufacturing process uniformity, reproducibility and control
10. Potential low production costs

*These neglect efficiency losses due to thermal distortion

2.2 Manufacturing, Testing, Handling, and Transportation

The fabrication of the large Brayton cycle collectors will be similar to the processes developed at EOS for smaller mirrors. The mirror will be made of electroformed nickel. It will be replicated from an accurate, polished, convex parabolic master.

2.2.1 Master Design and Fabrication

Because of the large size and deep curvature of the paraboloidal master, conventional glass grinding and polishing techniques are not suitable. Several other techniques have been evaluated.

2.2.1.1 Template Machining

In this process, the master consists of a fabricated metal substructure coated with a polishable material such as epoxy or polyester plastic. The surface shape of the master is generated by a machine tool which is supported above the master and guided over its surface by a rigid overarm. The path of the machine tool is guided from the center to the rim of the master by an accurate template mounted on the overarm. The overarm rotates about the optical axis as the machine tool traverses the surface. (Alternately, the overarm is fixed and the master rotates about the optical axis.)

This process has been developed at EOS for making masters for segmented solar collectors.

2.2.1.2 Blade Grinding

The blade grinding process is a method of generating a paraboloid of revolution automatically. This is made possible by a basic geometric property of the paraboloid of revolution and does not require any accurate preshaped guide templates (see Subsection 4.1.2). Structurally, a blade ground master would be identical to one made by the template machining process. However, the surface would be generated by a blade which would be moved back

and forth over the rotating master surface by a mechanism which maintains the blade at all times parallel to the mirror optical axis. This process was successfully demonstrated on 2-foot diameter masters for this program as a method of producing accurate parabolic surfaces.

2.2.1.3 Plastic Overlay Process

This process provides a method of obtaining an accurate polished master without the necessity of polishing the final paraboloidal surface. First, a master substructure is prepared in the same way as for the previous two processes. Next, a thin layer of plastic is cast between two glass sheets. Prior to final cure, the plastic layer is removed from the glass and is draped over the master surface, being brought into conformity by mechanical stretching. The plastic is then permanently bonded to the master surface and allowed to complete curing.

This process has also been demonstrated on this program as a method for producing accurate, specular paraboloidal surfaces.

2.2.1.4 Spin Casting

This process utilizes another natural phenomenon to generate a paraboloidal surface automatically. If a container of liquid, such as an epoxy resin, is rotated about a vertical axis and allowed to solidify while rotating, a permanent paraboloidal surface will be formed.

2.2.1.5 Comparison of Master Fabrication Techniques

The first three techniques allow direct fabrication of the convex master. The final process, spin casting, requires that a concave surface be made first. This is then replicated to form the convex master. This extra step increases the process cost and decreases accuracy, making the spin casting process less desirable than the other three techniques. It has been shown at EOS that the

template machining, blade grinding, and plastic overlay processes are all suitable for forming large, accurate, highly polished masters. A choice between these techniques will be made on the basis of more detailed economic considerations.

2.2.2 Mirror Fabrication

2.2.2.1 Torus Fabrication

The first manufacturing step is the fabrication of the torus. This will either be made of nickel by electroforming on a prepared aluminum mandrel, or it will be made of titanium by conventional forming techniques.

The torus is laid on the master surface and a wax mandrel for the mirror skin edge radius is cast against it. The torus is then removed and the master is made electrically conductive by chemically depositing on it a layer of pure metallic silver.

2.2.2.2 Mirror Plating

During plating of the collector skin the master serves also as the bottom of the plating tank. The tank sides are a removable cylindrical shell. The plating solution is stored in a separate tank and is pumped into the plating tank through filters and pumps. Current is fed to the anodes and the master surface (cathode) until the desired thickness of deposit has been built up. Finally, the plating solution is pumped out and the deposit is washed.

2.2.2.3 Torus Attachment

The torus is then placed on the nickel skin (still attached to the master). It fits into the edge radius and is bonded to the skin by means of an electroformed joint.

2.2.2.4 Parting

The mirror is parted from the master by a combination of mechanical lifting, air pressure between the mirror and the master, and differential thermal expansion caused by localized heating. After the mirror has been separated from the master it is cleaned.

2.2.2.5 Coatings

If the recommended silver coating is to be used, no further coatings are applied except for protective layers. If some other coating is to be applied, the silver is removed chemically and the desired coatings are applied by vacuum deposition.

2.2.3 Testing, Handling, and Storage

Optical and structural tests would be performed on the mirror in much the same manner as has been developed for smaller mirrors. The detailed nature of tests to be run must be determined by system design requirements. Optical tests will probably involve primarily solar calorimetric and Hartmann testing.

In-plant handling and storage should involve no radically new techniques. A handling and storage container will be provided for each mirror. This container will also serve as a handling fixture for use in parting and moving the mirror. One of several available protective methods will be used to prevent tarnishing of the silver coating during ground storage.

2.2.4 Transportation

Transportation of this mirror is made difficult by its large bulk. Surface transportation over the public highways is awkward even for short distances. Four methods of moving the mirror over short and long distances are potentially available:

1. Helicopter
2. Barge or ship
3. Blimp
4. Airplane

The helicopter would be used for most short-distance transportation.

2.3 Efficiency

The total power absorbed by the cavity absorber (exclusive of the cavity thermal losses due to sources other than the cavity aperture reradiation losses) is directly proportional to the combined collector-absorber efficiency. Collector-absorber efficiency is herein defined as the net power absorbed by the cavity absorber (assuming only blackbody cavity aperture reradiation losses) divided by the gross power which would be intercepted by an unobstructed collector. This collector-absorber efficiency includes these losses:

1. Collector obscuration
2. Reflective coating reflectance loss and degradation
3. Cavity reradiation
4. Misorientation
5. Alignment and focus
6. Surface errors
7. Errors due to thermal distortion
8. Centrifugal effects

2.3.1 Collector Obscuration

A collector obscuration factor of 6 percent was used in all calculations. This yields a net of 94 percent of the original power striking the collector reflective surface. It is well to note that collector obscuration as well as cavity reradiation at operating temperature are often omitted in reporting collector efficiency.

2.3.2 Reflective Coating: Reflectance and Durability

The reflectance of the chemically deposited silver reflective coating will be 91 percent or greater. Based on calculated space environmental degradations, a loss of less than 1 percent reflectance over the 10,000 hour design life of this collector is predicted.

2.3.3 Absorber Assumptions

For convenient comparison the absorber was assumed to be an isothermal blackbody cavity. A blackbody cavity cannot be made in practice; therefore, it can reasonably be expected that the overall collector-absorber efficiency will be less than values quoted using blackbody assumptions.

2.3.4 Surface Errors

At the cavity design aperture of 8 inches and a collector misorientation of 0.267° (16 minutes) the following table lists radial surface errors (standard deviation) and the corresponding collector-absorber efficiencies.

σ <u>minutes</u>	η_{c-a} <u>%</u>
0	82.0
2	81.8
4	81.4
6	80.5
15	72.5

This rapid decrease in collector-absorber efficiency with increasing surface error demonstrates the high premium which must be placed on collector surface accuracy if a highly efficient Brayton cycle power system is to be achieved.

2.3.5 Misorientation

The effect of collector misorientation up to 0.533° was determined for collectors having 0, 2, 4, 6, and 15 minutes standard deviation radial error, respectively. For a given cavity aperture highly accurate collectors are much less sensitive to misorientation and achieve the highest collector-absorber efficiency.

2.3.6 Alignment and Focus

An axial misfocus of the cavity aperture of ± 0.5 inches will produce less than 1.5 percent of collector-absorber efficiency loss for a 6 minute standard deviation mirror and an 8 inch aperture. With the same errors and aperture, a radial misalignment in the focal plane of $\pm 1/2$ inches will result in a 1/2 percent loss.

2.3.7 Thermal Errors

The maximum axial misalignment due to a uniform ambient temperature change will be less than ± 0.1 inches assuming a constant ambient temperature for the struts and collector assembly. If the collector shell edge is unrestrained, the maximum angular error due to an expected temperature gradient through the collector shell of $0.156^{\circ}\text{F}/\text{inch}$ will be less than one minute of error at the rim. One could reasonably expect that the shell temperature gradient would produce a collector-absorber efficiency loss of considerably less than one percent.

The torus can be maintained within $\pm 10^{\circ}\text{F}$ of the average integrated collector surface temperature from the center to the rim. Such a 10°F temperature difference produces edge deflections and rim distortions which may cause a collector efficiency loss of up to 1-1/2 percent. Since the edge distortions caused by the torus differential thermal expansion and the collector shell thermal gradient rim effects occur in the same area, maximum rim efficiency losses of 1.7 percent or less may occur.

The effect of transient thermal variations across the collector surface due to thermal flux changes during orbit will tend to cause axial misfocus of less than 0.1 inches. Therefore, the total collector-absorber efficiency loss due to temperature effects can reasonably be expected to be 2 to 4 percent or less. Based on these assumptions, the 80.5 percent performance value might be reduced to between 76.5 and 78.5 percent.

2.3.8 Centrifugal Acceleration Effects

Deflections of the collector torus caused by centrifugal acceleration during orbit may produce collector-absorber efficiency losses in the same order of magnitude as the thermal losses. The exact loss in efficiency depends to a large extent upon the design of the collector torus and collector-to-cavity supporting struts. These performance losses were not included in the 80.5 percent figure.

2.4 Structural Integrity

The proposed toroidally supported collector shells are of all-metal construction. Exclusive of the reflective coating, the construction will be either all nickel or a nickel shell joined to a titanium torus. The titanium torus can achieve lower total weight, at a sacrifice in differential thermal expansion control.

The one-piece electroformed shell design provides good uniformity of shell thickness, near-zero residual forming stress, and near-maximum structural efficiency. The use of only a single structural joint and the absence of any closed pockets to entrap gas minimize the problems of localized structural failure.

2.4.1 Static Acceleration Effects

The tensile stresses caused by axial accelerations will not damage the structure. Using the extrapolated results of recent empirical investigations on thin electroformed spherical caps, it can be shown that a collector shell of the design thickness (10.7 mils) will withstand the maximum negative accelerations specified in the environmental specification.

The shell stresses produced by centrifugal acceleration collector assembly are quite low. No difficulties due to compressive buckling are expected.

The stresses produced by centrifugal acceleration during orbit are less than 17 lbs/in^2 maximum and will have no adverse effect on the structural integrity.

2.4.2 Dynamic Characteristics

The collector vibration characteristics will depend largely on the mounting designs for the launch and orbit cases. During launch, and assuming a continuously supported torus, the collector shell is assumed to vibrate in the axisymmetric breathing mode. For these assumptions, the natural frequency is in the range of 80-150 cycles per second. For the cases of 3-, 4-, or 8-point suspension of the torus during either launch or orbit, collector vibrations will be

determined primarily by the torus natural frequencies. For these cases the collector natural frequencies will range between 2 and 20 cycles/sec. Because of the high degree of air dampening for this structure for high frequency vibrations (greater than 36 cycles/second), a continuously supported torus design is preferred for launch. During orbit, the quadrapod strut design is preferred from a vibrational standpoint.

The 35g shock loading will have no permanent effect on the continuously supported structural design. The 8-point torus mounting during launch, appears marginal for the present torus design.

The static pressure equivalent to the net positive radiation pressure of a 148 db acoustical noise field, Re 0.002 microbar, is an order of magnitude less than the critical buckling pressure and should present no buckling problems. The dynamic effects of the collector shell, compared with available test data on aluminum plates, indicate that the nickel shell stress due to acoustical noise conditions should be low.

2.4.3 Thermal Effects

The transient temperatures encountered by the collector should not cause collector structural failure due to the effects of thermal shock, ambient and transient changes, and the thermal gradient across the collector shell.

2.5 Reliability

Analytical calculations indicate that the proposed design concept will have a high reliability and structural integrity throughout the ground test, launch, and orbit phases. These calculations are based on the analysis of the following possible problem areas:

1. Environmental specifications
2. Ground atmospheric environment
3. Micrometeorites (computed)
4. Temperature
5. Ultraviolet radiation
6. Vacuum
7. Charged particles
8. High energy, electrons, protons, photons, x rays

The potential high reliability of the proposed design is due to the following factors:

1. All-metal construction
2. One-piece electroformed nickel shell
3. Low residual stress
4. No pockets for gas entrapment
5. Single joint
6. Electrochemical bonds between torus and shell
7. Low thermal expansion material(s)
8. Low thermal gradient across collector shell
9. High air dampening
10. Reflectance coating with potentially high resistance to space environment
11. High collector-absorber efficiency

2.6 Recommendations

Based on this design study additional information is required in two areas:

1. Additional structural investigation
2. Space reflectance measurements

It is recommended that work be performed in the following areas:

1. Static buckling
2. Vibration
3. Acoustical noise
4. Thermal stress

Optical tests would be performed before and after structural tests to determine the degree of collector deterioration, if any. Based on the results of these structural tests the design calculations used in this study can be verified and improved.

In-space measurements of collector reflectance degradation are necessary to verify predicted degradation rates. Space experiments to obtain this data are in the planning stages. No final proof of collector durability will be available until these experiments are run.

3. COLLECTOR DESIGN

The collector design proposed by EOS is shown in Fig. 3-1. The proposed structure is a paraboloidal nickel shell supported by a rim mounted torus with suitable mounting brackets for the torus-to-radiator and absorber-to-torus supports.

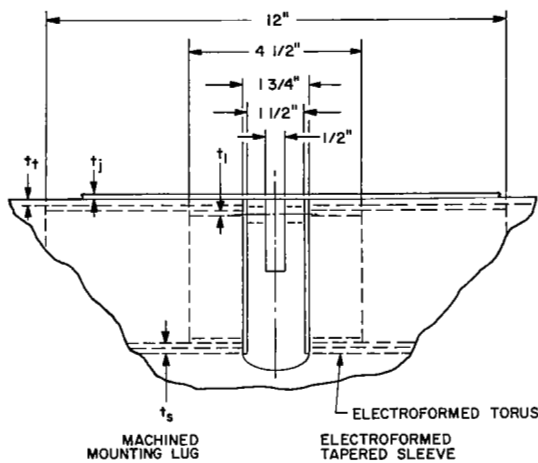
The maximum diameters for collectors intended for integration with the Saturn S-4B and S-2 stages will be 20 ft and 30 ft respectively.

For the 30-ft diameter collector a rim angle of 55° is proposed, corresponding to a 14.4-ft focal length paraboloid. As a first choice it is suggested that the 20-ft diameter collector be fabricated from the same 14.4-ft focal length paraboloidal master. This would result in a 38.3° rim angle 20-ft diameter collector. As a second choice the 20-ft diameter collector would be fabricated from a 9.6-ft focal length master corresponding to a 55° rim angle. The 55° rim angle collector was chosen primarily for packaging, weight, and structural integrity considerations. A detailed analysis of the optimum rim angle is given in Section 5.

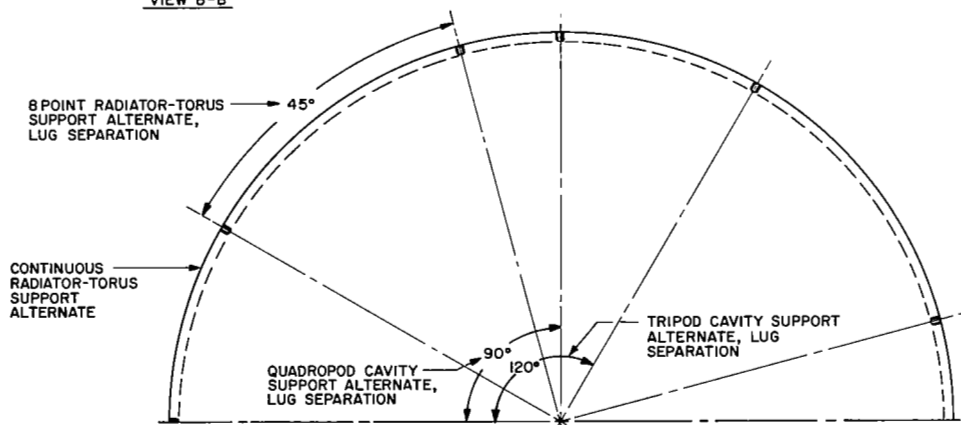
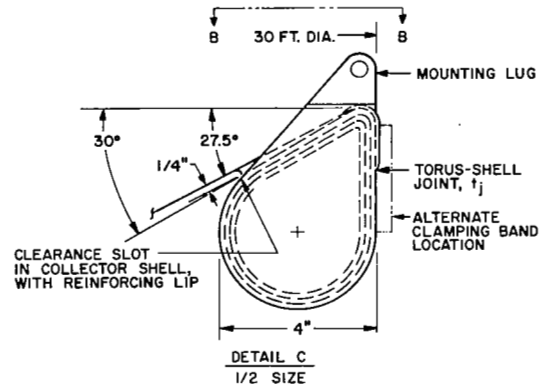
As a first choice the collector will be mounted by a continuous torus support during launch. Alternatively, an 8-point mounting support with the necessary toroidal and radiator brackets can be used. In orbit either a telescoping tripod or quadrapod strut support of the collector torus from the cavity absorber can be used. A quadrapod support is recommended for structural reasons.

3.1 Material

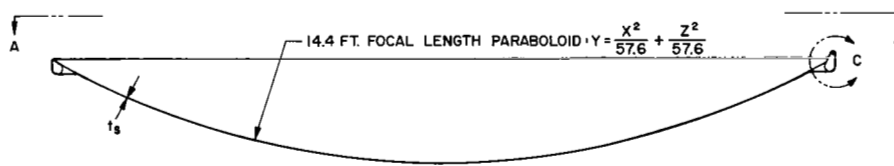
The collector shell will be fabricated from electroformed nickel (see Section 4). The residual shell stresses will be less than 500 lbs/in² because of the excellent stress control possible with



VIEW B-B



VIEW A-A MOUNTING LUG LOCATIONS



CROSS-SECTION OF 30 FT. COLLECTOR

SEE SECTION 4 FOR MANUFACTURING DETAILS

ITEMS	ALL-NICKEL COLLECTOR	TITANIUM TORUS NICKEL SHELL
t _t	.030 inches	
t _s	.030	.015
t _l	.080	.040
t _s	.0107	.0107
t _j	.020	.020

FIG. 3-1 30-FT COLLECTOR DESIGN DETAILS

nickel electroformed from the sulphamate solution. The joint between the torus and shell will also be of electroformed nickel. The torus will either be nickel or titanium. The mounting brackets between the radiator and torus and between the cavity absorber and torus can be fabricated from either aluminum, titanium, magnesium, or nickel.

3.2 Reflective Coating

The first choice for the reflective coating will be chemically deposited silver applied prior to electroforming on the master surface. The coating thickness will be $800\text{\AA} \pm 200\text{\AA}$. The durability of the silver coating will be discussed in Section 7.

As a second choice the electroformed nickel shell would be coated with a vacuum deposited multiple coating in the following sequence:

(Nickel substrate)

Chromium - $200\text{\AA} \pm 100\text{\AA}$

Silicon monoxide - $2500\text{\AA} \pm 250\text{\AA}$

Aluminum - $1000\text{\AA} \pm 200\text{\AA}$

3.3 Weight

The weight of electroformed collectors can be varied greatly merely by varying the thicknesses of the nickel skins and the nickel or titanium torus walls. The actual design weight for a particular collector is chosen to meet the specified environmental conditions. For the Brayton cycle collector, a specific weight ranging from 0.7 lbs/sq ft for a nickel shell-titanium torus collector to 0.8 for an all nickel structure appears adequate to meet the specified requirements. A weight summary for this design is given in Section 8.

3.4 Performance Characteristics

A collector-absorber efficiency of 80.5 percent can be expected, based on:

Maximum surface error	- 6 minutes standard deviation
Misorientation	- 16 minutes (0.267°)
Obscuration	- 6 percent
Reflectivity	- 91 percent

Blackbody cavity absorber at 2110°R

Cavity aperture - 8 inches diameter

Additional efficiency losses may occur from misalignment and misfocus, thermal effects, and centrifugal structural effects (see Section 5).

3.5 Alternate Structural Design

The main structural problem for the toroidally supported shell collector is compressive buckling. Early in this program several alternate design concepts were considered. However, all except the toroidally supported structure were disregarded either because they did not help to prevent buckling or because they suffered from a loss of efficiency or reliability compared with the toroidally supported shell structure. Some of these concepts do have greater resistance to compressive buckling. If it should be found that compressive buckling is more serious than is now calculated, certain features of these designs could be applied to the toroidally supported structure at some expense in performance and reliability. Under some circumstances, the proper use of these concepts could result in a slight weight reduction.

3.5.1 One-Piece Monocoque Structure

In this design concept, Fig. 3-2, the front skin is rigidized by a second compound-curved shell of deeper curvature attached to the front skin at the edge. However, this concept does not provide the high edge rigidity required for the strut support brackets. Furthermore, it adds nothing to the compressive buckling resistance of the front shell. Consequently, it is not recommended for this application.

3.5.2 One-Piece Reflective Skin with Segmented Monocoque Backing Structure

In this concept, Fig. 3-3, the front skin is plated in a single piece as in the toroidally supported structure. However, the backing structure consists of petal-shaped monocoque shells, which are attached to the front skin along the edges of the petal-shaped segments, as well

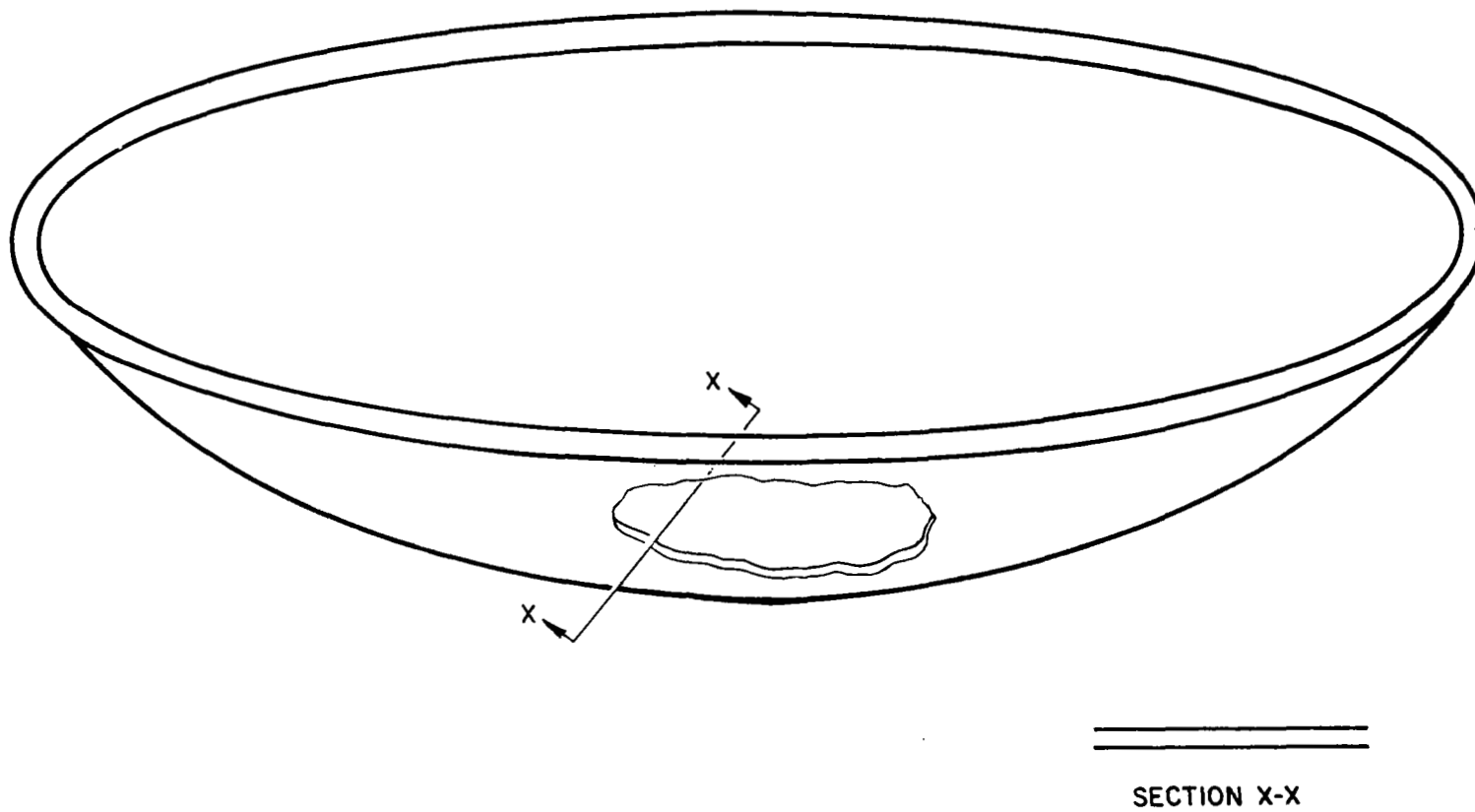


FIG. 3-2 ONE-PIECE MONOCOQUE STRUCTURE

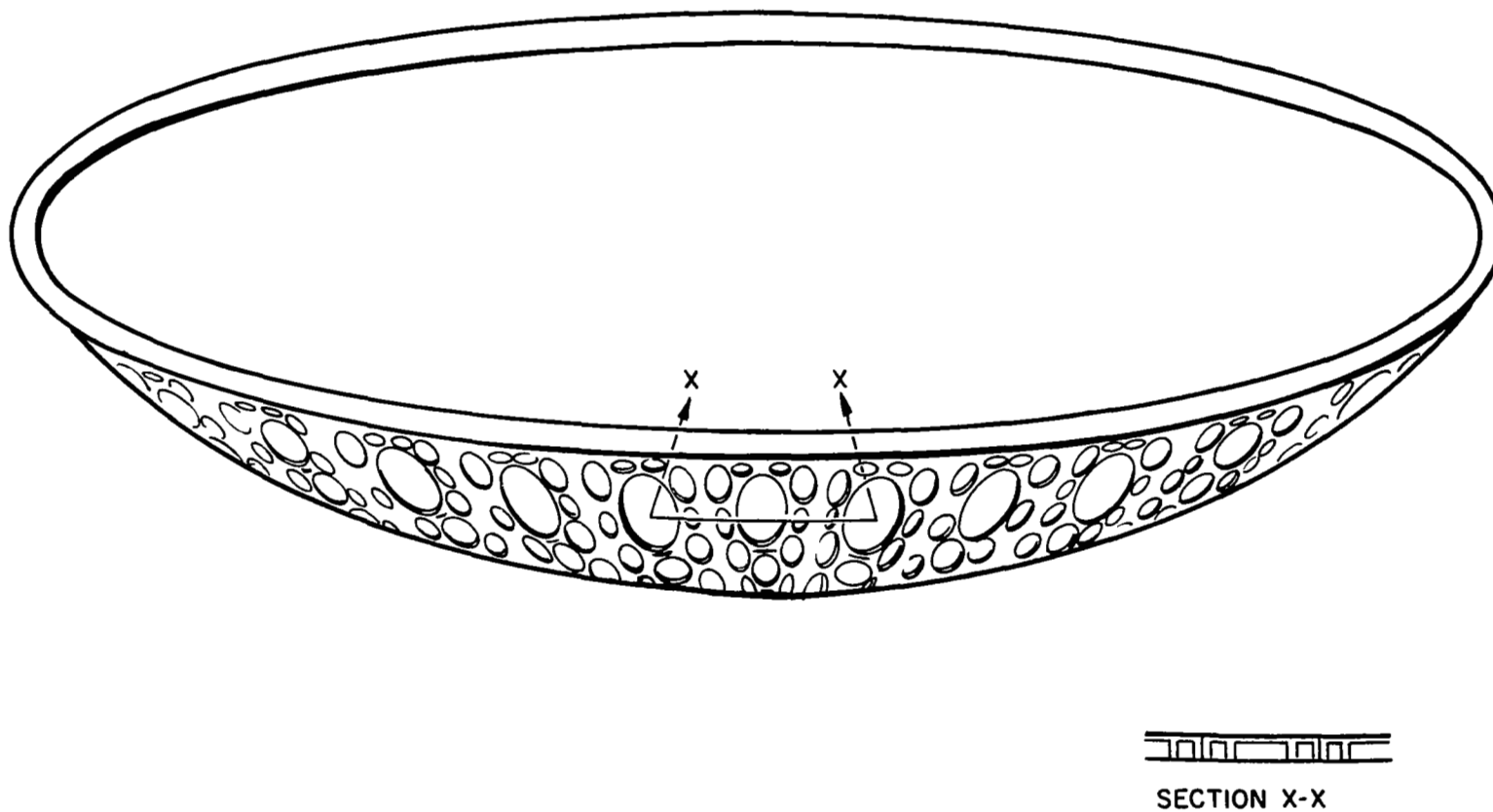


FIG. 3-3 ONE-PIECE REFLECTIVE SKIN WITH SEGMENTED MONOCOQUE BACKING STRUCTURE

as at some intermediate points. Although the compressive buckling resistance of this structure may be somewhat better than for the toroidally supported shell structure, the edge rigidity is low unless a torus is used and the optical performance is degraded by distortion at the attachment points on the reflective skin.

3.5.3 Honeycomb Structures

The rigidity of the toroidally supported shell structure can be somewhat improved by applying honeycomb stiffeners to the back surface of the shell, Fig. 3-4. The honeycomb would not be the common expanded metal type, but would be an electroformed configuration made in one piece and having its own structural rigidity. These honeycomb sections could be bonded to the shell structure wherever needed to increase rigidity. The bonding could be accomplished either by relatively conventional adhesive techniques or by direct electroforming. The latter would retain the advantage of an all-metal structure, free from organic materials. The efficiency loss with this concept would probably be less than for any of the above approaches. Even so, it is not recommended unless the simple, toroidally supported shell structure suffers from unexpectedly severe buckling problems. If this should occur, the use of these special electroformed honeycomb stiffeners would provide a positive method of assuring the integrity of the basic electroformed collector structure.

The use of the electroformed honeycomb stiffening structure would allow the design of a collector structure which would be somewhat lighter than the toroidally supported shell structure. However, the reduced collector performance and the increased thermal distortion problems would no doubt more than compensate for the weight saving, unless the stiffeners are needed to prevent buckling.

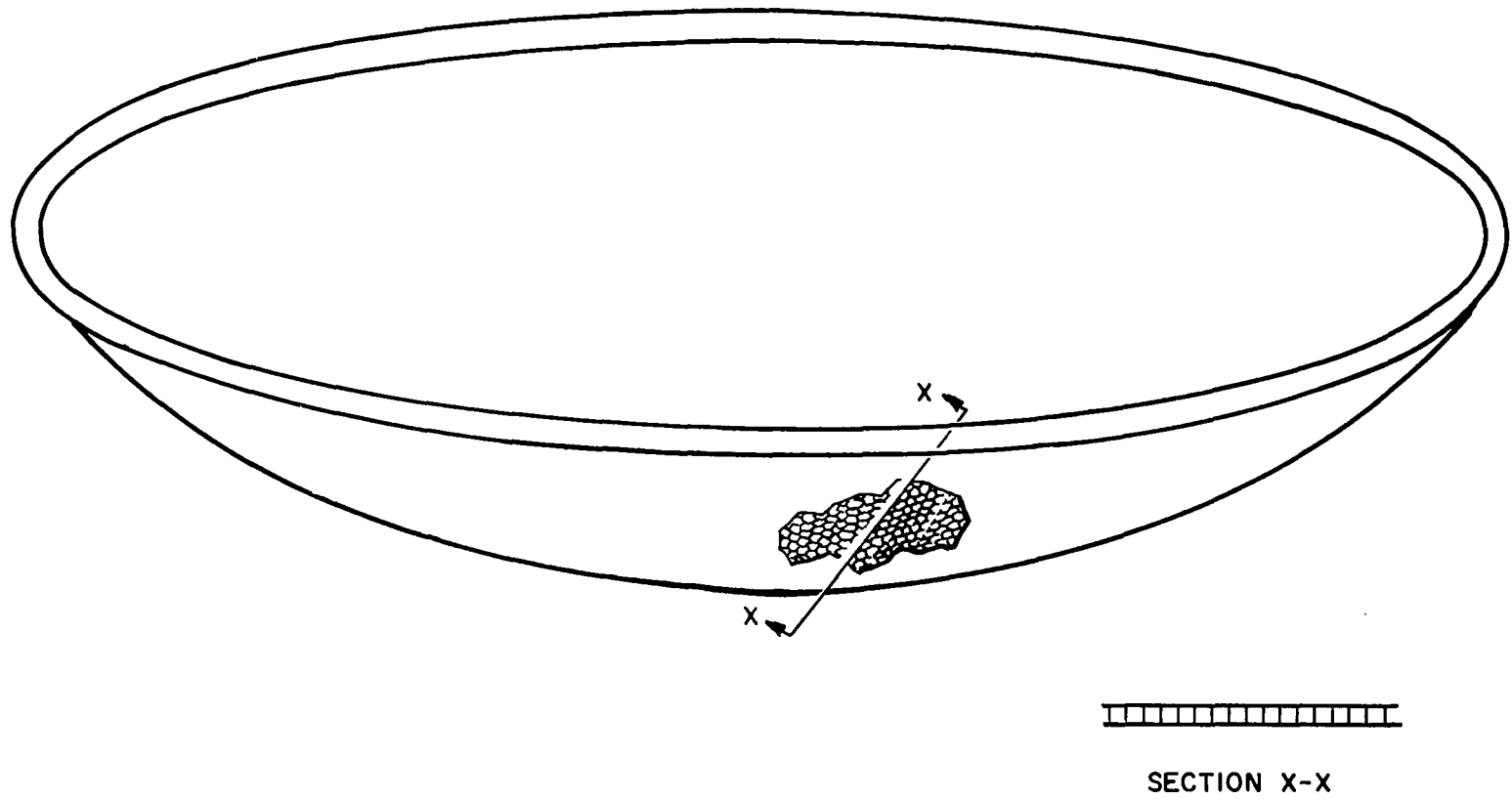


FIG. 3-4 ONE-PIECE REFLECTIVE SKIN WITH HONEYCOMB BACKING STRUCTURE

4. MANUFACTURING, TESTING, HANDLING, AND TRANSPORTATION

The steps involved in the manufacture of the large Brayton cycle collectors will be similar to those developed for smaller mirrors at EOS. Aside from making the master, the difficulty in making electroformed replica mirrors does not increase proportionately with size. In some cases, process modifications will be necessitated by the larger scale of the big mirrors, because of the impracticality of handling the larger components in ways that are relatively simple for five-foot mirrors. However, very few new technical problems inherently related to the larger size are contemplated.

The elements of the proposed fabrication process were summarized in Subsection 2.2. The main features of the process are examined in greater detail in this section.

4.1 Master Design and Fabrication

The first manufacturing step is the design and fabrication of a geometrically accurate and highly polished master. The master surface is to be a convex paraboloid of revolution. Several techniques have been developed for generating paraboloidal surfaces for optical elements. Concave paraboloidal telescopic mirrors are made by generating, first, a spherical surface. The center of the sphere is then deepened by hand corrections until the desired paraboloid is produced. This is a laborious and exacting process and is only suitable for very shallow curves, for which the difference between the sphere and paraboloid is slight. Deeply curved shapes, such as solar collectors, require other methods of generating the surface contour. Several methods will be described in this section.

Consideration must also be given to the material from which the master surface is formed. Ground and polished glass masters have been used successfully for solar collectors up to five feet in diameter. The largest glass telescope mirror is that of the 200-inch Palomar telescope. However, casting the blank for the Palomar telescope was an extraordinarily difficult challenge to the glass makers' art. For example, an annealing period of 18 months was required to relieve stresses adequately. Casting of a glass blank for a 20- or 30-foot diameter master would be of comparable or greater difficulty and cost. Although it is conceivable that the master surface could be built up from smaller glass sheets (perhaps slump molded over a substrate form) there are at least two other major objections to use of glass for large collector masters:

1. Glass masters may be cracked or broken during plating if plating stresses are not adequately controlled or if the parting layer adhesion is excessive.
2. Parting is more difficult from glass masters because of the greater adhesion of the parting layer to glass as compared with other proposed materials.

Although it is technically feasible to make a 30-foot diameter master of glass, practical considerations weigh heavily against considering glass masters for this application.

Fortunately, several other methods and materials are available. This section will begin with a detailed description of four such methods: template machining, blade grinding, plastic overlay, and spin casting. This will be followed by a comparative evaluation and recommendations for the full-scale mirror development program.

4.1.1 Template Machining

4.1.1.1 Process Description

In this process, the master consists of a rigid substructure coated with a polishable material. The surface is shaped and polished by a template-guided grinding and polishing tool supported in a suitable traversing mechanism.

A schematic diagram of a typical setup is shown in Fig. 4-1. The master substructure must be quite rigid to withstand stresses encountered during polishing and plating of the mirror. The substructure is built up from fabricated steel. The upper surface is a welded steel shell formed to the approximate curvature of the final master. If necessary, the steel surface would be machined (using the method described below) to bring the surface more nearly into conformity with the paraboloidal shape. At this point, a linear deviation of not more than $\pm 1/8$ to $1/4$ inch is adequate. The master surface is then coated with a layer of filled epoxy resin between $3/8$ inch and $3/4$ inch thickness. After curing, this layer is machined to within $\pm 1/16$ inch of the paraboloidal curve. A final surface layer of a polishable material is then applied. Typically, this layer would be an unfilled epoxy or polyester plastic. (Specific results regarding polishing experiments for these materials are discussed in Appendix C.) This surface layer is then ground and polished to the best accuracy and surface finish obtainable.

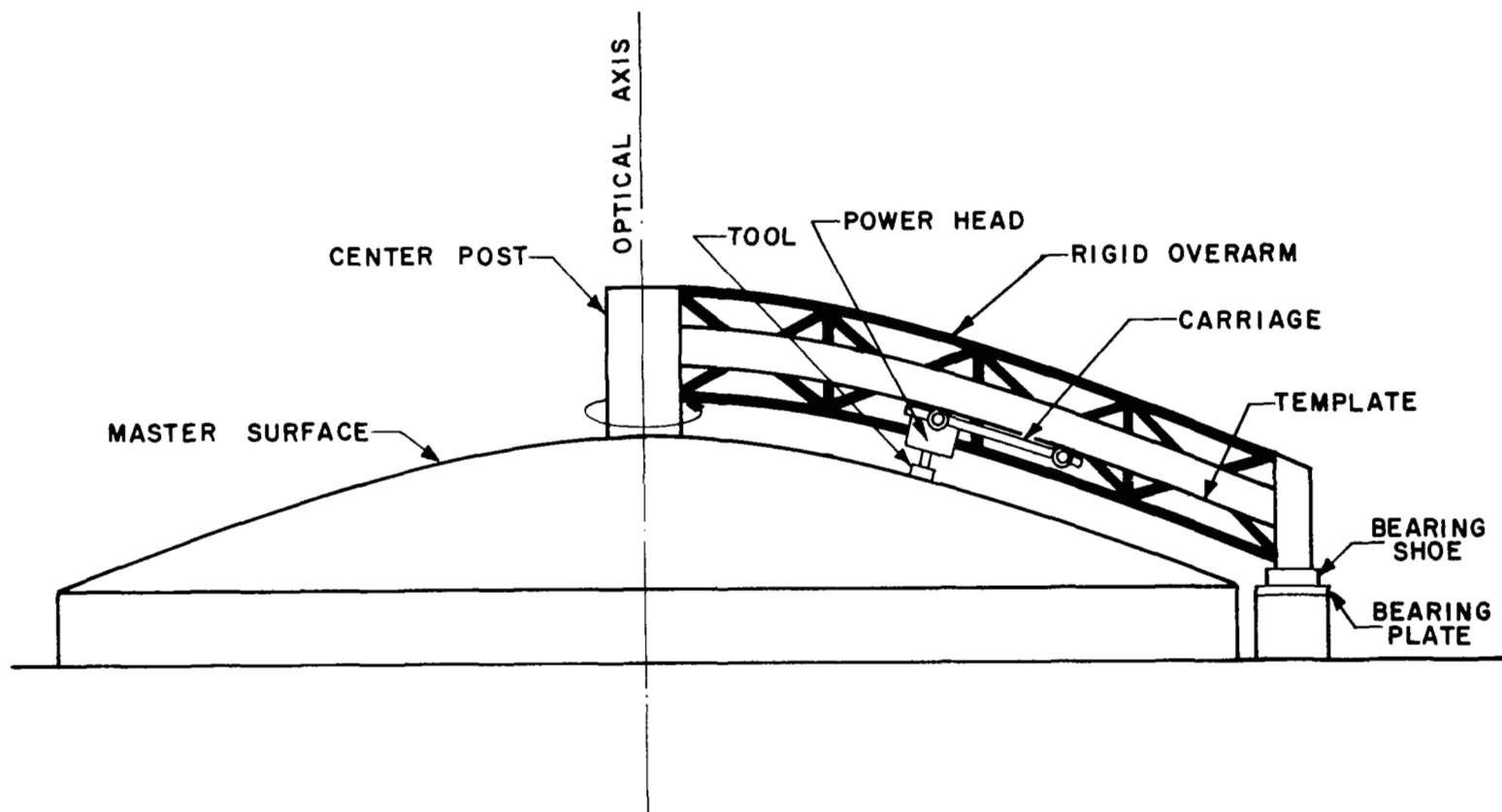


FIG. 4-1 TEMPLATE MACHINING OF PARABOLOIDAL MASTER

All machining, grinding, and polishing operations are accomplished using the apparatus shown schematically in Fig. 4-1. The master is mounted on a rigid base. A rigid overarm is mounted above the master surface. An accurate template or set of templates is mounted on the overarm. This template (or templates) guides the motion of a carriage which in turn carries the machining, grinding, and polishing tools. A drive mechanism is provided to move the carriage along the overarm between the center and rim of the master. At the same time, the overarm is rotated about the master optical axis. The outer end of the overarm is supported by a flat bearing. In this way, all points on the mirror surface can be reached. (An alternate, but equivalent, arrangement can be devised in which the overarm remains fixed and the master rotates about its optical axis.) In this case, the master rotation must be held so that $\text{RPM} \times r \approx K \pm 25\%$, where r is the radius at which machining occurs, K a constant and RPM the rotations per minute. A variety of tools can be used depending on the particular operation:

1. Single point cutters for rough machining
2. Rotating for wheels for grinding or polishing
3. Vibrating tools for fine grinding or polishing

The guide templates are curves developed from the ideal parabola in such a way that the tool will traverse the desired curve while at all times remaining at the proper angle with the surface.

The master is maintained at a constant temperature during the grinding and polishing operations and throughout the mirror plating operations. This temperature is to be equal to the bath plating temperature and is maintained by a thermostatically controlled water passage below the surface shell of the master (see Subsection 4.2.1). Maintenance of the constant temperature is necessary to minimize thermal stressing and distortion of the plastic surface layer.

4.1.1.2 Current Status

In all its essential features, this process is akin to conventional machining operations as well as conventional optical grinding and polishing techniques. It differs from conventional

practice only in size and in the specific configuration of the equipment.

An evaluation of the process for making solar collector masters has been performed at EOS on three different scales, 2-foot, 10-foot, and 44.5-foot diameter.

Two-Foot Diameter One-Piece Master. On a previous program at EOS, a 2-foot diameter paraboloidal master and machining set-up was made to evaluate this process. This setup is shown in Fig. 4-2. The templates are parabolic cams placed on either side of the master. A straight edge placed between the two rails is approximately tangent to the master surface. A carriage rides on these rails and is moved back and forth by a drive mechanism. The master substructure consists of a steel tankhead with a welded base plate. The tankhead was coated with a thick layer of filled epoxy resin that was machined to the approximate curvature desired. On the previous program, the surface layer material was an unfilled layer of polyester resin. Machining, grinding, and polishing were accomplished by a single point cutter or a rotary power head mounted on the carriage to perform the various machining, grinding, and polishing operations. During the previous program, a series of experiments was run in which the master was machined and ground to shape using a high speed router as the cutting tool. Final polishing was then done by hand. It was found that a satisfactory geometry could be obtained during the machining and grinding operations. Although, hand polishing produced an excellent finish, the pressure irregularities degraded the geometry somewhat during the polishing phase. Several replica mirrors were made from this master.

On the present program, this master was re-activated with the objective of continuing polishing experiments to see if better results could be obtained by completely mechanical methods. A preliminary series of experiments was run to check out the equipment.

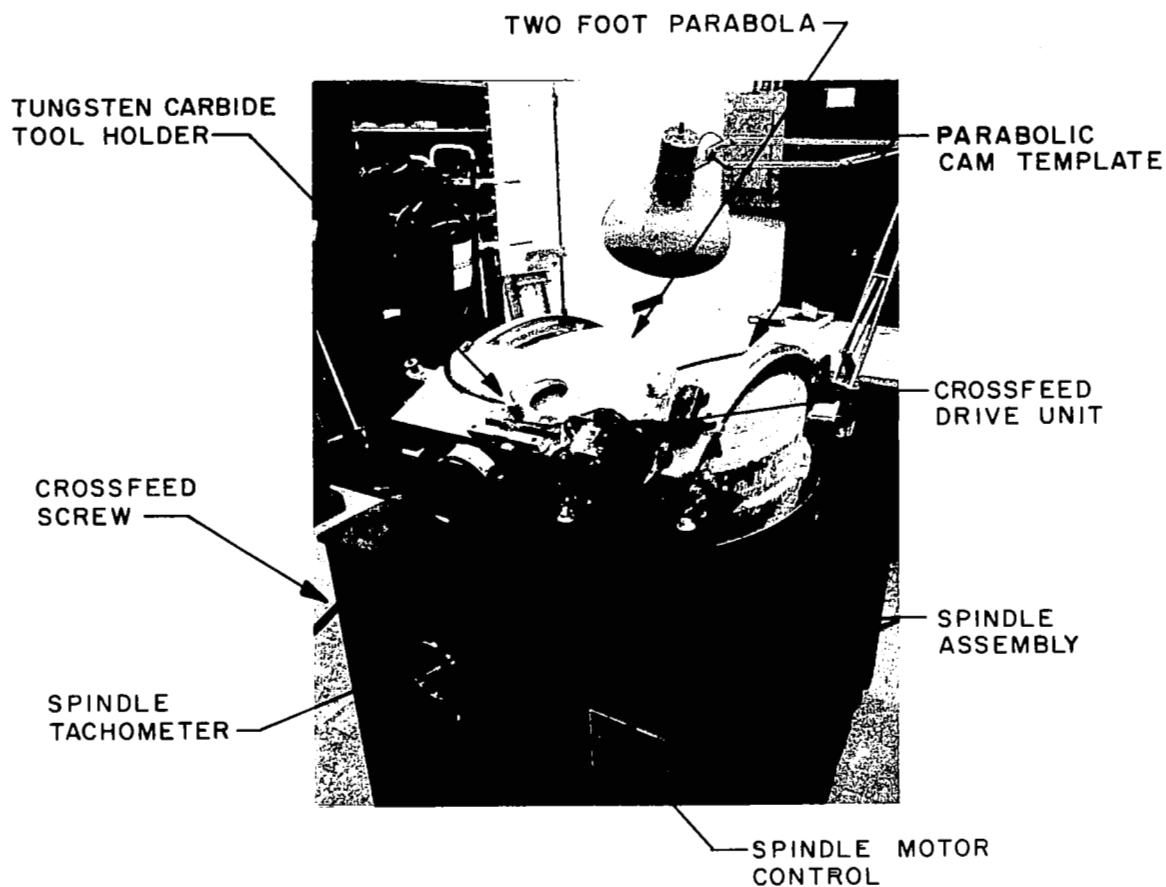


FIG. 4-2 CAM-TEMPLATE MACHINING ASSEMBLY
WITH TWO FOOT PLASTIC MASTER

At about this time in the program, the machine for polishing segments of a 10-foot mirror was put into operation on another program at EOS (see next Subsection). It was felt to be redundant to evaluate the same process on two different programs at EOS. Therefore, the two-foot diameter master equipment was modified to perform the blade grinding process (see Section 4.1.2).

Segment Masters for 10-Foot and 44.5-Foot Diameter Mirrors

Under a series of programs, EOS has been investigating methods of making segments for furlable 10-foot and 44.5-foot diameter solar collectors. The first program was on the larger diameter mirror and was aimed at proving the feasibility of the monocoque structural technique for fabricating large, lightweight mirrors. The mirror elements developed on this program were approximately 20-feet long and 5-feet wide. The master fabrication set-up is as shown in Fig. 4-3. Inasmuch as the objective of this program was to prove the structural feasibility of large segments, no effort was made to completely finish the master surface. It was machined and roughly polished to the approximate contour. Optical replication properties were determined by means of flat glass inserts placed in the master surface at known locations. Figure 4-3 shows the inserts being mounted in the master surface. The angles of rays from these inserts were compared with those from the replicated mirror. This program did, however, prove the feasibility of the cam-guided machining, grinding, and polishing process.

Under a more recent program, a more highly sophisticated machine of the same type has been developed for making segments of 10-foot diameter furlable mirrors. In this case, two sets of cam rails are provided in order to position the tool at all times perpendicular to the true parabolic surface. Great care has been exerted to minimize errors resulting from machine tolerances or deflections. The master substrate is an iron casting. This is machined to the parabolic

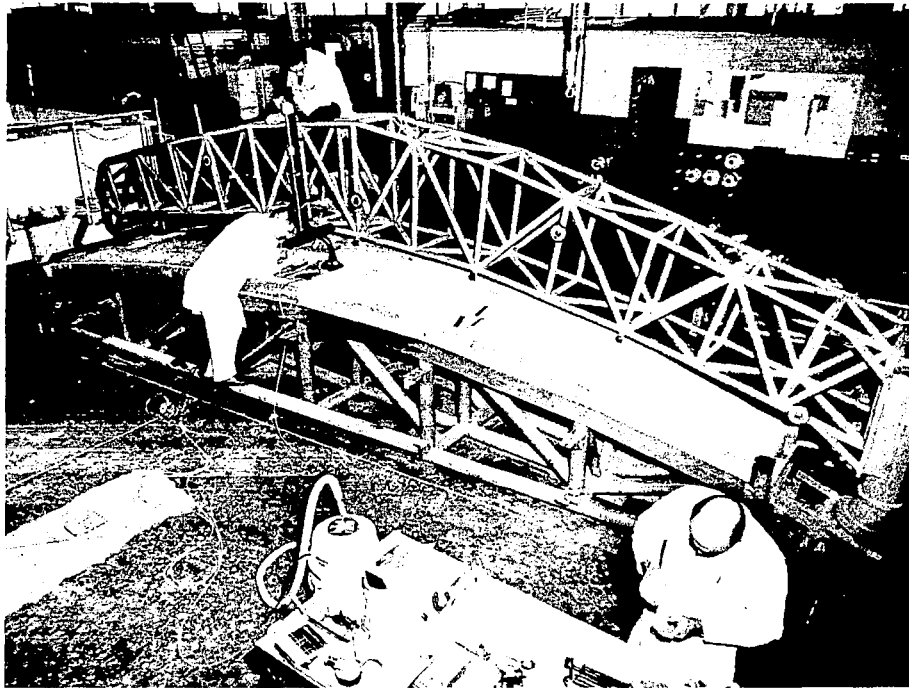


FIG. 4-3 MASTER AND OVERARM FOR 20-FT PETAL MIRROR

curve using a rotating grinding wheel having its axis parallel to the surface. The master surface is then covered with a layer of polyester resin approximately 1/4 inch thick. This surface is also rough machined with the rotating wheel. This tool is then replaced by a vibrating tool which moves in a plane tangent to the master surface. The abrasive medium is Polysand cloth of varying grades mounted on the vibrator with a sponge rubber backup. The tool is slowly moved from one end of the master to the other as the overarm pivots about the optical axis. Initial results look promising. Tests are under way to evaluate the master accuracy and reflectance obtainable by this method.

4.1.1.3 Accuracy Considerations

Master accuracy is controlled by several factors:

1. Rigidity of master structure and overarm structure
2. Bearing tolerances
3. Template accuracy
4. Thermal conditions
5. Tool wear
6. Resiliency of tool or surface material

These factors are common to all conventional machining processes, of which this is an example. There is nothing unique about this particular process except that the equipment is designed specifically to form a particular shape.

A criterion for master accuracy must be established as a basis for evaluating machining, grinding, and polishing accuracy limitations. A surface slope error of one minute of arc is a useful criterion. Errors less than this amount will have no measurable effect on collector performance. An angular error of one minute of arc corresponds to a gradient of one mil in 3.44 inches (or 10 mils in 34.4 inches). Therefore, conventional machine design practice should be adequate to eliminate significant errors from bearing slop and lack

of structural rigidity. The guide templates can be readily formed to an accuracy of ± 10 mils from the ideal curve over their entire length.

Thermal problems can be minimized by maintenance of constant temperature conditions. For example, if the master structure is steel with an average depth of three feet, then adjacent areas 34 inches apart must be held with temperature extremes of approximately 30°F to maintain the surface figure within one minute of arc. This is readily accomplished by using circulating water passages beneath the master surface and by holding the general master environment at a fairly constant temperature.

Therefore, the main sources of error would seem to be tool wear and the resilience of the tool and the master surface. This has been qualitatively confirmed by experiments at EOS on another program. However, quantitative values for errors to be expected from these sources must await further testing. Visual examination of the surfaces produced so far indicate that maximum errors may considerably exceed one minute of arc in local areas of the surface, but the mean errors should be adequately small for good collector performance.

4.1.2 Blade Grinding

In the previous section, a master fabrication process using a template guided machine was described. However, it is also possible to generate a paraboloid of revolution through the use of the inherent properties of the paraboloidal geometry. A process for doing this is known as blade grinding.

4.1.2.1 Process Description

The blade grinding process is derived from a fundamental geometric property of paraboloids of revolution: if a paraboloid of revolution is cut by a family of planes lying parallel to the axis of the paraboloid, the intersections of these planes with the paraboloidal surface will be a family of identical parabolas. No

other surface of revolution, when sectioned in this manner will form a family of identical curves of any type. Therefore, a machine can be devised which will automatically generate a paraboloid of revolution. This is done as shown in Fig. 4-4, by rotating a surface of revolution about its axis and grinding it with a flat blade which is maintained at all times parallel to the axis of the surface of revolution and is moved back and forth from one side of the rotating surface to the other. If the rotating surface is not a paraboloid, (and if the blade is not a corresponding parabola) the blade and the rotating surface will make only partial contact. Then both will wear preferentially until they make full contact throughout the entire cycle. Under these conditions, by the previous geometrical argument, the surface must be a paraboloid of revolution and the blade must be a parabola. This principle is valid even if the blade is not of infinitesimal thickness. In fact, the blade can be of any thickness, since at any position only a line contact will exist between the blade and the rotating surface. Therefore, the blade will wear into a saddle-shape surface (if the surface of revolution is convex). If the blade is sectioned by planes parallel to the flat faces, intersections of these planes with the blade "edge" will be the same parabola as that obtained by sectioning the surface of revolution. Both convex and concave surfaces of revolution can be generated by blade grinding with approximately equal ease. However, only convex masters are of interest in the present discussion of solar concentrator fabrication.

Both the blade and the rotating surface are preshaped to the approximate desired paraboloidal shape in order to minimize the amount of material to be removed and to allow better control of the focal length of the final surface. The structure is made by a process quite similar to that described in Subsection 4.1.1.1. The structure is built up from fabricated steel with an upper surface of welded steel formed to the approximate curvature of the final master. This will be coated with a layer of filled epoxy which will be blade

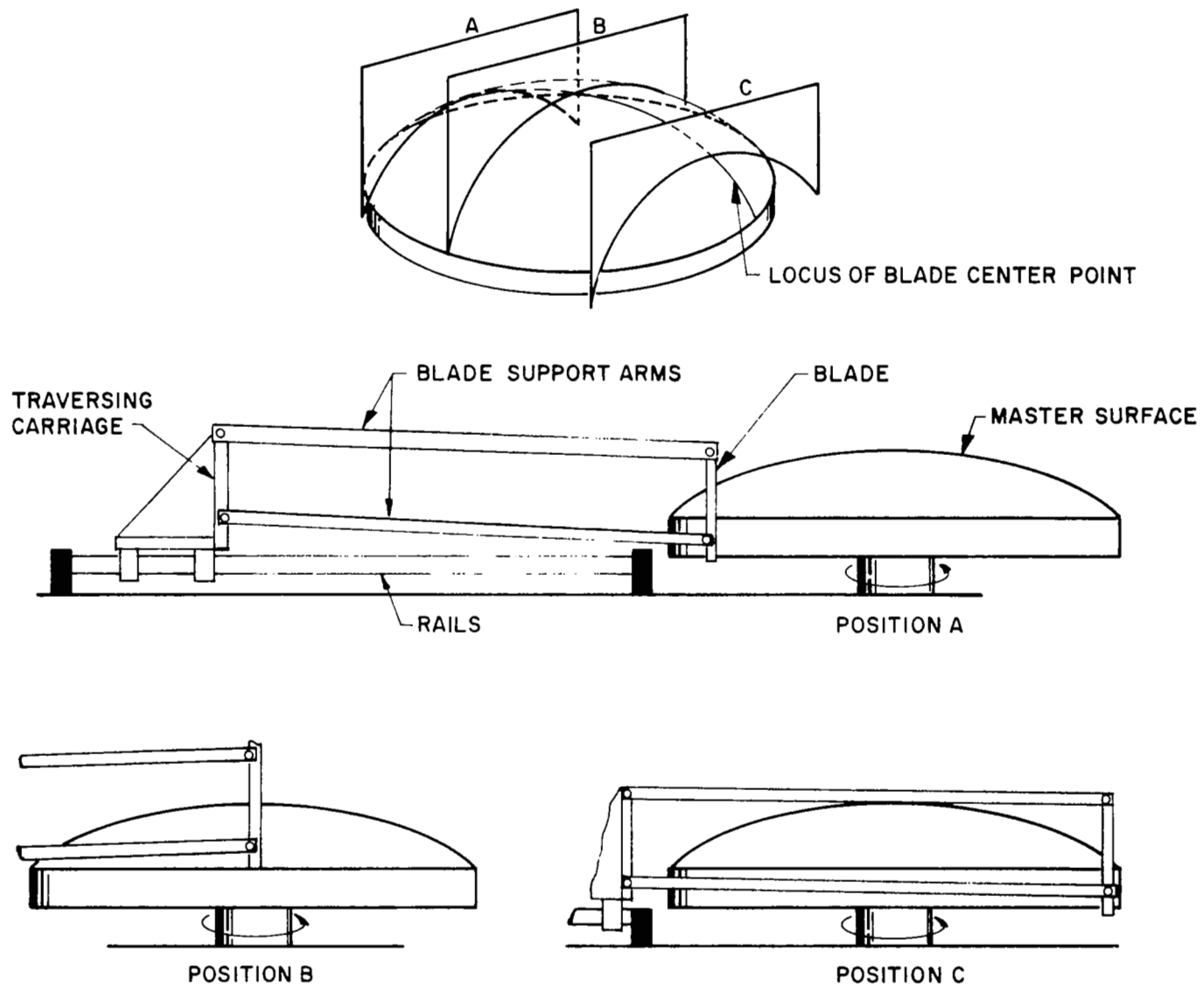


FIG. 4-4 BLADE GRINDING OF PARABOLOIDAL MASTERS

ground to the desired curvature. A final layer of unfilled plastic will be applied and cured. The blade will be of plastic such as acrylic or cast epoxy. The master will be maintained at a constant temperature throughout the finishing and plating operations.

The master is mounted on a large shaft such that it can be rotated about its optical axis. The blade is moved back and forth by a traversing mechanism illustrated schematically in Fig. 4-4. The blade is maintained parallel to the optical axis by means of a parallelogram linkage. The blade support arms are positioned by a carriage which moves back and forth on a pair of accurate machined rails.

Grinding begins in a conventional manner using coarse powdered abrasives. After the blade and rotating surface are brought into good contact at every point, the surface finish is improved using succeeding finer grades of powdered abrasives until a fine-ground surface is obtained. The blade edge is then covered with a suitable polishing lap material such as felt and polishing is commenced using polishing agents appropriate to the material from which the master surface is made.

4.1.2.2 Current Status

The principle of the blade grinding process for generating parabolic surfaces of revolution has been known for many years. This process was used by Bausch and Lomb prior to and during the second world war for fabricating five-foot diameter glass searchlight mirrors for military use. Although the records have been lost, it is believed that both the front (concave) and back (convex) surfaces of the glass masters were ground by blade grinding. Polishing was accomplished using rotating soft polishers mounted on oscillating arms. As far as is known, no attempt was made to correct the figure generated in this manner. These glass mirrors are accurate within one to two minutes of arc mean angular deviation.

More recently, a form of the blade grinding process has been used for making deep parabolic masters for search-light reflectors. It is the only known economical method of generating deep parabolic surfaces which are free from concentric zones within a minute of arc.

The successful use of the blade grinding process in the past stimulated its evaluation on the present program as a method of forming the large Brayton cycle collector master. The two-foot diameter master was converted to the blade grinding process after initial experiments had been run with the template guided machining and polishing process. The blade grinding machine is illustrated in Fig. 4-5. Details of this machine and the experimental program and results are given in Appendix C. In summary, it was found that the process readily generated parabolic surfaces having maximum slope errors of the order of one minute of arc or less. Various methods of obtaining a satisfactory surface polish have been investigated.

4.1.2.3 Accuracy Considerations

Factors affecting the accuracy of a blade ground master include:

1. Rigidity of master structure
2. Alignment of blade with master axis
3. Uniformity of master surface material and of blade material
4. Thermal conditions
5. Resiliency of polishing lap

The blade grinding process is less sensitive to machine tolerances than is the template guided machining process. In the blade grinding process, it is only necessary that the axis of rotation be stable and that the blade be always held in a constant alignment with this axis. The blade should be nearly parallel to the axis but misalignment by a few degrees is not important as long as the alignment between the axis and the blade is constant. Constant alignment can be assured if:

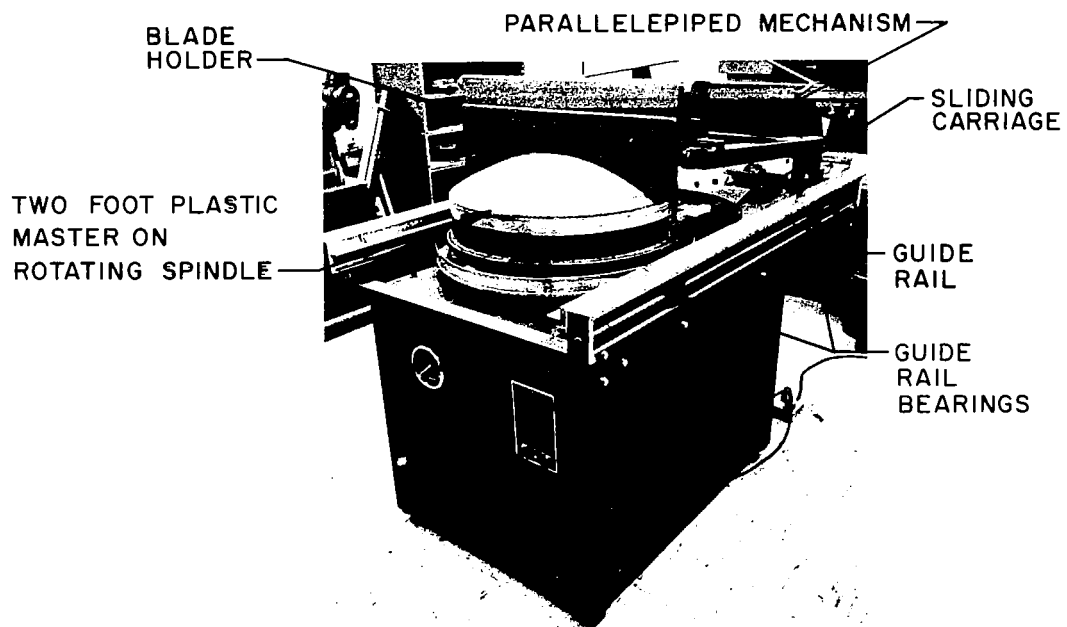


FIG. 4-5 BLADE GRINDING ASSEMBLY WITH
TWO FOOT DIAMETER PLASTIC
MASTER

1. The carriage rails are straight and parallel
2. The parallelogram support arms are of equal length
3. The bearings in the parallelogram linkage, carriage travel, and master rotation mechanism are free from slop

Equal length parallelogram arms can be assured by building a positive length adjustment into the upper arms. The required straightness of the carriage rails can be calculated by considering the blade tilting angle tolerance. If the blade changes in angle, it will no longer conform to the parabolic surface. If, for example, the blade tilts toward the optical axis, it will pivot at the center point and the tips will lift away from the surface. The worst possible situation would occur if the grinding action was so rapid that the master surface was brought into contact with the tilted blade during one portion of a traverse. In this case, the angular error would be approximately given by the separation of the blade tip from the ideal paraboloid (in the tilted condition) divided by the length of contact between the blade from the center to the tip. (In reality, this situation could not occur, since a great many traverses are required to remove even a small amount of material from the master surface. Some compensating effects would take place to reduce the total error.) As the blade is tilted, two effects tend to increase the separation between the blade and the master:

1. The blade tip moves in an arc
2. The master surface falls away from the blade tip because of its local slope angle (except when the blade is crossing a diameter of the master)

The first effect is extremely small. The lifting of the blade tip because of blade tilting is proportional to the cosine of the tilt angle. If the blade is crossing a diameter of the mirror, the error angle, e_1 , caused by tilting of the blade, δ , is given by

$$e_1 = \frac{2h_c}{L_c} (1 - \cos \delta)$$

or

(4-1)

$$\delta = \arccos \left(1 - \frac{e_1 L_c}{2h_c} \right)$$

where

h_c = Sagitta of contact line between blade and master

L_c = Length of contact line between blade and master

For a 30-foot master the sagitta would be about 4 feet and the contact length between the blade and the master would be approximately 34 feet. Then for a one minute of arc error angle, e_1 , the blade tilt angle would be about 4° .

The second effect does not occur when the blade is crossing a diameter of the master (because the master has no local slope angle at that point) and it disappears as the blade approaches the rim because the contact between the blade and the master approaches a straight line. The maximum effect is probably approximately halfway between the center and the rim of the master. The angular error contributed by the second effect is given approximately by

$$e_2 = \frac{2h_c \sin \delta \tan \mu}{L_c}$$

or

(4-2)

$$\delta = \arcsin \left(\frac{e_2 L_c}{2h_c \tan \mu} \right)$$

where

μ = local slope angle of master surface

At a point approximately halfway between the center and the rim of the master, the sagitta of the contact line would be approximately 3 feet, the length of contact would be approximately 30 feet, and the local slope angle would be approximately 15° . For a one minute of arc error angle, the blade tilt angle would be about $1/2^{\circ}$. Actually, however, a tilt angle of at least one degree could be tolerated, since the above analysis determines the deviation from a given parabola rather than from the best-fit parabola. Furthermore, because of the relatively slow grinding action and various compensating effects, it is probable that an even larger blade tilt angle could be tolerated. However, it is simple to maintain the blade angle within one degree, by conventional machine design procedure.

Side motion of the blade has not been, nor is it expected to be, a problem.

Uniformity of the blade material and surface material is of some importance. If these materials are extremely non-uniform, preferential wear may occur in the softer areas preventing full contact from ever being completely established. However, with reasonable care in preparing the surface material and blade, the geometric constraints imposed by the blade grinding process will take precedence over the effects of material nonuniformity.

Rigidity of the blade is relatively unimportant since there is no appreciable weight on the blade, the process is self-correcting. Plastic blades, metal backed, have performed satisfactorily in the grinding of 2-foot masters. Blade cooling, if required, is easily accomplished by impinging a cooling fluid on the blade.

Rigidity of the master structure is important to eliminate bending when the blade is near the rim. It is also important that the blade support and traversing mechanism be rigid to prevent chattering. However, the blade support arms are always in tension or compression and never need support any significant bending moments.

As in the case of the template machining process, it is important to maintain the master at a constant temperature to minimize thermal distortion and stressing.

Since the weight of the blade is spread over a fairly large area, resilience of the surface material does not seem to be a serious problem. However, the blade is counter weighted to permit any required surface pressure to be imposed. Speed control on the master rotating mechanism or the blade traversing mechanism has not been critical in experimental studies. The relative speeds of rotation and traversing will be varied throughout the process in accordance with the characteristics of the various grinding and polishing agents. These speeds will also be varied to eliminate the possibility of errors being introduced into the surface because of periodically repeating patterns in the motions of the components.

4.1.3 Plastic Overlay Process

4.1.3.1 Process Description

The plastic overlay process provides a method of producing an accurate, polished master without the necessity for polishing the surface after generating the surface shape. In this process, a master substrate is prepared in the same way as for the template machining or blade grinding processes. The master consists of a steel substructure covered by a layer of filled epoxy, which is cured and ground as closely as possible to the final desired curvature. This grinding operations would be done either by the template grinding or blade grinding process. Next, a thin ($1/8$ to $1/4$ inch) sheet of unfilled plastic is cast between two flat glass plates. (These glass plates need be only of ordinary plate glass quality). After the plastic layer has gelled and is sufficiently stiff to be handled, it is parted from the glass plates and is draped over the substrate surface. It is then drawn into close conformity with the master substrate surface either by mechanical stretching or by conventional vacuum bag techniques. After sufficient stretch has occurred to bring the plastic layer into conformity with the substrate, curing is allowed to proceed to completion. The surface layer is then bonded permanently to the substrate.

For a full scale 30-foot master, two methods are available for casting and applying the surface layer. It can either be cast as a single piece membrane or as segments that are formed to shape,

trimmed, and butt-joined. The second method would involve making the surface layer in sections small enough to be cast from individual glass plates. These sections might be typically either petals or hex shapes. The finishing operation would then proceed with the following steps:

1. The substrate surface would be marked off with the desired pattern of sections.
2. The plastic sections would be cast oversize between two glass plates. After partially curing they would be removed from the plates, draped over the master surface, and allowed to complete curing. For this step, no adhesive would be placed on the substrate.
3. The plastic section would then be cut to the shape of the inscribed pattern on the substrate.
4. It would then be lifted off the substrate and stored.
5. The other surface sections would be made in the same manner.
6. After all the sections have been finished, they would be bonded to the substrate surface, one at a time, leaving a very slight gap between each section.
7. The gaps would then be filled with liquid plastic of the same type used for the surface layer.
8. After curing, the joints would be butted out by hand to produce a smooth transition between the sections.

An alternate approach involves casting the plastic surface layer as a single piece. The glass plates between which the surface layer is cast would be made in sections. Typically, these glass sections would be approximately ten feet square. Their edges would be lapped together to provide a good fit. The glass sections would be layed on a flat platten and would be bonded together with cast plastic joints. The upper plate would be made in a similar manner and would have a lifting fixture. Spacing between the two plates would be accomplished by means of small plastic spacers cast of

the material which is to be used for the master surface layer. These would have been pre-cast between glass plates and cut to size, typically 1/4 inch diameter. They would be chosen to have highly uniform thicknesses. These would be placed on the surface of the lower plate at spacings of about one foot apart. The liquid resin would then be poured on the lower plate, and the upper plate would be laid in place. After the proper curing period, the upper plate would be removed and a handling ring, slightly over 30 feet in diameter would be attached to the plastic membrane. The membrane would then be lifted from the lower plate, inverted, and draped over the master substrate surface. A liquid adhesive would be placed on the substrate prior to the draping operation.

The first approach (casting the plastic layer in sections) has the advantage that it minimizes the handling of large, bulky sheets of plastic. It also minimizes the amount of stretch required for each section. However, because of the joints, the surface might not be quite as uniform as that of a single-piece surface layer.

4.1.3.2 Current Status

Methods similar to the plastic overlay technique have been used for many years for making glass objects such as searchlight reflectors. The difficulty with glass is that the entire structure must be heated to the softening point of glass. Plastics have the advantage that the process can be performed at or near room temperature. The plastic overlay process is now under intensive investigation at EOS as a means of making large low-cost collector masters. Under another program, the process has been investigated for making petal masters for petalline solar collectors. Several masters for segments of 10-foot diameter unfurlable mirrors have been made successfully. Results appear most encouraging. The master surface finish is virtually indistinguishable from that of polished glass and is remarkably free from geometric defects such as waves or ripples. Experiments are being performed by EOS to assess the feasibility of forming full-circle

masters by this technique. An 18-inch diameter master was made successfully using a glass substrate. This has been followed up by two-foot diameter masters having metal substrates. Results have been very promising. A more detailed description of the experimental work will be given in Appendix C.

4.1.3.3 Accuracy Considerations

The accuracy of the final master is determined both by the accuracies of the substrate and the surface layer. The substrate would be shaped by the template machining or blade grinding processes which have already been discussed. This section will be limited to the characteristics of the surface layer.

Several factors could give rise to geometric errors on the master surface. If the master substrate is an accurate paraboloid and if the surface layer is of constant thickness, then the resulting surface will not be true paraboloid. Furthermore, since the final surface layer is made by stretching a flat sheet, some differential thickness must occur. These two types of errors are inherent. Other errors resulting from lack of process control include:

1. Nonuniform thickness of surface layer caused by spacing variations between glass plates.
2. Differential stretching caused by nonuniformities of surface layer properties.
3. Show-through of defects on substrate surface or on back surface of plastic layer, including air bubbles, dirt particles, inclusions in adhesive, etc.
4. Nonuniform adhesive thickness.

The magnitudes of the inherent errors can be determined analytically. Those resulting from process control considerations must be evaluated experimentally.

Inherent Errors. If the master substrate is an accurate paraboloid, then the addition of a constant thickness skin will no longer produce an exact paraboloid. The error introduced in

this way can be determined by calculating the angular deviation from the best-fit paraboloid of a surface that is separated from a true paraboloid by distance, t_o (skin thickness).

Consider a convex paraboloid having the form

$$y = \frac{x^2}{4f} \quad (4-3)$$

With the addition of a constant thickness skin, a new surface will be formed. If the new surface were a paraboloid, it would be defined by

$$y' = \frac{x^2}{4 \left(f + \frac{t_o}{2}\right)} - t_o \quad (4-4)$$

The difference between y and y' is

$$(y - y')_{\text{parab.}} = t_o + \frac{x^2}{4} \left[\frac{1}{f} - \frac{2}{2f + t_o} \right] = t_o + \frac{x^2}{4} \left[\frac{2f + t_o - 2f}{2f^2 + ft_o} \right] \quad (4-5)$$

when $t_o \ll f$,

$$(y - y')_{\text{parab.}} = t_o + \frac{x^2}{4} \left(\frac{t_o}{2f^2} \right) \quad (4-6)$$

However, the actual difference between the curves is

$$(y - y')_{\text{actual}} = \frac{t_o}{\cos \theta} \quad (4-7)$$

where θ is the angle between the optical axis and a radius of curvature vector. Then the net difference between the actual curve and a parabola of focal length $\left(f + \frac{t_o}{2}\right)$ is:

$$\begin{aligned}
\Delta &\equiv (y - y')_{\text{actual}} - (y - y')_{\text{parab.}} = \frac{t_o}{\cos\theta} - \left(t_o + \frac{\chi^2 t_o}{8f^2}\right) \\
&= t_o \left[\frac{1}{\cos\theta} - \frac{\chi^2}{8f^2} - 1 \right]
\end{aligned} \tag{4-8}$$

The angular error between the actual curve and the ideal parabola is

$$e = \frac{d\Delta}{ds} \tag{4-9}$$

where s is the coordinate measured along the parabola. For any increment of length along the curve,

$$\frac{d\Delta}{ds} = \cos\theta \frac{d\Delta}{d\chi} \tag{4-10}$$

Approximately,

$$\cos\theta = \frac{\sqrt{(2f + t_o)^2 - \chi^2}}{(2f + t_o)} \approx \frac{\sqrt{4f^2 - \chi^2}}{2f} \quad \text{if } t_o \ll f \tag{4-11}$$

Then from Eqs. 4-8, 4-9, 4-10, and 4-11 :

$$\begin{aligned}
e &= \frac{\sqrt{4f^2 - \chi^2}}{2f} \left\{ \frac{d}{d\chi} \left[t_o \left(\frac{2f}{\sqrt{4f^2 - \chi^2}} - \frac{\chi^2}{8f^2} - 1 \right) \right] \right\} \\
&= \frac{\sqrt{4f^2 - \chi^2}}{2f} \left[t_o \left(\frac{2f\chi}{(4f^2 - \chi^2)^{3/2}} - \frac{\chi}{4f^2} \right) \right]
\end{aligned} \tag{4-12}$$

Assume

$$\begin{aligned}f &= 14.4 \text{ ft} \\ \chi &= 15 \text{ ft (rim of master)} \\ t_o &= 0.25 \text{ in} = 0.0208 \text{ ft}\end{aligned}$$

Then

$$e = 1.94 \times 10^{-4} \text{ radians} = 40 \text{ secs of arc}$$

By substituting smaller values for χ , it can be verified that the greatest error occurs at the rim ($\chi = 15 \text{ ft}$).

This error could be eliminated by generating the substrate as a surface a distance, t_o , below a true paraboloid. However, this could not be done if the substrate is prepared by the blade grinding process, which can generate only paraboloidal surfaces. Furthermore, as will be shown next, it may not be desirable to attempt to eliminate this error because of a compensating error.

The second inherent error is that caused by the stretching of a flat sheet in order to conform with the paraboloidal surface. In this analysis it will be assumed that the sheet acts as an elastic diaphragm, which is brought down over the paraboloidal surface contacting it first at the center. The diaphragm is then further pulled down over the master in such a way that all stretching is radial (concentric circles on the diaphragm move down and contact their projections on the paraboloid without increasing in circumference). Since the plastic volume and the hoop lengths are constant

$$t ds = \text{constant} \quad (4-13)$$

where t is the local thickness of the stretched sheet. Each radial increment, $d\chi$, of the original (flat) sheet stretches to a length ds . But,

$$ds = d\chi / \cos\theta$$

At the center of the master ($\chi = 0, \theta = 0$)

$$t = t_0 \text{ and } ds = d\chi \quad (4-14)$$

Then everywhere

$$\begin{aligned} t ds &= t_0 d\chi \\ \frac{t}{t_0} &= \frac{d\chi}{ds} = \cos\theta \end{aligned} \quad (4-15)$$

For the stretching skin the difference between the actual curve and the substrate curve, from Eq. (4-7) is:

$$(y - y')_{\text{actual}} = \frac{t}{\cos\theta} \quad (4-16)$$

But using Eq. (4-15)

$$(y - y')_{\text{actual}} = \frac{(t_0 \cos\theta)}{\cos\theta} = t_0 = \text{constant} \quad (4-17)$$

Therefore, the new surface is displaced from the paraboloidal substrate surface by a constant distance in the y direction. Then the new surface is also a paraboloid. Thus, the two inherent errors are exactly compensating, under the assumptions used in this analysis. Furthermore, taken individually, they are negligibly small. Therefore, even if precise compensation does not occur, these errors can still be considered negligible.

Process Control Errors. The effect of process control errors on master geometry must be evaluated in relation to the required dimensional tolerances. As stated above, a one minute of arc slope error is equivalent to a dimensional error of one mil in

3.44 inches or 10 mils in 34.4 inches. Some of the causes of and remedies for the processes control errors will now be considered.

The thickness of the surface layer is controlled by the spacing between the glass sheets during casting. This spacing can be most readily controlled by using spacers placed between the glass sheets. The spacers would be pre-cast discs of the same material from which the surface layer is to be cast. However, the spacers would be made in a small setup with precisely controlled spacing, such that they would have a uniform thickness. Furthermore, they would be measured prior to use to assure thickness uniformity within 1 or 2 mils. These spacers would then be placed about between the surfaces of the large casting sheets at spacings of the order of one foot between centers. This technique allows accurate control of surface layer thickness within a few mils over any desired span. Note that the glass casting sheets need not be maintained flat within this tolerance, as long as the parallelism between the sheets is accurately maintained.

Differential stretching of the surface layer during the draping operation is another possible source of error. This could be caused by nonuniform characteristics of the surface material. The former has been successfully overcome by thorough mixing of the resin components and by curing under controlled temperature conditions. This problem can also be greatly alleviated by allowing the cure to proceed to a point where the surface layer has considerable local stiffness, prior to draping. This also minimizes show-through of defects on the substrate surface or the lower surface of the skin, such as air bubbles, dirt particles, or irregularities in the substrate surface. By choosing the proper time for draping, the surface layer will be sufficiently flexible to conform to the overall substrate geometry but yet locally stiff enough to bridge small-scale defects without serious show-through.

The problem of non-uniform adhesive thickness can best be overcome by:

1. Use of a thin adhesive layer
2. Use of a slow curing and low viscosity adhesive
3. Use of a resilient adhesive

The problem of adhesive uniformity is of small consequence if the master surface layer is cast as a single-piece skin. In this case, very little adhesion is required between the surface layer and a substrate. The surface layer can be maintained in contact with the substrate by a mechanical locking ring at the edge. If the surface layer is made in sections some additional adhesive strength is required to keep the individual sections from peeling away from the substrate surface because of residual stresses. Even so, the large bonding area and the relative thinness of the plastic skin indicate that relatively little adhesive strength is required. In model tests at EOS, surface skins have been firmly attached by such resilient adhesives as RTV silicone rubber.

For the sectioned master surface, careful control of adhesive thickness will be required primarily near the edges of the sections in order that adjacent sections can be smoothly joined without a discontinuity in surface curvature. The actual joint is a fillet between the sections cast of the same plastic material from which the skins are cast. This joint would be cast in place using a flexible, conforming, polished tool, which also provides positive alignment between the adjoining sections.

4.1.4 Spin Casting

In Section 4.1.2 a process, blade grinding, was described which generates a paraboloid of revolution automatically through the use of the inherent properties of the paraboloidal geometry. This section describes the spin casting process, which uses another natural phenomenon to generate a paraboloid of revolution.

4.1.4.1 Process Description

If a partially filled container of liquid is rotated about a vertical axis, the free surface of the liquid, under the combined influence of gravitation and centrifugal forces, will form a paraboloid of revolution. The focal length of the paraboloid is determined only by the local gravitational attraction and the speed of revolution. It is in no way a function of the physical properties of the liquid. If a liquid is caused to solidify while rotating, a permanent paraboloidal surface can be formed. In order that this surface be an accurate paraboloid and be free from surface defects, several requirements must be met:

1. The liquid must be one that solidifies by becoming increasingly more viscous (rather than by having a definite freezing point) and that undergoes a very small volume change between the liquid and solid phases. Epoxy plastic resins seem to meet these requirements sufficiently to be of interest for collector masters.
2. During the casting operation, the rotational speed must be held constant with extreme accuracy (within one part in 10^4).
3. The rotating mechanism must be extremely free from vibration, particularly that of a periodic nature.
4. The casting must be done in a dust-free atmosphere to prevent dust particles from settling on the surface, causing defects. Better results are obtained by enclosing the rotating vessel, to prevent air currents from rippling the surface.
5. Long-term, low-temperature curing of the plastic appears to be essential to maintain low exotherm and low shrinkage during cure.

The process described above is amenable only to the formation of concave surfaces. This means that an additional convex master (called a sub-master) must be made from the concave surface prior to making the final

mirror. The general steps in making this submaster are similar to those described later for making electroformed mirrors. After the convex master has been electroformed and parted from the original concave plastic master, the parting layer is removed from the nickel surface. From this point on, the process is similar to that followed when using masters made by any of the other three processes. Fabrication of the submaster poses some difficult engineering problems. The original concave plastic master must have an extremely rigid structure to prevent vibration from degrading the plastic surface during cure. The convex submaster must also have a rigid structure to withstand subsequent handling and plating stresses. Accuracy considerations require that this rigid structure be attached to the electroformed nickel shell (which forms the surface of the submaster) before removal of that shell from the concave original master. Thus, the parting operation is extremely difficult because the two large, rigid structures are in intimate contact over a large area. So far, no way has been found to separate these two components without destroying the original plastic master. This means that each plastic master can be used only once.

4.1.4.2 Current Status

The spin casting process has been known for many years. An astronomical telescope was made as early as 1909 using a primary mirror formed of a rotating pan of mercury. It was suggested many years ago that if a suitable hardening material could be rotated in this fashion a permanent paraboloid could be formed. With the development of modern epoxy resins, this process became a reality. Many organizations have investigated the spin casting process for making parabolic mirrors. The main effort on large paraboloids that would be potentially suitable for solar collector masters has been done by the Kennedy Antenna Division of the Electronic Specialty Company and by General Electric. Under a NASA contract (administered

by Jet Propulsion Laboratory) GE has made a 9.5-foot diameter spin-cast master from which a convex electroformed nickel submaster and a proof mirror were subsequently replicated. It is understood that the original master was tested and found to be accurate within two minutes of arc. Although detailed test data are not yet available, preliminary tests indicate that the final mirror is considerably less accurate. However, it is not known whether the loss of accuracy occurred during fabrication of the submaster, the mirror, or whether the mirror was damaged in shipment to the West Coast. The submaster was parted from the plastic original by deliberately destroying the latter using thermal shock from cold nitrogen gas. Thus, the original is no longer available for test or comparison with the final mirror.

4.1.4.3 Accuracy Considerations

The accuracy of spin casting is affected by many factors including:

1. Speed control of spin table
2. Vibration environment
3. Curing characteristics of plastic
4. Cleanliness of atmosphere next to plastic surface
5. Freedom from wind rippling
6. Uniformity of plastic thickness

It is impossible to evaluate these effects in any way other than experimentally. The first plastic layer is seldom acceptably accurate because of the nonuniform thickness of the plastic surface layer. The curing shrinkage then causes surface distortion because of differential contraction. By building up several layers this distortion usually can be reduced to an acceptable level.

The only estimate which can be placed on the obtainable surface accuracy of spin casting is that original masters having accuracies in the order of two minutes of arc have been made. These accuracies are roughly equivalent to those obtainable by other techniques.

4.1.5 Comparative Evaluation and Recommendations

Some of the relative advantages and disadvantages of the four master fabrication processes are summarized in this section.

4.1.5.1 Cost

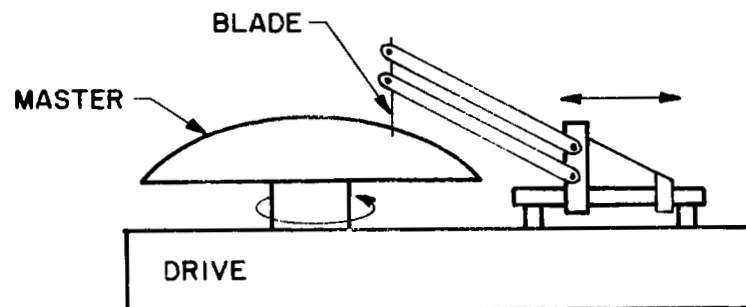
Template machining, blade grinding, and the plastic overlay process produce convex masters directly. A schematic process sequence for blade grinding is shown in Fig. 4-6. The spin casting process produces a concave original master, which must be replicated to produce a convex nickel submaster as shown in Fig. 4-7. Based on the reasonable assumption that the cost of generating the initial surface, including generating machinery, foundations, etc., would be roughly comparable for the processes, the extra step of replicating the submaster would make the spin casting process more expensive, overall. However, it is possible that a portion of the tooling needed for spin casting may already be available at one of the companies doing this kind of work.

Other cost considerations are mentioned in the discussion of repairability (Subsection 4.1.5.5) and transportation (Subsection 4.1.5.6).

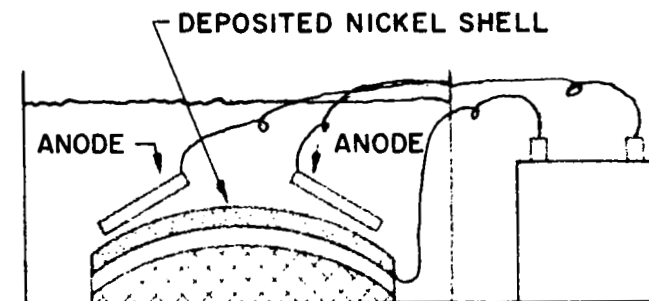
4.1.5.2 Accuracy

If it is also assumed that the accuracy and surface quality of the original surface are similar for the four processes, then the extra replication required for the spin casting process would potentially give a less accurate final mirror. However, the actual accuracy loss may be insignificantly small.

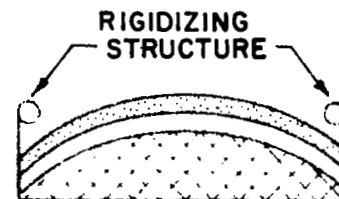
The accuracy to be expected from each of the four processes has not been conclusively demonstrated. Surfaces accurate within one or two minutes of arc have been made by each process, except the template machining process. However, it is quite likely that this accuracy can be achieved in the latter process with relatively minor improvements. The first 9.5-foot diameter mirror made using the spin



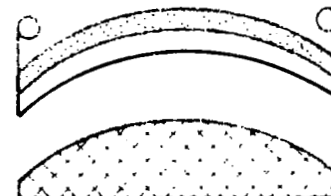
1. BUILD BLADE GRINDING MACHINE
2. PREPARE MASTER SUBSTRUCTURE
3. COAT PREFORM WITH PLASTIC LAYER
4. GRIND AND POLISH MASTER



5. PREPARE PLATING EQUIPMENT
6. SENSITIZE MASTER
7. PLATE NICKEL SHELL

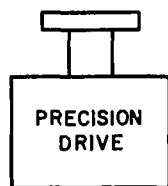


8. REMOVE FROM PLATING TANK AND CLEAN
9. ATTACH RIGIDIZING STRUCTURE

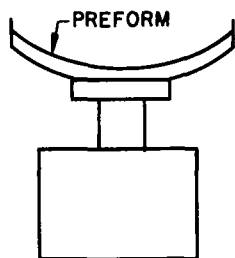


10. PART MIRROR FROM SUBMASTER
11. APPLY PROTECTIVE COATING TO SILVER REFLECTIVE LAYER

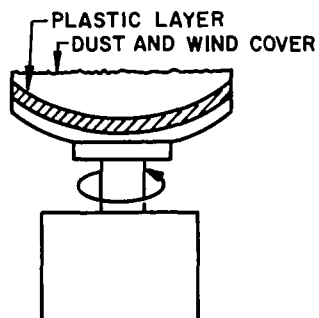
FIG. 4-6 SCHEMATIC DIAGRAM OF BLADE GRINDING PROCESS FOR ELECTROFORMING SOLAR COLLECTORS



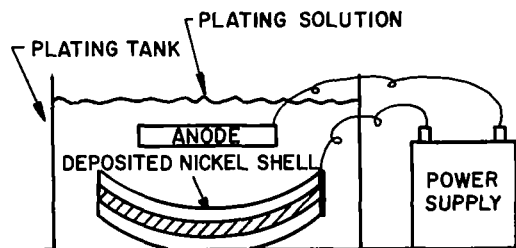
1. BUILD ROTATING MACHINERY AND TABLE



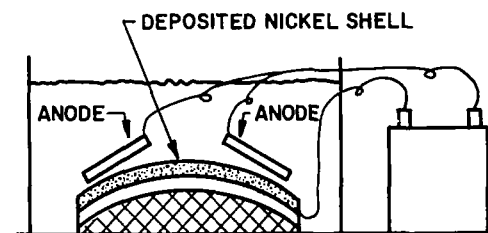
2. BUILD CONCAVE SUBSTRUCTURE



3. CAST CONCAVE PLASTIC PARABOLA



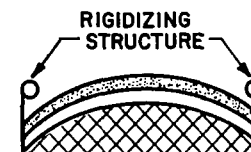
4. PREPARE PLATING EQUIPMENT
5. SENSITIZE MASTER WITH SILVER
6. PLATE NICKEL SHELL



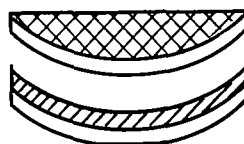
11. MODIFY PLATING EQUIPMENT FOR CONVEX SUBMASTER
12. APPLY PARTING LAYER TO SUBMASTER
13. PLATE NICKEL SHELL



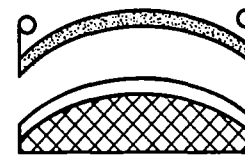
7. REMOVE FROM PLATING TANK AND CLEAN NICKEL SHELL
8. ATTACH RIGIDIZING STRUCTURE TO NICKEL SHELL



14. REMOVE FROM PLATING TANK AND CLEAN
15. ATTACH RIGIDIZING STRUCTURE



9. PART CONVEX SUBMASTER FROM CONCAVE PLASTIC PARABOLA
10. REMOVE SILVER LAYER FROM NICKEL



16. PART MIRROR FROM SUBMASTER

FIG. 4-7 SCHEMATIC DIAGRAM OF SPINCASTING PROCESS FOR ELECTROFORMING SOLAR COLLECTORS

casting process was much less accurate than the original spin casting. Additional work is now being performed to ascertain whether the problems of the first 9.5-foot collector were caused by techniques or are inherent in the process.*

4.1.5.3 Surface Finish and Accuracy

Best specularity (and highest reflectance) should be obtainable from the plastic overlay process. Samples made so far have had surface finishes equivalent to that of ground and polished glass. The reflectances obtainable from the other three processes may be somewhat lower because of the orange peel sometimes found on spin cast surfaces and the sleeks (microscopic scratches) inherent in polished plastic surfaces.

4.1.5.4 Mirror Parting

Experimental evidence at EOS indicates that the adherence of electroformed nickel to plastic masters is much less than to nickel masters. This is important considering the relative weakness of the shell structure to compressive buckling.

4.1.5.5 Repairability

Local damage or overall surface degradation can be repaired easily either by the template machining or plastic overlay processes, using the same methods that were used to finish or form the original surface. Repair can also be done by blade grinding, but the entire surface must be refinished even to effect a local repair. (However, small local repairs could be refinished by hand). The spin casting process does not lend itself to repair. Only very minor local damage of the nickel submaster can be repaired and this must be done by hand finishing techniques. Nickel is a difficult material to polish, and

*For a more complete assessment of the spin casting process, contact General Electric, Valley Forge, Pennsylvania.

overall refinishing is not feasible. Since the problem of separating the submaster from the concave original has not yet been solved without destroying the original, the entire process must be repeated from the beginning should the nickel submaster be damaged or degraded beyond acceptability.

The implications of this in terms of total program costs are evident.

4.1.5.6 Handling and Transportation

The handling and transportation problems for the four processes are roughly equivalent unless, in the case of spincasting, it is necessary to transport the submaster. This would be necessary unless the entire mirror fabrication process, from the original spincasting through final mirror assembly, is performed in the same facility. Transportation of the lightweight replica mirror is difficult enough, although feasible. Moving the equally bulky but much heavier masters might be an insuperable problem depending on the particular route to be traveled and on the availability of aircraft. It is unlikely that either the helicopter or the blimp would be capable of carrying the masters. Transportation of the masters would increase program cost significantly.

4.1.5.7 Tooling Requirements

The spincasting turntable requires precise bearings and a very accurate speed control (1 in 10^4 accuracy). Provision must be made to protect the plastic layer from atmospheric dust and wind. The machine must be vibration free. Template machining requires high mechanical precision and freedom from vibration but does not require precise speed control. The blade grinding mechanism must be massive but does not require great precision. A moderate amount of vibration is not detrimental. Normal lab cleanliness is adequate for template machining or blade grinding.

The plastic overlay process requires careful control of surface layer thickness.

4.1.5.8 Recommendations

Based on the above considerations, the spin-casting process is presently considered less desirable than the other three approaches. Although any of the other three processes will probably result in a satisfactory mirror, it now appears that the best combination of accuracy, specularity, and low total cost may be achieved with the plastic overlay process using either the template machining or blade grinding process for generating the substrate geometry.

4.2 Mirror Plating Equipment

The large scale of the 30-foot collector will require some plating techniques which are somewhat different from conventional practice for smaller parts. However, most of these techniques have already been developed at EOS in connection with another program for electroforming large segments of unfurlable solar collectors.

4.2.1 Plating Tank

For electroforming large structures, EOS has developed a technique of using the master as the bottom of the plating tank. For the Brayton cycle collector master, the tank sides will consist of a removable cylindrical wall (or a conforming top shell) which is only put in place for the actual plating operation (Fig. 4-8). Master preparation before plating, as well as post plating operations, are conducted with the tank wall removed. This approach has two advantages. It eliminates the necessity of moving the master and it reduces the required amount of plating solution. A schematic diagram of the master/tank construction is shown in Fig. 4-8. The detail illustrates a method of sealing the wall using an inflatable gasket. This technique was worked out under a previous program for plating trapezoidal-shaped mirror segments.

A water passage is provided just beneath the upper steel shell of the master structure to maintain the master at a constant temperature. Baffles (not shown in Fig. 4-8) will be provided to assure good circulation of the water. The water passage can also be used, if necessary, for hydrostatic balancing to offset the weight of the plating solution. In this case, the main load would be borne by the shell beneath the water passage. Nonuniform deflections of this shell caused by the truss structure underneath would not cause distortion of the upper shell.

This same tank arrangement will also be used for plating the torus and the joint between the skin and torus. For the latter operation, the master surface will be covered by a protective plastic sheet.

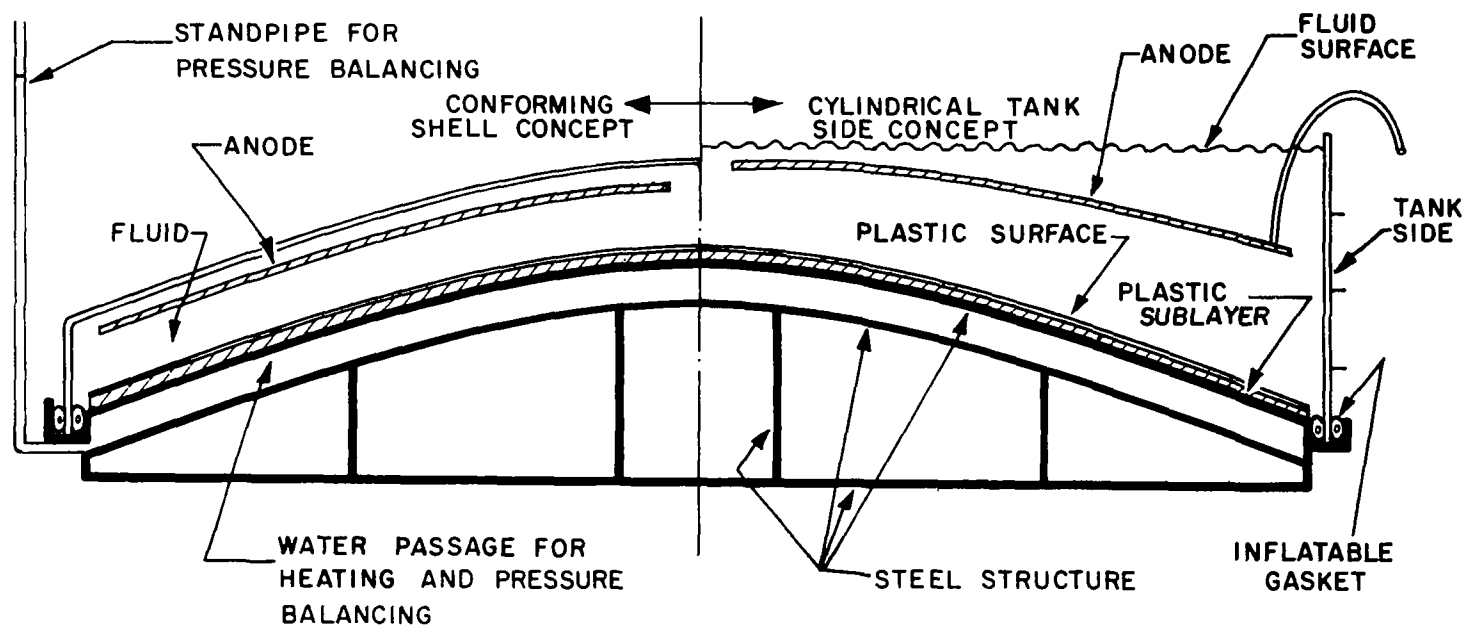


FIG. 4-8 SCHEMATIC DIAGRAM OF MASTER STRUCTURE AND TANK CONSTRUCTION

4.2.2 Fluid Storage and Treatment

Except during plating, the fluid will be stored in a separate tank where it will be continuously filtered and treated. Figure 4-9 illustrates a schematic layout of the plating fluid circulation system. Between plating operations, the valves (V1) are turned so that the fluid passes out of the storage tank through the filter pumps (FP1) and back to the storage tank. During plating, valves (V1) are turned so that the fluid passes out of the storage tank, through filter pumps (FP1) and into the plating tank. The desired fluid level in the plating tank is maintained by the control valve (V2) and the scavenging pump (FP2). Multiple inlets to the plating tank are provided to increase the agitation of the plating solution near the master surface. Additional agitation will be provided by propellor-type stirrers in the plating tank.

Plating solution will be maintained at the desired plating temperature in the storage tank. The plating temperature will be thermostatically controlled using sensors placed in the solution near the master. In this way, no heating of the solution in the plating tank is required.

An inventory of approximately 20,000 gallons of solution will be required assuming a depth of one foot at the center of the master. This inventory can be reduced considerably by using a conforming upper shell on the plating tank (Fig. 4-8). For example, with a conforming shell placed two feet above the mirror surface, the fluid inventory could be reduced to less than 14,000 gallons. Assuming that the full 20,000 gallons of inventory is required, the storage tank would be approximately 20 feet square and 9.5 feet deep.

4.2.3 Power Supply

The power requirements for mirror plating are determined by the mirror area and a chosen set of plating parameters. These parameters are governed in turn by desired plating rate, stress condition in plated shell, and allowable bath temperature. The choice of

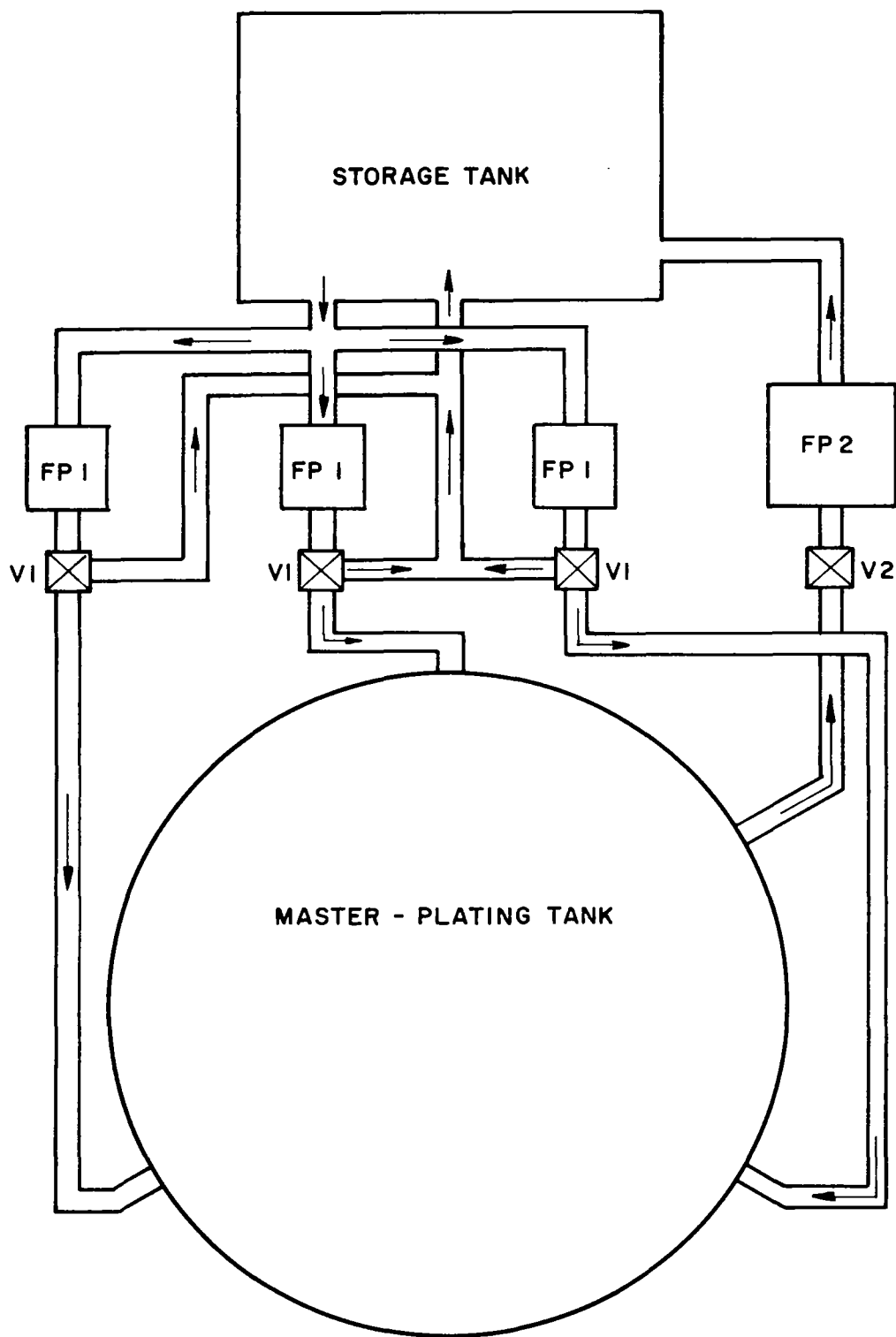


FIG. 4-9 SCHEMATIC DIAGRAM OF PLATING FLUID CIRCULATION SYSTEM

conditions for the 30-foot collector is explained in Section 4.3.3. It is shown that the optimum plating current density is 7 to 10 amps/ft² at a maximum potential of 15 volts. Assuming that the total area to be plated may be as much as 32 feet diameter, the area will be approximately 1000 square feet (including an allowance for the surface curvature). Thus, a total current of 7,000 to 10,000 amps must be supplied.

The power is dc supplied by standard industrial plating rectifiers, which are available in any required size. The efficiency of these units is about 75 percent. Thus, the total power requirement will be from 140 to 200 kw. Lesser power levels are required for plating the torus and the plated joint between the skin and the torus. This can be supplied by the same equipment.

4.2.4 Anodes

The mirror skin will be plated using an array of flat sheet nickel anodes arranged as a conforming shell at an average distance of approximately one foot from the surface. The anodes are enclosed in linen bags to prevent foreign particles from falling on the mirror surface as the anodes are etched away. The anode surface area should be at least equal to the area to be plated, for good plating efficiency. Special anode arrays will be used for plating the torus and the joint between the skin and torus.

4.3 Mirror Fabrication

The EOS mirror concept is very simple, involving only a torus with brackets, a mirror skin, and suitable coatings. The fabrication and assembly of these elements will be discussed in order.

4.3.1 Torus Fabrication

4.3.1.1 Nickel Torus

The electroformed nickel torus is made by plating on a prepared aluminum mandrel. The mandrel is then dissolved out leaving the hollow nickel shell. The aluminum mandrel is made by welding a skirt on a circular cross section aluminum tube. The welds

are dressed and the tube is rolled to the proper torus curvature. The sections are cut to the lengths between brackets. The brackets are made with a short tapered tubular extension which extends into the torus sections with a smoothly faired joint. The various torus sections and brackets are aligned and a nickel shell of the desired thickness is plated onto the mandrel. The nickel skin encapsulates the tubular extensions on the brackets, forming a permanent joint. A row of holes for the electroformed rivets are drilled through the torus (see Fig. 4-10). The torus is then placed in the etching tank, which contains a dilute solution of hydrochloric acid. This solution is circulated through the torus until the aluminum mandrel is etched out. For this process, the brackets must be made of some material other than aluminum. If aluminum brackets are to be used, an alternate process can be followed in which the brackets are mounted in the torus after it is plated and etched.

4.3.1.2 Titanium Torus

The titanium torus will be assembled in a manner similar to that for the aluminum mandrel of the nickel torus. The torus sections will be formed, rolled to shape, cut to length, and welded to the brackets. Depending on the particular bracket design, it may be possible to roll the torus into a complete tube and insert the brackets in cutouts in the torus.

4.3.2 Master Preparation

The first step in master preparation is the casting of the edge radius mandrel. The mandrel is cast of wax using the already-prepared torus as a mold to insure good mating of the torus to the plated skin. Figure 4-10 shows the sequence of steps in forming the mandrel, plating the skin, and attaching the torus. First, the torus is covered with a layer of tape approximately the same thickness as that expected for the mirror skin. Next, the torus is carefully placed on the master, concentric with the optical axis, and its position

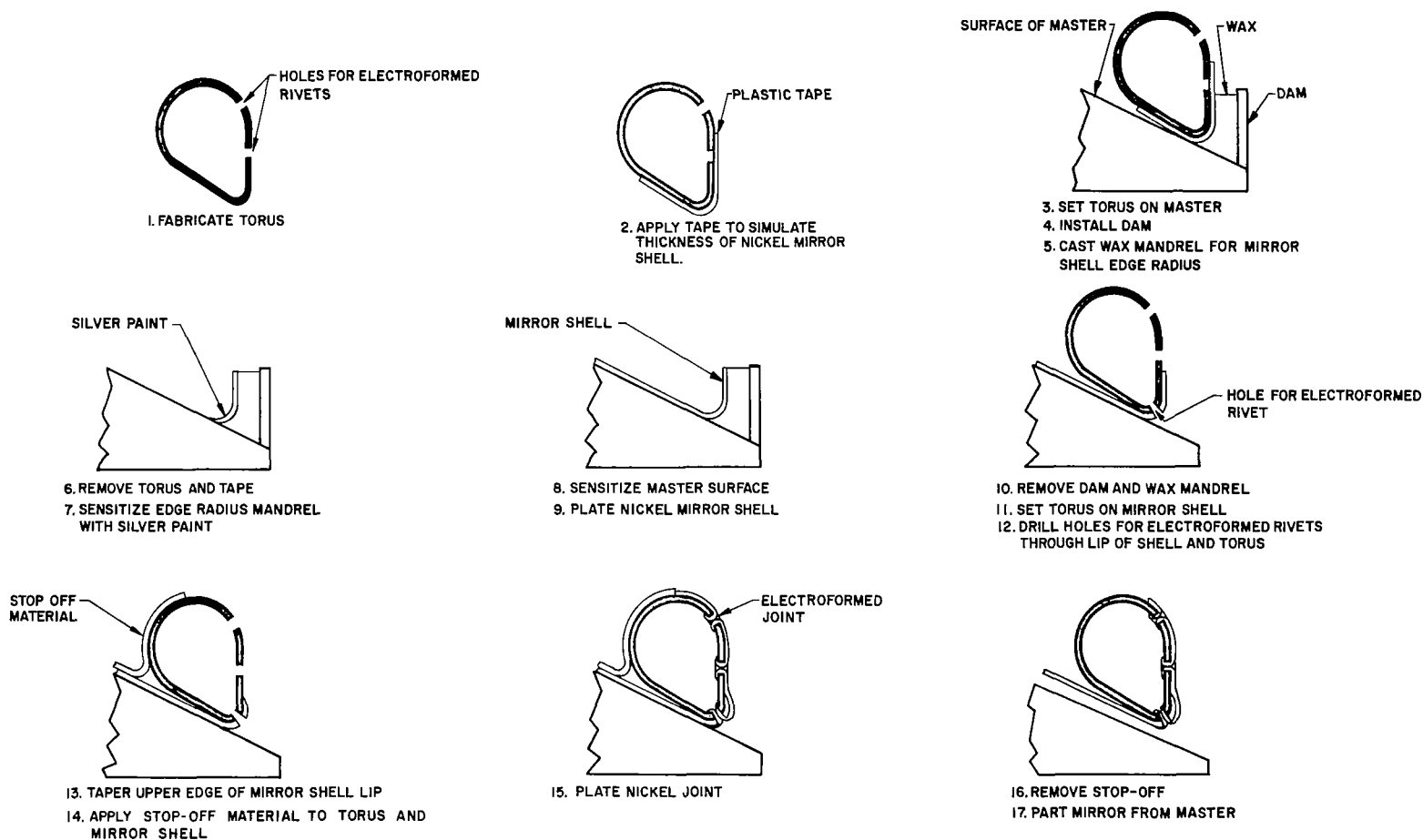


FIG. 4-10 TORUS ATTACHMENT SEQUENCE

is marked. A dam is then placed on the master surface a short distance outside the torus. Any gaps between the torus and the master are sealed with tape. Melted wax is poured between the torus and the dam and allowed to harden. The torus is then removed. The curvature of the wax mandrel is smoothly faired with the master surface. The portion of the mandrel to be plated is overcoated with a layer of conductive silver paint. If a central torus is to be used, a similar mandrel is placed near the center of the master.

The entire master surface is then carefully washed with a mild detergent solution, followed by a distilled water rinse and rapid drying to prevent water marks.

Immediately after the master is cleaned, it is made electrically conductive by a chemically-deposited coating of metallic silver. The silver is reduced by formaldehyde from a silver nitrate solution. The silver nitrate solution and formaldehyde are stored in separate containers and are simultaneously mixed and sprayed on the master surface using a 2-head spray gun. The solutions atomize, mix in the air, and fall upon the master surface leaving a coating of pure metallic silver. When the coating becomes opaque, it will have a thickness of approximately 600 \AA (approximately $1/10$ wavelength of visible light). Coating thickness is not at all critical. If the silver coating is to be used as the mirror reflecting layer, the surface which was next to the master will be the reflecting surface. Therefore, thickness variations in the coating would have no effect on optical accuracy. However, even if the silver were to be removed, errors in the nickel surface resulting from a thickness variation in the original silver layer would be trivially small. Even if the coating thickness could not be controlled to better than a factor of 10 (say from 600 to 6000 \AA) the resulting deformation would only be $1/2$ micron, which is completely negligible.

4.3.3 Plating of Mirror Skin

4.3.3.1 Choice of Plating Conditions

Values must be chosen for several plating parameters prior to designing the plating equipment and specifying the plating procedure. Among the most important of these parameters are current density, bath temperature, and bath composition. Taken together, these parameters control the deposition rate and the stress conditions in the deposited skin. The current density should be as low a value as possible (consistent with other requirements) to reduce the total power requirement when plating this large structure. Deposition rate is not important because of the moderate skin thickness. The bath temperature should also be fairly low because of the necessity of maintaining the master at the bath temperature throughout the fabrication and plating sequence in order to minimize thermal stressing. Figure 4-11 shows a typical stress curve for a nickel sulfamate plating solution at 100°F. These stress values are in arbitrary units. The zero stress point is at approximately 7 amps per ft². Although this stress curve has a fairly deep slope, flatter and more desirable stress curves can be produced by changing the bath composition slightly through the addition of stress-reducing agents. The physical properties of the deposited skin are inferior if plated at temperatures much below 100°F. For purposes of this discussion, a bath temperature of 100°F and a current density of 7 to 10 amps per ft² are satisfactory.

4.3.3.2 Plating Procedure

First, power supply leads will be attached to the master. The electrical connection to the silver sensitizing layer will be beneath the inner and outer edge radius mandrels. Next, the tank sides are attached and sealed and the anode array is lowered into place. The plating solution is then pumped into the plating tank. A voltage is applied sufficient to initiate plating at a small percentage of the steady state current density. The current is gradually

STRIP TEST - NICKEL

DATE 4/11/62 TANK NO. 6 TEMP 100°
120° SOLUTION Normal + .005 oz/gal.
SNSR SpGr 1.270 pH 4.6

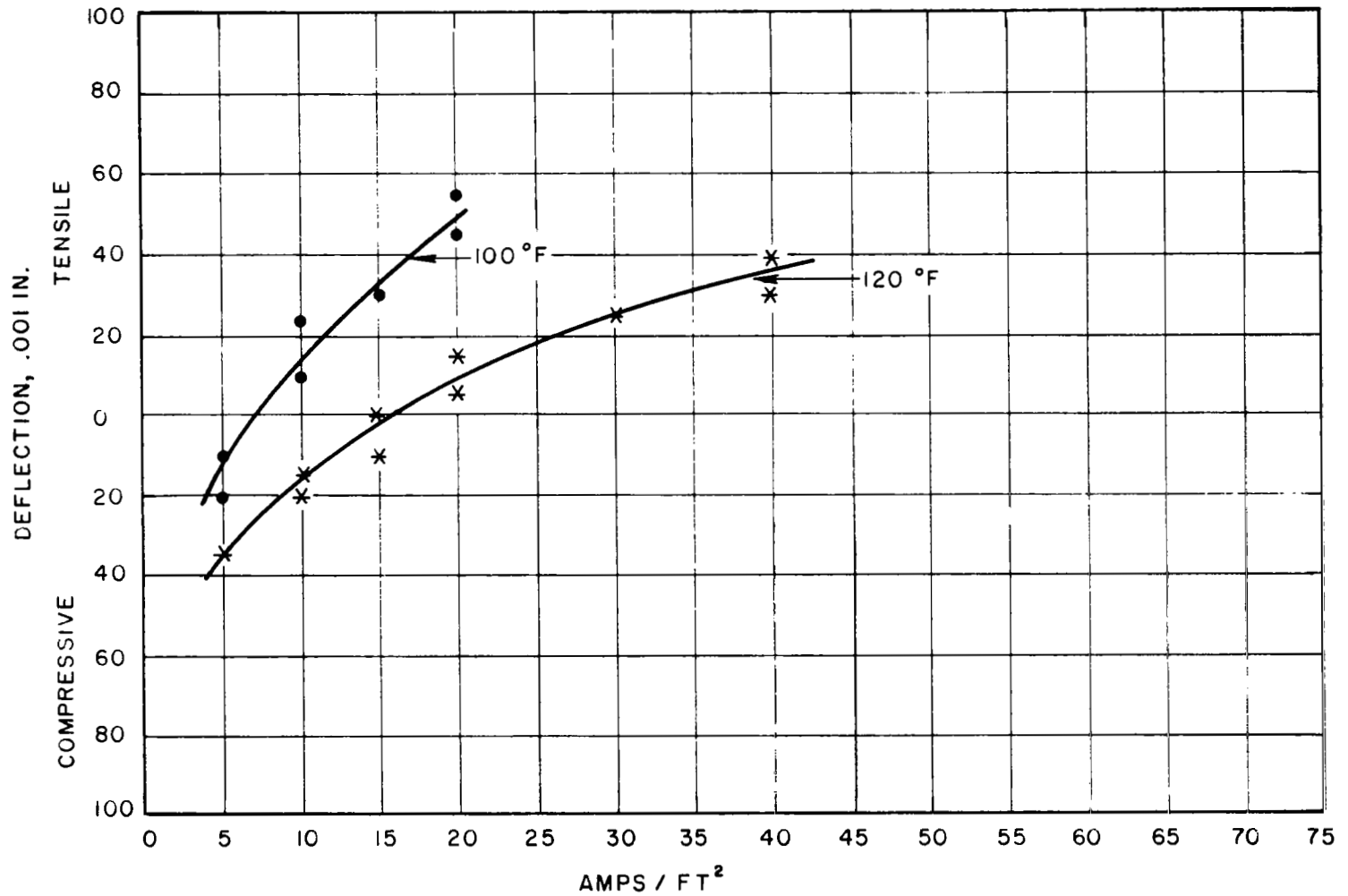


FIG. 4-11 STRESS VS CURRENT DENSITY FOR TYPICAL NICKEL SOLUTION

brought up to the full value in 15 to 30 minutes. If the current is increased too rapidly, the initial thin layer of nickel will not be able to carry the current, and the lead attachments will burn. Plating continues until the desired thickness of nickel has been deposited. The thickness is related to the following plating parameters:

$$\text{Skin Thickness} \sim (\text{Current Density})(\text{Plating Time})(\text{Bath Efficiency})$$

The bath efficiency is known approximately for mirror configurations of this type, but it must be confirmed experimentally for this particular configuration. This will be done by plating a few test skins prior to attempting to make a complete mirror. The test skins will be sectioned, and thickness profiles will be plotted to determine both plating rate and thickness uniformity.

If necessary the anode array configuration will be altered to give a better thickness distribution. When the desired thickness has been built up, the power is shut off and the scavenging pumps (FP2, Fig. 4-9) drain the fluid from the plating tank. After the solution has been drained, the anode array is lifted and the skin is washed with water to remove residual traces of plating solution.

Next, the edge mandrels are removed along with any traces of wax or silver paint. The skin is now ready for the attachment of the torus.

4.3.4 Torus Attachment

The prepared nickel or titanium torus is lowered into place so that it fits inside the upturned edge on the mirror skin, as shown in Fig. 4-10. The edge of the skin is tapered (or a fillet of wax or plastic is placed between the edge of the mirror skin and the side of the torus) in order to provide a smooth transition between the skin and the torus. If this joint is not smooth, it will be extremely weak because of a cleavage in the crystal structure emanating from the inside corner of the joint.

Thickness can and has been easily controlled to $\pm 5\%$ over large structures. Maximum optical errors, due to electroforming variations, of less than 30 seconds can be reasonably expected from experience.

Since the actual torus was used to case the edge mandrel, an excellent fit will be obtained with no large gaps to bridge. A series of holes is now drilled through the upturned edge of the skin and the torus (a ring of holes has already been placed in the torus above the mirror skin edge). All portions of the torus which are not to be plated when forming the joint are covered with plastic tape. The mirror skin is covered with a large plastic sheet taped in place at the edges. The area of torus and skin on which the joint is to be placed is now carefully cleaned. The tank sides and the anodes are put in place, and the joint between the skin and torus is plated in the same manner as was the original mirror skin.

Essentially the same procedure is used for both an outer and inner torus if both are incorporated in the collector design.

After plating is completed, the solution is removed and the plated area is washed. The tape and any other plating inhibitors are removed. The mirror is now ready for parting.

4.3.5 Parting of Mirror From Master

An advantage of the plastic surfaced master is that the adherence of the electroformed nickel skin is very slight. Parting is accomplished by the use of mechanical force, air pressure, and differential thermal expansion. The master handling fixture (see Section 4.5) is attached to the inner and outer tori. Flexible seals are placed between the tori (both inner and outer) and the master surface. The mirror is then gently lifted using the mirror handling fixtures, as the air pressure is increased between the mirror and the master. In this way, the parting line will move across the surface of the master starting both at the outer and inner radii. If any difficulty is encountered in advancing the parting line, local differential thermal expansion is used by heating the surface with a hot air gun. After the mirror has been separated from the master, the air seals are removed to complete the parting operation.

4.3.6 Coatings

4.3.6.1 Reflective Coatings

Immediately after the mirror has been removed from the master, the surface is flushed with a mild solution of detergent in distilled water and finally rinsed with distilled water to remove any residual traces of plating solution. If the silver is to be used as the final reflective layer, the mirror is now complete except for application of protective coatings, if any.

If the mirror is to be vacuum coated, the silver is first removed using a proprietary EOS technique which takes off the silver without damaging the nickel substrate. The mirror will then be placed in a suitable coating chamber and coated with the following vacuum-deposited layers:

<u>Coating</u>	<u>Thickness</u>
(Nickel substrate)	
Chromium	$200 \text{ \AA} \pm 100 \text{ \AA}$
Silicon monoxide	$2500 \text{ \AA} \pm 250 \text{ \AA}$
Aluminum	$1000 \text{ \AA} \pm 200 \text{ \AA}$
Silicon monoxide	$2500 \text{ \AA} \pm 250 \text{ \AA}$ (optional)

If the mirror is to be transported to another facility for application of the vacuum-deposited surface layers, it will be placed in a box or plastic bag with a clean dry nitrogen atmosphere to protect the nickel surface.

4.3.6.2 Protective Coatings

Three kinds of protective coatings are being considered for silvered mirrors:

1. Strippable plastic (removed before launch)
2. Photolyzable film (evaporates in space)
3. Amino silane (permanent)

The strippable plastic coatings are of the cellulose acetate type and are applied by spraying. The photolyzable film can also be applied by

spraying. It may be possible to do limited mirror testing with the strippable coatings or the photolyzable film. The amino silane coating is applied from a hydrocarbon solution in very thin layers. It offers specific protection for silver and should not affect optical characteristics. However, further tests are required before this coating can be fully evaluated.

4.4 Testing

Both the optical and structural testing of the full-scale collector can be accomplished in a manner similar to that developed for smaller mirrors. The particular tests to be run depend on the type of test data required for system design and development. For that reason, the tests will not be detailed here.

It is expected that the primary optical and performance testing will center around Hartman and the calorimetric evaluation of development mirrors. Several solar test facilities are available in the United States for testing mirrors as large as or larger than 30-feet diameter. Other than protecting the mirror against surface degradation and excessive wind loading, no problems are seen in ground testing.

The structural tests will probably include at least:

1. Static spring rate tests
2. Static buckling tests
3. Vibration tests - mechanical and acoustical

The size of the unit may pose problems in performing acceleration, shock, or acoustic noise tests. Some thermal testing can be accomplished during the solar tests. Temperature gradients can be induced by heat lamps placed behind and about the periphery of the structure.

4.5 Handling and Storage

The major handling problems arise from:

1. The large size of the structure

2. The susceptibility to damage from local impact
3. The necessity of protecting the reflective surface from dirt and corrosive agents

The problems in handling the large mirror are most severe when moving it from one facility to another. These are discussed in more detail in Section 4.6, Transportation. Within the manufacturing facility, no severe handling problems are expected. All required movement of the mirror can be accomplished by normal industrial procedures.

The problems of protecting the mirror against local impact and surface damage are more severe. For this reason, a special handling and storage container will be constructed to protect the mirror during all handling operations. This container consists of a framework having attachments to the mirror and external handling points. The front and rear surfaces of the mirror are protected by removable covers. The rear cover will conform to the mirror shape. The covers will be made in self-interlocking sections of plastic reinforced fiberglass for maximum impact protection.

Except for special test purposes, the mirror will never be left unprotected at any time during the normal manufacture, handling, testing, or storage operations.

Normal storage procedures will be adequate. If the mirror is coated with silver, the surface must either be provided with a permanent or removable protective coating or the atmosphere in the storage container must be maintained free from sulfide contaminants. The latter is easily accomplished by providing the box with a moderately good seal and by purging with dry nitrogen. In addition, the box can be lined with a special lead acetate impregnated paper which absorbs sulfides. The special handling and storage container will be designed to protect the mirror during long-term storage.

4.6 Transportation

The large bulk of the 30-foot diameter mirror, when mounted in its handling and storage container, makes normal surface transportation

methods rather cumbersome. Transportation over the public streets is probably possible for short distances but would require a special escort. However, there are four methods of short distance and long distance transportation which appear to be either practical or worthy of serious consideration.

4.6.1 Helicopter

Inquiries were placed with companies specializing in helicopter handling and construction work regarding the feasibility of transporting the 30-foot collector by this means. The larger helicopters are capable of transporting this size mirror, mounted in its protective container. The helicopter provides probably the most convenient short-distance transportation method, particularly within the city. Transcontinental transportation of the mirror by helicopter also appears worthy of consideration. The cost, although not negligible, does not seem out of proportion to other program costs.

4.6.2 Ship or Barge

Transporting the collector by ship or barge is feasible. However, there are some disadvantages, including:

1. Long shipping time
2. Danger of corrosion from sea atmosphere
3. Difficulty of controlling handling procedures

The corrosion problem should be avoidable by careful design and sealing of the shipping container.

4.6.3 Air Ship

Lighter-than-air craft such as blimps would seem to be ideally suited for transporting bulky, delicate structures such as the Brayton cycle collector. An inquiry was placed with the Goodyear Aircraft Corporation in this regard. Goodyear indicated that they presently have no blimps which are suitable for transporting structures of this size. Since the Navy has control of larger blimps, an inquiry to the appropriate Navy authority could possibly provide a suitable craft.

4.6.4 Airplane

No conventional transport aircraft is nearly large enough to carry the 30-foot Brayton cycle collector. However, Aero Spacelines, Inc., builder of the Pregnant Guppy, has obtained options to buy two English-built Saunders-Roe Princess flying boats which would be converted into turbo-fan powered, land-based aircraft to haul Saturn rocket stages. This airplane could carry rocket stages up to 33 feet diameter and 82 feet long. It could easily accommodate one or several of the 30-foot diameter collectors. If any planes of this type are built, they would provide a ready solution to the collector transportation problem.

It might also be possible to build a special shipping container which could be slung beneath the fuselage of a large airplane.

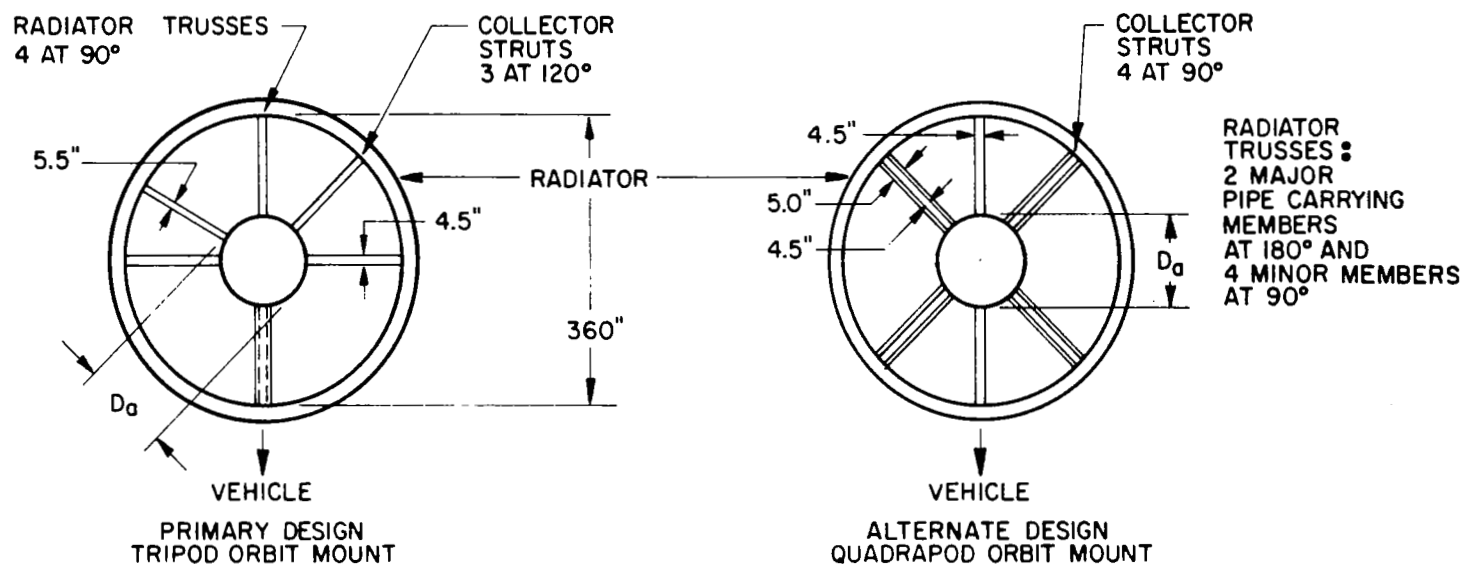
5. EFFICIENCY

The electrical power output of the Brayton cycle power system is proportional to the collector-absorber efficiency. Collector-absorber efficiency is the net power absorbed by the cavity absorber (exclusive of the cavity heat losses other than losses through the cavity aperture) divided by the gross power that could be intercepted by an unobstructed collector. For missions that are power limited or that have high-power requirements, efficiency is probably the most important system evaluation criterion.

A collector-absorber efficiency of greater than 75 percent, inclusive of all absorber heat losses, is desirable for as large a range of misorientations as possible. Many efficiency losses are unavoidable, although some losses can be regulated. Therefore, it is imperative that those efficiency losses that can be minimized receive particular attention. A detailed discussion of efficiency losses follows.

5.1 Collector Obscuration

All collector-absorber efficiency values calculated in this report were based on an assumed collector obscuration of 6 percent. This value was derived from preliminary structural details provided by NASA, Lewis. Figure 5-1 shows various obscuration losses based on later data for the probable extremes in cavity obscuration and on two different structural designs. The obscuration for these cases ranges from 6.2 to 7.2 percent. These calculations are based only on the effects of two dimensional obscuration. This assumes that the sun is a point source, perfectly oriented. Additional obscuration can occur because of misorientation effects and the finite solar disc.



		PRIMARY DESIGN		ALTERNATE DESIGN	
DIAMETER OF CONVERSION EQUIPMENT, D_a		60"	48"	60"	48"
	UNITS				
TRUSS AREA	FT ²	14.1	14.6	9.4	9.8
STRUT AREA	FT ²	17.2	17.9	20.8	21.6
ABSORBER AREA	FT ²	19.7	12.6	19.7	12.5
TOTAL AREA	FT ²	51.0	45.1	49.9	43.9
OBSCURATION	%	7.2	6.4	7.1	6.2

FIG. 5-1 30-FT DIAMETER COLLECTOR OBSCURATION

The width of any obscured area on the mirror due to the radiator will be a maximum of $l \tan \beta \approx l\beta$ where l is the distance from the collector rim to the top of the radiator and β is the misorientation angle.

For a perfectly oriented mirror a ray from the edge of the sun, corresponding to a ray misoriented 16 minutes or 0.267 degrees from the optical axis, would be obscured in the extreme case from the area $(R_r - 0.87)$ inches where R_r is the internal radius of the radiator. Initial increments of misorientation will obscure the collector area at the rate of 0.04 percent of the total area per minute of misorientation.

The lost rim area due to misorientation effects is consistent with the rim area lost due to the collector shell-torus joint and the radiator-collector nesting tolerances.

5.2 Reflective Coating

Important considerations for a reflective coating are:

1. Reflectance
2. Application
3. Preorbit and orbital environmental resistance.

Silver has the highest reflectance of any single metallic coating. Figure 5-2 shows a reflectance comparison among silver, aluminum, and silicon monoxide protected aluminum over the solar spectrum. Laboratory deposited silver coatings have achieved reflectances between 94 and 95 percent averaged over the solar spectrum. However, for practical purposes a 91 percent reflectance is a reasonable value to be expected in production.

Figure 5-3 shows the effect of reflectance on collector-absorber efficiency based on an 80.5 percent efficiency for a 91 percent reflective silver coating. In this comparison, practical reflectance values of 88 percent for aluminum and 85 percent for silicon monoxide protected aluminum are used. Though the practical reflectance

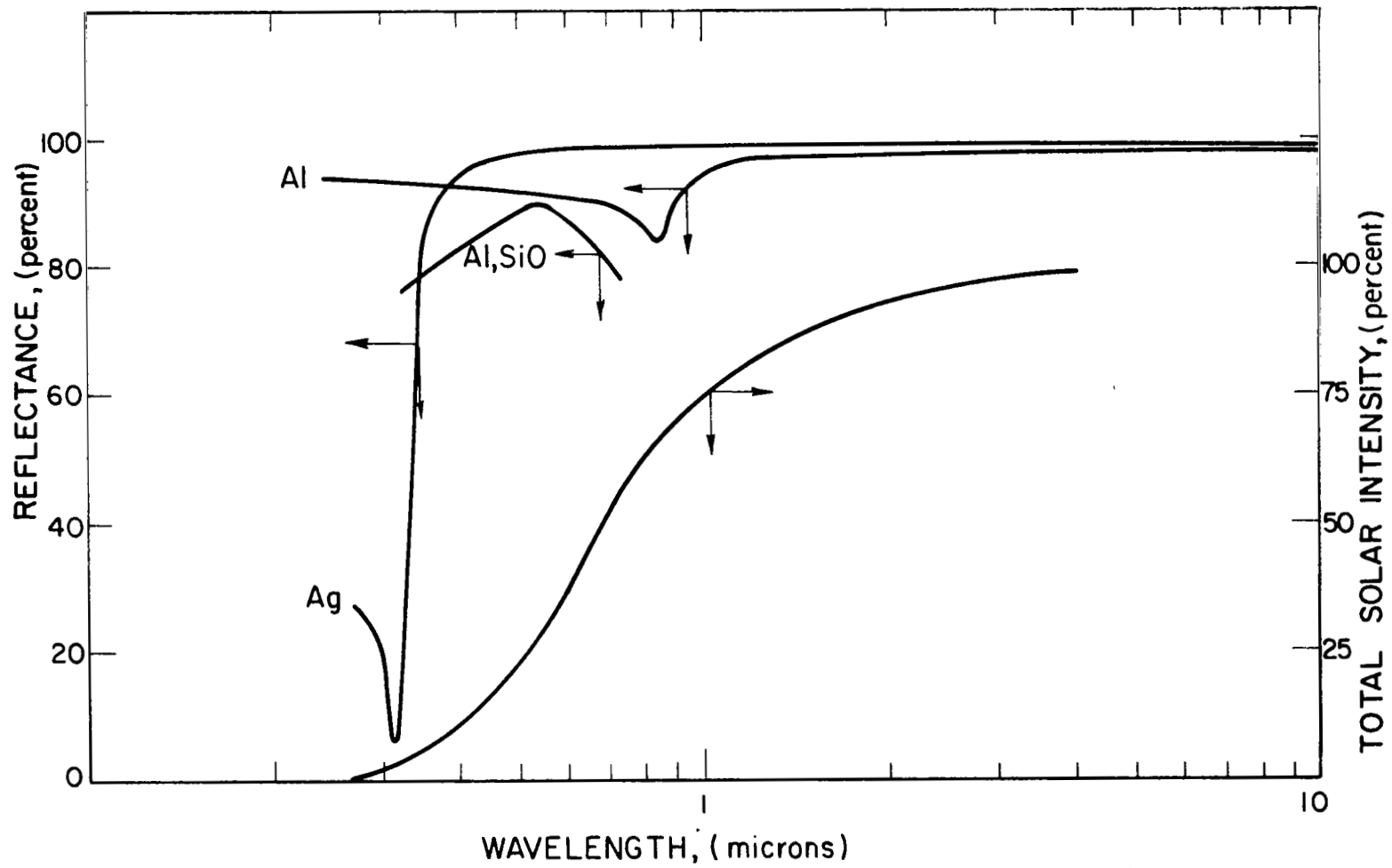


FIG. 5-2 REFLECTANCE AND TOTAL SOLAR INTENSITY VS WAVELENGTH

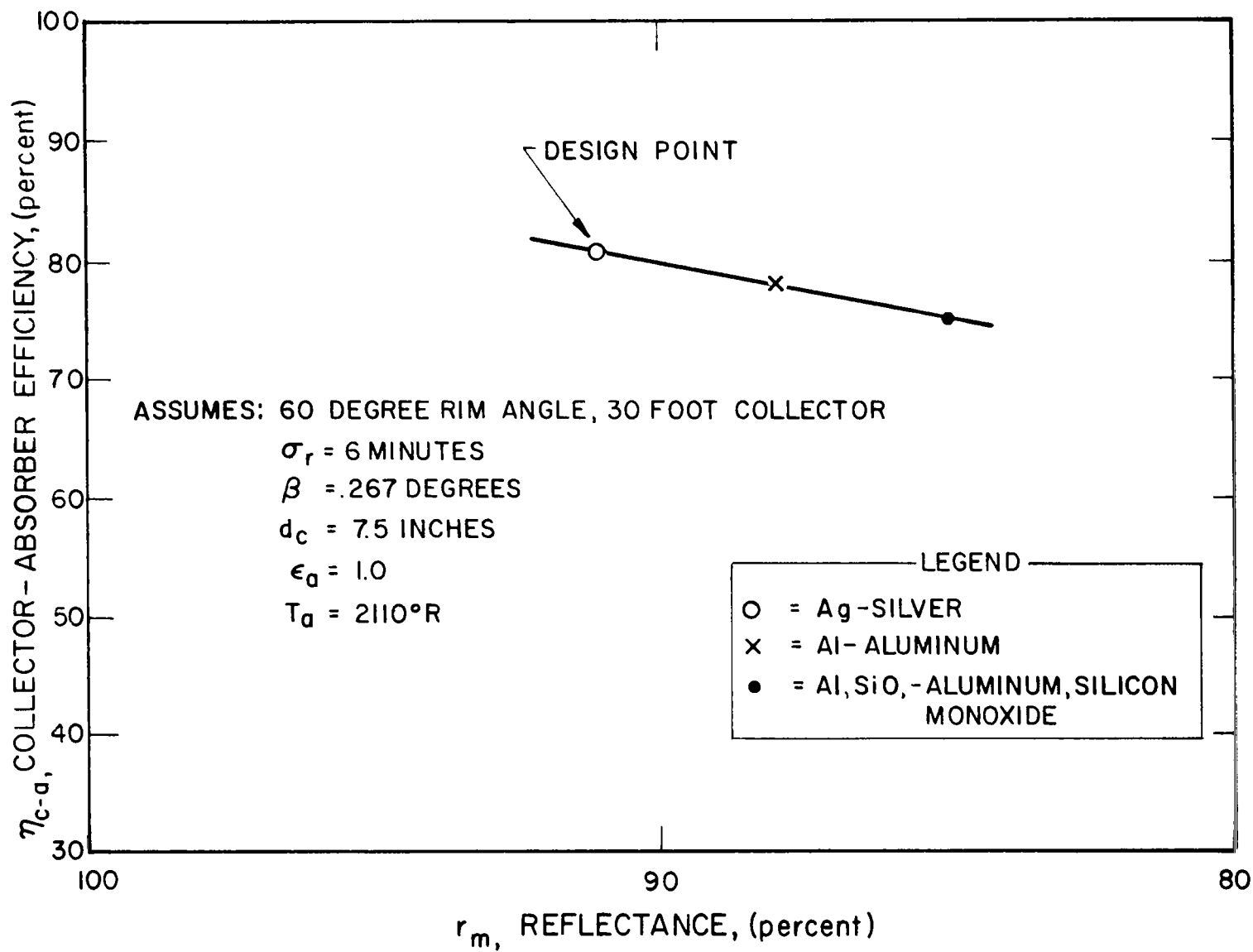


FIG. 5-3 COLLECTOR-ABSORBER EFFICIENCY VS REFLECTANCE

values for aluminum and silver are about 2 percent to 4 percent lower than the theoretical reflectance values, these values are based on actual collector tests. On two-foot and five-foot solar collectors EOS has achieved cold calorimeter, unobscured efficiencies of 91 percent using chemically deposited silver. Aluminum coated five-foot collectors have never exceeded a cold calorimeter unobscured efficiency of 88 percent. For practical purposes the collector surface reflectance is equal to the maximum efficiency achieved under cold calorimeter testing (using a large aperture) with no obscuration. Chemically deposited silver is the recommended coating for the Brayton cycle collector because of its significant performance advantage. Extensive experience with the use of silver at EOS indicates that silver is a practical coating for large collectors. However, if for some unforeseen reason silver proves unsatisfactory, aluminum or Al/SiO can be applied to the collector by vacuum deposition. The methods of applying silver or other coatings to collector surfaces are discussed in the manufacturing section (4.3.7). The durability of these coatings before launch and in space is discussed in the Reliability Section 7.0.

5.3 Optimum Collector Rim Angle

For a given collector diameter various factors affect the choice of the optimum collector rim angle. These include:

1. Structural integrity of collector shell
2. Total of collector and strut weight
3. Surface error distribution over collectors of different rim angles, as a function of rim angle
4. Cavity axial misfocus and radial misalignment
5. Subtended angle of the solar source and limb darkening effects
6. Thermal errors
7. Angular misorientation as a function of time

8. Structural errors caused by orbiting forces

9. Packaging height

For a perfect collector with perfect focus and orientation when 100 percent of the reflected energy is focused into the cavity aperture, the maximum collector-absorber efficiency occurs at a 45 degree rim angle. Based on 6 percent obscuration, a reflectance of 91 percent and an absorber temperature of 2110°R , the variation in total collector-absorber efficiency between a 45 degree rim angle and a 60 degree rim angle "perfect" collector as above would be less than 0.4 percent. A comparison of 45 and 60 degree rim angle collectors is given in Table 5-I.

TABLE 5-I
COMPARISON OF HIGH AND LOW RIM ANGLE COLLECTORS
TYPIFIED BY 45 AND 60 DEGREE RIM ANGLES

<u>Advantages</u>	
<u>45 Degree Rim Angle</u>	<u>60 Degree Rim Angle</u>
Smaller theoretical image	More rigidity
Smaller surface area	Less shell weight, for the same rigidity
Low packaging height	Shorter and much lighter struts
Less efficiency loss due to:	Much less total weight
Axial misfocus	Less efficiency loss due to:
Misorientation	Random errors
Rim errors	Radial misalignment in the focal plane

The optimization of efficiency as a function of rim angle is highly dependent on the weighting given to each factor affecting efficiency. Many factors which affect optical errors can only be determined by experimental studies of full scale collectors. Therefore, as a first approximation the collector-absorber efficiency can be considered as a constant for rim angles between 45 and 60 degrees.

Under this assumption the optimum rim angle would be a function of structural integrity, packaging, and weight. For efficiency calculations a rim angle of 60 degrees was used throughout this analysis. For analysis purposes consider the figure of merit $K_1 \eta / W$, where $K_1 \eta$ is the system power, η the system efficiency and W the system weight. K 's used in this study are proportionality constants which do not vary in the analysis. For a constant efficiency only W will change with rim angle.

$$W = W_c + W_s + W_p$$

where W_c is the collector weight

W_s is the strut weight

W_p is the remaining system weight

Since W_p is constant for constant power, the maximum figure of merit,

$$\frac{\text{power}}{\text{system weight}}$$

will occur at minimum $W_c + W_s$. Therefore, the optimum rim angle from a weight standpoint will occur at the point of minimum $W_c + W_s$.

W_s , strut weight, varies with the allowable strut deflection, given by

$$w = F(W_c, W_s, I_s, \ell_s)$$

where I_s and ℓ_s are the moment of inertia and length of the strut.

Assuming as a first approximation that the collector and torus weight are constant for all rim angles and neglecting the effect of strut weight on strut deflection, then strut deflection, w , is given by

$$w = \frac{K_2 \ell^3}{D_o^4 - D_i^4}$$

These assumptions only understate the total weight at low rim angles.

For strut weight comparisons the following basic design was assumed:

design = tubular, tripod
 ℓ_s = 17.3 feet (rim to focal point distance for a 60 degree rim angle)
 D_o = 5.5 inches (outside diameter of strut)
 D_i = 5.25 inches (inside diameter of strut)
 ρ = 0.097 lb/in³ (density of strut material)

Strut lengths for other rim angles were calculated from the equation

$$\ell_s^2 = \left(f - \frac{R^2}{4f}\right)^2 + R^2$$

Where f is the mirror focal length and R is the rim radius. The tubular moment of inertia was varied by changing D_i and keeping D_o constant so that η_{c-a} would not be changed by increased strut obscuration.

For a constant deflection w ;

$$\frac{\ell_s^3}{D_o^4 - D_i^4}$$

must be a constant. Therefore both ℓ_s and D_i must change with rim angle and the strut weight can be calculated for any rim angle, ξ , such that $W_s = \frac{3\ell_s \pi (D_o^2 - D_i^2) \rho}{4}$. A plot of W_s vs ξ is shown in Fig. 5-4.

The collector weight for any rim angle can be calculated by assuming:

1. For constant shell rigidity shell thickness, t , $\propto fA_c$
2. Collector shell weight $\propto tA_c$
3. Torus weight \propto shell weight
4. Collector weight at 60 degrees rim angle = 500 pounds;

Therefore, the weights of collectors of other rim angles having the same structural strength were determined by assuming the following relative focal lengths and relative shell areas:

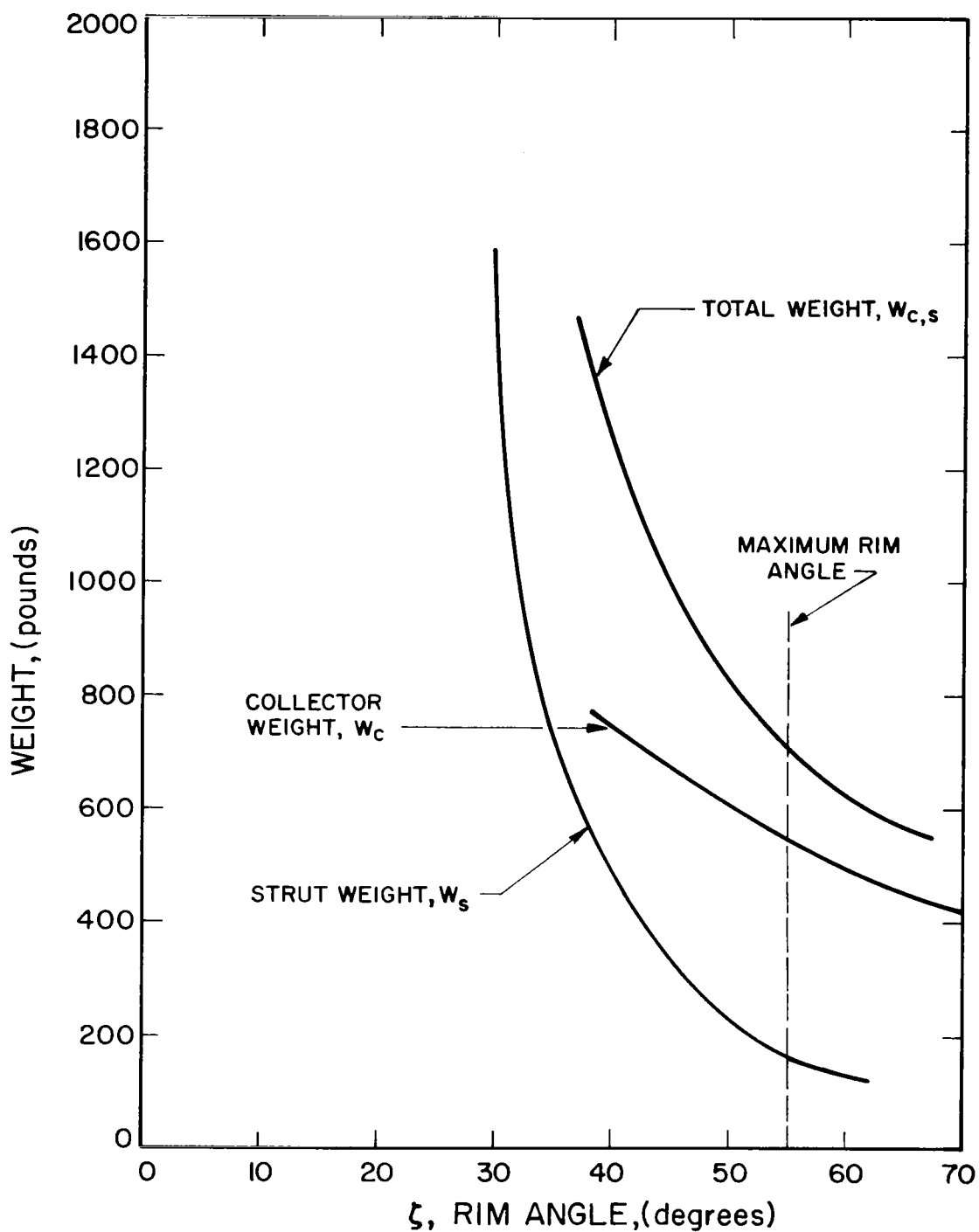


FIG. 5-4 COLLECTOR WEIGHT, STRUT WEIGHT AND TOTAL WEIGHT AS A FUNCTION OF RIM ANGLE FOR A 30-FT COLLECTOR

$$W_{c,\zeta} = W_{c,60} \frac{f_{\zeta}}{f_{60}} \cdot \frac{A_{c,\zeta}}{A_{c,60}}$$

A plot of $W_{c,\zeta}$ and $W_{c,\zeta} + W_{s,\zeta}$ vs. ζ is also shown in Fig. 5-4. This indicates that the minimum weight occurs at a rim angle greater than 60 degrees.

The radiator height h_r now limits the maximum rim angle to 55 degrees for a 30-foot collector. The optimum radiator height for a 20-foot collector will be considered below.

The paraboloid packaging height, h_p , equals the sagitta, h :

$$h_p = h = \frac{D^2}{16f}$$

System power is a function of collector area:

$$P_s = K_3 A_c = \frac{K_1 \pi D^2}{4}$$

Radiator area is a function of radiator height and diameter.

$$A_r = K_4 \pi h_r D_r$$

$$D_r \approx D$$

For equivalent system efficiencies, the ratio of power output to radiating area will be approximately the same, or:

$$\frac{P_s}{A_r} \approx K_5 = K_6 \frac{D}{h_r}$$

transposing

$$\therefore h_r = K_7 D$$

but

$$h_p = 16 D \left(\frac{D}{F} \right)$$

∴ for constant rim angles, i.e., $\frac{D}{f} = K_8$

$\frac{h_r}{h_p} = K_9$ and ∴ is independent of diameter.

Therefore if the packaging height, h_p , limits the 30-foot diameter collector rim angle to a maximum of 55 degrees, the rim angle for the 20-foot diameter collector would also probably be limited to 55 degrees.

The efficiency would have to change appreciably between 45 and 60 degree rim angles to make any difference in the trend of the power/system weight figure of merit. The term

$$\frac{K_1 \eta}{(W_s + W_c) + W_p}$$

must be a constant for equivalent figures of merit, where $\eta \approx K_{\eta c-a}$.

Therefore

$$\frac{\eta_{c-a}}{W_s + W_c + K_{10}}$$

must be constant. Based on a system weight of 2000 lb, a collector and strut weight of 700 lb, and a 55 degree rim angle efficiency of 80.5 percent, the following efficiencies would be required to maintain a constant power/system weight ratio for the 30-foot collector.

Rim Angle	Weight	Efficiency	<u>Efficiency</u> Weight
55°	2000 lb	80.5%	0.0403 %/lb
50°	2130 lb	85.8%	0.0403 %/lb
45°	2300 lb	92.5%	0.0403 %/lb

Since it is theoretically impossible to achieve an efficiency of over 85.5 percent with 6 percent obscuration and 91 percent

reflectivity even if the efficiency was not constant over the range of 45 to 55 degrees, the 55 degree rim angle would still have the best power/system weight ratio.

The use of tapered tubular struts or tapered rectangular struts of high I and similar cross section could achieve lighter strut weights for the same deflection and obscuration. Lighter struts would decrease the advantage of the 55 degree rim angle.

5.4 Computer Analysis Program

When this design study began no one computer program could adequately handle all the calculations necessary for a detailed collector-absorber efficiency analysis. Also a detailed analysis of surface errors of collectors made by various fabrication techniques was not available. Therefore the decision was made to use an existing optical ray-trace program with a surface error approximation to generate efficiency calculations. The choice of the ray-trace program still appears to be a good one, because of the limited surface error distribution data on actual collectors and the high cost of making an accurate misorientation trace using a more rigorous program which is being developed. This advanced computer program involving a collector, cavity absorber and absorber heat exchanger is being developed by the Aerospace Corporation with the assistance of Dr. George Shrenk, consultant to the Allison Division of General Motors. The collector part of this program can handle collector-absorber configurations of the following characteristics:

1. Collectors of any size, shape, or configuration
2. Orientation errors
3. Sun of any angular diameter
4. Limb darkening of the sun
5. Surface errors due to thermal distortion
6. Any diameter cavity aperture
7. Absorber surfaces of any configuration

Although this program is extremely rigorous, it is based on an assumed normal distribution of surface mirrors, which is probably invalid, and requires relatively long computer running time for cases of limb darkening, misorientation, and a combination of both circumferential and radial errors. For example, one case of misorientation run by Aerospace Corporation using this collector program took 60 minutes on an IBM 7094 to accumulate 76 percent of the total energy for one cavity aperture diameter trace. This example was run without corrections for limb darkening. Adequate corrections for limb darkening might have increased the running time from 4 to 10 times. Since an accurate analysis of any misorientation case might require at least three diametric traces, the cost of a rigorous analysis of one misorientation case, assuming 3 to 4 hours of computer time at \$600.00 an hour, does not seem economically sound for parametric analysis purposes when the input error data is questionable.

In summary, the EOS ray-trace analysis was found to be more suitable for economical parametric studies involving many variables. However, for detailed system design calculations, a rigorous and accurate program, such as that being developed by Aerospace, should be used.

The following subsections summarize the EOS analysis.

5.4.1 Collector Grid

The EOS mirror analysis was based on the IBM 1620 ray-trace and energy distribution program. This program can handle a total of 500 rays. To accommodate the limb darkening effects and collector misorientation the solar disc was represented by ten different angular misorientations representing the division of the solar disc into ten areas of equal energy contribution. Therefore, a total of 50 points maximum was used in each ray trace. These points were equally spaced on a square grid across the unobstructed collector. Because of symmetry only 1/2 the collector was traced. In practicality, only 48 spots fit across the aperture, so a total of 480 rays were traced for any given case.

5.4.2 Limb Darkening Effects

Using a solar energy distribution defined in Ref. 5-1, an equation was derived for solar radiation intensity as a function of radius on the solar disc.

The loci of the ten equal energy zones were then converted to a misorientation angle and used with the IBM 1620 ray-trace program. The ray-trace program is similar to that used in geometric optics. From the output of the ray-trace program an energy distribution across the focal plane was calculated.

5.4.3 Representation of Surface Errors

Frequently, for lack of actual data, random Gaussian error distributions have been used to represent collector surface errors. The random Gaussian distribution does not adequately represent:

1. Radial errors at the collector rim joint
2. Circumferential errors at any radial joints or ribs
3. Zonal defects of the mirror

In actual practice it appears that the maximum errors of an electroformed mirror are radial at the collector-torus rim joint or due to zonal defects of the mirror.

A tenth order polynomial error representation was chosen for mathematical and computer program simplicity. This error distribution concentrates the errors near the rim and therefore causes a higher efficiency loss, for any standard deviation error, than an equivalent random Gaussian error.

Therefore, the tenth order polynomial error distribution appears conservative but provides a good approximation of the actual error distribution for electroformed mirrors.

Computer runs were performed on collectors having the polynomial error terms of $1x$, $2x$, $3x$ and $7.5x (+ 0.18145380 \times 10^{-4} z^4 - 0.1569039 \times 10^{-5} z^6 + 0.4414007 \times 10^{-7} z^8 - 0.3999201 \times 10^{-9} z^{10})$, where z equals $\frac{R(\text{feet})}{2.5}$.

Based on the grid used in the ray-trace program, these polynomial error terms correspond to collectors having surface errors with a standard deviation of 2, 4, 6, and 15 minutes, respectively, and maximum surface errors of 5, 10, 15, and 37-1/2 minutes, respectively. The computer energy distribution program generated a table of energy in 5 percent increments as a function of the cavity aperture radius to encompass a given percentage of total energy. Two typical curves derived from the energy distribution program are shown in Figs. 5-5 and 5-6 for cases in which there was a 0, ± 1.2 and ± 2.4 inch axial focus shift. Note that in Fig. 5-5 and diameter required to encompass 100 percent of the energy at the focal point, 4.4 inches, is larger than the theoretical radius, 3.86 inches, because the vignettted aperture computation program uses points beyond the 30-foot diameter. This has the effect of making the collector-absorber efficiencies conservative by 1/2 percent or less.

The results from these curves were then plotted on Fig. 5-7, which is calculated from blackbody radiation losses, resulting in a plot of collector-absorber efficiency vs. cavity aperture diameter. These plots were then used to generate the collector-absorber efficiency curves presented throughout this report.

5.5 Collector Surface Errors

Collector surface errors can be classified as: microscopic, macroscopic, and long wave. A collector efficiency cannot be adequately predicted unless each of these surface errors is considered. Too often one or two of these types of surface errors are disregarded in the estimation of collector-absorber efficiency. Table 5-II illustrates several examples, and measurement techniques, with comments on these three types of surface errors. Figure 5-8 depicts the effects of each of these errors. If the microscopic surface errors are disregarded, the surface reflectance is often overstated. If surface errors characteristic of macroscopic effects on a collector are neglected, the standard deviation of the collector surface is underestimated.

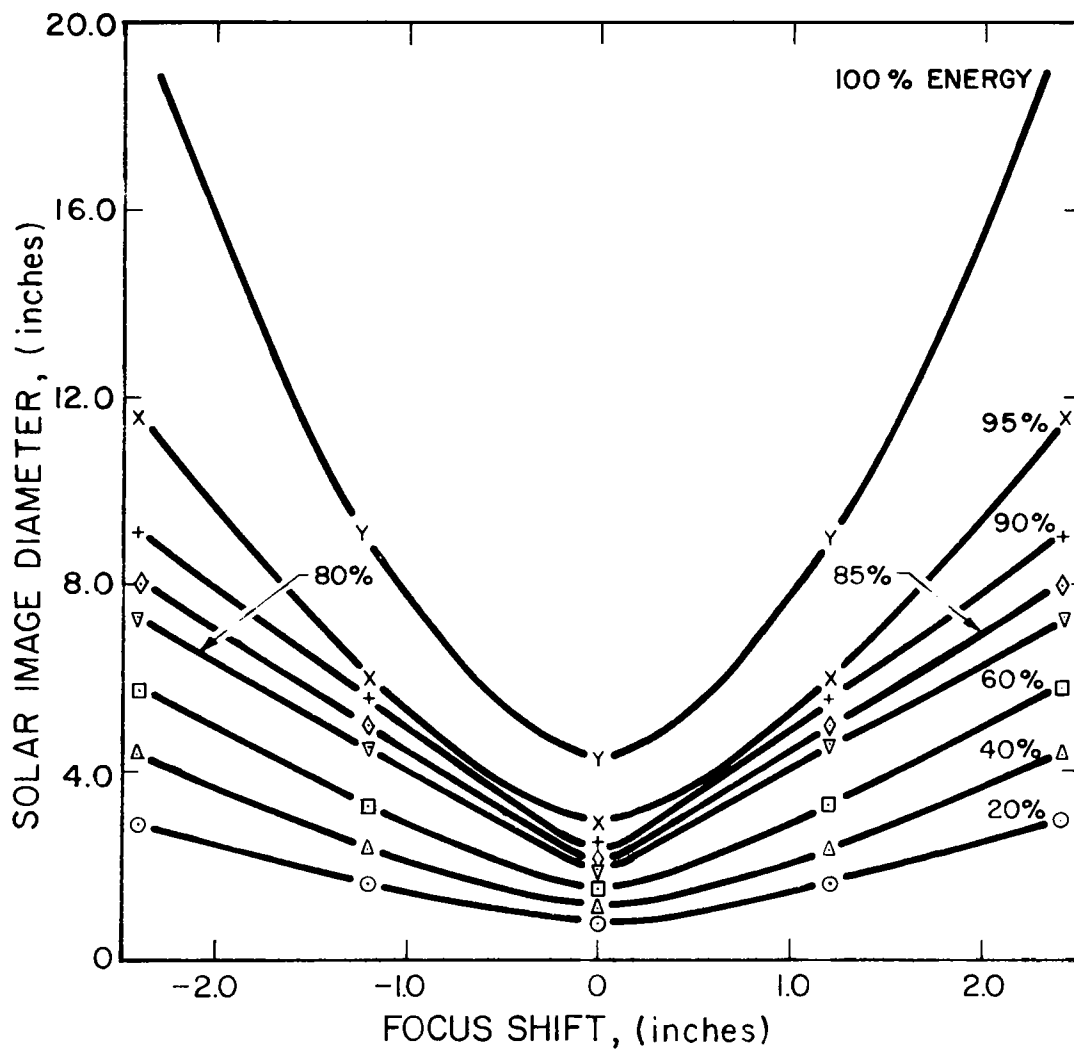


FIG. 5-5 SOLAR IMAGE DIAMETER VS FOCAL PLANE SHIFT FOR VARIOUS REFLECTED ENERGY LEVELS; A PERFECT 30 FT. DIAMETER, 60° RIM ANGLE, $f = 12.99$ FT., CONCENTRATOR WITH NO MISORIENTATION

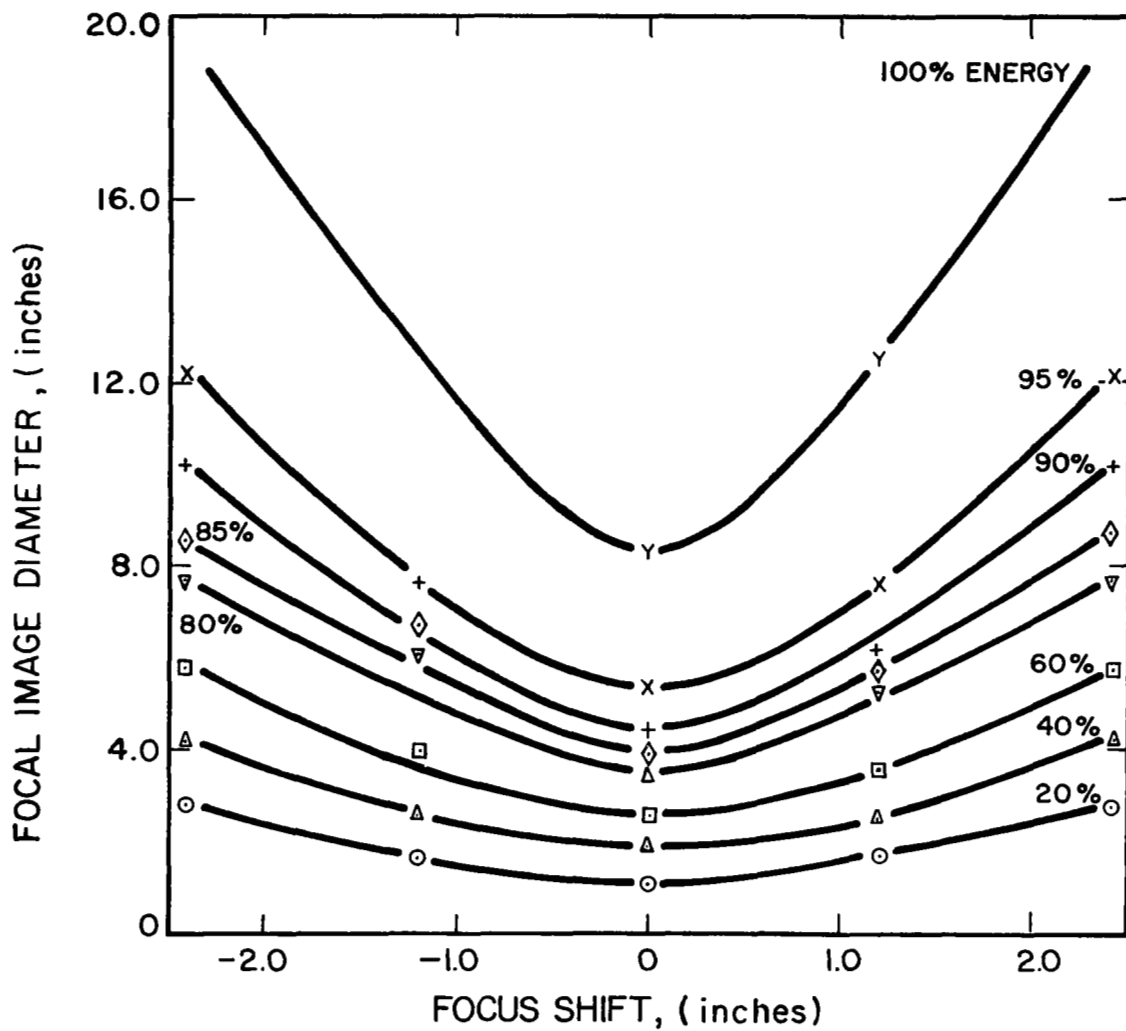


FIG. 5-6 SOLAR IMAGE DIAMETER VS FOCAL PLANE SHIFT FOR VARIOUS REFLECTED ENERGY LEVELS; A PERFECT 30 FT. DIAMETER 60° RIM ANGLE, $f = 12.99$ FT., CONCENTRATOR WITH 16 MINUTES MISORIENTATION

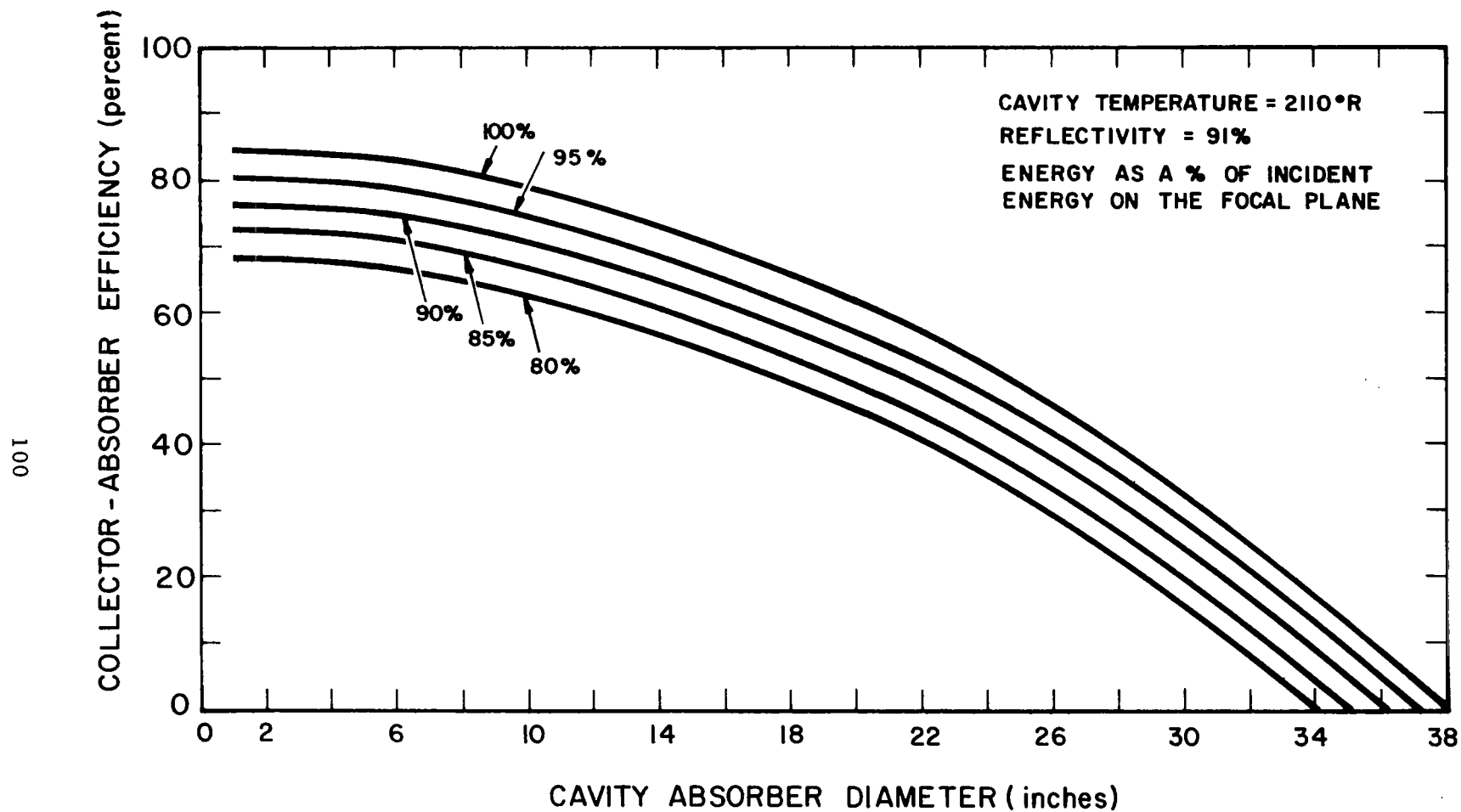


FIG. 5-7 COLLECTOR-ABSORBER EFFICIENCY VS CAVITY ABSORBER DIAMETER

TABLE 5-II

COLLECTOR REFLECTIVE SURFACE ERRORS

<u>Type</u>	<u>Examples</u>	<u>Measurement Technique</u>	<u>Comments</u>
1. Microscopic	Sleeks, scratches, fine scale orange peel, crazing, micrometeorite damage	1. Cold calorimeter, 2. Extremely accurate reflectance measurements 3. rms roughness measurements	Difficult to measure except by calorimetric performance. (Generally the difference between expected reflectance and maximum cold calorimeter performance)
2. Macroscopic	Backing structure mark off, gross orange peel, short wavelength waviness	1. Precise Hartmann or collimator tests on a macroscale	Difficult to differentiate by standard Hartmann or collimator tests - error affects the diameter rather than the locus of the axis of the reflected light cone
3. Long Wave	Joint edge roll, master waviness residual internal stress, thermal distortion	1. Hartmann test 2. Collimator test 3. Cold calorimeter	Easy to measure with Hartmann and collimator test. Error measured by the locus of the axis of the reflected light cone.

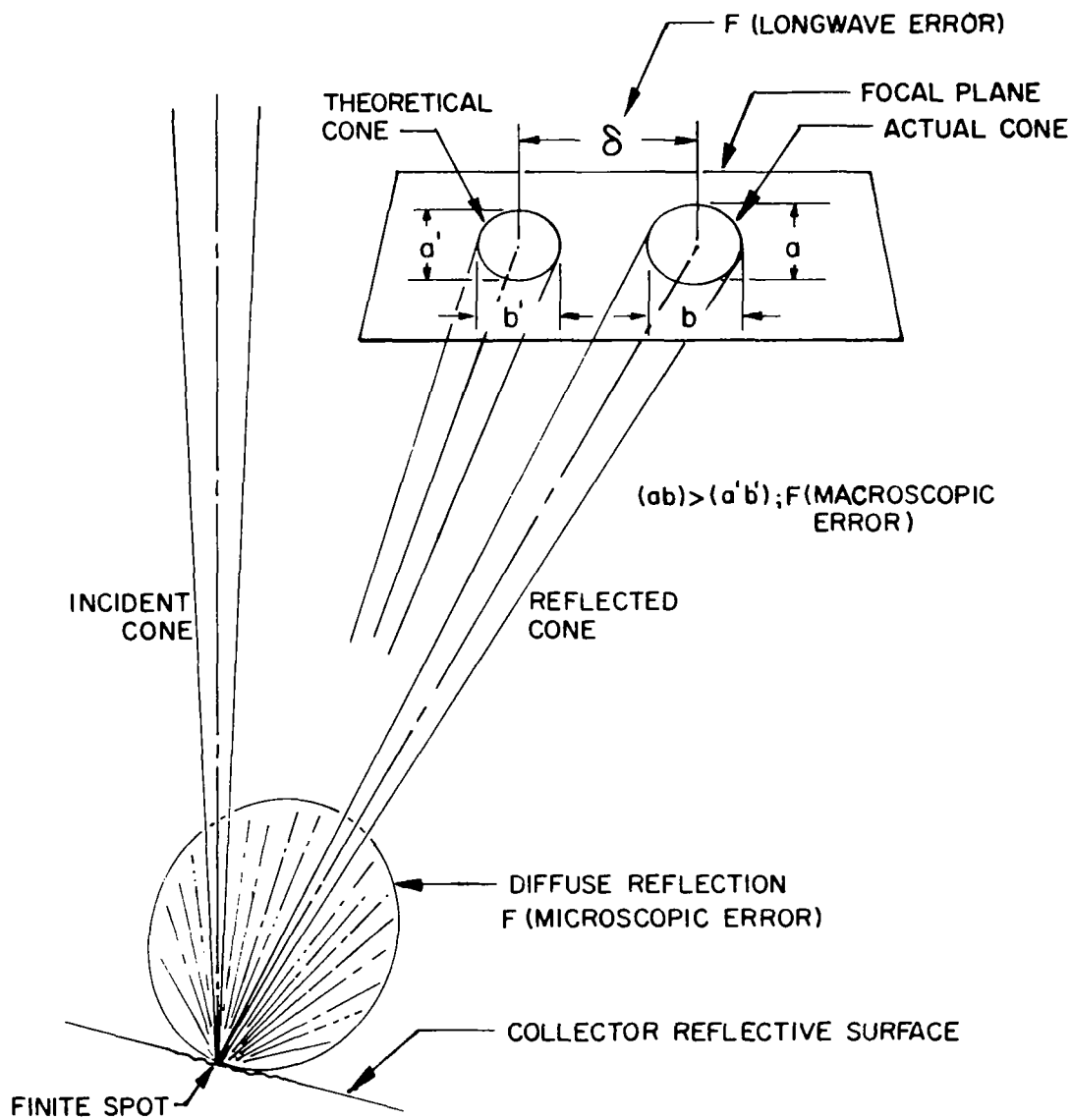


FIG. 5-8 COLLECTOR REFLECTIVE SURFACE ERRORS

5.5.1 Microscopic Errors

Microscopic surface errors cause diffuse reflection which results in a lower effective surface reflectance. These errors can result from optical polishing techniques, telegraphing of substrate defects, haziness of free-cast plastic surfaces such as occurs on spuncast masters, or micrometeorite degradation. Microscopic errors explain the difference between the expected collector reflectance (as determined from the reflectance of specially prepared coating samples) and the actual maximum cold calorimeter efficiency of the complete mirror.

5.5.2 Macroscopic Errors

Macroscopic errors are those which are individually visible to the unaided eye but which are very small compared with overall mirror dimensions. They can result from gross polishing defects, stress concentrations due to backing structure attachment, or ripples in the surface of plastic spun cast masters. These errors may easily escape notice in standard Hartmann or collimator tests because they may be small compared with the Hartmann spot or the beam from the collimator. These macroscopic errors increase the area of the reflected cone of light whereas the standard Hartmann test measures the displacement of the reflected cone center from the theoretical image point. As shown in Fig. 5-8 macroscopic errors are present when product ab is greater than the product $a'b'$ where a and b , a' and b' are the minor and major axes of the actual and theoretical images of the reflected light cone on the focal plane.

5.5.3 Long Wave Errors

Long wave errors are produced by overall collector fabrication errors, gross master distortion and residual or environmental stresses. These errors can be measured readily by Hartmann or collimator test methods.

5.5.4 Surface Error Analysis

Figures 5-9, 5-10, and 5-11 depict the change in collector absorber efficiency as a function of the standard deviation of surface error for cavity diameters of 8, 9, and 10 inches, respectively. A collector with a σ_r of 6 minutes, 6 percent obscuration, 91 percent reflectance, 0.267 degrees misorientation and a 2110°R blackbody absorber has a maximum efficiency of 80.5 percent at an 8-inch cavity diameter. Based on previous experience it can be reasonably expected that an ultimate collector-absorber efficiency of about 82 percent under the same conditions can be met by reducing the surface error to a reasonable goal of 1-1/2 minutes, standard deviation. For a 0.533 degree misorientation of the same mirror the maximum efficiency would be 76.6 percent at a 10-inch cavity diameter. Apertures of 8, 9, and 10 inches were used throughout the analysis, since these diameters cover the probable range of cavity apertures. The collector-absorber efficiency drops rapidly with increasing mirror error.

System goals are for a 75 percent collector-absorber efficiency, inclusive of the 3 to 5 percent cavity insulation losses, for about 0.25 degrees misorientation. When insulation losses, together with alignment misfocus, thermal losses and structural losses (which will be discussed below) are considered, system goals can only be met by collectors having surface errors less than 6 minutes standard deviation.

5.6 Misorientation

Figures 5-12, 5-13, and 5-14 show the collector absorber efficiency for various mirror errors as a function of misorientation angle for cavity apertures of 8, 9, and 10 inches, respectively. These figures indicate that up to at least 1/2 degree misorientation the more accurate mirrors not only have higher efficiencies but also lose less efficiency with increasing misorientation angle.

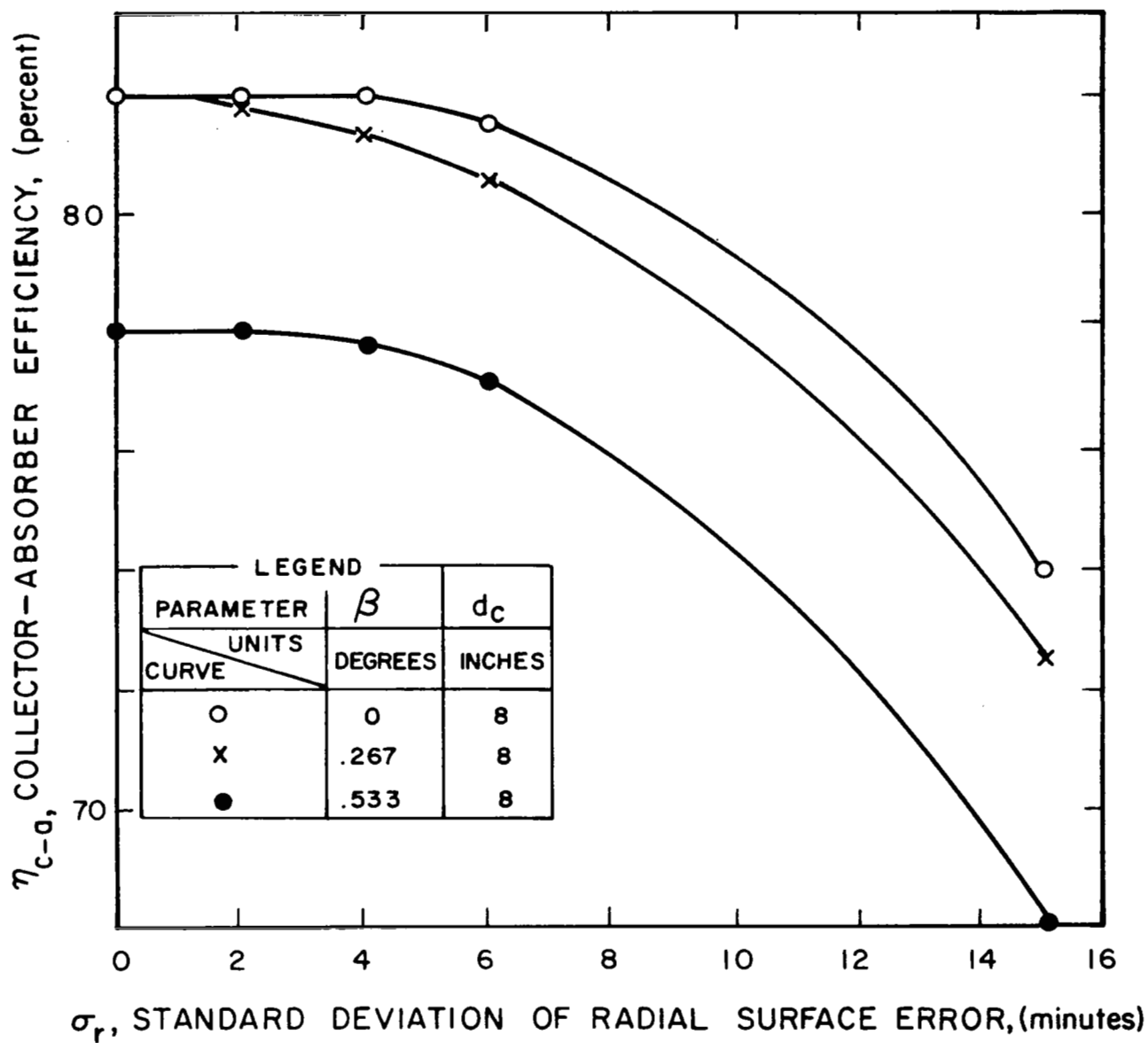


FIG. 5-9 COLLECTOR-ABSORBER EFFICIENCY VS SURFACE ERROR

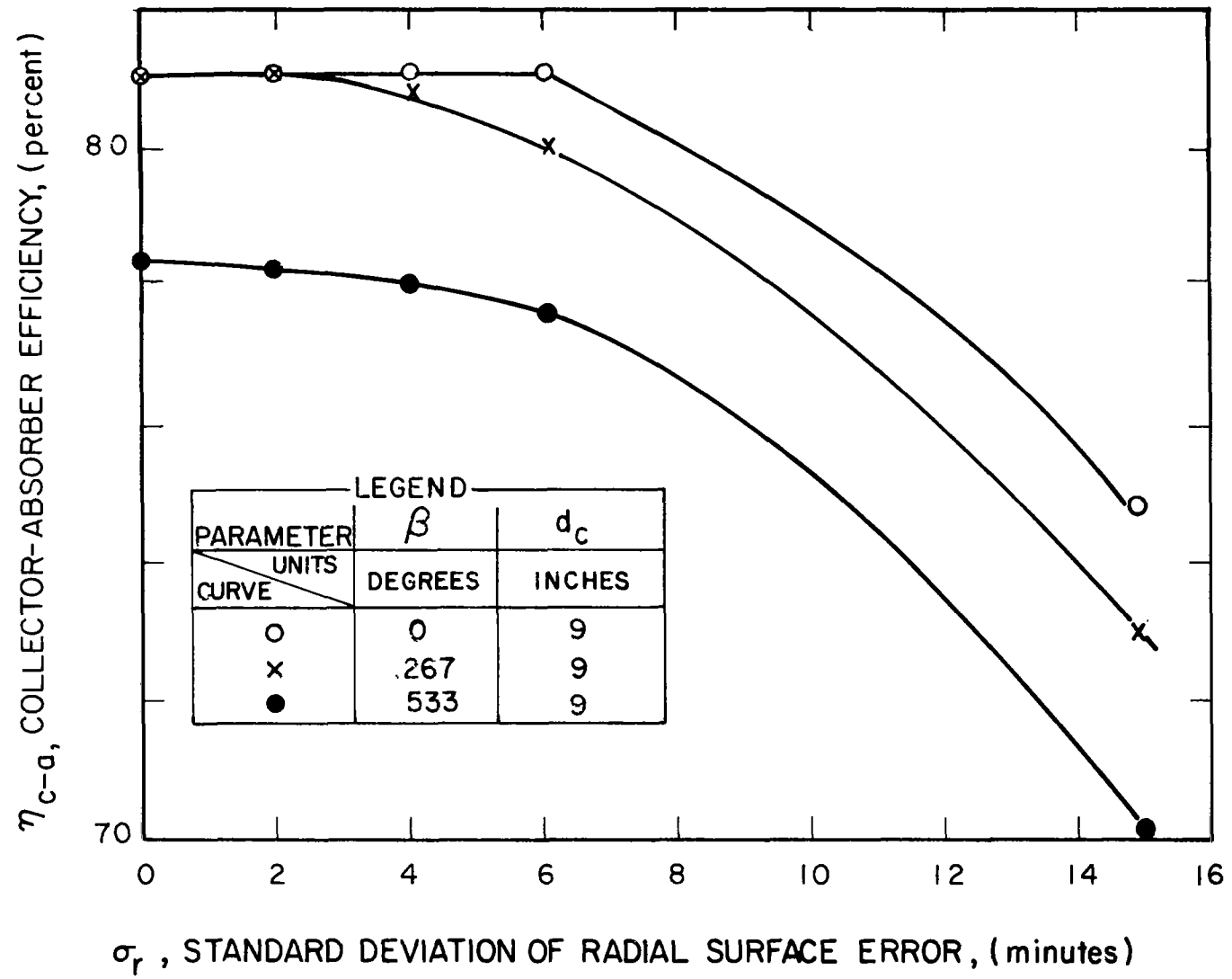


FIG. 5-10 COLLECTOR-ABSORBER EFFICIENCY VS SURFACE ERROR

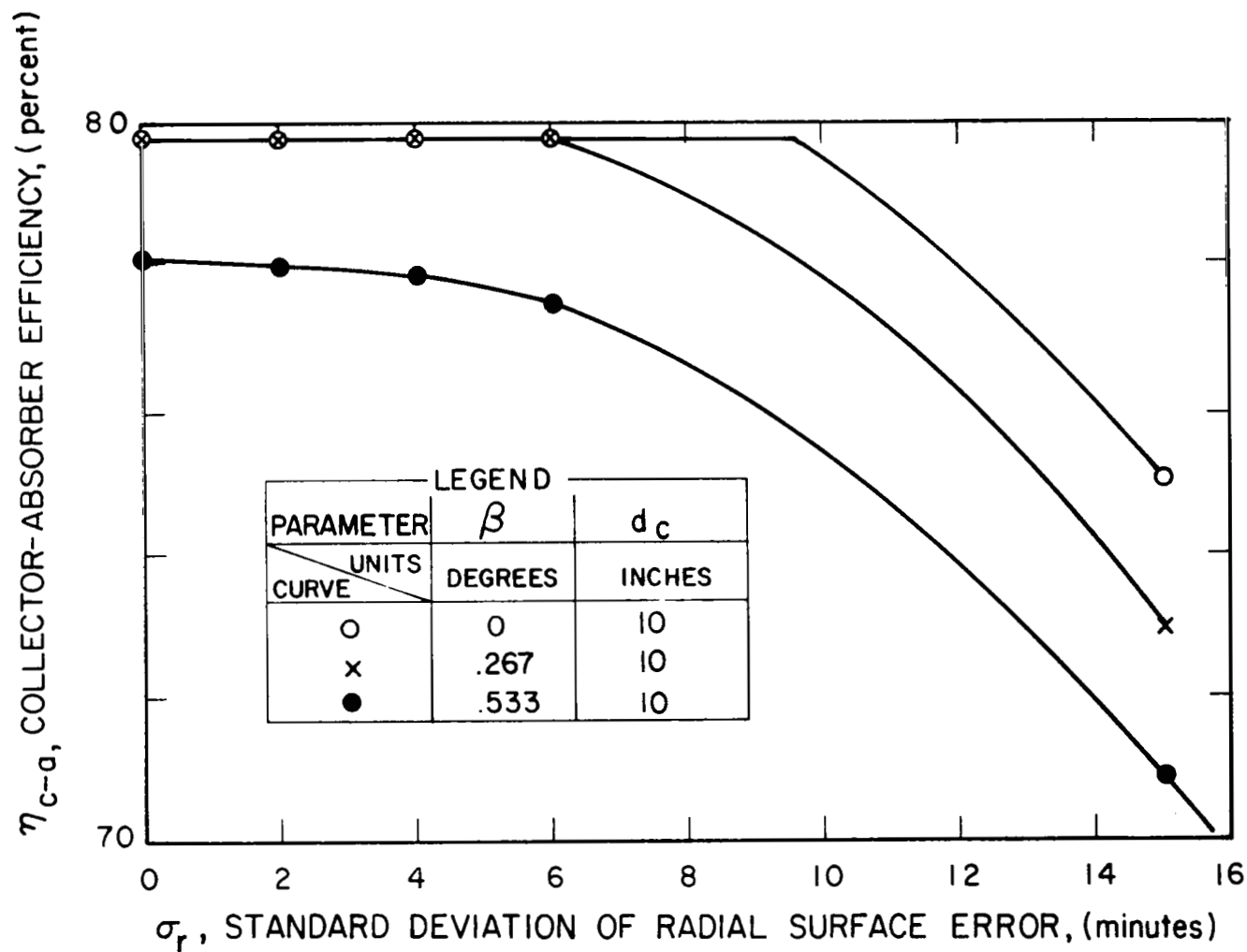


FIG. 5-11 COLLECTOR-ABSORBER EFFICIENCY VS SURFACE ERROR

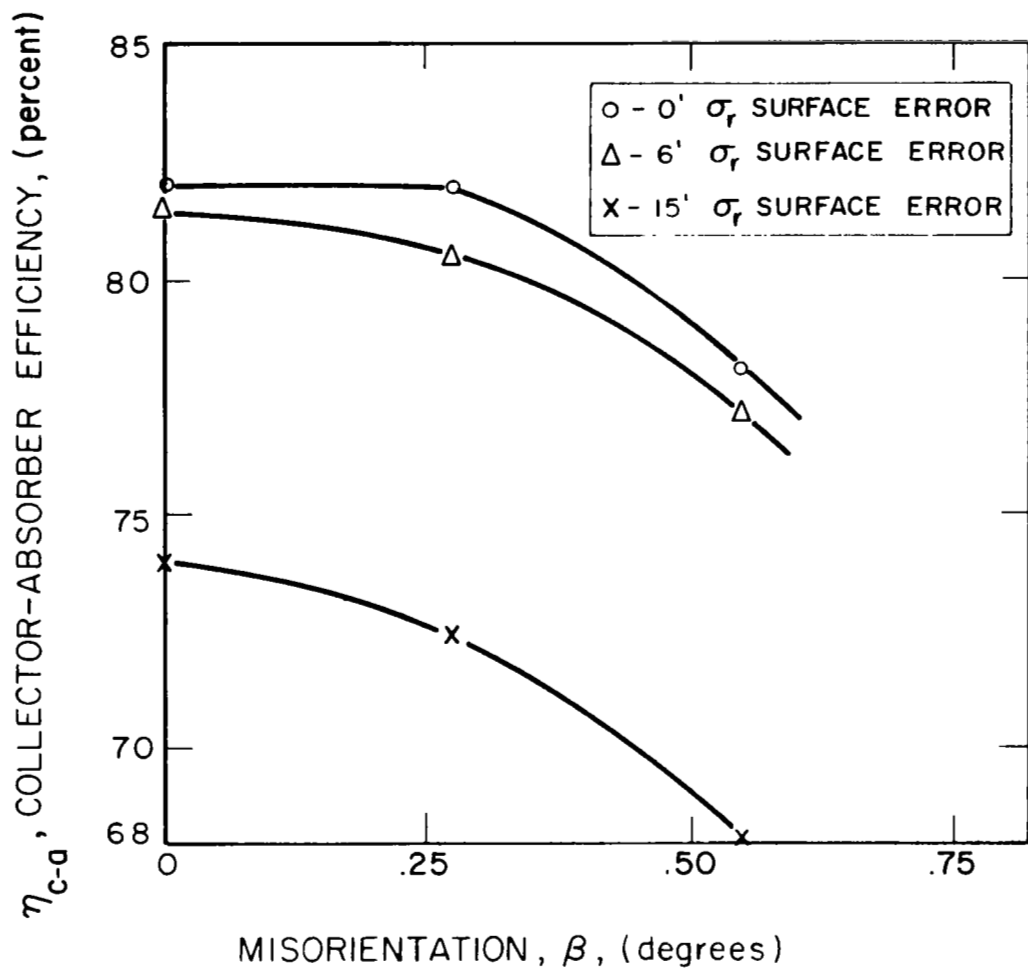


FIG. 5-12 COLLECTOR-ABSORBER EFFICIENCY VS MISORIENTATION FOR AN 8-INCH CAVITY APERTURE

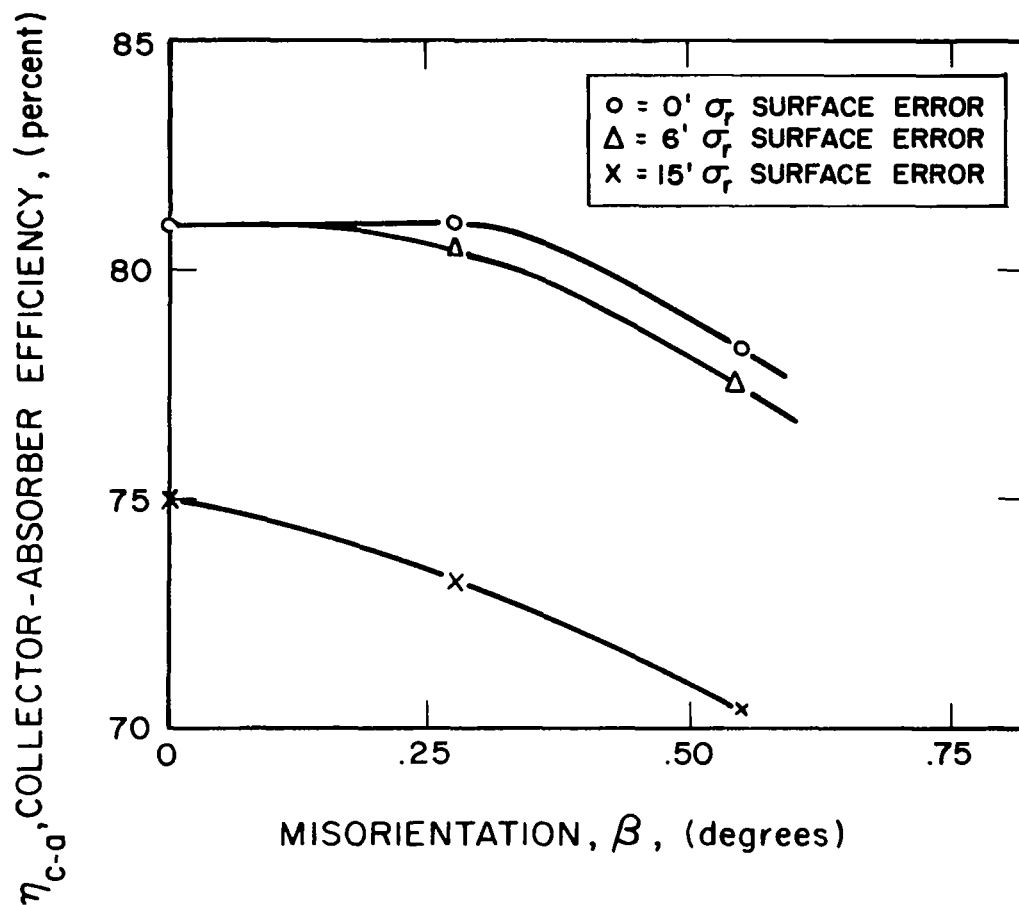


FIG. 5-13 COLLECTOR-ABSORBER EFFICIENCY VS MISORIENTATION FOR A 9-INCH CAVITY APERTURE

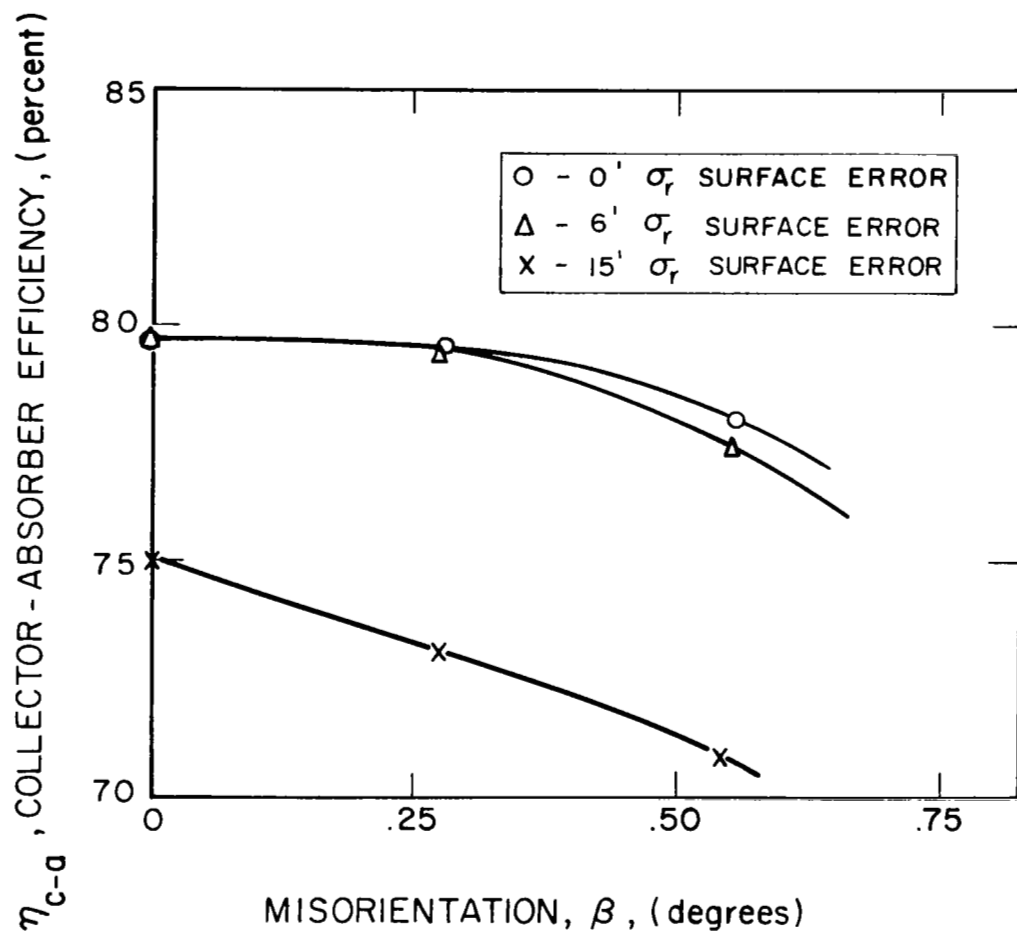


FIG. 5-14 COLLECTOR-ABSORBER EFFICIENCY VS MISORIENTATION
FOR A 10-INCH CAVITY APERTURE

These figures also demonstrate that accurate collectors have a wide misorientation tolerance for a given aperture before any efficiency drop occurs or have relatively less efficiency loss for any given misorientation. Therefore, surface error is a predominant factor in the reduction in efficiency due to misorientation.

The values for any time-averaged misorientation can be attained by integrating efficiency as a function of misorientation angle for any misorientation vs time distribution for a collector of given surface accuracy. As a rough approximation the collector-absorber efficiency value at the median misorientation angle will be the maximum time-averaged collector-absorber efficiency.

5.7 Cavity Absorber Assumptions

Since the Brayton cycle cavity design data was not available during the study period, the cavity was assumed to be an isothermal blackbody. Figure 5-15 shows a typical collector-absorber efficiency curve vs cavity aperture diameter for both a cold calorimeter absorber and a Brayton cycle absorber cavity. The upper curve depicts the unobscured, cold calorimeter efficiency. Below a cavity aperture diameter of two inches the cold calorimeter efficiency curve has been omitted. These curves are based on a blackbody cavity absorber.

For the remainder of this report the cavity absorber will be assumed to be a blackbody radiator.

The effect of a "gray" body cavity on efficiency is shown in Fig. 5-16 where collector-absorber efficiency is plotted vs cavity absorber wall emissivity. This curve was plotted using the following formula:

$$\eta_{c-a,g} = \frac{\eta_m r_m \epsilon_1}{1 - (1 - \theta)(1 - \epsilon_1)} - \frac{A_2}{A_1} \left[\frac{\epsilon_1 \theta}{1 - (1 - \theta)(1 - \epsilon_1)} \right] \frac{\sigma T_1^4}{CH_s} \quad (\text{Ref. 5-2})$$

The calculated efficiencies for "gray" body cavity absorbers, assumed the following:

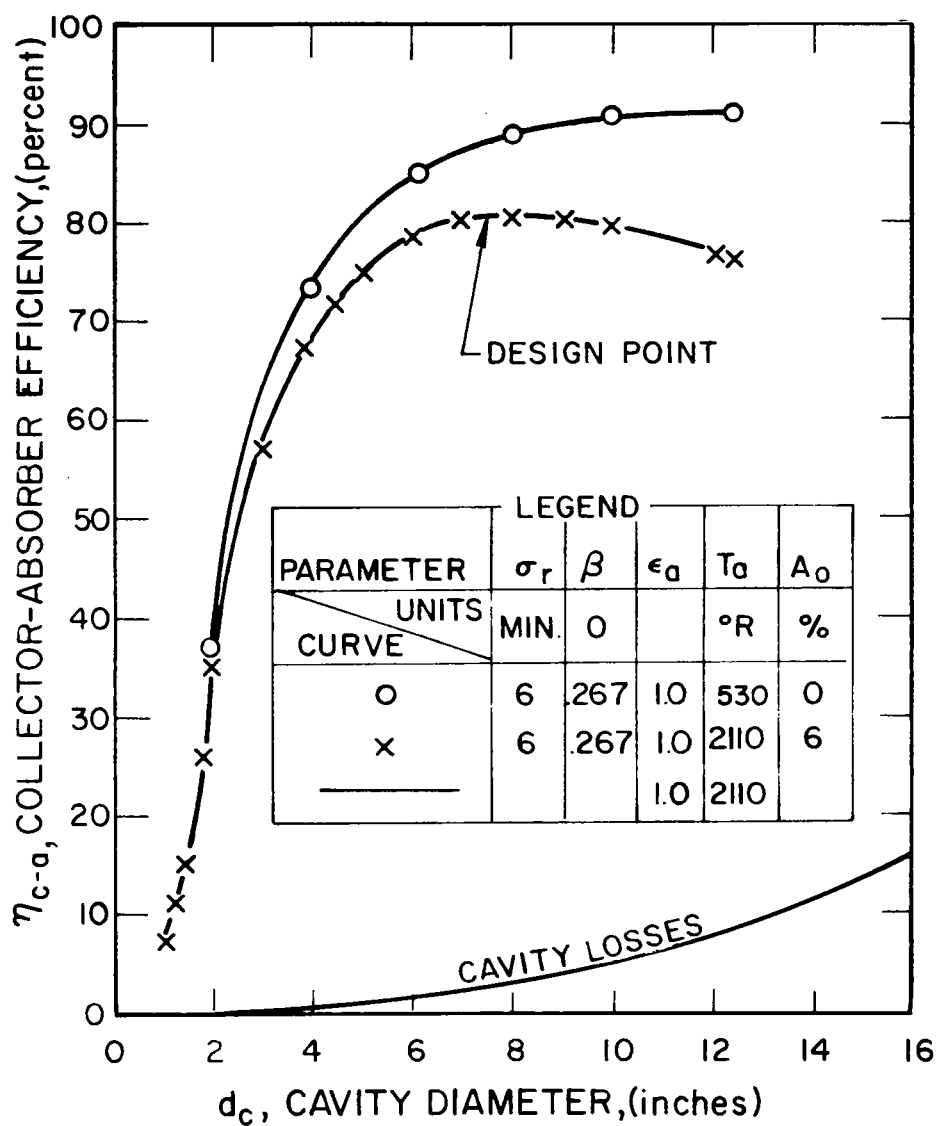


FIG. 5-15 CAVITY LOSSES AND COLLECTOR-ABSORBER EFFICIENCIES VS CAVITY-APERTURE

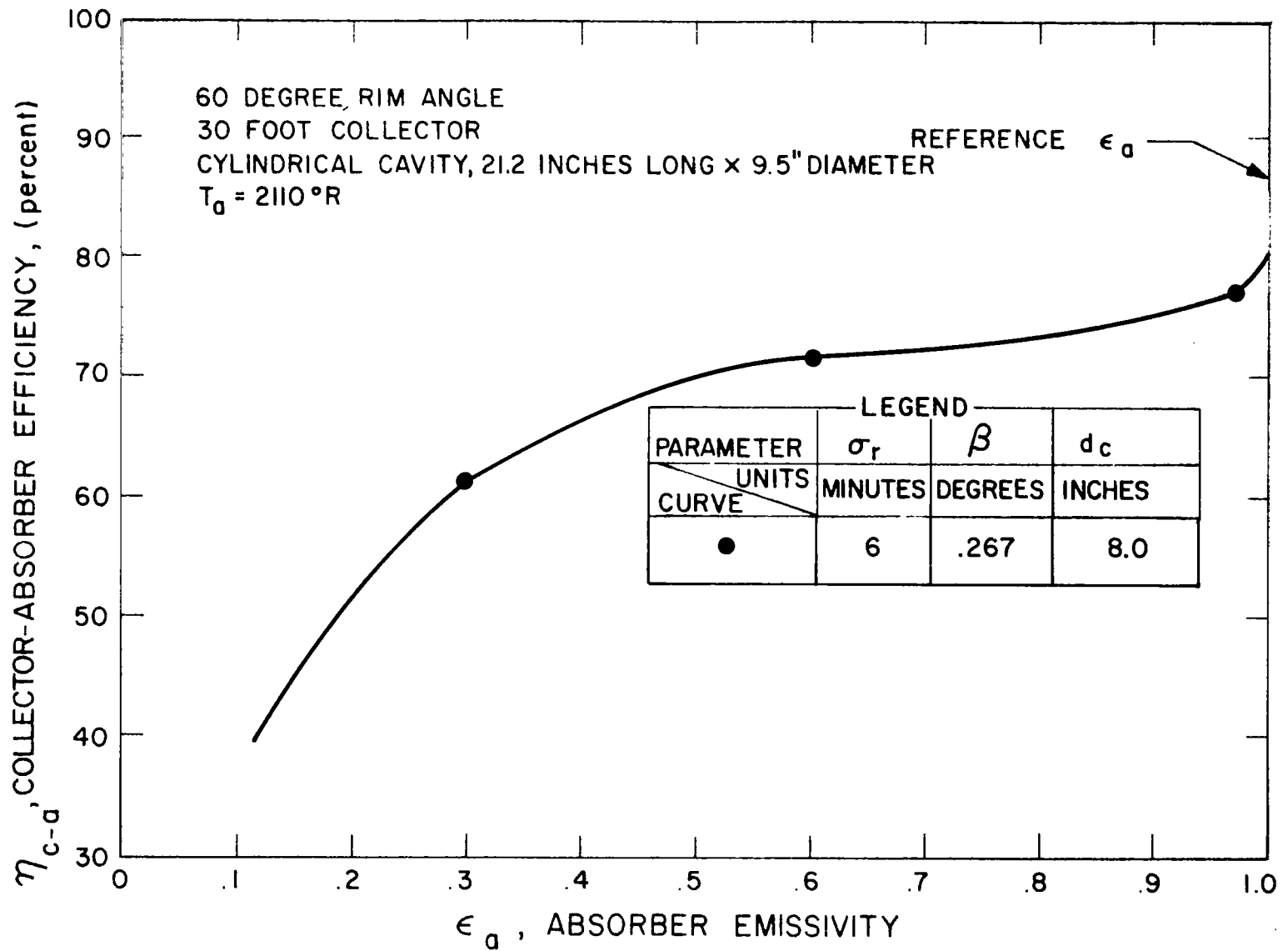


FIG. 5-16 COLLECTOR-ABSORBER EFFICIENCY VS ABSORBER EMISSIVITY

A_1	- aperture area	πr^2
A_2	- cavity area, constant for all cases	705 inches ²
β	- cavity length to aperture radius ratio	$\frac{21.2}{r}$
C	- concentration ratio	$\left[\frac{D}{d}\right]^2$
D	- collector diameter	360 inches
ϵ_1	- cavity emissivity = absorptivity	
H_s	- solar constant	442.7 Btu/hr-ft ²
η_m	- intercepted percent of reflected energy, varies with r	$\leq 94\%$ (6% obscuration)
d	- cavity aperture diameter computed by the optical program for a 60° collector	
T_1	- cavity temperature	2110°R (assumed constant)
θ	- form factor (see Fig. A-3, Ref. 5-2) varies with A_1/A_2 , β , and cavity shape	
r_m	- collector reflectivity	91%

The above cavity assumptions tend to overestimate the total efficiency loss due to cavity absorptivity and emissivity effects on the actual Brayton cycle cavity. Figure 5-16 is based on these assumptions and illustrates that blackbody assumptions should be investigated further. The actual losses will be dependent on realistic design considerations and are expected to be lower than indicated in Fig. 5-16.

5.8 Alignment and Focus

The effects of alignment and focus on collector-absorber efficiency are shown in Figs. 5-17 and 5-18.

5.8.1 Axial Misfocus

Figure 5-17 depicts the change in collector-absorber efficiency as a function of axial misfocus for collectors having radial surface errors of 0, 6, and 15 minutes standard deviation, respectively, and an 8-inch cavity aperture. These curves indicate that the axial focus of the cavity aperture within ± 0.5 inch will produce a loss in collector-absorber efficiency of less than 0.2 percent, 1.5 percent,

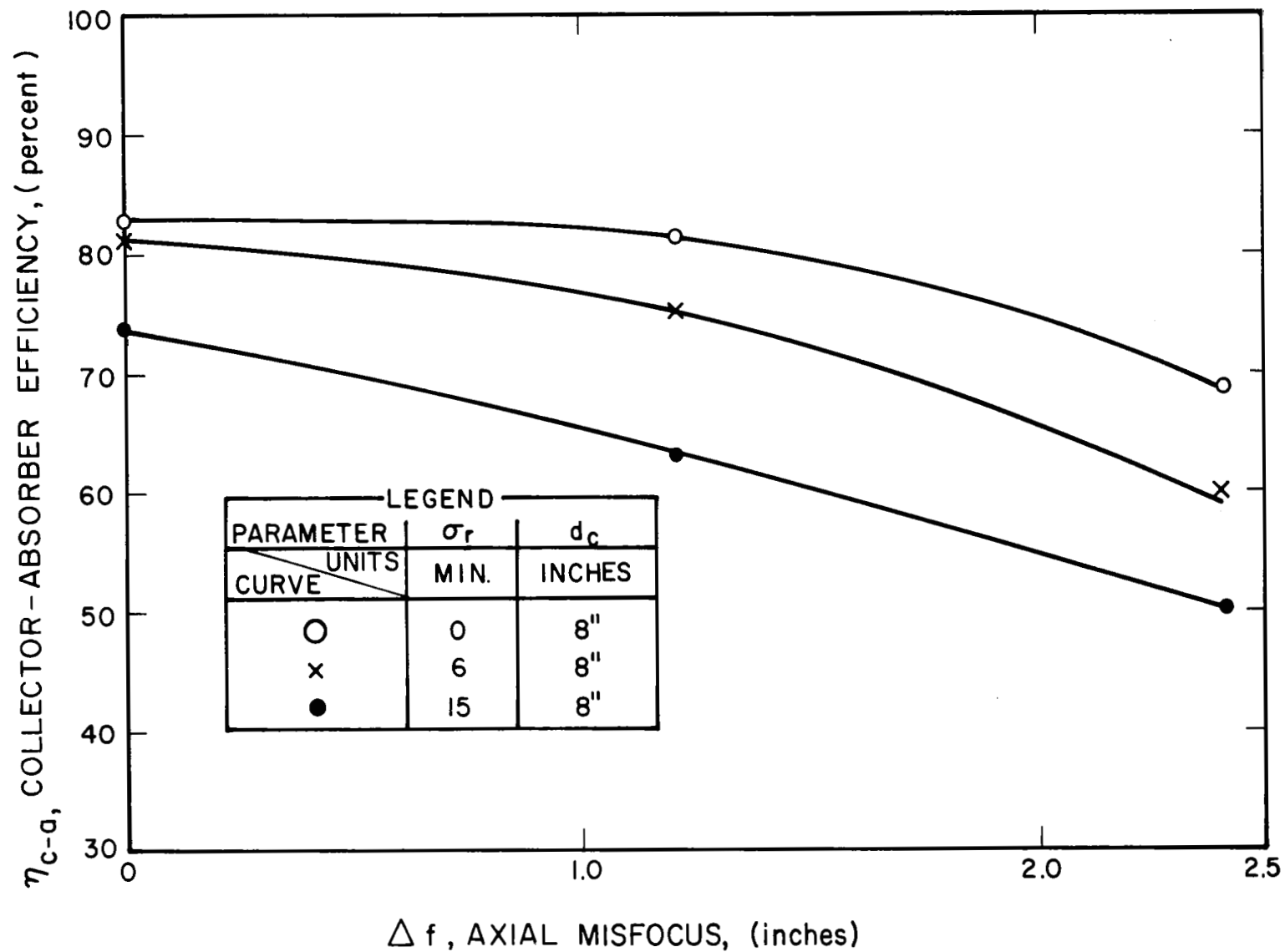


FIG. 5-17 COLLECTOR-ABSORBER EFFICIENCY VS AXIAL MISFOCUS

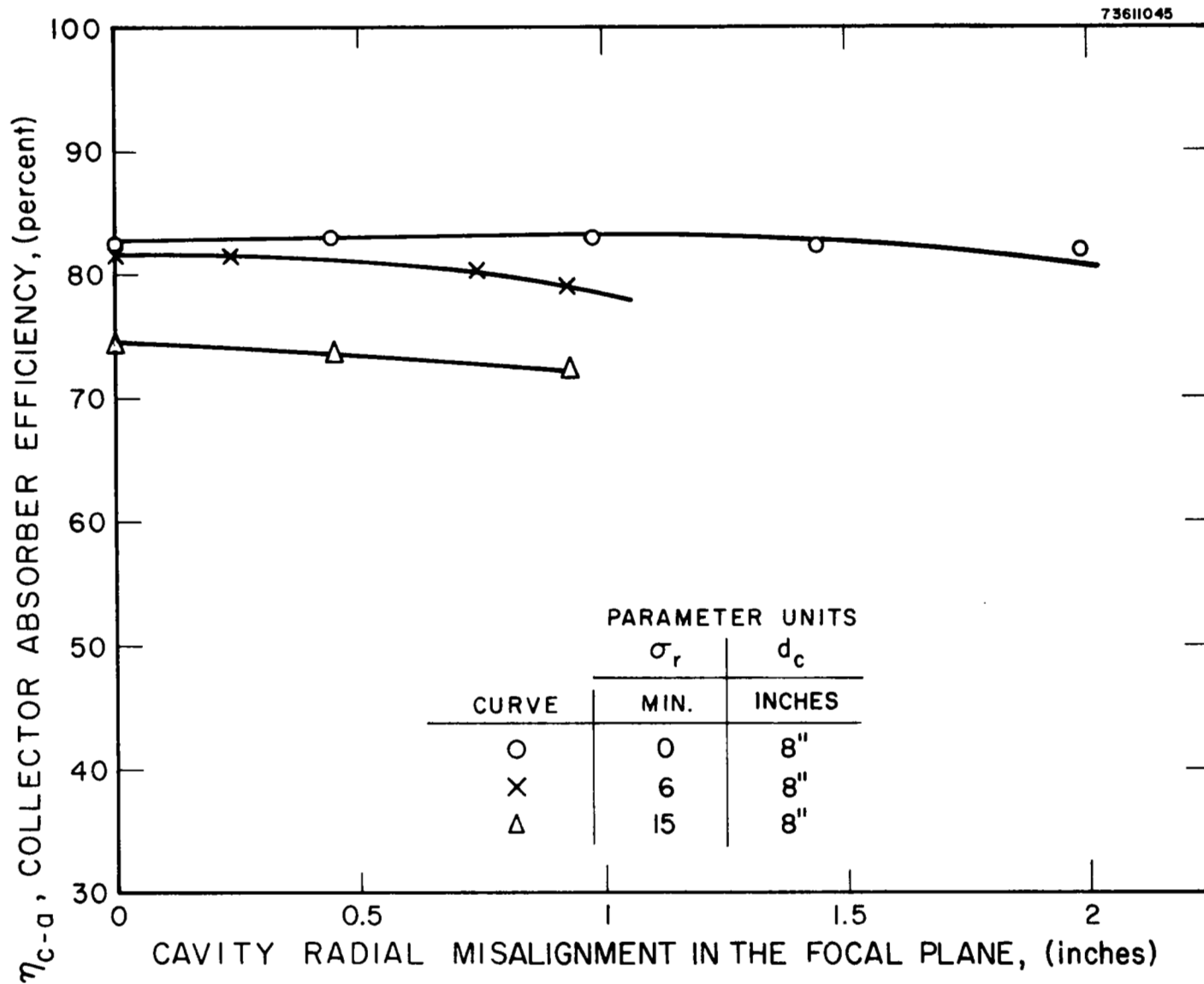


FIG. 5-18 COLLECTOR-ABSORBER EFFICIENCY VS CAVITY RADIAL MISALIGNMENT

and 3.5 percent for collectors having surface errors of 0, 6, and 15 minutes respectively.

5.8.2 Radial Misalignment

Figure 5-18 shows the effect of the radial misalignment in the focal plane on the collector-absorber efficiency for mirrors having 0, 6, and 15 minutes standard deviation and an 8-inch cavity aperture. A radial misalignment of ± 0.5 inch will decrease the collector-absorber efficiency less than 1/2 percent for 0, 6, and 15 minute surface errors. Though combined efficiency losses of a misaligned and misoriented collector are not readily calculated, such a case will probably produce similar efficiency losses over the first 0.5 inch of misalignment. Therefore, a misalignment tolerance of ± 0.5 inch is desirable.

5.9 Thermal Errors

Collector-absorber efficiency is affected by the following temperature effects:

1. Ambient temperature changes of the collector and collector struts
2. Thermal gradient across and through the collector shell
3. Differential thermal expansion effects between the rigidizing torus and collector shell

To determine the transit orbital temperatures on the collector a computer program was written to include the following thermal sources:

1. Solar
2. Earth emission
3. Earth albedo
4. Cavity absorber reradiation
5. Radiator

For simplicity the collector was divided into five different areas, one central area and four rim areas 90° apart. Figure 5-19 shows

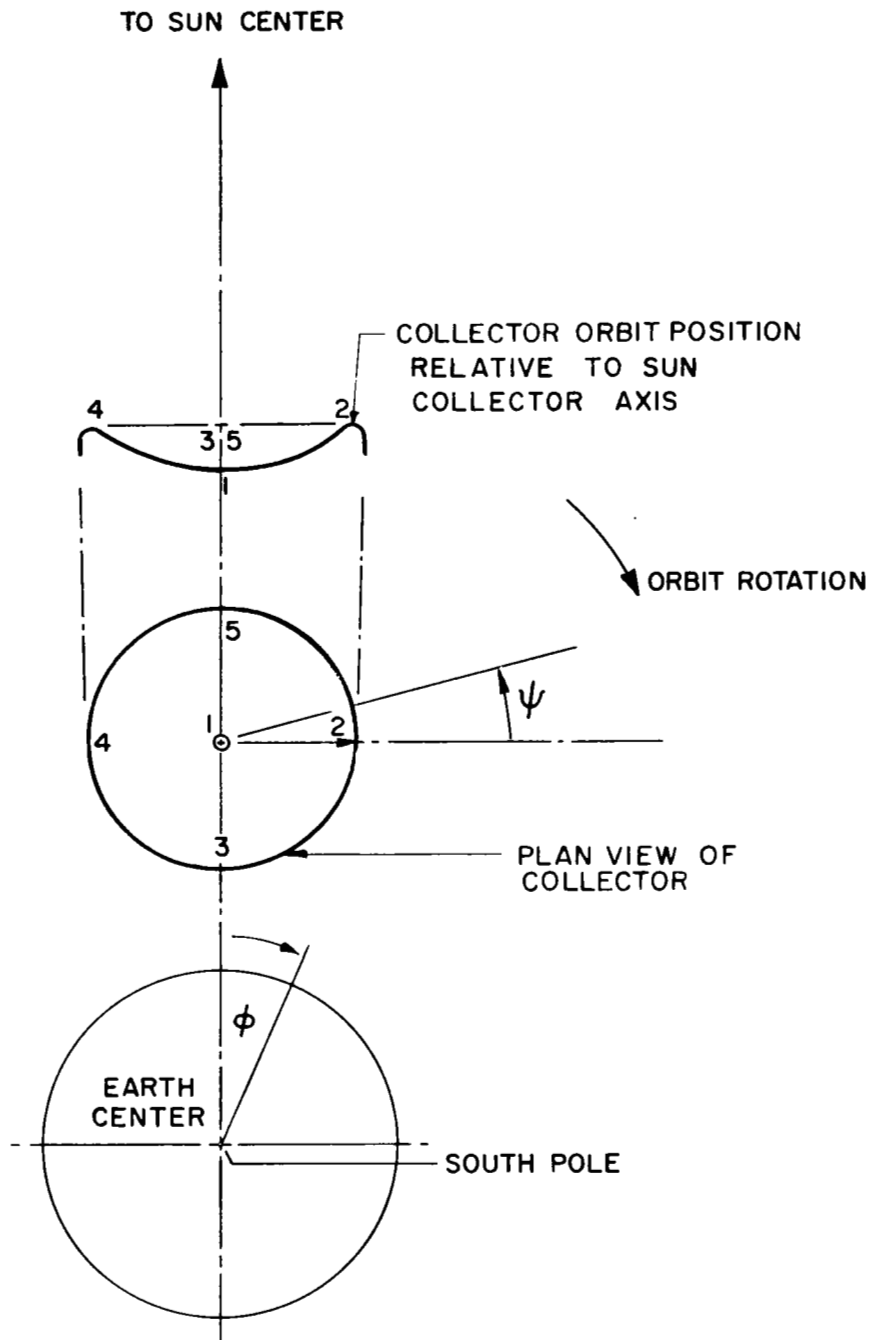


FIG. 5-19 LOCATION OF COLLECTOR POINTS WITH RESPECT TO THE ORBIT ROTATION AND SUN-EARTH AXIS

the various temperature area locations. The input form factors for various thermal sources for a 300 mile equatorial orbit are shown in Figures 5-20, 5-21, and 5-22. The heat transfer equation used, together with a summary of the constants, emissivities, and absorptivities is given in Table 5-III. For the temperature calculations of the rim positions, the form factors were adjusted to take into account the variations in incidence angle with respect to all the thermal sources. Figures 5-23, 5-24, 5-25, and 5-26 show the transient temperatures of various surface points neglecting thermal conduction effects. Figure 5-27 shows the central collector temperatures for a 22,000 nautical mile orbit. With thermal conduction between the collector points the plotted temperatures are within $\pm 5^{\circ}$ Rankine. These analyses indicate that the collector shell temperatures will range from 344° to 572° Rankine during orbit.

Table 5-IV depicts the steady state maximum temperature which might be obtained using various combinations of absorptivity and emissivity. A back surface emissivity of 0.9 would require a coating such as chemically deposited platinum black. The 0.3 emissivity value can easily be achieved by electroformed nickel. Coatings having an absorptivity and emissivity of 0.1 can be achieved by spraying chemically deposited silver on the back of the collector surface. A mirror emissivity of 0.02 is probably more realistic than an emissivity of 0.1 for the temperatures at which the collector operates. This change in emissivity counts for a maximum change of 89° and a minimum change of 22° .

Table 5-V shows the difference in torus and collector rim temperatures which might be achieved for various cases of absorptivity and emissivity, neglecting conduction effects between the torus and collector shell. Conduction would reduce the ΔT by less than 10 percent. This indicates that with a highly emissive and absorptive coating between the collector shell rim and torus and low absorptive and emissive coatings on the front of the collector shell and rear of the torus, a temperature difference of less than 9°F can be achieved between the collector rim and the collector torus. The desirability of such a low temperature

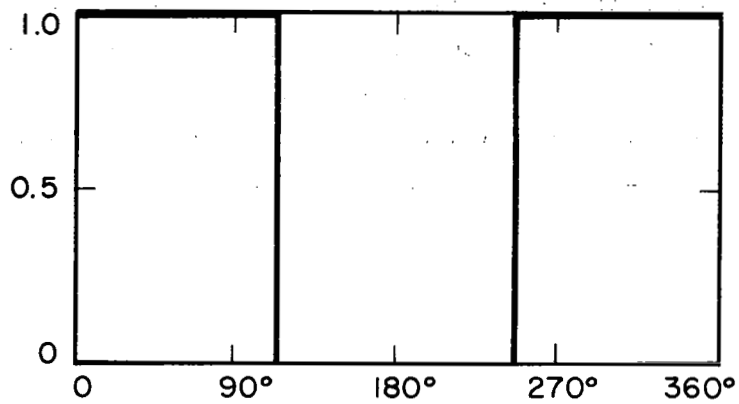


FIG. 5-20 $F_s(\phi)$ AND $F_a(\phi)$ AS A FUNCTION OF ϕ

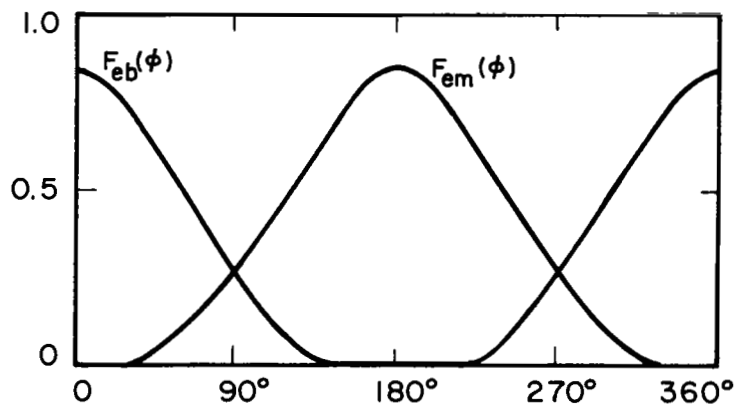


FIG. 5-21 $F_{eb}(\phi)$ AND $F_{em}(\phi)$ AS A FUNCTION OF ϕ

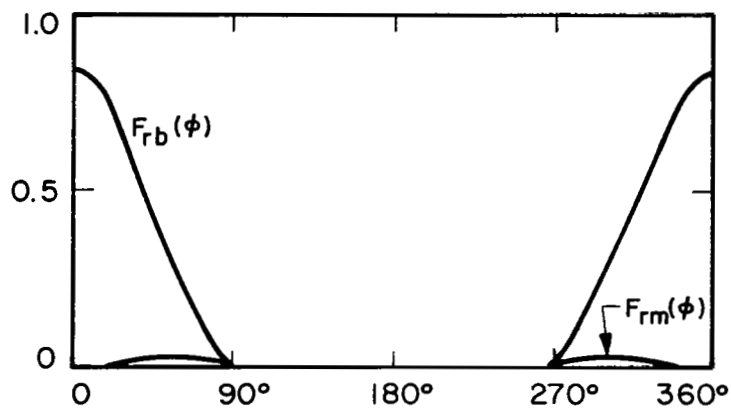


FIG. 5-22 $F_{rb}(\phi)$ AND $F_{rm}(\phi)$ AS A FUNCTION OF ϕ

300-NAUTICAL-MILE EQUATORIAL ORBIT FORM FACTOR FUNCTIONS VS ORBIT ANGLE

TABLE 5-III
TEMPERATURE EQUATIONS, ASSUMPTIONS AND CONSTANTS

Equation

$$\frac{dT_m}{d\phi} = \frac{K_{11}}{K_{12}} \left[-\sigma(F_{mA}\epsilon_m + \epsilon_b)(T_m^4 - T_o^4) + \alpha_{ms}H_sF_s(\phi) + H_e(F_{em}(\phi)\alpha_{me} + F_{eb}(\phi)\alpha_{be}) + AH_s(\alpha_{br}F_{rb}(\phi) + \alpha_{mr}F_{rm}(\phi)) + (F_a(\phi)F_a\epsilon_a\alpha_{ma}\sigma)(T_a^4 - T_m^4) + F_d\alpha_{md}\epsilon_d\sigma(T_d^4 - T_m^4) \right]$$

Assumptions and Constants

$K_{11} = \frac{\text{orbit time}}{360^\circ} = 0.00443 \text{ hr}/^\circ \text{ and } 0.0783 \text{ hr}/^\circ \text{ for } 300 \text{ and } 22,000 \text{ nautical miles respectively}$

$K_{12} = \text{cpt}$

$c = 0.11 \text{ Btu/lb}\cdot^\circ\text{F}$

$\rho = 46.1 \text{ lb/in}\cdot\text{ft}^2$

$t = 0.0107 \text{ in}$

$\sigma = 0.1713 \times 10^{-8} \text{ Btu/hr}\cdot\text{ft}^2\cdot^\circ\text{R}^4$

$F_{ma} = 1.0$

$\epsilon_m = \alpha_{ms} = \alpha_{me} = \alpha_{mr} = \alpha_{ma} = \epsilon_{md} = 0.1$

$\epsilon_b = \alpha_{be} = \alpha_{br} = 0.9$

$T_m = T_b = \text{unknown of the equation}$

$T_o = 0^\circ\text{R}$

$H_s = 442.7 \text{ Btu/hr}\cdot\text{ft}^2$

$H_e = 74.4 \text{ Btu/hr}\cdot\text{ft}^2$

$A = 0.35$

$F_a = \text{absorber-collector view factor}$

$T_a = 2110^\circ\text{R}$

$F_d = \text{radiator-collector view factor}$

$T_d = 900^\circ\text{R}$

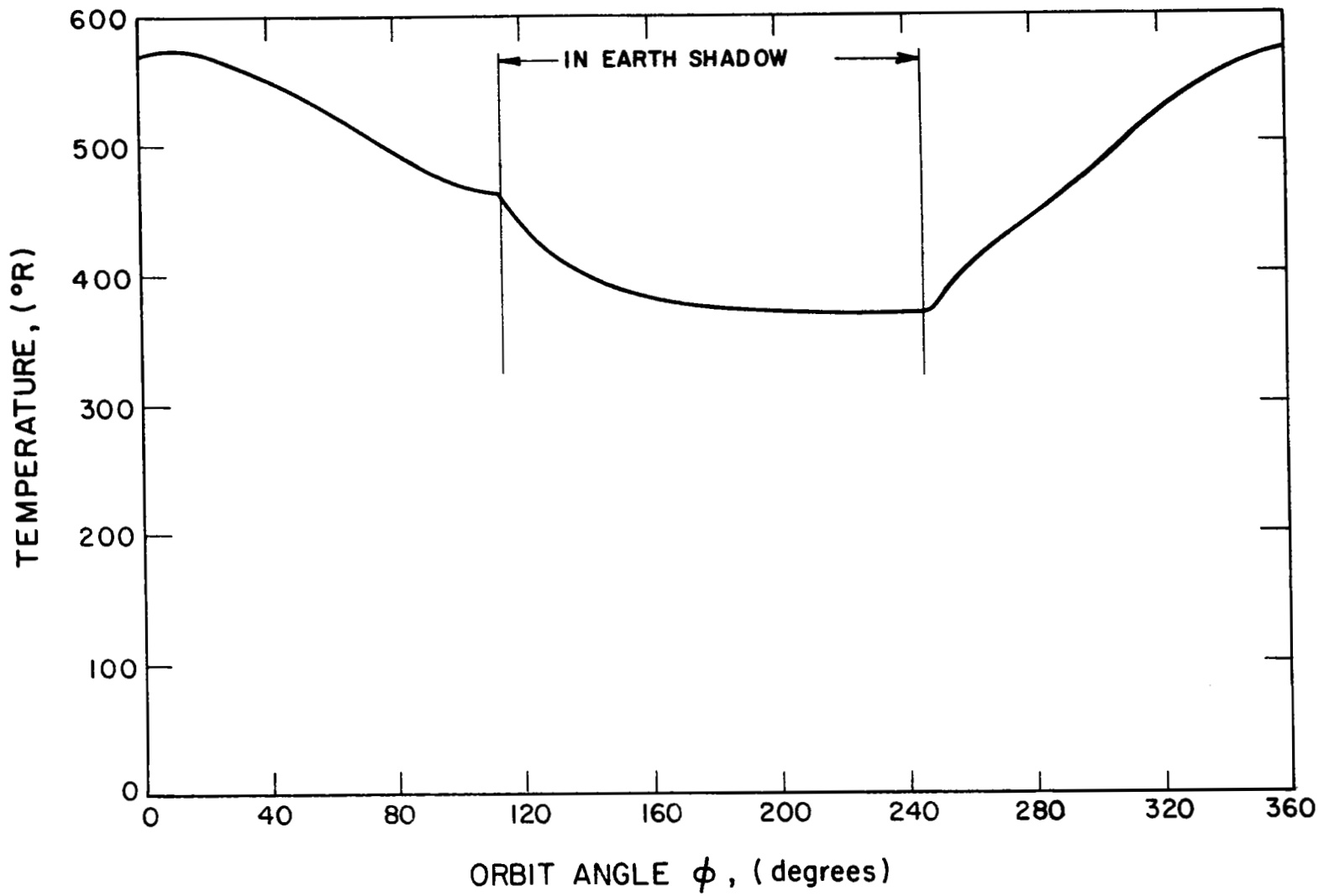


FIG. 5-23 POINT 1, CENTRAL COLLECTOR SURFACE, TEMPERATURES FOR A 300-NAUTICAL-MILE ORBIT

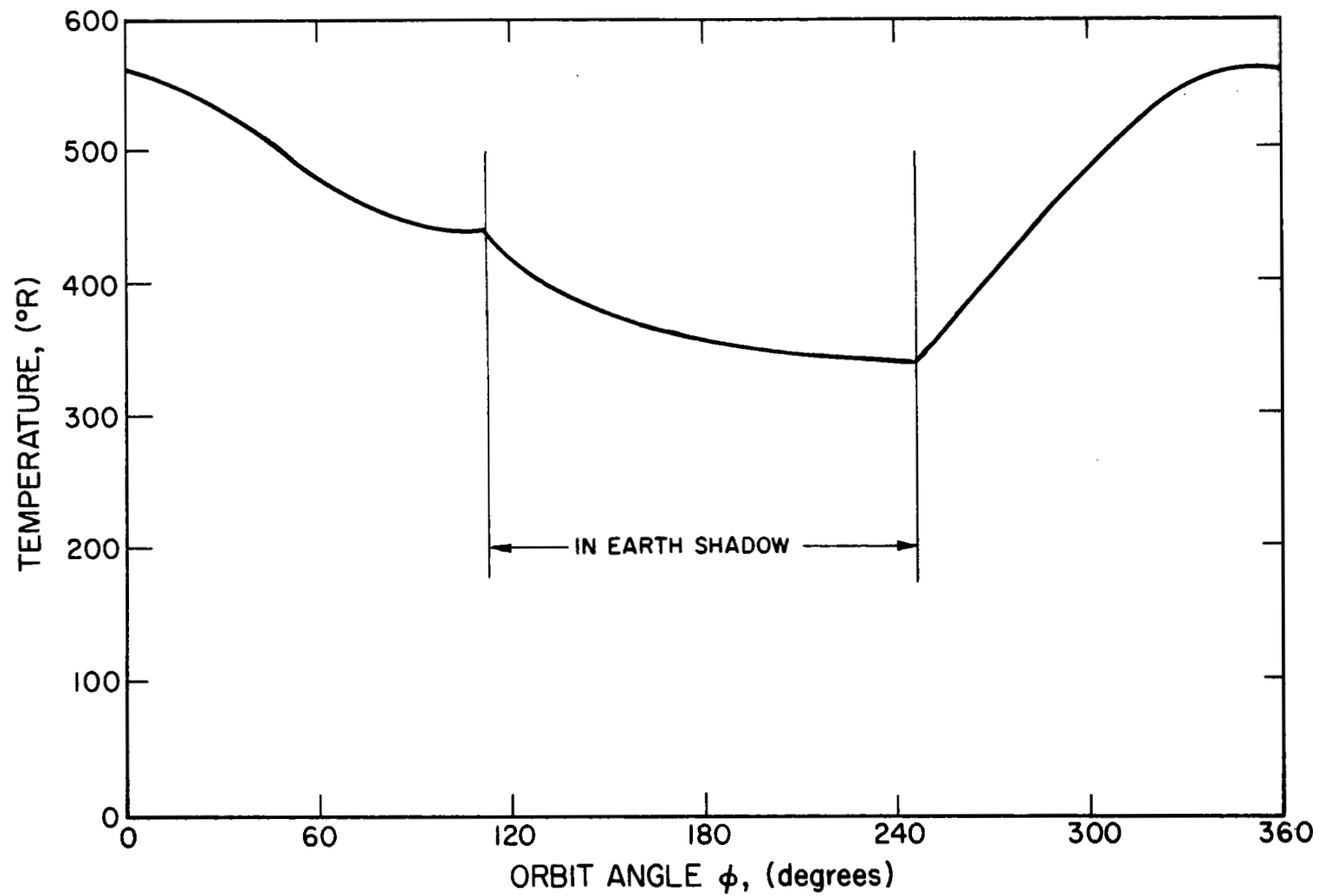


FIG. 5-24 POINT 2, COLLECTOR SURFACE TEMPERATURES, $\psi = 0^\circ$, FOR A 300-NAUTICAL-MILE ORBIT

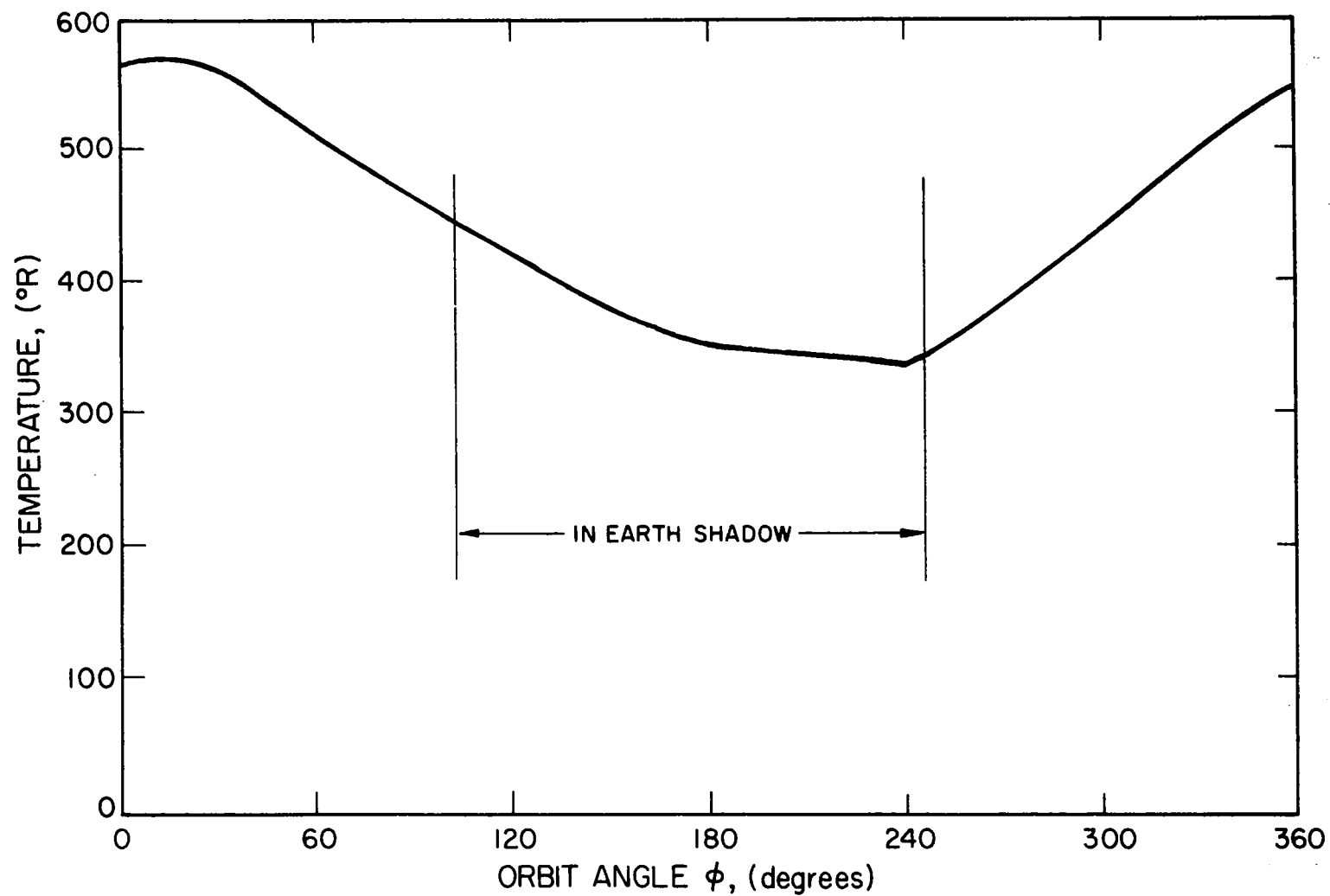


FIG. 5-25 POINT 3 AND 5, COLLECTOR SURFACE TEMPERATURES, $\psi = \pm 90^{\circ}$, FOR A 300-NAUTICAL-MILE ORBIT

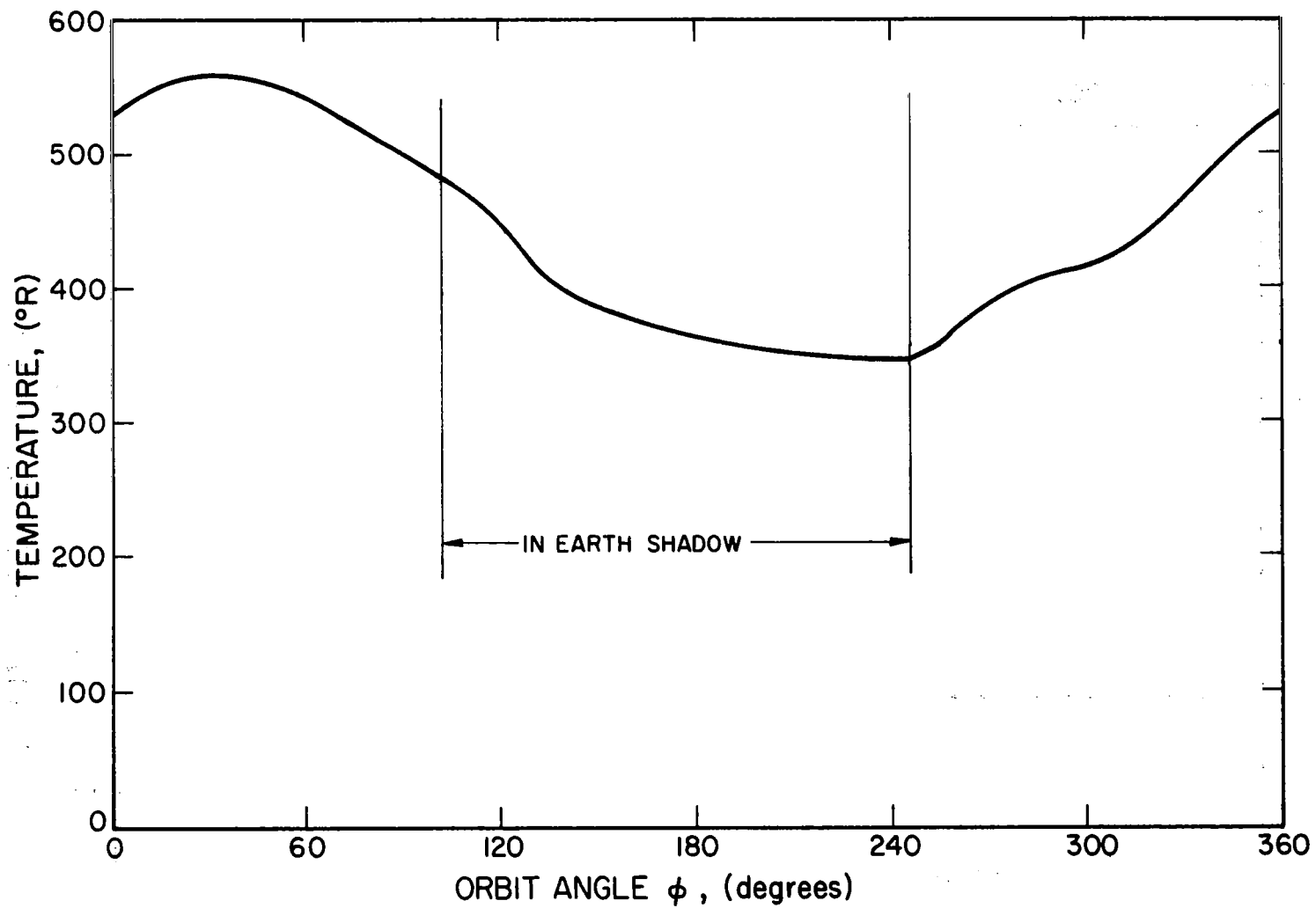


FIG. 5-26 POINT 4, COLLECTOR SURFACE TEMPERATURES, $\psi = 180^{\circ}$, FOR A 300-NAUTICAL-MILE ORBIT

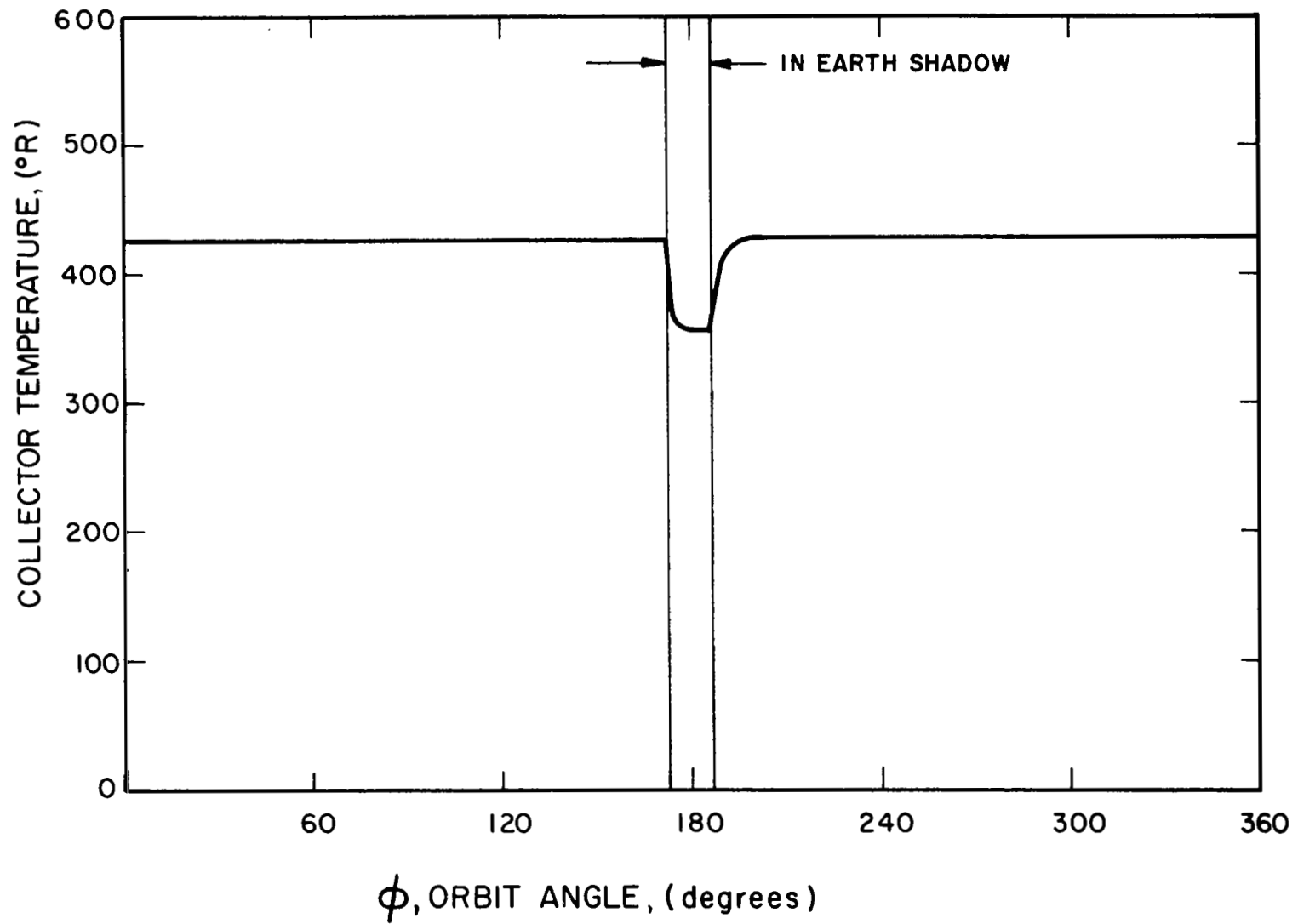


FIG. 5-27 CENTRAL COLLECTOR TEMPERATURE VS ϕ FOR A 22,000-NAUTICAL-MILE ORBIT

TABLE 5-IV
STEADY STATE MAXIMUM COLLECTOR SHELL TEMPERATURE

α_m	α_b	ϵ_m	ϵ_b	T_m (°R)
0.1	0.9	0.1	0.9	590
0.1	0.3	0.1	0.3	620
0.1	0.1	0.1	0.1	656
0.1	0.9	0.02	0.9	612
0.1	0.3	0.02	0.3	659
0.1	0.1	0.02	0.1	745

Equation:

$$T_m = \left[\frac{H_s \alpha_m + A H_s \alpha_b + F_{eb}(\phi)_{\max} H_e \alpha_b}{\sigma(\epsilon_m + \epsilon_b)} \right]^{1/4}$$

See Table 5-III and Fig. 5-21 for unspecified constants

TABLE 5-V
COLLECTOR - SHELL-TORUS TEMPERATURE DIFFERENTIALS

α_m	ϵ_m	ϵ_b	ϵ_r	ϵ_{br}	ΔT_{m-r} (°F)
					79
0.1	0.02	0.9	0.9	0.9	
					40
0.1	0.02	0.9	0.9	0.3	
					9
0.1	0.02	0.9	0.9	0.1	

Equation:

$$\Delta T_{m-r} = \frac{H_s \alpha_m \cos \theta}{\sigma \epsilon_m + \frac{\epsilon_{br} Z}{\epsilon_{br} + Z}} \left[1 - \left(\frac{Z}{\epsilon_{br} + Z} \right)^{1/4} \right]$$

where $Z = \frac{\epsilon_b \epsilon_r}{\epsilon_r + (1 - \epsilon_r) \epsilon_b}$

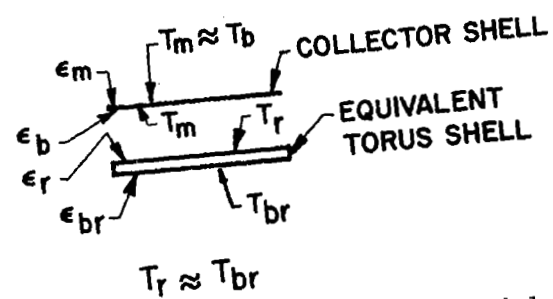


Diagram of shell torus radiation model

difference and therefore low back and front surface emissivities and absorptivities will be shown in the thermal error analysis below.

Estimated thermal maps derived from the collector surface points are shown in Figure 5-28, for various orbit positions.

5.9.1 Ambient Temperature Effects

The total change in the ambient temperatures from the original alignment temperature is less than 260°F under any conditions. Based on a ΔT of 260°F the net change in the focal point due to the change in strut length, mirror expansion, and focal length change is less than 0.16 inch. As indicated in Section 6.7 this axial misalignment would result in an efficiency loss of less than 1/2 percent. Localized transient temperature differences on the collector shell will produce even smaller efficiency losses due to the smaller incremental ΔT .

5.9.2 Collector Shell Thermal Gradient

Based on a maximum heat flux of 65 Btu/hr/sq ft, which is appropriately conservative, considering the 0.09 absorptivity of the collector for solar and earth albedo radiation and less for other radiation, a temperature gradient of less than 0.156°F per inch would be produced through the collector shell thickness. If the moment resulting from this temperature gradient is not resisted by a moment at the rim, a maximum error of 0.7 minutes would be produced at the rim. Such a thermal gradient would create a moment of 0.32 lbs/in per lineal inch at the collector rim. The application of an opposite moment at the edge of an equivalent sphere (Timoshenko, Ref. 5-3) neglecting cancellation effects of the thermal moment, would reduce the effective collector area by as much as 3 to 4 percent due to gross distortions of the rim edge. The fact that a restorative moment cancels the thermal gradient moment at the edge lowers the distortion area considerably. Reference 5-4 describes a rigorous thermal analysis of a 9.75-foot diameter all-nickel toroidally supported collector. However,

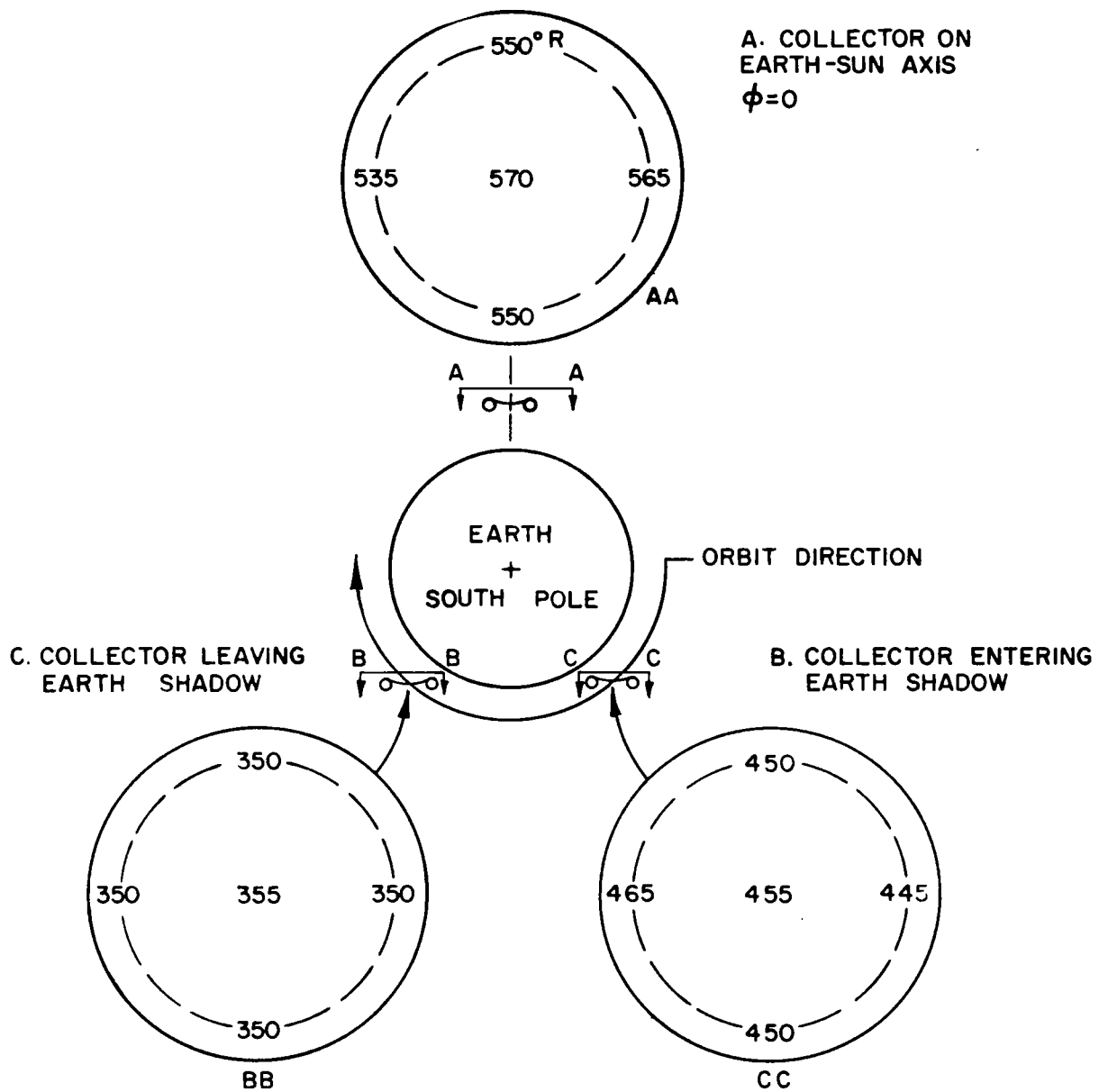


FIG. 5-28 COLLECTOR SHELL TEMPERATURE FOR 3 ORBIT POSITIONS FOR A 300-NAUTICAL-MILE ORBIT BASED ON RESULTS TABULATED IN FIGS. 5-23 THROUGH 5-26

the results of this analysis are not readily adaptable to a 20- or 30-foot diameter collector because they do not scale with diameter. A computer solution must be developed. Additional work in the collector thermal response area should include a computer analysis using this referenced work.

5.9.3 Differential Thermal Expansion Effects

Differences between the torus temperature and the integrated shell temperature will result in a differential thermal expansion between the shell and torus. Assuming an entirely rigid connection between these two elements, this difference will cause an edge displacement which would result in shell rim distortions. Using Timoshenko (Ref. 5-3) for an equivalent spherical cap, the maximum area that would be affected by a 9° temperature difference would result in a loss of less than 1.7 percent of the collector area due to gross distortion. This analysis, based on a rigid torus acting on a spherical cap, is conservative. The edge effects from the thermal gradient and torus-collector thermal expansion are not additive. In practice an area less than 2 percent of the total area might be affected by the thermal gradient and differential thermal expansion.

5.10 Effect of Centrifugal Acceleration

Collector-absorber efficiency can be decreased by the effects of centrifugal acceleration during orbit on the:

1. Collector absorber struts
2. Torus
3. Collector shell

Since the torus is not completely rigid some efficiency loss due to the torus distortion may occur depending on the design of the collector-absorber struts and the rigidizing torus. Efficiency losses due to the shell distortions exclusive of the torus are negligible.

As a first approximation the orbit acceleration field acting on the torus can be assumed constant and equal to the acceleration at the center of the collector or 0.18 g.

Torus deflections were then calculated assuming that the total collector weight is uniformly concentrated at the torus and that the torus deflections can be represented by linear equations. Therefore, using the super-position of Cases 18 and 19, page 160, Ref. 5-5, the diametrical deflections of the torus can be calculated for a tripod support assuming a 120° separation between three struts, with the in-board strut on the collector-vehicle axis. See Figure 5-1 for a plan view of both the tripod and quadrapod strut designs.

Assuming that the absolute value of the changes in perpendicular diameters represents the average diameter change from a true circle, then the average deflection of the 30-foot torus from a true torus is 0.035 inch. Using the analysis of angular distortions of spherical caps represented in Ref. 5-3 and described in Section 5.9, a total maximum loss in surface area would be approximately 2.2 percent due to distortions beyond collector tolerances at the rim. If at the same time the collector struts rotated 0.035 inches due to torus deflection, the total collector rotation would be less than one minute.

The analysis of the alternate quadrapod design indicates that there would be no net change in the perpendicular diameters equidistant between the struts and that the maximum torus deflection would occur at the strut-torus connection. The maximum deflection can be determined assuming the following:

1. A 90° arc of the torus is a continuous beam
2. Ends of the continuous beam are fixed
3. The deflection force = $\frac{W_c}{\pi/2}$

Therefore, the deflection, w , equals

$$w = - \frac{W_c \left(\frac{\pi D}{4} \right)^3}{384 \sqrt{2} EI_r}$$

Based on a torus moment of inertia of 0.78 inch^4 , the maximum deflection at the torus-strut point will be 0.012 inches. The average deviation from a circular torus will be one-fourth of the maximum deflection or 0.003 inches. By using this average deflection in the analysis of rim deflections given by Timoshenko, Ref. 5-3, this average deflection would result in a distortion of less than 0.1 percent of the total collector area beyond surface error tolerances. A 0.012 inch torus deflection would result in a maximum strut rotation of 0.5 minute.

Therefore, use of the quadrapod instead of the tripod supporting mechanism would reduce the average edge distortions by a factor of about 20. The actual distortions will be less than the figures above since the actual torus design has a moment of inertia higher than 0.78 inch^4 .

REFERENCES

Section 5

- 5-1 Jòse, Paul D., "The Flux through the Focal Spot of a Solar Furnace," Journal of Solar Energy Science and Engineering, Volume 1, 19, April-July 1957
- 5-2 Stephens, Charles W., and Haire, Alan, "Appendix A - Internal Design Considerations for Cavity Type Solar Absorbers" of the report "Mathematical Model of Factors Affecting Solar Energy Collector Efficiency," Contract No. AF 33(616)-7316, December 1960
- 5-3 Timoshenko, S. and Woinowsky-Krieger, S., "Theory of Plates and Shells," McGraw Hill Book Co., Inc., 1959
- 5-4 Stern, G. S., "Thermal Elastic Analysis of a Parabolic Shell," Jet Propulsion Laboratory Technical Report No. 32-479, August 1963
- 5-5 Roark, Raymond J., "Formulas for Stress and Strain," McGraw Hill Book Co., Inc., 1954

6. STRUCTURAL INTEGRITY

The reliability of the Brayton cycle solar collector depends not only on the environmental resistance of the reflective coating and substrate but also on the structural resistance of the collector to environmental forces which tend to cause localized or gross structural failure.

Although the proposed EOS Brayton cycle collector design, a paraboloidal shell joined to a rigidizing rim torus, is relatively simple, the structure is still very complex analytically. In this study the following initial approaches were used to obtain a better insight into the structural problems:

1. A detailed literature survey was made on the empirical and analytical treatments of similar thin shell structures.
2. Authorities on the various environmental aspects of thin shell structures were consulted. These included:
 - a. California Institute of Technology:
Dr. C. Babcock on compressive buckling
 - b. Jet Propulsion Laboratory Structures Group on vibration and shock
 - c. Bolt, Beranak and Newman Inc. on acoustics and vibration
 - d. Mr. Karpenko at UCLA on the general structure problem
3. Previous environmental and structural data on 5-foot diameter paraboloidal collectors were reviewed.

These investigations indicated the following state of the art for this collector design:

1. Practically no solutions for a paraboloidal shell are available other than simple membrane analyses.
2. Analyses of most paraboloidal shells are simplified by using a shallow spherical cap approximation, which is not completely valid for the collector in question.

3. Very few experimental data are available for shells of the size and radius to thickness ratio of the proposed solar collector.
4. Practically no work has been done on dynamic instability, even for spherical cap structures.
5. Most shell solutions either assume a clamped or free edge. While the torus design closely approximates a clamped edge, the assumption requires experimental verification.
6. Analytically even the most simple dynamic responses of such a design require detailed computer analysis, and these responses are generally axisymmetric rather than asymmetric. In practise the asymmetric responses will probably be dominant.

Despite the lack of extensive analytical and empirical data on equivalent or related structures, there is a sufficient analytic framework to perform a first attempt at analyzing the structural response to the environmental specifications, in Appendix A. This preliminary analysis will provide a basis of directing further experimental studies and help correlate similitude model data.

6.1 Structural Materials

As a first choice the one-piece, all-metal structure would be fabricated from nickel. Therefore the entire structure would have a matched thermal expansion coefficient. However, if collector weight is critical, the torus would be made of titanium. Titanium has a thermal expansion coefficient of 2×10^{-6} in./in./°F less than that of nickel. This alternate composite structure would require more sophisticated temperature control than the all-nickel collector to minimize collector surface distortions caused by differential thermal expansion.

By using an electroformed shell, the designer can assume high structural efficiencies because of:

1. Low residual stress
2. Very uniform thicknesses and material properties

3. High process control
4. Lack of surface imperfections
5. Close control of crystal size

This high structural efficiency has been demonstrated in the use of thin shell electroformed cylindrical and spherical models for static buckling tests (Refs. 6-1 and 6-2).

6.2 Design

The one-pieced toroidally supported all-nickel or titanium-nickel collector design offers maximum efficiency with good launch and orbital reliability. The design is simple, involving only one joint. There are no enclosed cavities to entrap gasses. The design will now be analyzed with respect to the environmental specifications in Appendix A.

6.3 Axial Acceleration Effects

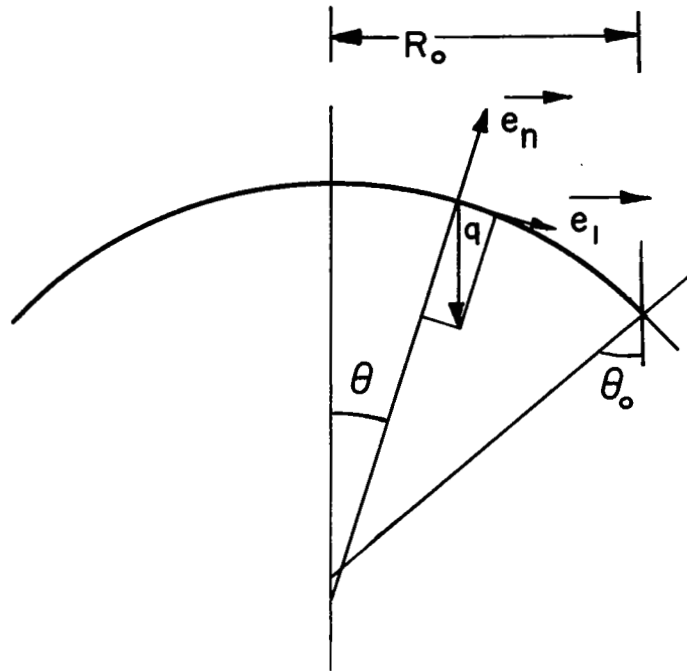
6.3.1 Membrane Analysis

For convenience in relating previous structural work on five-foot diameter collectors the structural calculations were based on a 61 degree rim angle, 30-foot diameter collector. Structural elements for the 55 degree rim angle design are appropriately scaled to maintain the same rigidity as for this 61 degree collector. A membrane analysis of the collector shell subjected to axial g loading is given below assuming the following constants:

$$\begin{aligned}
 \theta_o &= 30^\circ 25' && \text{(See diagram next page)} \\
 R_o &= 180 \text{ inches} && \text{(rim radius)} \\
 \rho g &= 0.32 \text{ lb/in}^3 && \text{(weight density of nickel)} \\
 f &= 153.6 \text{ inches} && \text{(focal length)} \\
 R &= 334 \text{ inches} && \text{(radius of curvature)}
 \end{aligned}$$

$$= 2f \left(1 + \frac{R_o^2}{16f^2} \right)$$

The diagram following depicts the shell loading criteria.



where q is the unit area shell load:

$$q = \rho g t n$$

and q_l and q_n the meridional and normal components:

$$q_l = q \sin \theta$$

$$q_n = -q \cos \theta$$

and R_1 and R_2 the meridional and hoop radii:

$$R_1 = \frac{2f}{\cos^3 \theta}$$

$$R_2 = \frac{2f}{\cos \theta}$$

The acceleration in g 's is denoted by n .

From Novozhilov (Ref. 6-3) for a parabolic shell the meridional and hoop forces per lineal inch T_1 and T_2 are:

$$T_1 = -\frac{2qf}{3} \left[\frac{1}{\cos^2 \theta} + \frac{1}{1 + \cos \theta} \right]$$

$$T_2 = -2qf \left[1 - \frac{1}{3} \left(1 + \frac{\cos^2 \theta}{1 + \cos \theta} \right) \right]$$

The meridional and hoop stresses are respectively:

$$\sigma_1 = \frac{T_1}{t}$$

$$\sigma_2 = \frac{T_2}{t}$$

or

$$\sigma_1 = -\frac{2}{3} \rho g f n \left[\frac{1}{\cos^2 \theta} + \frac{1}{1 + \cos \theta} \right]$$

$$\sigma_2 = -\frac{2}{3} \rho g f n \left[2 - \frac{\cos^2 \theta}{1 + \cos \theta} \right]$$

Therefore at the apex, $\theta = 0$, these stresses are:

$$\sigma_1(0) = \sigma_2(0) = 49n \text{ lb/in}^2$$

For a spherical shell covering the same area and having the same height the meridional and hoop stresses are:

$$\sigma_1 = -\rho g n R_o \frac{1}{1 + \cos \theta}$$

$$\sigma_2 = -\rho g n R_o \left(\cos \theta - \frac{1}{1 + \cos \theta} \right)$$

Figure 6-1 shows the summary of membrane stresses for the parabolic shell and the spherical approximation for θ from 0 to 30° , where θ is the angle between the collector axis and radius

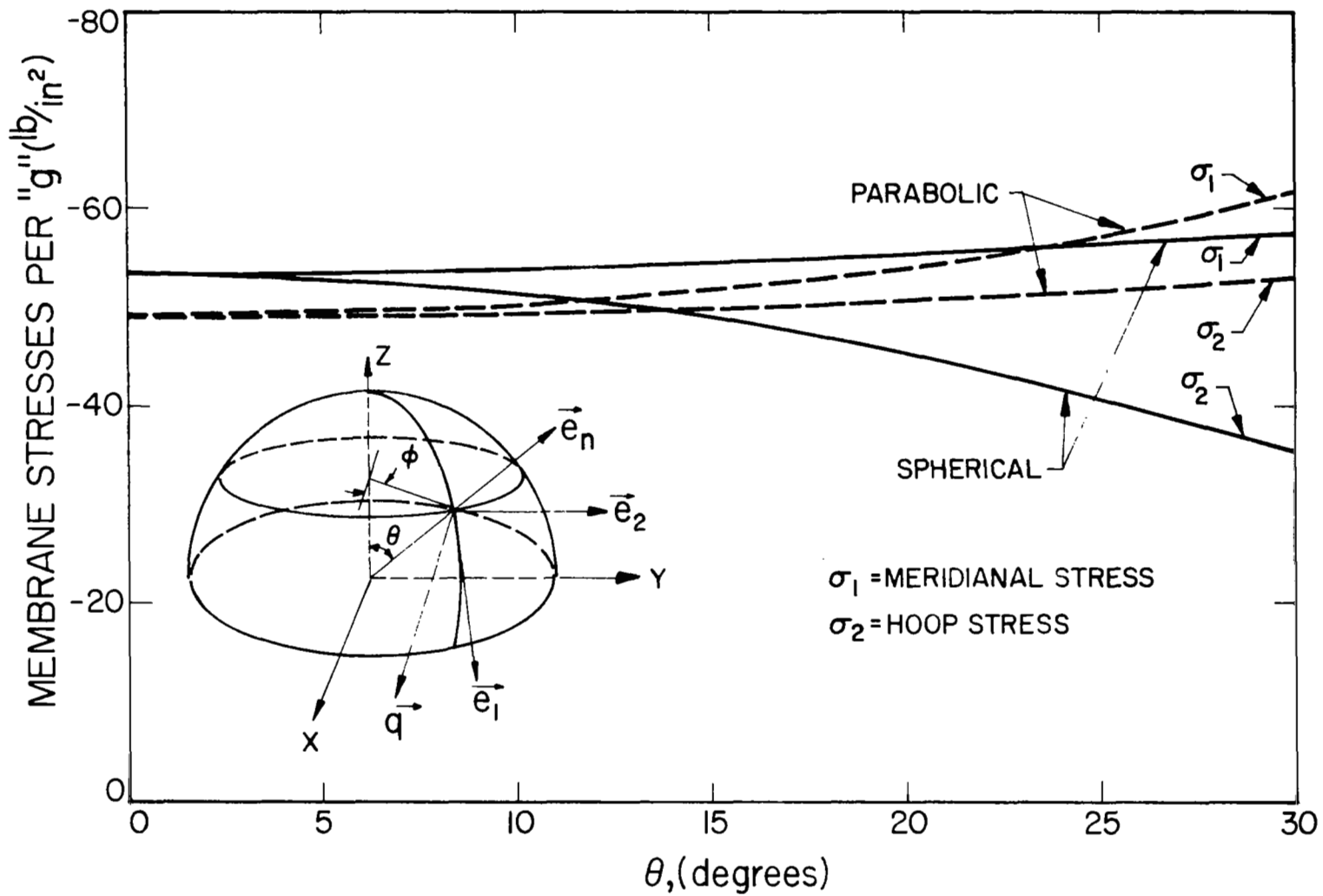


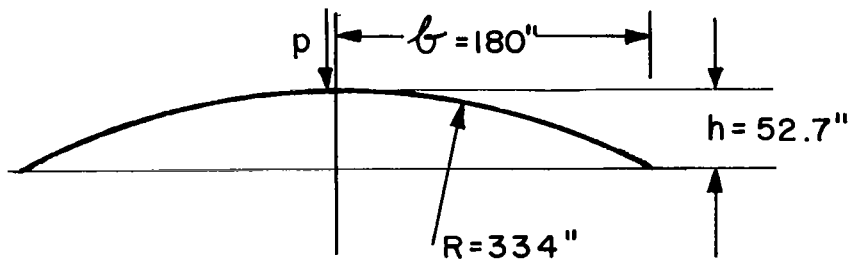
FIG. 6-1 MEMBRANE STRESSES DUE TO "g" LOADING ALONG AXIS OF REVOLUTION

of curvature. This figure shows that the spherical approximation to the parabolic shell is a fairly good approximation and can be used without significant error. The relatively low stresses per g indicate that the tensile stresses will be less than 400 lb/sq in. for the maximum 7g axial acceleration given in the environmental specifications. However, since the collector shell has a high radius of curvature to thickness ratio a careful investigation of compressive buckling stresses is required.

6.3.2 Compressive Buckling Stress

In considering the buckling of the collector subjected to a 3g acceleration (the maximum negative acceleration during launch) along the axis of revolution, it will be assumed that the 3g acceleration is equivalent to an external pressure given by the following,

$$p = 3g\rho t = 0.96t \text{ lb/in}^2$$



where b is the radius of the equivalent spherical shell.

The buckling pressure of a complete spherical shell under external pressure is given by the following equation,

$$p_{c1} = \frac{2}{\sqrt{3(1-\nu^2)}} E \left(\frac{t}{R} \right)^2$$

In practice structures never can withstand the theoretical buckling pressure. Therefore the fraction

$$\frac{p}{p_{cr}} \equiv \text{"critical buckling factor"}$$

has been used to represent the experimental or predicted buckling pressure where p is the experimental buckling pressure. There is wide scatter in the experimental buckling pressures of spherical and hemispherical shells. In the range of R/t from 500 to 2000, the range of p/p_{c1} is from 0.10 to 0.33. At an R/t of approximately 85,000 tests on the Echo I spherical balloon gave values of p/p_{c1} ranging from 0.12 to 0.18, (Ref. 6-4).

If one considers the collector to be a shallow shell, more experimental and theoretical results are available. The shallow shell approximation is violated by the collector, but the information is useful for pointing out trends in the experimental data.

For a shallow spherical shell,

$$\left(\frac{h}{b}\right) \ll 1$$

For the collector,

$$\left(\frac{h}{b}\right) = 0.29$$

The only case of a shallow spherical cap subjected to external pressure that has received much attention is the case of clamped edges. For this case the buckling pressure is a complicated function of a parameter λ defined as follows,

$$\lambda = \left[12(1-\nu^2)\right]^{1/4} \frac{b}{\sqrt{Rt}}$$

which is

$$= \frac{17.9}{\sqrt{t}} \approx 180$$

for the collector.

All of the shallow shell data reported is for λ less than 30. For values of λ greater than 20 the experimental data gives p/p_{c1} ranging from 0.20 to 0.70, with the higher values given by the more carefully manufactured shells.

As corroborated by Dr. Babcock, the best theoretical analysis now available is Huang's (Ref. 6-5) which gives the following,

$$p/p_{c1} = 0.86 \text{ for large } \lambda.$$

This analysis and related experiments are for the case of clamped edges. The effect of other boundary conditions is unknown, but one would expect this effect to be less in the high λ range as compared to the low λ range.

With the scarcity of theoretical and experimental data available, any prediction of the buckling pressure is somewhat in question. To more accurately predict this pressure, experimental data in the range of parameters corresponding to the collector are necessary.

The large scatter in the buckling pressures obtained from experimental studies can largely be traced to geometric irregularities. In general, it can be said that the better the shell the higher the buckling pressure. From this consideration, one would expect the buckling pressure for the electroformed collector to be quite high. This is borne out by the fact that the data for complete spherical shells, which are hard to manufacture, show low buckling pressures. However, shallow spherical shells with ratios of radius to thickness up to 4,000 show high buckling pressures compared to the classical pressure, $0.60 \leq p/p_{c1} \leq 0.86$, if the shell is carefully manufactured, (Ref. 6-2).

Assuming the buckling pressure is given by $p/p_{c1} = 1/3$, which is a logical compromise between the data of Ref. 6-2 and 6-4, the required thickness would be,

$$p = \frac{1}{3} p_{c1} = \frac{2}{3 \sqrt{3(1-\nu^2)}} E \left(\frac{t}{R} \right)^2 = 3\rho g t$$

$$\begin{aligned} \therefore t &= 9.5 \times 10^{-3} \text{ inches for a } 61^\circ \text{ rim angle} \\ &= 10.7 \times 10^{-3} \text{ inches for a } 55^\circ \text{ rim angle} \end{aligned}$$

Figure 6-2 shows the number of -g's a collector shell of thickness t will withstand before buckling for the design p/p_{c1} ratio and the p/p_{c1} ratios suggested by the work in Ref. 6-2 and 6-4. Figure 6-3 lists the critical buckling pressure as a function of t , collector thickness, for the same p/p_{c1} ratios. Another consideration in the buckling problem is the question of what constitutes failure of the collector.

To assess the structural integrity of the collector, it is necessary to establish a criterion for failure. It is clear that either of the following conditions would constitute local failure:

1. Exceeding the yield stress such that the surface is permanently distorted
2. Buckling to the extent that snap-back does not occur

If a sufficient portion of the mirror area is affected by these conditions, to the extent that performance suffers significantly, the mirror may be considered to have failed. The first task of the structural analysis, then, is to assure that the material yield stress is never exceeded under any unforeseeable conditions. This can be accomplished rather readily for static conditions. Yielding under dynamic conditions is more difficult to determine. It depends on amplification of the vibration under resonance conditions and is strongly dependent on vibration mode shapes, natural frequencies, and damping of the structure, and on the characteristics of the vibration spectrum.

Most of the available theory and data on buckling is concerned with determining the stresses or pressures at which buckling begins. However, this does not necessarily represent a good criterion for structural failure. If the local yield stress is never greatly exceeded, and if the buckled area snaps back after the buckling stress is removed, there is no reason to consider that the structure has

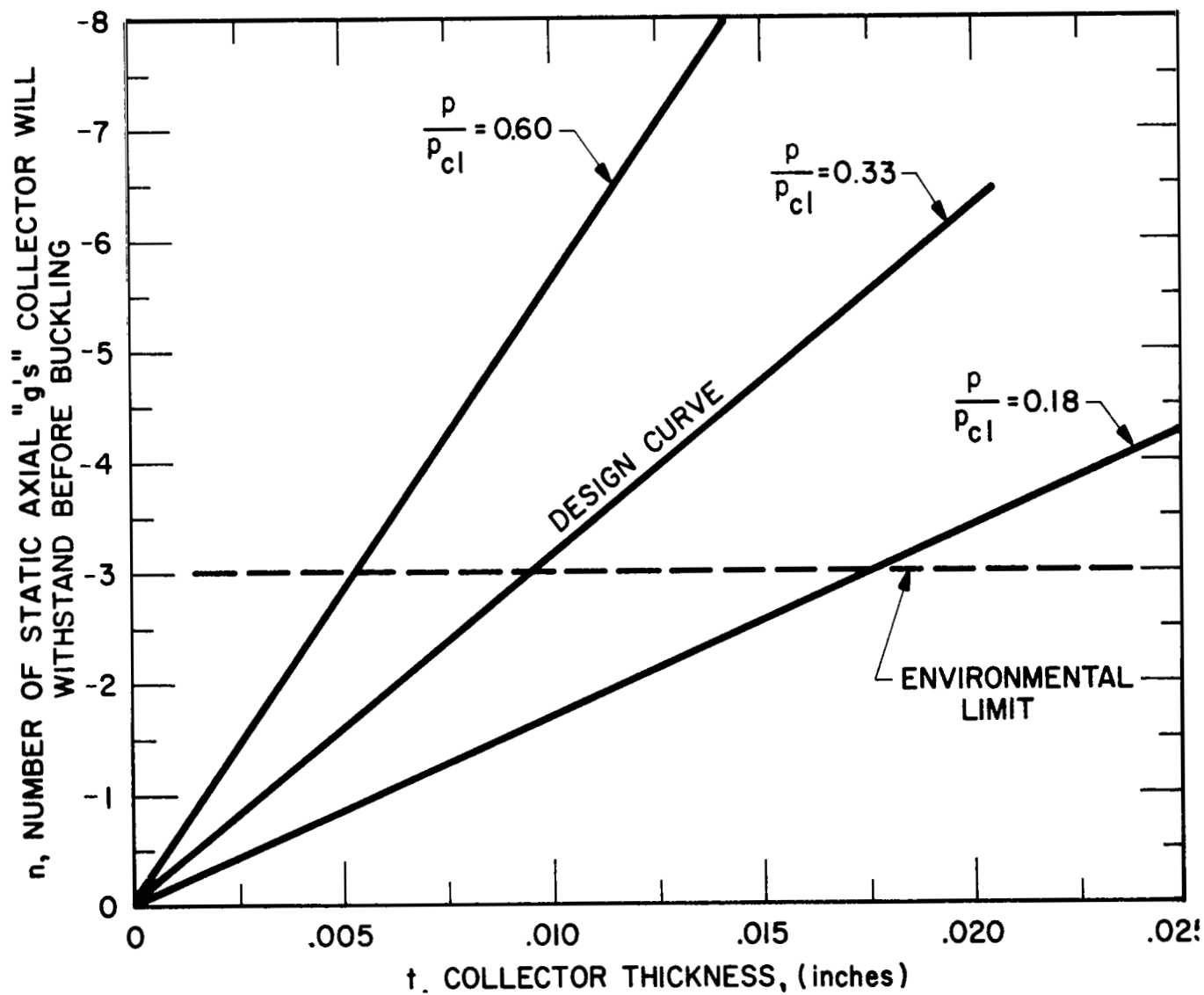


FIG. 6-2 STATIC BUCKLING RESISTANCE VS COLLECTOR SHELL THICKNESS

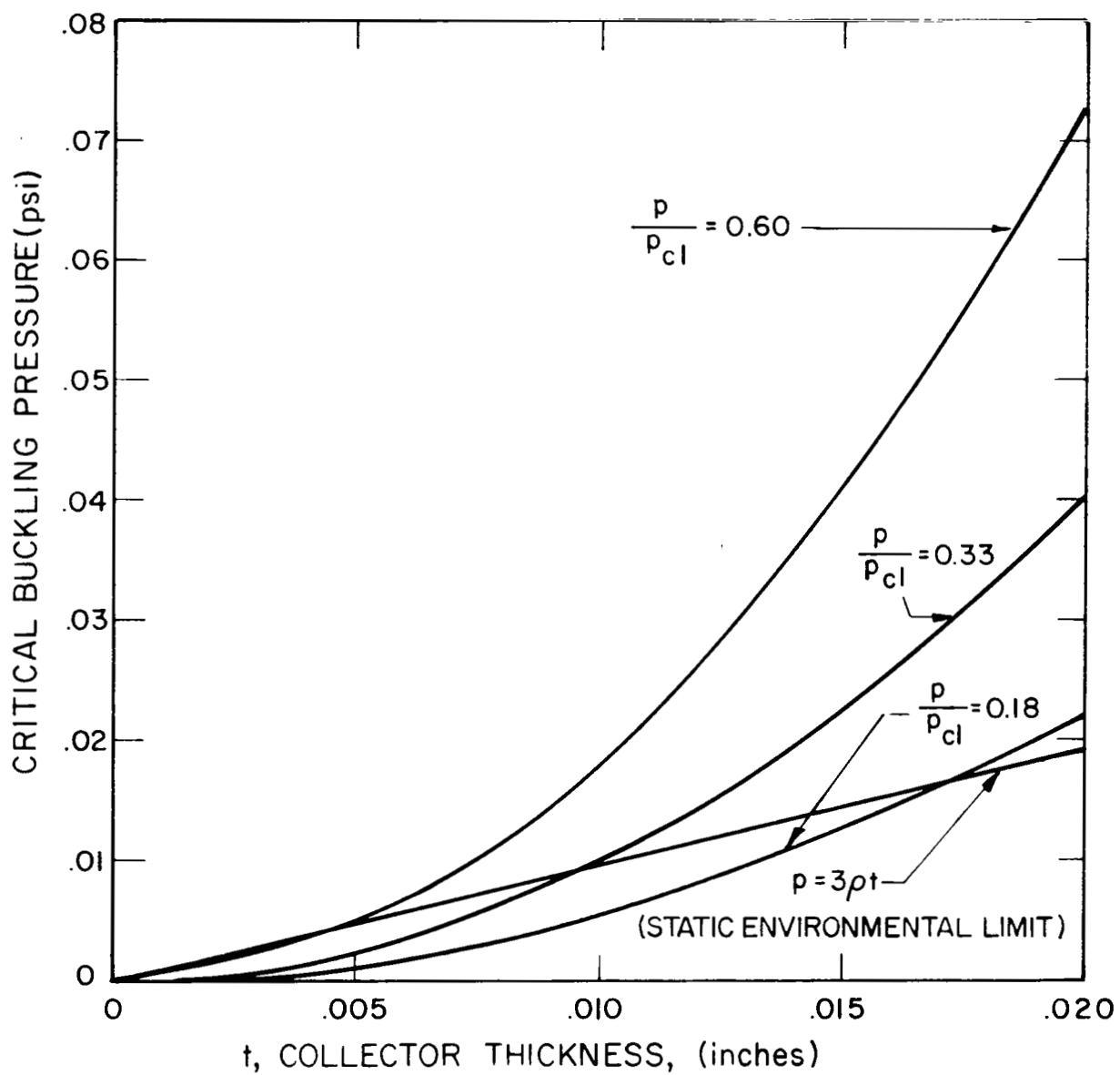


FIG. 6-3 CRITICAL BUCKLING PRESSURE VS COLLECTOR SHELL THICKNESS

failed. It is the experience of EOS that considerable local buckling of thin concentrator structures can occur under vibration and shock conditions without resulting in any permanent damage to the surface. Unfortunately, little work has been done to determine the extent to which buckling can occur without resulting in permanent degradation of optical properties. At the present state of development, it is not believed feasible to attack this problem analytically. Some experimental investigation will be required for specific configurations of interest.

6.4 Lateral Acceleration Effects

In the membrane analysis of the collector shell subjected to uniform transverse or lateral acceleration, the analysis is simplified by assuming that the collector is a spherical cap having the same base diameter and height as the parabolic shell. The shell diagram in Fig. 6-1 depicts the nomenclature used for the lateral acceleration analysis below.

The spherical cap radius $R_1 = R_2 = R = 334$ inches. The unit load vector \vec{q} is $\vec{q} = q \vec{l}_x = \rho g n t \vec{l}_x$ and the unit load is therefore $q = \rho g n t$. Therefore the meridional hoop and normal loads are:

$$q_1 = \vec{e}_1 \cdot \vec{q} = q \cos \theta \cos \phi$$

$$q_2 = \vec{e}_2 \cdot \vec{q} = -q \sin \phi$$

$$q_n = \vec{e}_n \cdot \vec{q} = q \sin \theta \cos \phi$$

Using the notation of Novozhilov, Ref. 6-3,

$$q_1 = q_{1,1} \cos \phi \quad \text{where} \quad q_{1,1} = q \cos \theta$$

$$q_2 = q_{2,1} \sin \phi \quad \text{where} \quad q_{2,1} = -q$$

$$q_n = q_{n,1} \cos \phi \quad \text{where} \quad q_{n,1} = q \sin \theta$$

The meridional and hoop and shear forces per lineal inch are respectively

$$T_1 = \frac{1}{R^2 \sin^3 \theta} \left[\int_0^\theta \Phi R \sin \theta \, d\theta \right] \cos \phi = T_{1,1} \cos \phi$$

$$T_2 = \left[q_{n,1} R - \frac{1}{R^2 \sin^3 \theta} \int_0^\theta \Phi R \sin \theta \, d\theta \right] \cos \phi = T_{2,1} \cos \phi$$

$$S = \left[T_{1,1} \cos \theta + \chi(\theta) \right] \sin \phi$$

where the function:

$$\begin{aligned} \Phi &= (q_{n,1} \cos \theta - q_{1,1} \sin \theta) R^2 \sin \theta \\ &\quad - \int_0^\theta (q_{n,1} \sin \theta + q_{1,1} \cos \theta - q_{2,1}) R^2 \sin \theta \, d\theta \\ \Phi &= 2qR^2 [\cos \theta - 1] \end{aligned}$$

and

$$\begin{aligned} \chi(\theta) &= \frac{1}{R \sin \theta} \int_0^\theta (q_{n,1} \sin \theta + q_{1,1} \cos \theta - q_{2,1}) R^2 \sin \theta \, d\theta \\ \chi(\theta) &= 2Rq \frac{1 - \cos \theta}{\sin \theta} \end{aligned}$$

The meridional, hoop, and shear stresses are therefore:

$$\begin{aligned} \sigma_1 &= T_1/t = -\rho g n R \cos \phi \frac{\sin \theta/2}{2 \cos^3 \theta/2} = \sigma_{1,1} \cos \phi \\ \sigma_2 &= T_2/t = \rho g n R \cos \phi \frac{\sin \theta/2}{2 \cos^3 \theta/2} [1 + 4 \cos^4 \theta/2] = \\ &\quad -\sigma_{1,1} [1 + 4 \cos^4 \theta/2] \cos \phi \\ T_{12} &= S/t = \rho g n R \sin \phi \frac{\sin \theta/2}{2 \cos^3 \theta/2} [1 + 2 \cos^2 \theta/2] = \\ &\quad -\sigma_{1,1} [1 + 2 \cos^2 \theta/2] \sin \phi \end{aligned}$$

Figure 6-4 shows the membrane stresses as a function of θ plotted from the above equations. Hoop and meridional stresses are of the same order of magnitude as in axial loading and have opposite signs at the same position. Therefore compressive buckling will not be a problem.

6.5 Centrifugal Acceleration Effects

The effects of centrifugal acceleration have been considered on:

1. Collector shell
2. Torus-absorber struts
3. Torus deflection

6.5.1 Collector Shell

A membrane analysis of the collector shell in the deployed position, subjected to an inertial loading, follows.

A plan view of the spinning collector is shown below where L is the separation between the vehicle and collector axis, \vec{q} the unit loading vector, r the radial distance from the vehicle axis, ω the angular velocity, ρ the density and t the shell thickness.

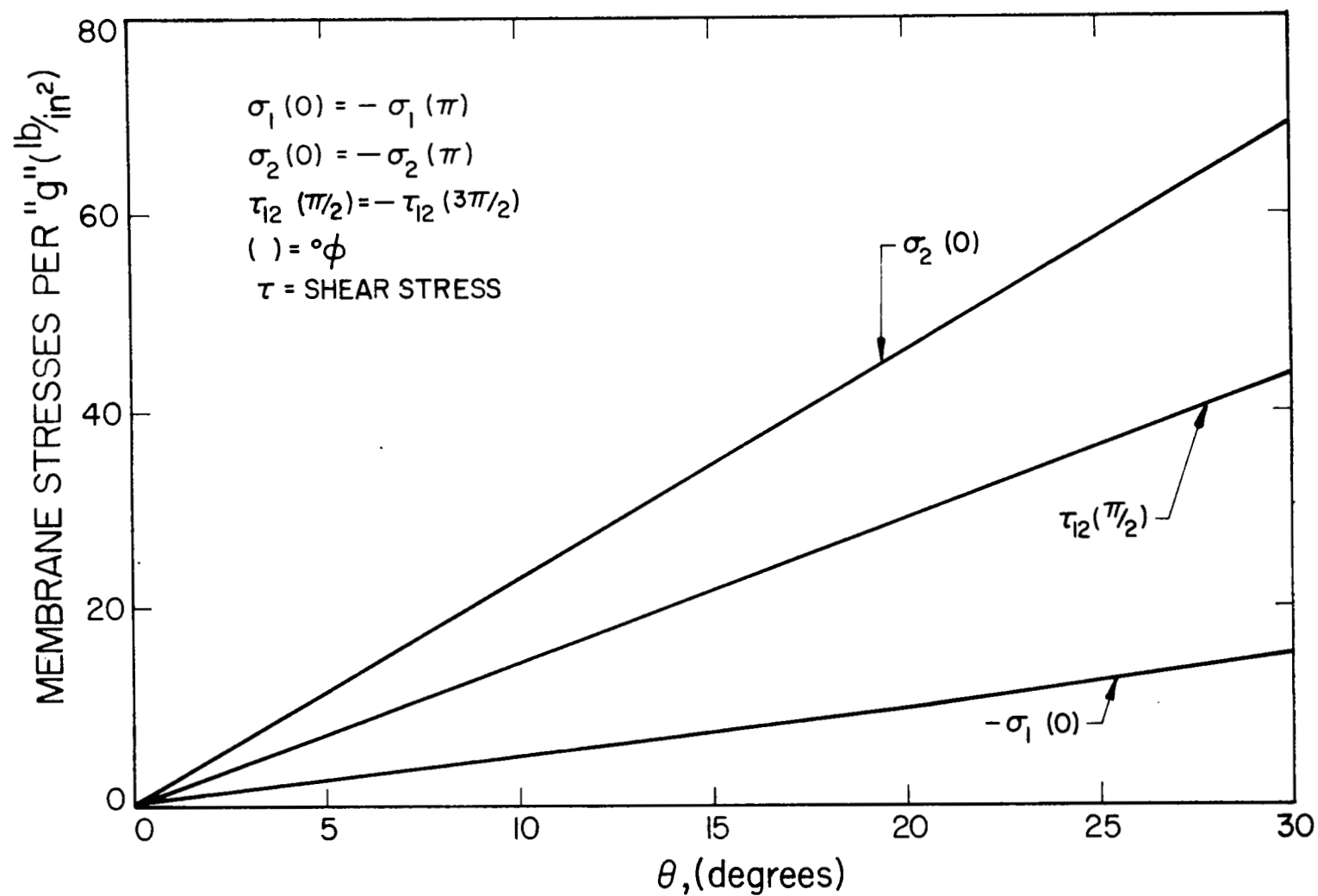


FIG. 6-4 MEMBRANE STRESSES DUE TO A TRANSVERSE "g" LOADING

The absolute value of the loading vector is:

$$|\vec{q}| = r\omega^2 \rho t$$

$$\vec{q} = r\omega^2 \rho g t [\cos\alpha \vec{l}_x + \sin\alpha \vec{l}_y]$$

where

$$\cos\alpha = \frac{L+x}{r}, \quad \sin\alpha = \frac{y}{r}$$

therefore

$$\vec{q} = \rho\omega^2 t [(L+x) \vec{l}_x + y \vec{l}_y]$$

The coordinates can be expressed as:

$$x = R \sin\theta \cos\phi$$

$$y = R \sin\theta \sin\phi$$

$$z = R \cos\theta$$

Direction Cosines

	x	y	z
\vec{e}_1	$\cos\theta \cos\phi$	$\cos\theta \sin\phi$	$-\sin\theta$
\vec{e}_2	$-\sin\phi$	$\cos\phi$	0
\vec{e}_n	$\sin\theta \cos\phi$	$\sin\theta \sin\phi$	$\cos\theta$

Substituting for x, y and z

$$\vec{q} = q[(L + R \sin\theta \cos\phi) \vec{l}_x + R \sin\theta \sin\phi \vec{l}_y]$$

where

$$q = \rho\omega^2 t$$

Therefore the meridional, hoop and normal forces are respectively

$$q_1 = \vec{e}_1 \cdot \vec{q} = q[(L + R \sin\theta \cos\phi)\cos\theta \cos\phi + R \sin\theta \sin^2\phi \cos\theta]$$

$$q_1 = qL \cos\theta \cos\phi + qR \sin\theta \cos\theta$$

$$q_2 = \vec{e}_2 \cdot \vec{q} = q[(L + R \sin\theta \cos\phi)(-\sin\phi) + R \sin\theta \sin\phi \cos\phi]$$

$$= -qL \sin\phi$$

$$\begin{aligned}
q_n &= \vec{e}_n \cdot \vec{q} = q[(L + R \sin\theta \cos\phi) \sin\theta \cos\phi + R \sin^2\theta \sin^2\phi] \\
&= qL \sin\theta \cos\phi + qR \sin^2\theta
\end{aligned}$$

or

$$q_1 = q_{1,1} \cos\phi + q_1 \quad \text{where} \quad q_{1,1} = qL \cos\theta$$

$$q_2 = q_{2,1} \sin\phi \quad \text{where} \quad q_{1,2} = -qL$$

$$q_n = q_{n,1} \cos\phi + q_n \quad \text{where} \quad q_{n,1} = qL \sin\theta$$

Therefore, the problem is divided into a symmetric problem and a $\sin\theta$ or $\cos\theta$ variation. The antisymmetric problem is identical to the problem solved for the collector under uniform lateral acceleration. The solution carries over by substituting $\rho\omega^2 tL$ for q in that problem.

The symmetric solution is found using Novozhilov

(Ref. 6-3).

$$q_1 = qR \sin\theta \cos\theta \quad \text{where} \quad q = \rho\omega^2 t$$

$$q_n = qR \sin^2\theta$$

Then the symmetrical meridional and hoop forces per lineal inch are:

$$T_1 = \frac{1}{R \sin^2\theta} \int_0^\theta (q_n \cos\theta - q_1 \sin\theta) R^2 \sin\theta d\theta \equiv 0$$

$$T_2 = q_n R = qR^2 \sin^2\theta$$

Adding the symmetric and $\sin\theta$ or $\cos\theta$ terms the meridional, hoop and shear stresses are:

$$\sigma_1 = -\rho\omega^2 LR \cos\phi \frac{\sin\theta/2}{2 \cos^3\theta/2} = -9.7 \frac{\sin\theta/2}{\cos^3\theta/2} \cos\phi = \sigma_{1,1} \cos\phi$$

$$\begin{aligned}
\sigma_2 &= \rho\omega^2 LR \cos\phi \frac{\sin\theta/2}{2 \cos^3\theta/2} [1 + 4 \cos^4\theta/2] + \rho\omega^2 R^2 \sin^2\theta \\
&= -\sigma_{1,1} [1 + 4 \cos^4\theta/2] \cos\phi + 16.3 \sin^2\theta
\end{aligned}$$

$$T_{12} = \rho\omega^2 LR \frac{\sin\theta/2}{2 \cos^3\theta/2} [1 + 2 \cos^2\theta/2] \sin\phi = -\sigma_{1,1} [1 + 2 \cos^2\theta/2] \sin\phi$$

The membrane stresses are shown as a function of θ in

Fig. 6-5.

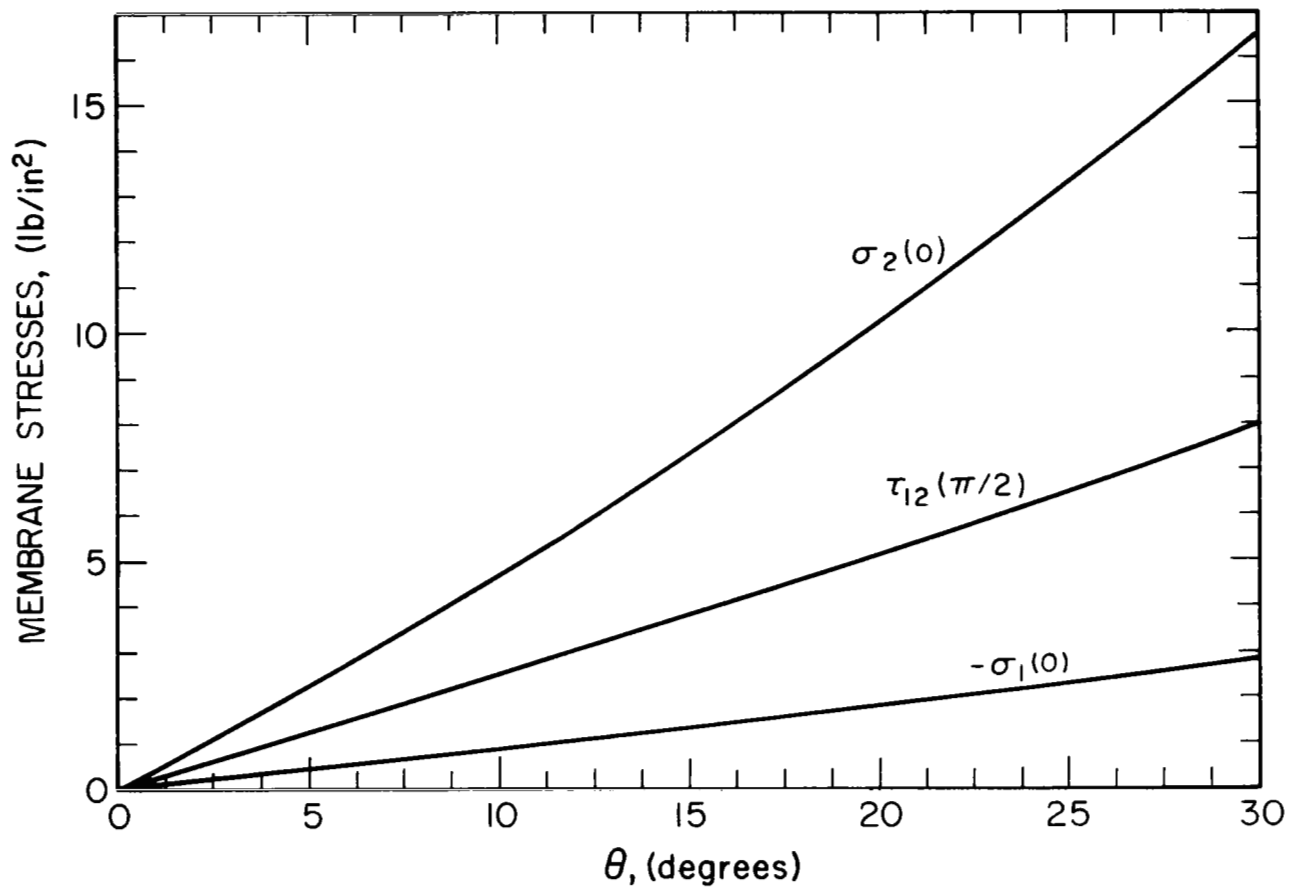


FIG. 6-5 MEMBRANE STRESSES OF COLLECTOR IN DEPLOYED POSITION DUE TO CENTRIFUGAL ACCELERATION

where

$$\begin{aligned}\omega^2 L &= 0.18g \\ \rho \omega^2 L R &= 0.18 \rho g R = 19.3 \text{ lb/in}^2 \\ \rho \omega^2 R^2 &= 16.3 \text{ lb/in}^2\end{aligned}$$

From Fig. 6-5 it can be seen that membrane stresses are extremely low, the maximum stress being less than 17 psi. These stresses will therefore present no structural or efficiency loss problems.

6.5.2 Strut Deflections

Strut and torus deflections are described in Section 5.9.

6.6 Vibration

The vibration characteristics of this structure will be dominated by the torus mounting since the collector shell and torus are rigidly joined. To better understand the analytical complexities of this problem, the structural frequency response will be broken into three parts:

1. Shell
2. Torus
3. Shell and torus.

6.6.1 Shell Frequencies

At least four possible edge mountings will determine the lowest natural frequency, f_n , of the shell. These result from the two alternate methods of supporting the collector in both the launch and orbit phases. These variations and the lowest fundamental nodal response are:

1. Eight-point torus support during launch (four nodal diameters)
2. Continuous torus support during launch (one nodal circle)
3. Tripod support during orbit (three nodal diameters)
4. Quadrapod support during orbit (two nodal diameters)

The fundamental responses for these frequencies are listed in Table 6-I. The fundamental frequencies for Cases 1, 3, and 4 were calculated from the following equation from Reissner (Ref. 6-6):

$$f_n = \frac{t}{2\pi R^2} \sqrt{\frac{E}{12\rho(1-\nu^2)}} \left[4(1-\nu)(n^2-1)n^2 \right]^{1/2}$$

where n = number of nodal diameters

ν = Poisson's ratio

ρ = density

R = collector radius

E = modulus of elasticity

The frequencies derived for Cases 1, 3, and 4 are 18, 13, and 8 percent higher than the corresponding frequencies derived from a flat plate of similar diameter and thickness.

Nomographs covering parabolic shells supported as in Cases 3 and 4 are given by Lin and Lee (Ref. 6-7). These results are also included for comparison in Table 6-I. The paraboloidal frequency for Case 3 may be in error as much as 50 percent since the referenced nomograph was extrapolated to obtain this value. Since the values are close to those evaluated for the spherical cap, the spherical cap approximation appears valid.

In each of the above cases the fundamental frequency is determined largely by the energy stored by inextensional bending. Therefore, frequency is dependent on the shell thickness and almost independent of shell curvature.

The fundamental frequency derived for Case 2 is high because the majority of the vibration energy is stored in stretching the shell. As can be seen in Table 6-I the lowest natural frequency for Case 2 is highly dependent on the approximation used. Naghdi (Ref. 6-8) shows that the lowest natural frequency for a thin shell hemisphere is

TABLE 6-I

SHELL NATURAL FREQUENCIES FOR VARIOUS TORUS SUPPORT CASES

<u>Case</u>	<u>Torus Support</u>	<u>Node</u>	<u>Frequency in cps</u>	<u>Reference</u>
1	8	4 nodal diameters	0.074	6-6
2	Continuous	Breathing - 1 nodal circle	146.	6-8, R
			79.	6-8, R _c
			128.	6-9
3	3	3 nodal diameters	0.042	6-6
			~0.075	6-7, Parabola
4	4	2 nodal diameters	0.017	6-6
			0.015	6-7, Parabola

NOTES

Constants used in frequency calculations

$$E = 30 \times 10^6 \text{ psi}$$

$$h = 47 \text{ in}$$

$$n = 2, 3 \text{ or } 4$$

$$R = 180 \text{ in}$$

$$R_c = 334 \text{ in}$$

$$t = 0.0107 \text{ in}$$

$$\nu = 1/3$$

$$\rho = 0.32/386 = 0.00083 \text{ lb} \cdot \text{sec}^2/\text{in}^4$$

$$f_n = \frac{0.87}{2\pi R} \sqrt{\frac{E}{\rho}}$$

Therefore, for a hemisphere having the same rim radius as the collector the natural frequency would be 146 cycles per second; with the same radius of curvature as the average spherical radius of curvature, the natural frequency would be 79 cycles per second.

The following equation from Reissner (Ref. 6-9) approximates the natural frequency for clamped thin spherical shells:

$$f_n = \frac{2.98}{2\pi} \frac{t}{R^2} \sqrt{\frac{E}{\rho(1-\nu^2)}} \left[1 + (1+\nu)[0.9 - 0.2(1+\nu)] \frac{h^2}{t^2} \right]^{1/2}$$

where h is the collector sagitta.

However, at high h/t ratios this equation may be in error as much as +18 percent as demonstrated by Hoppmann (Ref. 6-10). The calculated frequency of 128 cycles per second is, as one would expect, between the two frequencies calculated for various hemispherical radii above. Based on the questionable assumption of a completely clamped edge, and on the scatter of answers from the analytical solutions for a clamped edge, the natural frequencies calculated for this case may be in error by a factor of 2.

6.6.2 Torus

The natural frequencies of the torus, $f_{n,r}$, Table 6-II were derived assuming that the torus is a complete circular ring whose radius is large with respect to ring thickness in the radial direction (Ref. 6-11). For the four types of mounting described in Cases 1 through 4 in Section 6.6.1, the extensional and flexural vibrations, both in the plane and normal to the plane of the torus ring, have been calculated. The flexural vibrations are applicable only to Cases 1, 3, and 4. The equations used to derive frequencies are based on Harris and Crede (Ref. 6-11). Extensional frequencies are derived from the equation:

TABLE 6-II

TORUS NATURAL FREQUENCIES $f_{n,r}$, FOR VARIOUS SUPPORTS

<u>Case</u>	<u>Torus Support</u>	<u>Mode</u>	<u>Frequency in cps</u>
1	8	$4\lambda \perp$	23.4
		$4\lambda =$	23.6
2	Continuous	Extensional	294
3	3	$3\lambda \perp$	12.2
		$3\lambda =$	12.4
4	4	$2\lambda \perp$	4.2
		$2\lambda =$	4.4

NOTES

Assumed a torus weight of 150 lb; $\therefore m_r = 3.43 \times 10^{-3} \text{ lb} \cdot \text{sec}^2/\text{in}^2$

λ wavelengths, flexural vibration

\perp perpendicular to torus plane

$=$ in torus plane

$$f_n = \frac{1}{2\pi} \sqrt{\frac{E\pi r^4}{m_r R^2} (1+n^2)}$$

where m_r is the torus mass per lineal inch, R the collector radius and r the torus cross sectional radius.

Flexural frequencies in the plane of the torus ring are derived from:

$$f_n = \frac{1}{2\pi} \sqrt{\frac{E\pi r^4}{4m_r R^4} \frac{n^2(n^2-1)^2}{(n^2+1)}}$$

The flexural frequencies normal to the plane of the ring are derived from:

$$f_n = \frac{1}{2\pi} \sqrt{\frac{E\pi r^4}{4m_r R^4} \frac{n^2(n^2-1)^2}{(n^2+1+\nu)}}$$

6.6.3 Torus-Shell

At present there is only limited published information on the empirical determination of natural frequencies of toroidally rigidized solar collectors (Refs. 6-12 and 6-13). This work was done on 5-foot diameter mirrors. Although JPL is performing experimental work in this area and although they are developing a computer program which can determine natural frequencies of any paraboloidal shell-torus combination, no simple analytical means are yet available for the calculation of the torus-collector shell natural frequency. Therefore, the determination of this frequency will be based on simplifying assumptions. First, assume that the torus will store all the vibrational energy. Next, a portion of the mass of the collector shell and a part of the shell stiffness will be added to the torus. Experimental work at JPL indicates that approximately 52 percent of the shell mass should be lumped to the torus. If one assumes that the shell stiffness is between 0 and 1 times the torus stiffness, the resultant combined

resonant frequency will be from 1 to $\sqrt{2}$ times the torus frequencies with lumped masses. A summary of the combined shell-torus frequencies for the four cases described above is given in Table 6-III as calculated from the following equation

$$f_{n,c} = f_{n,r} \left[\left(\frac{m_r}{m_r + m_s} \right) \left(\frac{D_r + D_s}{D_r} \right) \right]$$

where $f_{n,c}$ is the shell-torus or collector natural frequency, m_r the torus mass, m_s the shell mass, D_r the torus rigidity and D_s the shell rigidity.

6.6.4 Vibration Effects

The structural response to vibration effects is dependent on the structural dampening, which determines the resonance amplification factor, A_r .

$$A_r = \frac{C_{cr}}{2C} = \frac{1}{\eta}$$

where C is the dampening coefficient, C_{cr} , the critical dampening coefficient and η the dissipation factor. Structural dampening is a function of both the air dampening, C_a , and material dampening, C_m .

If the collector is approximated by a square plate with the same thickness as that of the collector and with a length and width equal to the collector diameter, the air dampening can be determined by either of two equations. When $\frac{\omega a}{2c} < 1$ (where ω is the frequency in radians/second, a the length and width, and c the velocity of sound) or $f < 12$ cps, the dampening on both sides of the plate is as follows (Ref. 6-14).

$$\frac{C_a}{C_{cr}} = 0.636 \frac{c_m}{c} \frac{\rho}{\rho_m}$$

TABLE 6-III
SHELL TORUS NATURAL FREQUENCIES FOR VARIOUS SUPPORTS

<u>Case</u>	<u>Torus Support</u>	<u>Mode</u>	<u>Frequency in cps</u>	
			$D_s = 0$	$D_s = D_r$
1	8	$4\lambda \perp$	15.5	21.9
		$4\lambda =$	15.6	22.1
2	Continuous	Extensional	194	274
3	3	$3\lambda \perp$	8.1	11.4
		$3\lambda =$	8.2	11.6
4	4	$2\lambda \perp$	2.8	4.0
		$2\lambda =$	2.9	4.1

NOTES

λ wavelength

\perp perpendicular to torus plane

$=$ in torus plane

D rigidity

m mass

$()_r =$ function torus

$()_s =$ function shell

$$m_s = 4.44 \times 10^{-5} \text{ lb} \cdot \text{sec}^2/\text{in}^2; \quad m_r = 3.43 \times 10^{-3} \text{ lb} \cdot \text{sec}^2/\text{in}^2$$

where c_m and ρ_m are respectively the speed of sound and density of the plate material. For air dampening on both sides of the nickel shell the air amplification factor $A_{r,a} = 400$. However, due to the high diameter to thickness ratio the amplification factor should be further reduced because of dampening due to inphase air acceleration. This reduction is not easily determined.

When $\frac{\omega a}{2c} > 3$ or $f > 36$ cps, the dampening is determined as follows:

$$\frac{C_a}{C_{cr}} = 0.175 \frac{\rho}{\rho_m} \frac{c}{c_m} \frac{D^2}{t^2} \quad (\text{Ref. 6-14})$$

where t is the shell thickness and D the collector diameter. $A_{r,a}$ for this case = 0.00025. The wide amplification variations above 36 cps and below 12 cps are due in part to the exclusion of inphase air acceleration dampening. Tests should be made to verify these formulae for large R/t ratios.

Mechanical dampening depends on such factors as:

1. Material
 - a. Composition, structure and homogeneity
 - b. Stress and temperature history
2. Internal stress
 - a. Initial stress
 - b. Changes caused by stress in temperature history
3. Stress conditions in use
 - a. Type, i.e., tension, compression
 - b. State of stress, i.e., triaxial and biaxial
 - c. Stress magnitude
 - d. Stress variations
 - e. Environmental characteristics

For most materials the amplification factor ranges between 6 and 1000. Since nickel is a magnetic material with high internal friction, a

material dampening amplification factor, $A_{r,m}$ of 100 appears conservative. A total amplification factor then is calculated as follows:

$$\frac{1}{A_r} = \frac{1}{A_{r,a}} + \frac{1}{A_{r,m}}$$

Therefore, for frequencies less than 12 cps the combined amplification factor is much less than 80; for frequencies greater than 36 cps the amplification is much less than one. The amplification factor for vacuum is 100.

The resonant stress, σ_r , is given by $\sigma_r = \sigma_{lg} \times A_r \times n$ where, σ_{lg} is the one "g" stress and n the number of g.

Table 6-IV lists the resonant stresses and ratio of yield stress to resonant stress for the four cases of torus mounting in launch and orbit. In Case 1, the 8-point torus suspension during launch, extremely high resonant stresses are calculated. Reduction of these stresses can be achieved by the following means:

1. Tapering the torus to equalize torus stresses
2. Increasing the torus moment of inertia
3. Designing for friction dampening between the torus and radiator
4. Friction dampening between the radiator mounts and torus brackets
5. Empirically determining the actual dampening of the torus-shell combination.

To achieve a safety factor of greater than 1.0, a 40-fold increase in dampening would be required.

Case 2, the continuously supported torus, exhibits extremely low air damped resonant stress. More complete analyses are required to determine whether resonant stresses may be a problem under partial vacuum conditions toward the final boost phases. The torus resonant stresses for the tripod orbit support are high. However, such stresses can be appreciably reduced by the use of either magnesium or magnesium-silicon struts which have an extremely high dampening and dissipation factor, or by any of the methods described above for Case 1.

The natural frequency for the quadrapod support, Case 4, is lower than the environmental specification and no stress problems should therefore be encountered from orbital vibration.

TABLE 6-IV
VIBRATION EFFECTS SUMMARY

Case	Torus Support	Natural Frequency in cps	Max. Input Acceleration	Amplification Factor			Max. Stress at 1 g (psi)	Resonance Stress (psi), σ_r		Yield Stress σ_y	
				$A_{r, a + m}$		$A_{r, m}$		$A_{r, a + m}$	$A_{r, m}$	Resonance Stress σ_r	
										Air & Material	Material Only
1	8 points	15.6	~6	<<80	100	shell	70	<<33,600	42,000	>>12.5	10
				<<80	100	torus	5,200	<<2,500,000	3,200,000	>> 0.028	0.022
2	Continuous	194	19	< 1	100	shell	70	<70	133,000	>1,000	10
				< 1	100	torus	13.0	<13	24,000	>5,400	54
3	3 points	8.2	0.25		100	shell	60	-	1,500		46.6
					100	torus	37,000		925,000		0.119
4	4 points	2.9	-								

Since the vibration response is highly dependent on dampening coefficients, natural frequencies, and mounting details, additional empirical studies of the detailed design are necessary.

By using vibration isolators for the torus support during launch the amplification at the natural resonant frequency can be reduced by at least a factor of two.

The vibration analysis indicates that a continuously supported torus is the preferred design during launch, and that a quadrapod supported torus is preferred during orbit.

The effects of dynamic loading on compressive buckling have not and cannot be readily determined from available analytical or empirical studies. Suggested tests for vibration and other dynamic loadings on similitude models of the proposed collector design are discussed in Section 10.

6.7 Shock

The most critical shock specification is the 35g shock loading by either a 10 millisecond triangular pulse, an 8 millisecond half sine wave pulse, or a rectangular pulse of 5 milliseconds. Table 6-V summarizes the results of this launch shock on the critical components for Cases 1 and 2. If the natural period of the element in question is greater than the shock period, the displacement of the element governs the ultimate stress. If the period of the element is less than the shock period the acceleration governs. This indicates that for an 8-point suspension, a torus deflection at the torus-radiator mount should be less than 0.54 inches, if the maximum torus stress is to be below the design yield stress of 70,000 psi.

For the continuously mounted torus the maximum shell stress would be < 2,100 pounds. In this case the high shell dampening will prevent any resonance amplification and limit the maximum g's to 35 or less.

TABLE 6-V
SHOCK SUMMARY

Case	Torus Support	Natural Period Seconds	Maximum Acceleration Determined by	Maximum Stresses psi
1	8-points	0.064	Torus displacement must be ≤ 0.54 inches	Torus $\leq 70,000$
2	Continuous	0.003	Acceleration - 35g's	Shell 2,100

6.8 Acoustical Noise

The effect of the 148 db acoustical noise field must be studied both from the standpoint of static buckling and dynamic stress.

The sound pressure level of 148 db Re 0.0002 microbar is equivalent to an rms pulsating pressure of 0.07 lb/in^2 . From Olson, Ref. 6-15, the net radiation pressure (assuming the shell is an infinite wall) from acoustical noise striking the shell from one side is given by the following relationship:

$$p_n = (\gamma + 1) \frac{p}{2\rho c}$$

where p_n = the net radiation pressure

γ = the ratio of the specific heat of air at constant pressure to the specific heat at constant volume = 1.4

p = the pulsating acoustical noise pressure

ρ = the air density

c = the velocity of sound in air

Therefore at a 148 db acoustical noise level the net radiation pressure is 6×10^{-4} psi which is an order of magnitude less than the critical buckling pressure for the electroformed shell design. Since the acoustical noise level will be approximately constant on both sides of the collector shell, there will effectively be no net radiation pressure. Therefore, from a static standpoint no buckling should occur.

For a flat plate the mean square stress value is given by the following equation from Ref. 6-14:

$$(\bar{\sigma})_n^2 = \frac{K_{14} c_m^2 a^2}{E^2 t^3 \xi} \phi_p(\omega_n)$$

$(\bar{\sigma})_n^2$ - mean square stress value

K_{14} - proportionality constant

c_m - velocity of sound in material

a - minimum plate or shell width

E - modulus of elasticity

t - plate, shell thickness

ξ - $\frac{C}{C_{cr}}$

$\phi_p(\omega_n)$ - pressure function of natural frequency, ω_n , and acoustical noise level

Some experimental data is available on the stresses arising from a 148 db acoustic noise pressure level on aluminum flat and curved plates (Ref. 6-16). The stress in a similar nickel plate can be inferred by dividing the stress equation for nickel by that of aluminum, thereby cancelling K_{14} and $\phi_p(\omega_n)$ so that

$$\overline{(\sigma^2)}_{n,ni} = (\bar{\sigma})_{n,al}^2 \frac{c_{m,ni}^2 a_{ni}^2}{c_{m,al}^2 a_{al}^2} \frac{E_{al}^2 t_{al}^3 \xi_{al}}{E_{ni}^2 t_{ni}^3 \xi_{ni}}$$

For the nickel shell ξ is determined from the air dampening equations in Section 6.6.4. In the case of the clamped shell, where the natural frequency is above 36 cps, ξ is 2×10^3 . For an aluminum plate of these dimensions the ratio of structural and air dampening to critical dampening ξ is less than 0.01. A summary of constants used follows.

Item	Units	Nickel (ni)	Aluminum (Ref. 6-16) (al)
$(\bar{\sigma})_n^2$	lb ² /in ⁴		25,000
c_m	in./sec	1.9×10^5	1.97×10^5
a	in.	360	9.36
E	psi	30×10^6	10×10^6
t	in.	0.0107	0.032
ξ	-	2×10^3	$\sim 10^{-2}$

Therefore, the nickel shell stress due to a 148 db acoustical noise level will be less than 230 psi. Even if the air dampening factor of the collector shell were in error by a factor of 200 to 300, the fatigue strength of nickel would not be exceeded.

In the proposed design, additional resistance to stress fatigue is provided by the curvature of the shell and the predominantly tensile loading provided by the launch acceleration. The improvement in resistance to acoustical failure as a function of shell curvature and static pressure, equivalent to static acceleration, on the concave side of curved plates is also discussed in Ref. 6-16.

From the experimental data of Ref. 6-16 the edge mounting design is very important. Therefore design details which increase friction dampening and which reduce localized edge stresses, will reduce any edge effects of acoustical noise.

Therefore the proposed design should have a high resistance to the static pressure and the dynamic stress produced by the 148 db acoustical noise field.

6.9 Thermal Effects

The all-nickel collector structure has a high resistance to thermal stress and thermal shock. At no time will the temperature over the entire collector vary by more than 200^oF. Based on a thermal

expansion coefficient of 7.4×10^{-6} and a modulus of elasticity of 30×10^6 , for nickel, the maximum possible thermal stress even assuming a completely rigid torus would be of 44,400 psi which gives a safety factor of greater than 1.5 relative to a 70,000 psi yield strength.

The resistance of this structure to thermal shock will be high. While no standard thermal shock resistance test exists, good thermal shock resistance appears to be a function of the ratio $Ks/\alpha E$, where K is the thermal conductivity, s the tensile strength, α the linear coefficient of thermal expansion, and E the modulus of elasticity. This ratio shows that thermal shock resistance is favored by high tensile strength, high thermal conductivity, low modulus of elasticity at failure and low thermal expansion. Based on comparative values of the above coefficients, for comparable structures and thermal variations nickel has a thermal shock resistance comparable to that of aluminum.

No structural degradation is therefore expected from either thermal stress or shock.

REFERENCES

Section 6

- 6-1 Parmerter, Robert R., "The Buckling of Clamped Shallow Spherical Shells under Uniform Pressure," *Aeroelasticity and Structural Dynamics*, SM 63-53, AFOSR 5362, November 1963
- 6-2 Babcock, Charles D. and Sechler, Ernest D., "The Effect of Initial Imperfections on the Buckling Stress of Cylindrical Shells," *NASA Technical Note D-2005*, July 1963
- 6-3 Novozhilov, V.P., "The Theory of Thin Shells," P. Noordhoff, LTD., Groningen, the Netherlands, 1959
- 6-4 McComb, Harvey G. and Fichter, Wilbur B., "Buckling of a Sphere of Extremely High Radius - Thickness Ratio," from "Collected Papers on Instability of Shell Structures - 1962," *NASA Technical Notes D-1510*, 561, December 1962
- 6-5 Huang, Nai-Chien, "Unsymmetric Buckling of Clamped Spherical Shells," *American Institute of Aeronautics and Astronautics Journal* 1, 945, April 1963
- 6-6 Johnson, Millard W. and Reissner, Eric, "On Transverse Vibrations of Shallow Spherical Shells," *Quarterly of Applied Mathematics* 15, 367, April 1958
- 6-7 Lin, Y. K. and Lee, F. A., "Vibrations of Thin Paraboloidal Shells of Revolution," *Journal of Applied Mechanics* 27, 743, December 1960
- 6-8 Naghdi, P. M. and Kalnis, A., "On Vibrations of Elastic Spherical Shells," *Journal of Applied Mechanics* 29, 65, March 1962
- 6-9 Reissner, Eric, "On Vibrations of Shallow Spherical Shells," *Journal of Applied Physics* 17, 1038, December 1946
- 6-10 Hoppmann II, W. H., "Frequencies of Vibration of Shallow Spherical Shells," *Journal of Applied Mechanics* 28, 305, June 1961
- 6-11 Stokey, William F., "Vibration of Systems having Distributed Mass and Elasticity," Section 7-1 of "Shock and Vibration Handbook - Volume 1," Harris, Cyril M. and Crede, Charles E., McGraw Hill Book Co., 1961

REFERENCES

Section 6

(contd)

- 6-12 Jet Propulsion Laboratory, "Appendix B - Vibration Survey - Mariner B, Nickel Solar Energy Thermionic Reflector," 1961
- 6-13 "Solar Energy Thermionic Conversion System - Appendix B - Concentrator Test Data and Observations," JPL Contract 950109, 1962
- 6-14 Hubbard, Harvey H. and Houboult, John C., "Vibration Induced by Acoustical Waves," Section 48 of "Shock and Vibration Handbook - Volume 3"
- 6-15 Olson, Harry F., "Acoustical Engineering," Van Nostren Co., 1957
- 6-16 Hess, Robert W., Herr, Robert W., and Mayes, William H., "A Study of the Acoustical Fatigue Characteristics of some Flat and Curved Aluminum Panels Exposed to Random and Discrete Noise," NASA Technical Notes D-1, August 1959

7. RELIABILITY

The collector reliability depends on the integrity of the paraboloidal geometry and the reflective mirror coating.

7.1 Ground Testing and Handling

The environmental specifications for ground testing and handling are much less severe than the static and dynamic loadings during launch and orbit. The ground specifications can easily be met by the proposed collector. Also, during the ground testing and handling phases weight is not a major criterion. Therefore, handling fixtures and tooling can be designed so that the collector has a large safety factor without adding to packaging or transportation costs appreciably.

The reliability of the reflective coating underground testing and handling conditions is discussed in the following sections.

7.1.1 Coating Adhesion

The EOS collector design involves the use of a chemical spray deposited silver reflective coating. The electrochemical bond between this chemically predeposited silver layer and the electroformed nickel shell is almost an order of magnitude greater than for any vacuum deposited metal coating. This electrochemical bond probably exceeds the strength of solid silver. No adhesion problems are expected between the nickel and silver. None have been encountered in previous EOS electroforming work. However, the use of chemically deposited silver on collectors fabricated by other processes is not practical. The alternative, vacuum deposited silver, would be unreliable. Vacuum deposited silver coatings exhibit relatively poor adhesive qualities, in fact they are often used as parting layers.

7.1.2 Silver Diffusion

Based on the phase diagrams included in Ref. 7-1, silver and nickel are immiscible over the temperature range in which a collector will operate. Therefore, no reflectance losses will be caused by nickel-silver diffusion.

7.1.3 Prelaunch Protection

The 91 percent value for practical silver reflectance was based on a nominal 1 to 2 percent degradation due to normal testing, providing the collector is suitably protected between tests. The silver reflectance is primarily degraded by the presence of the hydrogen sulphide ion. Therefore, the silver surface can be protected either by providing an impenetrable protective coating or by eliminating hydrogen sulphide ions from the presence of the silver coated mirror.

Protective methods include:

1. A very thin layer of amino silane, now being extensively used on all silver flatware made in the United States, can be deposited on the silver immediately after collector fabrication. This material can be deposited in a pinhole-free coating. It offers great promise for collectors requiring long terrestrial solar tests.
2. A sprayable photolyzable film could be used for protection from fabrication to orbit. This film readily evaporates under the influence of ultraviolet radiation and hard vacuum. The photolyzable film is compatible with silver surfaces.
3. A number of mechanically strippable plastic films, compatible with silver, could protect the silver from manufacturing to prelaunch preparations. Such films have been extensively used in the production of solar simulator mirrors and searchlights at EOS.
4. Collector storage in a bag of inert gas, such as nitrogen, will eliminate the presence of hydrogen sulphide.

5. Lead acetate impregnated paper will absorb the hydrogen sulphide ion if placed in the collector container. Several sample mirrors have been stored and repeatedly inspected without visible loss of reflectance for periods of six months or more using this lead acetate paper.

Based on previous experience and the numerous available methods of protecting silver, no problems concerning loss in reflectance prior to launch are expected if any of the above methods are followed. The overall collector reliability will, therefore, be very high during the prelaunch phase.

7.2 Launch Conditions

Based on reasonable assumptions for the "critical buckling factor", air and structural dampening, collector edge conditions, natural frequencies, and mode shapes the continuously supported torus collector design will withstand all specified launch and environmental conditions.

Since the chemically spray deposited silver reflective layer has high adhesion to the electroformed nickel substrate, no reflectance loss is expected due to dynamic environmental loadings.

7.3 Orbit Conditions

With a quadrapod torus cavity absorber strut design, the geometric integrity of the collector will be maintained throughout the 10,000 hour orbit design life with a loss of less than 2 to 3 percent of the total reflective area due to all possible structural distortion: thermal, torus deflection, strut rotation.

The orbital resistance of the reflective coating is dependent on the base material, electroformed nickel, as well as the coating material. The various aspects of the space environment that can be expected to affect the composite reflective surfaces and electroformed nickel base structure include:

1. Temperature
2. Micrometeorites
3. Charged particles
4. Changes in dielectric protective coatings due to ultraviolet radiation
5. Miscellaneous effects

All estimates of reflective surface degradation in space are based on ground simulation tests or on analysis. The analytical estimates depend on theories of unknown validity and on widely divergent values for energy and particle flux densities, depending on the source of the data. Instrumented samples of specularly reflective surfaces, representative of solar collector surfaces, have never yet been exposed to the actual space environment. Until this is done, there will be no final answer regarding the durability of any reflective surface in space. Fortunately, plans are now under way to implement such an experiment.

Being fully appreciative of the unavailability of positive knowledge on this subject, EOS has chosen a reflective coating system which seems to offer the best probability of withstanding the space environment, based on current theory and experimental data. Reference 7-2 discusses the effects of space environmental factors on surface reflectance degradation. This report will summarize these findings.

7.3.1 Temperature Effects

Over the practical range of absorptivities and emissivities considered, the toroidally supported electroformed nickel collector will encounter no problems due to material recrystallization, stress relief, creep, or evaporation.

7.3.2 Micrometeorites

It has been shown (Refs. 7-3 and 7-4) that the volume of material displaced to form a pit on the reflective surface is directly proportional to the kinetic energy of the impinging

micrometeorite particle. Various constants of proportionality have been developed by Whipple, Eichelberter, and Gehring and Barnes (Refs. 7-5, 7-6, and 7-7).

Based on particle velocities ranging from 2.2 to 7.2×10^6 centimeters/second and densities ranging from 0.44 to 8.9 grams per centimeter, fractional surface losses for nickel substrate materials could range from a maximum of 0.76 percent to a minimum of 0.06 percent per year. Depending on the proportionality constant used, an aluminum substrate could lose from 2 to 4 times as much surface area per year as a nickel substrate. For either plastic substrate type reflectors or reflective coatings involving dielectric layers, larger surface area losses might be expected.

Tests at NASA-Lewis using simulated micrometeorite fluxes have resulted in higher percentages of surface area degradation on representative reflective samples. There is some question whether the low velocity fluxes of the simulation tests actually represent the surface damage of the expected higher velocity space fluxes even though the total kinetic energy flux is the same in both cases (see Appendix B).

Experiments are continuing on a new group of reflective samples.

7.3.3 Charged Particles

Space proton bombardment of polished metal surfaces may have a significant effect on surface degradation. Depending on the references cited and on whether there is high solar activity, charged particle damage could range from very little to a significant amount in one to three years.

7.3.4 Ultraviolet

Since no dielectric protective coatings are expected to be used, ultraviolet degradation effects should not be a problem.

7.3.5 Miscellaneous

The effects of atomic displacement by high energy electrons and protons should not degrade the specular reflectivity as much as 1 percent per year. Also, the ionization produced by high energy photons, x-rays, and ultraviolet should create no static attraction of particles onto the all-metal mirror surface.

REFERENCES

Section 7

- 7-1 Hanson, "Constitution of Binary Alloys," McGraw Hill Book Co., 1958
- 7-2 "Study of a Flight Experiment of Solar-Concentrator Reflective Surfaces," Contract NAS1-2880, Nov 1963
- 7-3 Davison, E. H., and Winslow, P. C., "Space Debris Hazard Evaluation," NASA Technical Note, D-1105, 1961
- 7-4 Collins, R. D., and Kinard, W. H., "The Dependency of Penetration on the Momentum per Unit Area of the Impacting Projectile and the Resistance of the Materials to Penetration," NASA Technical Note, D-238, 1960
- 7-5 Whipple, F. L., "The Meteoric Risk to Space Vehicles," Vista in Astronautics, Vol. 1, Pergamon Press, New York, 1958, pp. 115-124
- 7-6 Eichelberter, R. J. and Gehring, J. W., "Effects of Meteoroid Impacts on Space Vehicles," J. ARS, No. 32, 1962, pp. 1583-1591
- 7-7 Barnes, R. S., "The Effect of the Radiations Encountered by Materials in Space," J. Brit. Interplanetary Society, Vol. 18, 1962, pp. 377-381

8. WEIGHT CONSIDERATIONS

8.1 Importance of Weight as an Optimization Parameter

The importance of weight in a space power system design must be evaluated in relation to two factors:

1. Competitive position of the power system relative to alternate systems of similar power output
2. Weight capability of intended boosters

8.1.1 Relationship to Competitive Systems

Only the solar photovoltaic system will compete with the solar Brayton cycle system during this decade in the 5 to 10 kilowatt power range. No nuclear systems of comparable power output and no other multikilowatt solar systems are anticipated on a development schedule compatible with that of the solar Brayton cycle system. A weight breakdown for a solar photovoltaic power system is shown in Table 8-I. This is for a 5 to 10 kilowatt system, using battery energy storage in a low altitude earth orbit. Even the weight of the solar panel array alone is equal to or greater than that anticipated for the total Brayton cycle system. Including the remaining system components, the photovoltaic system will weigh up to twice as much as the Brayton cycle system. However, even if it were as heavy as the photovoltaic system, the Brayton cycle system would still have a clear advantage in regard to unit cost. At the present time, the unit cost of a photovoltaic system is on the order of \$1,000,000 per kilowatt. If low efficiency cells were accepted as a means of reducing cost (with a corresponding weight increase), the system cost might be reduced to \$500,000 per kilowatt or slightly less. However, this is still on the order of \$4,000,000 per unit for an 8 kilowatt system.

TABLE 8-I

WEIGHT BREAKDOWN OF TYPICAL
SOLAR PHOTOVOLTAIC POWER SYSTEM

Design Conditions

Power level	5 to 10 kw
Orbit parameters	55 minute light per 35 minute dark

Weight Breakdown

Solar cell array (daylight only)	130 lb per kw*
Solar cell array (sized to supply output power plus battery charging power. Energy storage efficiency = 85 percent)	227 lb per kw
Battery weight (sealed silver cadmium batteries. Energy storage capacity = 8 watt hr per lb)	70 lb per kw
Auxiliary deployment gear, electronics and controls (excluding power conditioning equipment)	50 lb per kw
System weight (raw power)	347 lb per kw
System weight (assuming power conditioning equipment weighs 20 lb per kw and has efficiency of 85 percent)	428 lb per kw

*Specific weight is expressed in pounds per kilowatt of average system power output.

The solar Brayton cycle system enjoys a clear advantage both in regard to weight and cost over the photovoltaic system. Therefore, the Brayton cycle system could be increased in weight considerably before it would begin to lose this competitive advantage.

Near the end of the decade, the SNAP-8 system may begin to compete with an array of four Brayton cycle systems in the 30 to 35 kilowatt range. The SNAP-8 will weigh upwards of 200 lb per kw depending on shielding requirements. The competitive position of the Brayton cycle system relative to SNAP-8 is less clear cut and depends strongly on specific vehicle and mission requirements. Some factors to be considered are:

1. Total power requirement
2. Sensitivity of payload to nuclear radiation
3. Reliability advantages of multiple Brayton cycle units versus a single SNAP-8
4. Importance of power system volume during launch and in orbit

8.1.2 Booster Capability

The second major consideration is that of booster capability. The solar Brayton cycle system is to be launched in a Saturn 5 booster with either an S-2 or an S-4B upper stage. The latter combination, which can carry the 20-foot diameter collector, is capable of 240,000 lbs in a low altitude earth orbit. Even the two-stage Saturn 5 has a weight capability many times the expected weight of four solar Brayton cycle systems. Unless the remaining payload volume of the booster is filled with rather dense equipment, it is unlikely that weight capability of the booster will be exceeded.

8.1.3 Summary

Considering both the competitive position of the solar Brayton cycle system and the weight capability of the intended boosters, it is clear that the system and its components should be optimized for system efficiency and reliability rather than for minimum weight. The EOS collector design concept is compatible with this situation.

8.2 Weight of Collector

This weight discussion includes the collector shell and torus, torus-radiator brackets and torus-cavity strut brackets. Tables 8-II and 8-III show the various weights and packaging dimensions for collectors with nickel and titanium tori respectively, both with an eight-point radiator torus support and an alternative continuous radiator-torus support. Specific weights between 0.69 and 0.87 lb per ft² can be readily obtained with this design. Lighter weight one-piece electroformed collectors can be achieved, which have equivalent or greater structural integrity, at a sacrifice in optical efficiency. Some of these alternative designs are discussed in Section 3. Such designs would still offer the reliability of a high reflectance silver reflective coating, electrochemically bonded to a highly specular electroformed nickel shell. However, the optical losses that arise from the attachment of rigidizing structure are inherent in the lightening process and, therefore, set a maximum limit on effective collector efficiency, which is less than for a single shell nonrigidized collector.

TABLE 8-II
WEIGHT OF ALL-NICKEL COLLECTOR

Weight	NICKEL TORUS	
	Weight	Specific Weight
Collector Shell	372	0.525
Torus	154	0.218
Torus - Shell Joint	33	0.047
Reflective Surface	0.2	0.0002
Radiator - Torus Support Brackets*	40	0.056
Torus - Strut Support Brackets	15	0.021
Totals	614	0.87

Packaging Dimensions

Height	< 4.0 feet
Diameter	30.0 feet
Rim Angle	55 degrees

* Use of a continuous radiator-torus support would eliminate radiator-torus support brackets. Weights would be:

Total 574 lb
Specific 0.81 lb/ft²

TABLE 8-III
WEIGHT OF NICKEL-TITANIUM COLLECTOR

WEIGHT WITH TITANIUM TORUS - BRACKETS

	Weight	Specific Weight
Collector Shell	372	0.525
Torus	65	0.092
Torus - Shell Joint	33	0.047
Reflective Surface	0.2	0.0002
Radiator - Torus Support Brackets*	20	0.028
Torus - Strut Support Brackets	<u>10</u>	<u>0.014</u>
Total	510	0.72

Packaging Dimensions

Height	<4.0 feet
Diameter	30.0 feet
Rim Angle	55 degrees

* Use of continuous radiator-torus support would eliminate radiator-torus support brackets. Weights would be:

Total 490 lb
Specific 0.69 lb/ft²

9. CONCLUSIONS

The proposed design, a one-piece electroformed shell toroidally supported at the rim, offers the system designer high efficiency and reliability capability reasonable weight, suitable packaging volume and a manufacturing process that is highly amenable to low-cost, accurate reproduction, with high process and quality control.

9.1 Power

The useful system power is a function of the collector diameter and the power conversion, storage and collector-absorber efficiencies. (The collector-absorber efficiency as defined in this report does not include the cavity absorber thermal insulation losses. Such losses are assumed to be included as part of the heat storage efficiency). Based on Fig. 9-1, 20- and 30-ft collectors with 80 percent collector-absorber efficiencies in a system having a combined power conversion and storage efficiency of 15 percent, would produce 5 and 11 kilowatts, respectively. Even when all cavity insulation and collector-absorber losses are taken into account, the design goal of 75 percent efficiency should be met.

9.2 Reliability

The reliability of the proposed design should be high for all phases of its operation. Metallurgically the structure has high resistance to such environmental conditions as:

1. Temperature extremes - high yield stress at low and high temperatures
2. Micrometeorites - high volumetric heat of fusion
3. Vacuum - low vapor pressure at high temperatures
4. High energy protons, electrons, photons, x-rays
5. Ultraviolet - no dielectric coatings

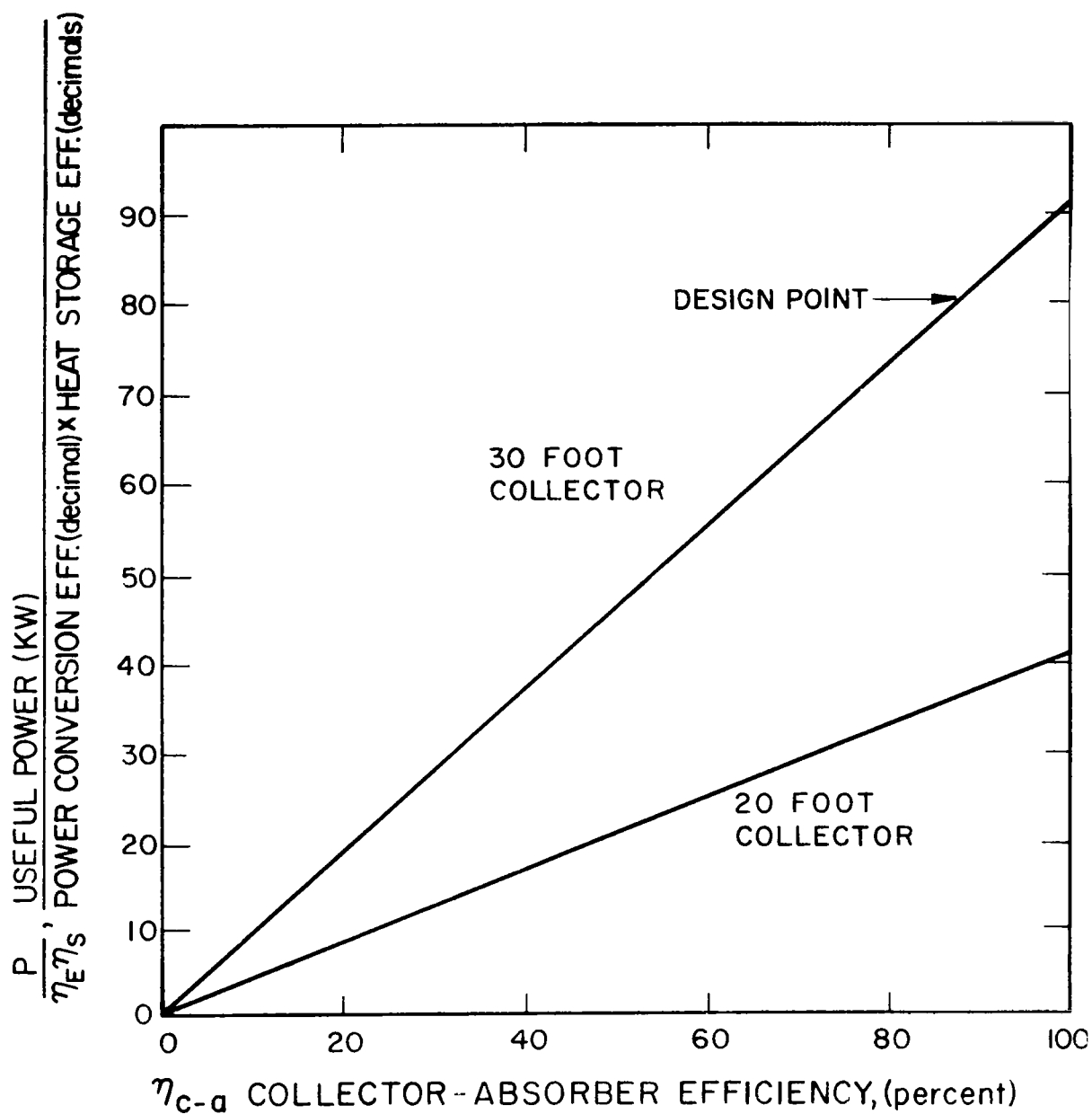


FIG. 9-1 POWER INPUT TO ABSORBER VS COLLECTOR-ABSORBER EFFICIENCY

6. Diffusion - immiscible with reflectance coatings
7. Shock - high yield stress
8. Creep - high yield stress at high temperatures
9. Corrosion - relatively unreactive to normal atmospheres

The integrity of the structural design, based on available empirical and theoretical analysis of similar shapes, indicates that this collector should have high structural reliability due to:

1. All metal construction
2. Highly efficient one-piece electroformed collector shell
3. Low residual stress
4. Single joint
5. No pockets for gas entrapment
6. Electro-chemical bonds between torus and shell
7. High air dampening
8. Low thermal gradient across the collector shell
9. Low thermal expansion materials

The reflectance coating of chemically deposited silver has also high resistance to the above factors. Possible tarnishing of the silver reflectance coating by hydrogen sulphide ions can easily be overcome by any one of several protective methods.

9.3 Weight and Volume Collector

A specific weight of 0.8 lbs per ft² should be adequate to meet environmental specifications. While other collector concepts may achieve slightly lower design weights, the loss in reliability and power for such designs does not compensate for the slight overall system weight reduction, particularly when the Saturn boosters, which will be used to launch the Brayton cycle solar power systems, have payload capability so that even a 2 to 300 percent increase in collector weight will not be detrimental to the overall mission capability.

The proposed collector will fit in a package 30-feet in diameter and less than 4-feet high. For the 20-foot diameter collector the packaging height will be less than 2.7-feet.

9.4 Cost

Relative to other design concepts the single shell toroidally rim supported collector offers the following cost advantages:

1. Automatic generation and reproduction of the paraboloidal shell geometry
2. Short production time
3. Automatic process controls
4. Exact reproduction and duplication between successive collectors
5. Controlled residual structural stresses ensuring high yield rates
6. Only a single joint

The exact cost of the collectors will depend on the final collector design, specifications, number, and delivery schedule.

With its high performance and reliability capability the EOS collector design will achieve the lowest total costs for any given power output and reliability.

10. RECOMMENDATIONS

As a result of this collector study program, it has been found that additional information is required in two areas in order to verify and improve collector reliability:

1. Investigation of collector structural integrity
2. Measurements of collector surface reflectance degradation in space

10.1 Structural Testing

To provide a firmer basis for determining structural feasibility of large, single-piece, solar collectors, a test program involving the most critical structural analysis areas is recommended. Such a program will provide values needed for analysis as well as check points for the verification of existing theories.

10.1.1 Model Types

Two model types are proposed: (1) paraboloidal mirrors with approximately the same rim angle and general structural characteristics as the full scale mirror; (2) spherical mirrors rigidized by a simple edge mounted toroidal ring with the same average radius of curvature as the full-scale mirror.

The first type of model would be used for tests related to or affected by overall collector structural characteristics. The second type of model (which approximates a section of the full-scale mirror) would be used for evaluation of local surface effects, such as local buckling or acoustic damage.

10.1.2 Experimental Tests

10.1.2.1 Static Buckling

Buckling by static acceleration can be approximated by a static differential pressure. Two types of information can

be determined by the buckling test. First, the experimental buckling pressure divided by the calculated classical buckling pressure should be compared with the "critical buckling factor" $\left(\frac{P}{P_{cl}}\right) = \frac{1}{3}$ used in the collector design. Also, the pressure at which significant permanent surface deformation occurs should be determined and compared with the critical buckling pressure.

10.1.2.2 Vibration Characteristics

Vibration tests should be run to determine natural frequencies, mode shapes and structural and air dampening characteristics. These characteristics are essential for structural analysis of large collectors under environmental vibration, shock, and acoustic excitation.

10.1.2.3 Acoustical Noise

Models should be subjected to noise levels up to those defined by the environmental acoustical noise spectrum, which has an average value of 148 db.

10.1.2.4 Temperature Variations

Using appropriate heat sources, structural models should be subjected to transient thermal variations and gradients similar to those that can be expected for the full-scale orbiting collector.

10.1.2.5 Optical Tests

Optical tests should be performed both before and after the above structural tests to determine the change in collector model performance, if any, caused by the various tests.

10.1.3 Analytical Correlation

The experimental results above can be used to predict structural performance of the full-scale mirror. While these tests cannot fully guarantee the structural integrity of the large mirror,

they should provide a much firmer basis of the assumptions used in the analysis.

10.2 Space Testing of Collector Surface Reflectance

In-space measurements of reflector surface degradation are needed to verify and correlate analytical predictions and the results of ground simulation tests.

A program to define a space experiment for this purpose, "Study of a Flight Experiment of Solar-Concentrator Reflective Surfaces" (Ref. 7-2), has been recently completed. Based on the desirability of space reflectance measurements, an actual flight experiment seems imperative if the reliability of any reflectance-based solar power system is to be determined with any certainty.

APPENDIX A

SOLAR BRAYTON CYCLE SPACE POWER SYSTEM ENVIRONMENTAL SPECIFICATION

APPENDIX A

SOLAR BRAYTON CYCLE SPACE POWER SYSTEM ENVIRONMENTAL SPECIFICATION

A.1 SCOPE

This specification covers the anticipated environmental conditions listed below to which the Solar Brayton Cycle Space Power System and components shall be designed to withstand without malfunction or performance degradation.

This specification does not cover development and/or acceptance tests.

Environmental conditions specified are applicable to each of the components and the complete solar space power system through manufacture, storage, transportation, lift-off, boost, orbit, and orbital transfer.

A.2 ENVIRONMENTAL CONDITIONS

A.2.1 Storage and Transportation

The components and their associated equipment shall be capable of withstanding without performance impairment the following loads applied along each of three perpendicular axes of its container.

A.2.2 Shock and Vibration

4g shock within one of the following times and wave shapes:

1. Triangular pulse of 10 milliseconds
2. Half-sine pulse of 8 milliseconds
3. Rectangular pulse of 5 milliseconds

Vibration:

2 - 10 cps	0.40 inch double amplitude
10 - 500 cps	2.0 g peak

A.2.3 Launch, Lift-Off, Boost

The nonoperating system and components shall be capable of withstanding without performance impairment the following simultaneous

launch loads applied at the system mounting points and in the directions and magnitudes specified:

1. Shock

35g shock along each of three mutually perpendicular axes within one of the wave shape and pulse times in A.2.2, above.

2. Vibration

Sinusoidal input applied at the system mounting points along each of three mutually perpendicular axes

16 - 100 cps	at 6g peak
100 - 180 cps	at 0.0118" double amplitude
180 - 2000 cps	at 19g peak

3. Acceleration

The nonoperating system and its accessory components shall be capable of withstanding the following launch accelerations for five minutes duration:

7g - along boost vehicle lift-off axis.

3g - along boost vehicle lift-off axis in opposite direction.

4.5g - all directions in plane normal to lift-off axis.

4. Acoustic Noise

The nonoperating system and its components shall be capable of withstanding the induced vibrations while subjected to an acoustic noise field with an integrated level of 148 db, Re 0.0002 micro bar.

A.2.4 Orbital Operation

The equipment shall be designed to be capable of startup and continuous operation at rated power in earth orbits of from 300 to 20,000 nautical miles without malfunction for 10,000 hours time.

A.2.4.1 Shock

Prior to system startup and deployment, the components shall sustain up to 7g shock (course correction) along the lift-off or flight axis with one of the wave forms and time durations indicated in paragraph A.2.2.

A.2.4.2 Vibration

The system and components will sustain vibrations in orbit while in operation of 0.25g peak over a frequency range of 5 to 2000 cps for a time period of five minutes for each occurrence.

A.2.4.3 Acceleration

A.2.4.3.1 Undeployed

The undeployed system and components will sustain accelerations of 3-1/2g in one direction along the lift-off axis, and plus or minus 1g in all directions in the plane normal to the lift-off axis. These accelerations will be sustained individually for a period of five minutes maximum for each occurrence.

A.2.4.3.2 Deployed

The deployed operating system will also be required to be capable of sustaining a continuous, unidirectional acceleration arising from a 4 rpm spin rate of the spacecraft. The g loading on the system components will be a function of their radial location with respect to the spin axis. For the purposes of this application, the centerline axis of the collector and system is located at a radius of 33 feet from the spin axis and experiences an 0.18g acceleration.

APPENDIX B

REFLECTANCE MEASUREMENTS AND SIMULATED
MICROMETEORITE TESTS

APPENDIX B
REFLECTANCE MEASUREMENTS AND SIMULATED MICROMETEORITE TESTS

In 1963, tests were performed at NASA/Lewis to determine the effects of simulated micrometeorite fluxes on selected reflective surfaces. Silicon carbide particles, accelerated by a shock tube, were impinged on the test surfaces. Resulting degradation in total reflectance was then measured and was found to be high when compared to analytical predictions based on available data.

To better understand and document the effects indicated by these initial experiments, another series of reflectance samples was tested. These samples, which were submitted to NASA/Lewis for testing, were made from electroformed nickel substrates 15/16 inch in diameter and about 0.060 inch thick. Surface to be tested were prepared in the following categories:

1. Chemically deposited silver, 600 to 1,000Å
2. Bare electroformed nickel
3. Vacuum deposited: chromium 100Å, aluminum 1,000Å
4. Vacuum deposited: chromium 100Å, silicon monoxide 2,500Å
aluminum 1,000Å
5. Vacuum deposited: chromium 100Å, silicon monoxide 2,500Å
aluminum 1,000Å
6. Vacuum deposited: chromium 100Å, silicon monoxide 2,500Å
aluminum 1,000Å, silicon monoxide, 20,000Å

The reflectance measurements of the samples before and after micrometeorite testing, as well as measurements of control samples retained by EOS, are listed in Table B-I. Figure B-1 shows samples 1 and 3 from the 6 groups. At EOS the samples were measured at 0.625, 0.7, and 1.0 micron with a Beckman DU spectrophotometer. Each sample was measured at least three times. The measurement given is an average of these

TABLE B-I
REFLECTANCE MEASUREMENTS
0.625 μ TEST WAVELENGTH

Group	Sample	<u>Reflectance</u>		Loss	Net Reflectance
		Before Test %	After Test %		
1	1	98.1	33.5	64.6	48.7
	2	96.8	81.6	15.2	
	3	97.2	—	—	
2	1	66.9	27.8	39.1	31.4
	2	66.8	63.0	3.8	
	3	66.7	63.3	3.4	
3	1	92.3	21.8	70.5	26.5
	2	91.6	86.6	5.0	
	3	91.9	87.5	4.4	
4	1	92.3	41.6	50.7	47.2
	2	93.1	—	—	
	3	92.1	86.5	5.6	
5	1	81.5	36.0	45.5	40.3
	2	92.0	86.9	5.1	
	3	92.0	87.2	5.2	
	4	79.9	77.4	2.5	
6	1	84.9	43.3	41.6	42.0
	2	69.2	70.0	(0.8)	
	3	61.2	65.0	(3.8)	
	4	84.1	83.5	0.6	

Samples:

Sample 1 was tested at NASA/Lewis. Samples 2, 3 and 4 were control samples.

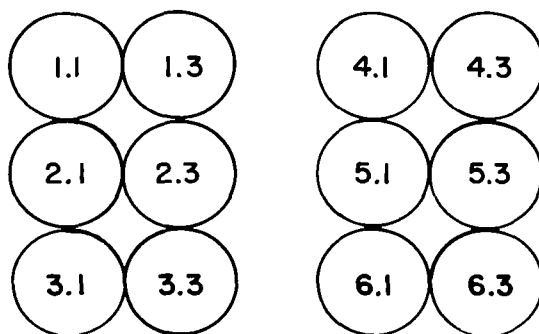
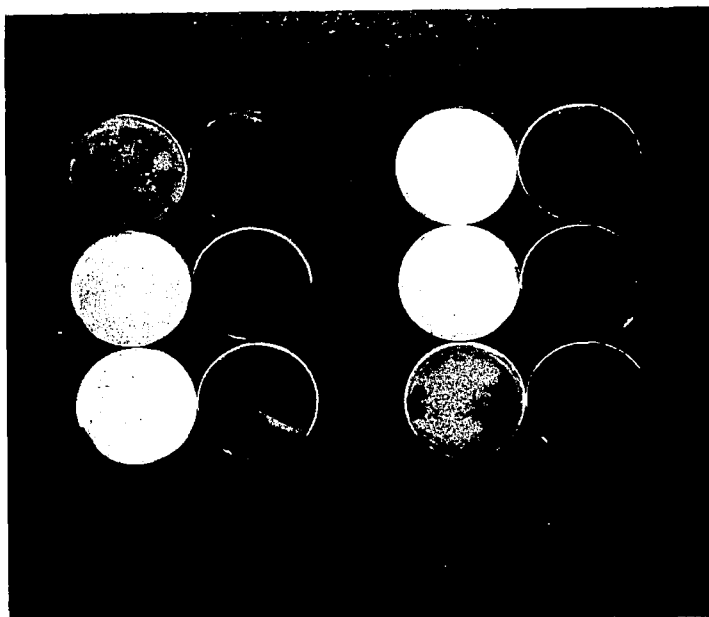


FIG. B-1 REFLECTANCE SAMPLES BEFORE (__.3) AND
AFTER (__.1) MICROMETEORITE TESTING

TABLE B-I
(continued)
1.0 μ TEST WAVELENGTH

Group	Sample	Reflectance		Loss	Net Reflectance
		Before Test %	After Test %		
1	1	98.5	54.5	44.0	65.6
	2	98.3	-	-	
	3	98.6	87.5	11.1	
2	1	74.6	29.6	45.0	32.2
	2	74.7	71.9	2.8	
	3	73.9	71.5	2.4	
3	1	94.6	23.0	71.6	26.4
	2	94.3	90.6	3.7	
	3	94.0	90.9	3.1	
4	1	94.2	44.1	50.1	45.8
	2	94.3	-	-	
	3	93.2	91.5	1.7	
5	1	93.1	41.8	51.3	43.0
	2	91.7	88.9	2.8	
	3	91.5	90.6	0.9	
	4	92.5	92.6	(0.1)	
6	1	92.6	50.8	41.8	52.4
	2	83.9	83.1	0.8	
	3	92.1	90.0	2.1	
	4	85.0	83.0	2.0	

TABLE B-I
(continued)
0.700 μ TEST WAVELENGTH

Group	Sample	Reflectance		Loss	Net Reflectance
		Before Test %	After Test %		
1	1	99.3	40.5	48.8	53.3
	2	99.8	86.5	13.3	
	3	100.1*	—	—	
2	1	69.9	29.2	40.7	34.3
	2	69.9	64.3	5.6	
	3	69.5	65.0	4.5	
3	1	91.1	22.2	68.9	26.4
	2	91.1	86.0	5.1	
	3	90.2	86.8	3.4	
4	1	89.0	42.5	46.5	44.8
	2	89.7	—	—	
	3	88.8	86.5	2.3	
5	1	79.5	33.4	46.1	36.0
	2	89.2	84.2	5.0	
	3	82.4	83.8	(1.4)	
	4	81.6	76.3	4.3	
6	1	83.0	46.2	36.8	40.1
	2	72.6	81.4	(8.8)	
	3	65.5	79.4	(13.9)	
	4	82.9	78.6	4.3	

*The 100.1 percent silver reflectance measurement, compared with published values, indicates that the experimental error was in the order of ± 0.6 percent.

three readings. Reflectance measurements were made by the goniometer method. The 100 percent reflectance level was measured by placing the photocell in line with the spectrophotometer beam. An aluminum standard was then referenced. This standard was referred to after testing each sample. The spectrophotometer beam made an angle of incidence of 34° with the reflective surface and the aluminum standard.

The initial reflectance measurements of Samples 1 to 3, Groups 1 through 4, correlated closely with each other and with published reflectance data. The maximum variation between samples within a group was 1.3 percent, which indicates the reproducibility between measurements and coating samples.

The initial reflectance variations among samples within Groups 5 and 6 were caused by differences in thickness of the silicon monoxide overcoating. The silicon monoxide overcoating acted as a selective spectral filter. Visual observation of these samples indicated a range of colors; i.e., the samples within a group did not have maximum absorption of the same wavelength. This observation correlated with the reflectance measurements.

The first and second samples of each coating group were sent to NASA/Lewis for testing. The first samples were exposed to a hypervelocity cloud of silicon carbide particles between 2 and 14 microns in diameter which were accelerated in a 3-inch shock tube to a velocity of 8,500 ft/sec. These articles were then impacted against the test samples at the following levels of kinetic energy:

<u>Sample</u>	<u>Kinetic Energy $\sum_i \frac{1}{2} m_i v_i^2$</u>
1-1	0.70 joule
2-1	1.21 joules
3-1	1.42 joules
4-1	0.66 joule
5-1	1.09 joules
6-1	1.22 joules

The test procedure used was similar to that discussed in the NASA/Lewis TP 8-63, "Alteration of Surface Optical Properties by High Speed Micron Size Particles". For these tests, the average silicon carbide particle size was 6.35 microns. Using kinetic energy as the appropriate independent variable for scaling damage, a test kinetic energy of 1 joule on a 15/16-inch disc diameter is equivalent to a near-earth space of about 8 months.

The second and third samples of each group were used as control samples to eliminate the effects of corrosion on the results of the experiment. Figures B-2 through B-7 summarize the diffuse and specular measurements made by both EOS and NASA/Lewis between the wavelength of 0.625 and 15 microns.

The 1 to 15-micron specular reflectance data were derived by subtracting the diffuse from the total reflectance. The NASA data covered this wavelength range.

Reflectance between the wavelengths of 0.02 to 1 micron is particularly important since about 75 percent of the total solar intensity is represented by this wavelength region.

Low specular and high diffuse reflectance in the 0 to 1-micron region are due to surface roughness caused by the simulated micrometeorite test. Small pits act as a diffuser of low wavelengths and a reflector to higher wavelengths.

Some of the differences between the reflectance values above and below 1 micron are also due to the differences in measurement techniques. Several readings above 1 micron indicate specular reflectances greater than 100 percent.

Electro-Optical Systems reflectance measurements taken on the control samples for Groups 1 through 4 indicate a consistent loss in reflectivity due to corrosion and aging effects. Control samples from Groups 5 and 6 do not show a similar pattern. This can probably be explained by a fact that, initially, the silicon monoxide coatings on these samples were absorbing at

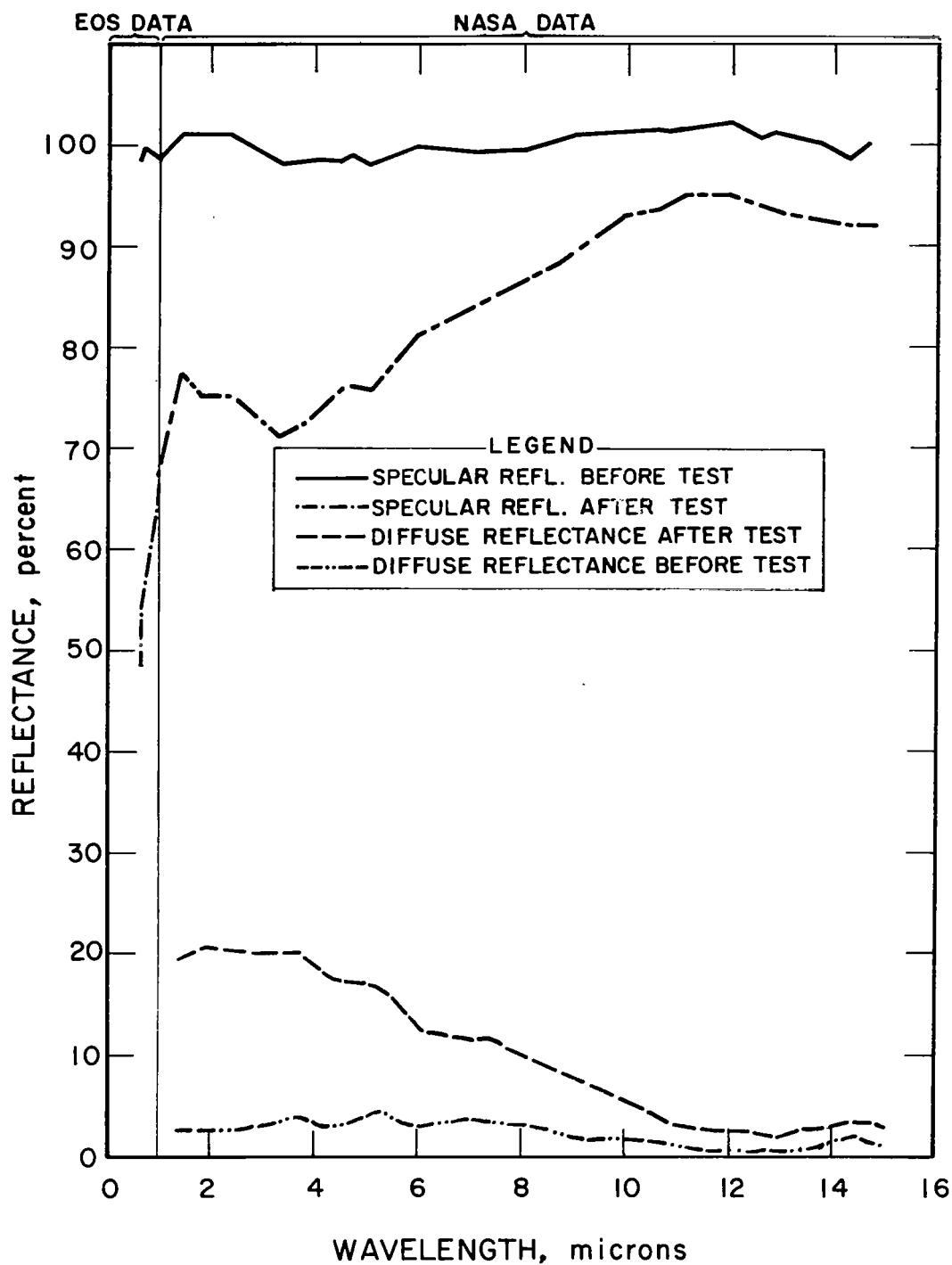


FIG. B-2 REFLECTANCE OF SAMPLE 1-1 BEFORE AND AFTER MICROMETEORITE TESTING

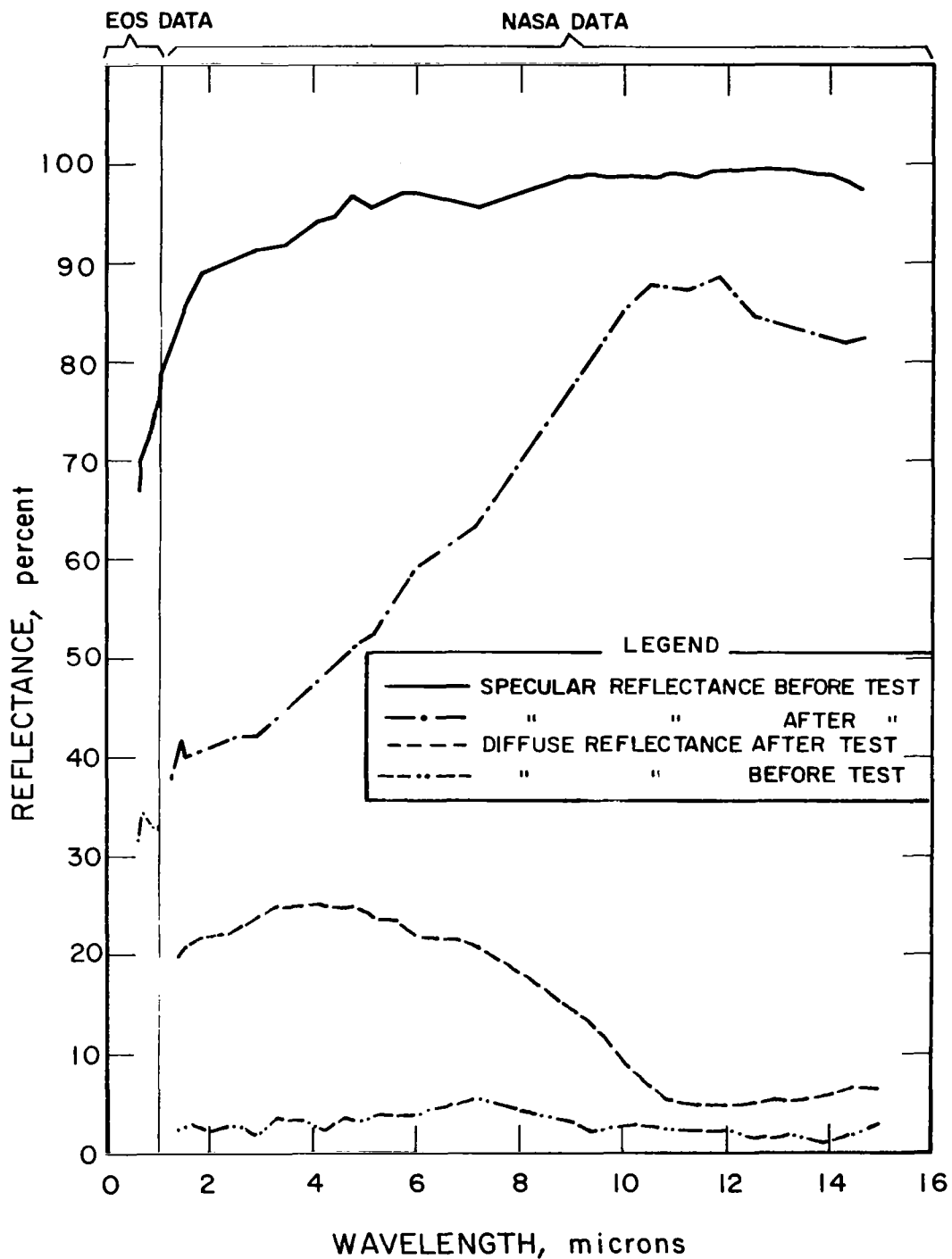


FIG. B-3 REFLECTANCE OF SAMPLE 2-1 BEFORE AND AFTER MICROMETEORITE TESTING

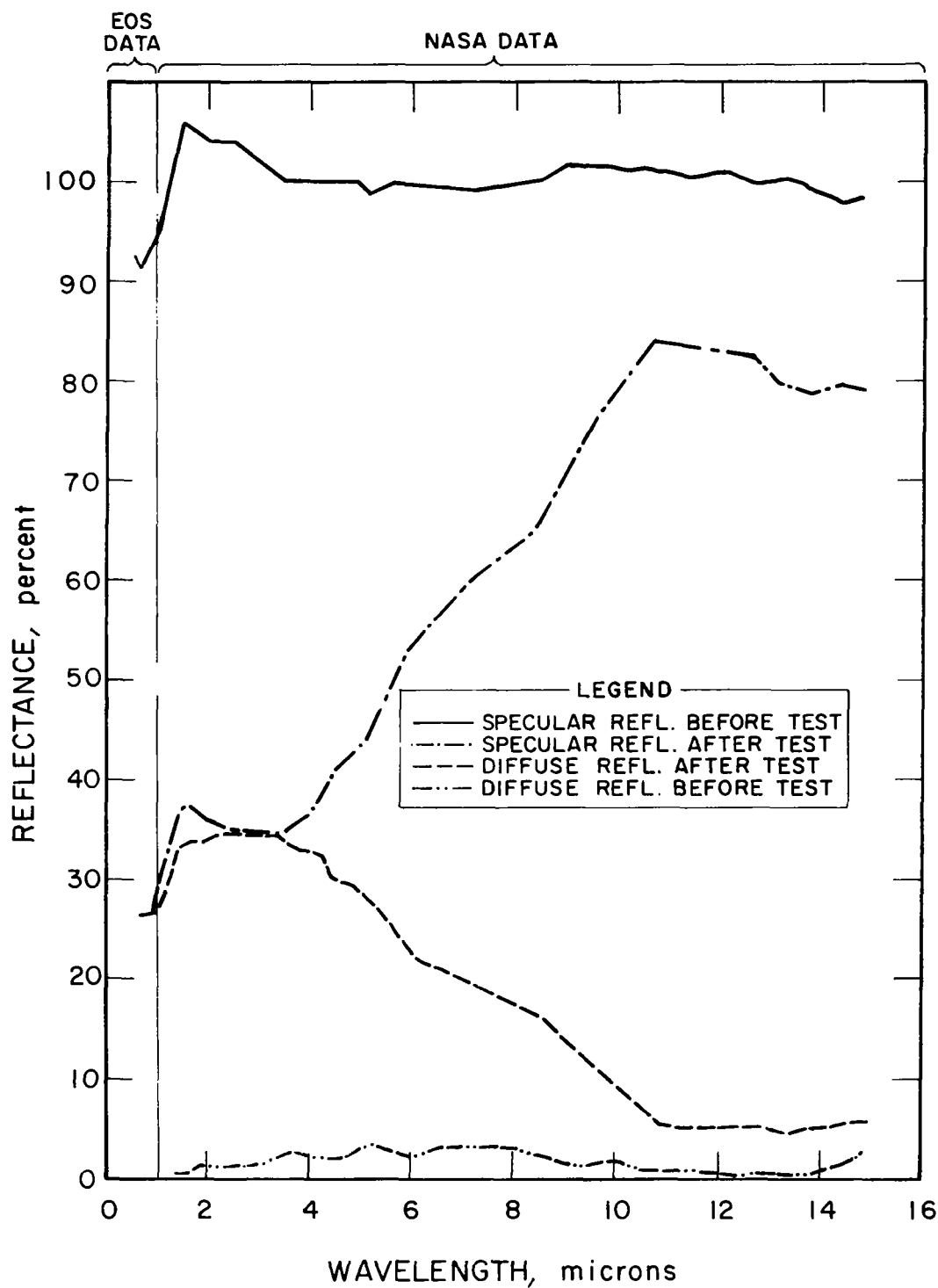


FIG. B-4 REFLECTANCE OF SAMPLE 3-1 BEFORE AND AFTER MICROMETEORITE TESTING

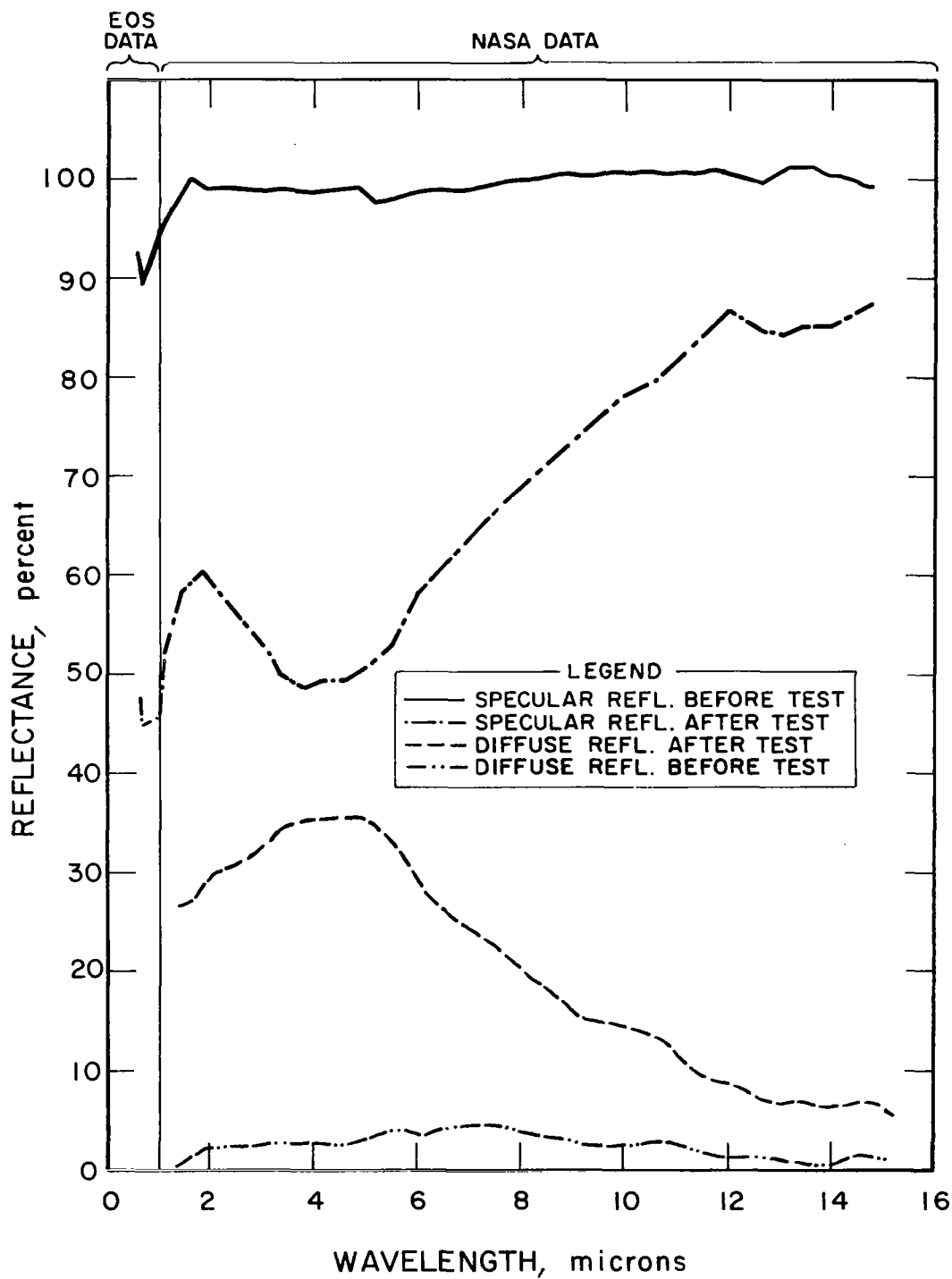


FIG. B-5 REFLECTANCE OF SAMPLE 4-1 BEFORE AND AFTER MICROMETEORITE TESTING

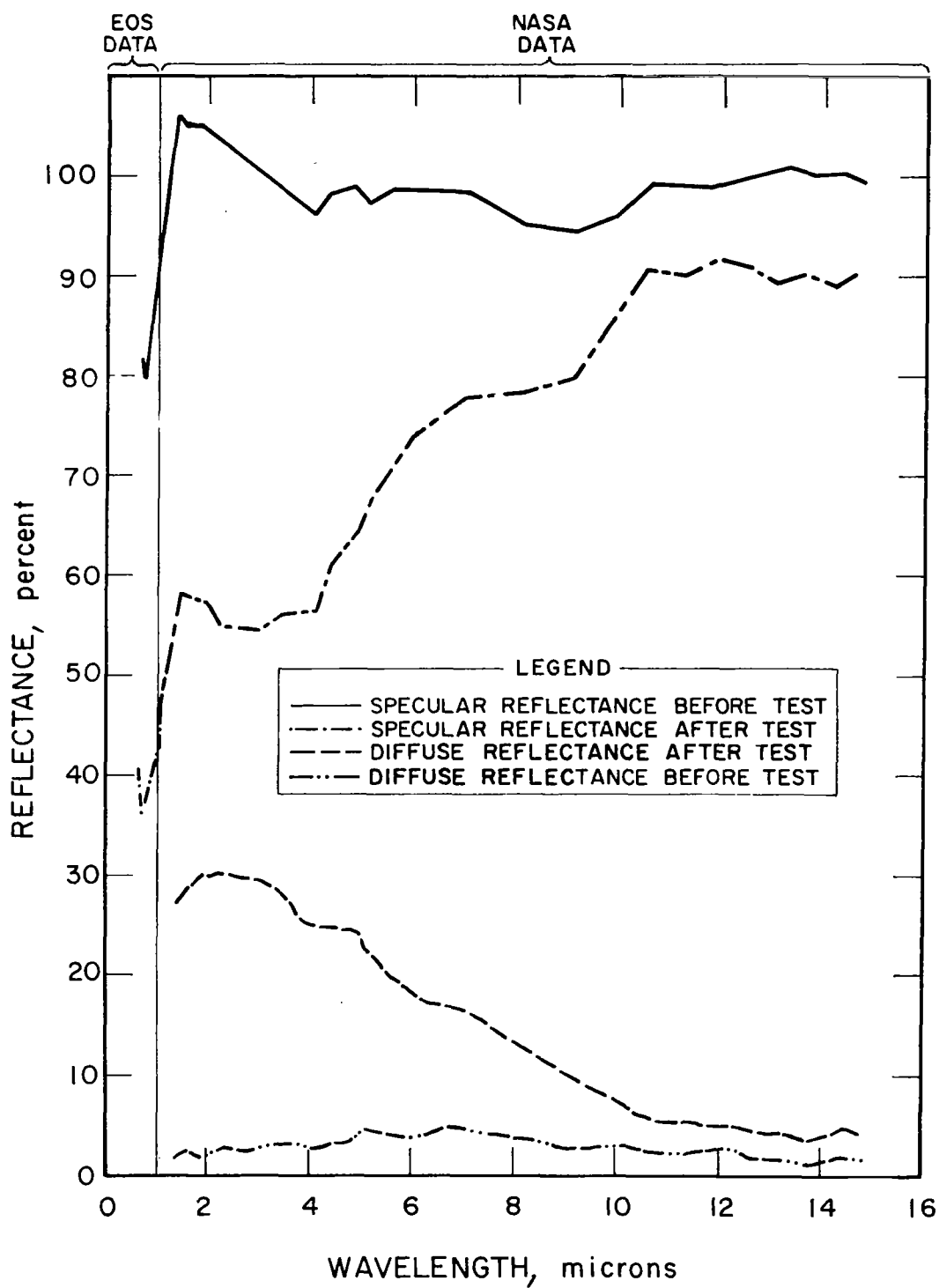


FIG. B-6 REFLECTANCE OF SAMPLE 5-1 BEFORE AND AFTER MICROMETEORITE TESTING

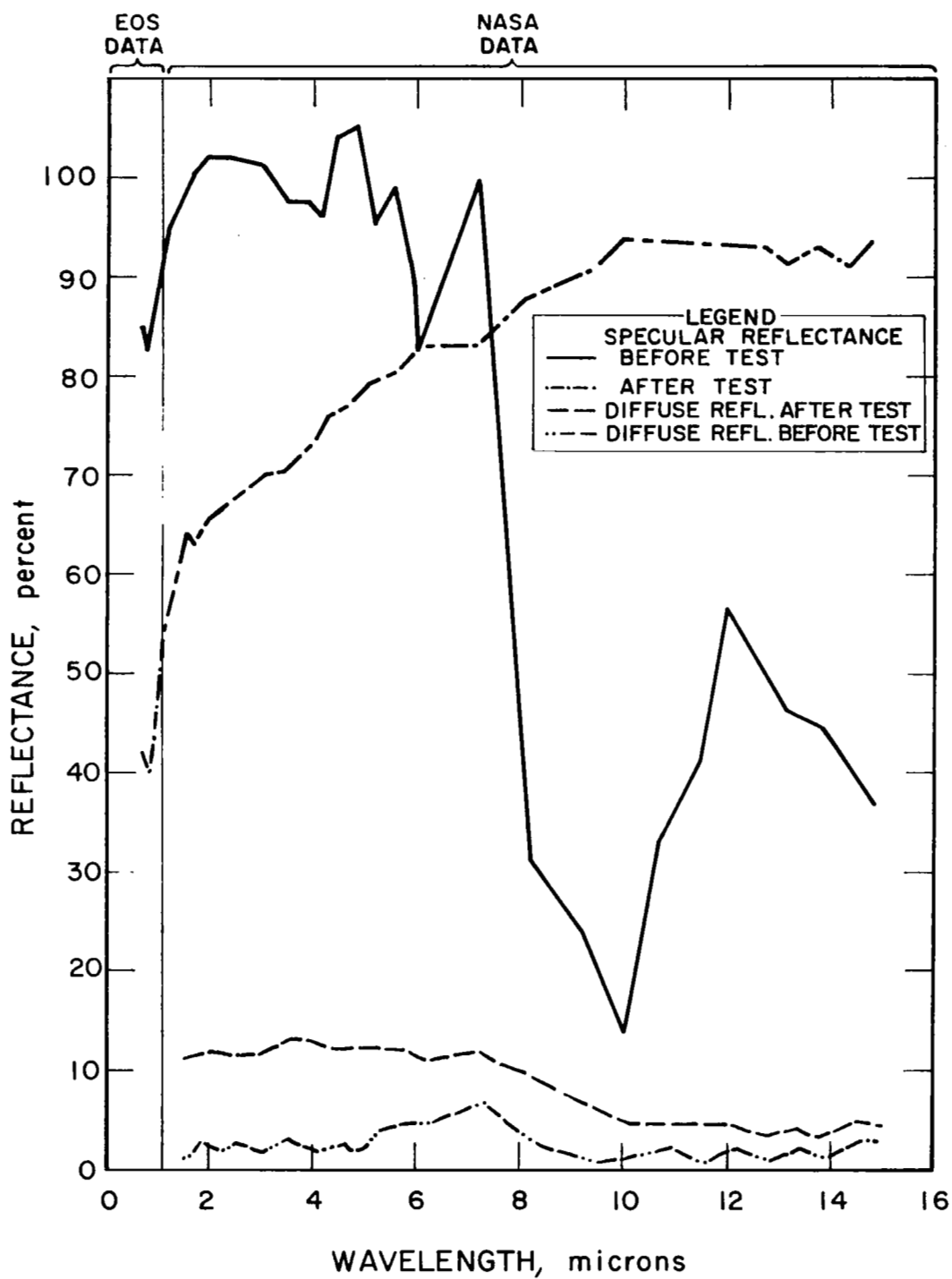


FIG. B-7 REFLECTANCE OF SAMPLE 6-1 BEFORE AND AFTER MICROMETEORITE TESTING

different wavelengths. Oxidation and water absorption then may have further altered the absorption characteristics of the silicon monoxide protective films.

Electro-Optical Systems reflectance measurements on the tested samples were corrected for corrosion degradation as measured on the control samples, to yield the net reflectance values.

Comparison of the micrometeorite resistance between coating groups is difficult because the kinetic energy of each test varied considerably. However, the following preliminary conclusions can be drawn from the limited sampling:

1. The reflectance of chemically deposited silver is superior (both before and after simulated micrometeorite impingement) to all other coatings, provided the silver is protected from chemical corrosion.
2. The reflectance of silicon monoxide-protected aluminum coatings (as in Group 6) is superior to that of bare electroformed nickel, both before and after micrometeorite testing. The Group 6 coating had a higher net reflectance after testing than the Group 5 coating. The relative reflectances were reversed before testing. This may indicate that the thick silicon monoxide coating has some advantage in protecting the collector surface, providing the thickness can be controlled to yield maximum collector reflectance throughout the mission.
3. It is difficult to compare the relative merits of various aluminum undercoatings as listed in Groups 3 and 4, since the test kinetic energy of each varied, by a factor of two. The control samples, however, indicate that the chromium-silicon monoxide-aluminum coating sandwich has better corrosion resistance than the chromium chromium-aluminum sandwich. The possibility of galvanic coupling between the chromium-aluminum sandwich in Group 3 may explain this. In Group 4, these materials are separated by the silicon monoxide dielectric coating. In calculating the net reflectance, it has

been assumed that the corrosion for the tested samples was the same as that incurred by the control samples. However, the tested samples probably corroded faster than the control samples. This may account for some of the large reflectance losses in the 0.625 to 1.0 micron range measured at EOS relative to those measured at NASA/Lewis at slightly higher wavelengths and immediately after the micrometeorite testing.

Up to wavelengths of 1 micron, the thermal properties of the coating materials do not appear to affect sample area degradation as one might expect if a comparison were made between solid target discs made from the coating materials. The thin-film mechanical and thermal properties of the coating materials are probably more dominant than the bulk thermal properties.

The results described above assume that the total kinetic energy is the appropriate independent variable.

Whatever the independent variable should be, these micrometeorite tests indicate the importance of testing reflectance degradation in space at the earliest possible date to accurately predict the life of reflective solar power systems.

APPENDIX C

MASTER GRINDING, POLISHING, AND TESTING

APPENDIX C

MASTER GRINDING, POLISHING, AND TESTING

The purpose of the experimental grinding, polishing, and testing phase of this program was to investigate techniques and materials which were amenable to the fabrication of high-accuracy, highly specular, 20- to 30-foot-diameter paraboloidal collector masters. The investigation involved 3 major areas:

1. The selection of a material which is best suited to the optical finishing required on masters for large high-performance concentrators
2. The selection of a fabrication technique which maximizes both collector surface accuracy and specularity
3. Testing of two experimental collector models

With reference to 2 and 3, above, three fabrication processes were considered:

1. Template machining, grinding, and polishing
2. Blade grinding and polishing
3. Plastic overlay

1. MATERIALS

A high-performance electroformed solar collector must be made from an accurate specular convex master. The superstructure of such a master must be designed to withstand the hydrostatic loads imposed by the electroforming process. Onto this superstructure, a transition base material, such as a filled epoxy, is deposited to minimize the thermal expansion effects between the final master coating and the superstructure. Finally, a master coating material is applied which should ideally have the following features:

1. Ability to be polished (or in some other way given a high specular finish)
2. Resistance to chemical attack, aging, and abrasion
3. Ease of application
4. Thermal expansion coefficient compatible with substructure
5. High adhesion to the base material
6. Ease of repair
7. History of use in similar applications

1.1 Materials Types

Three broad materials classes can be considered for large 20- to 30-foot-diameter collector masters: glass, metal, and plastic. Though ground and polished glass masters have been used successfully for replicating mirrors up to 5 feet in diameter, they are not economically feasible in larger sizes, based on presently available technology (see Subsection 4.1). Since the risk of glass master breakage during plating is high, the advantages of glass do not presently warrant funding to advance the art of producing large-diameter glass masters. Alternatively, either plastic or metal can be used for large concentrator masters. The comparative advantages of plastic and metal as master materials are given below:

<u>Plastic Advantages</u>	<u>Metal Advantages</u>
1. Low cost	1. High hardness and scratch resistance
2. Short fabrication time	2. High strength
3. Light weight	3. Low thermal expansion coefficient
4. Easily repairable	4. High electrical conductivity
5. Good corrosion resistance	
6. Easier parting of replica	

To date, the advantages of plastics seem to outweigh those of metals as master surface materials.

1.2 Plastics

Several types of plastics offer many of the advantages desired for a large diameter collector master material. These include:

1. Acrylic
2. Polyester
3. Diallyl phthalate-based polyester
4. Epoxy

The acrylic and diallyl-based materials are widely used for refractive plastic optics and have good transmission and polishing characteristics. Polyester resins have been used in previous EOS master studies, and epoxy resins are used extensively by EOS in the production of optical quality reflective submasters and replicas.

1.3 Experimental Plastics

The grinding and polishing experiments in this study were made on a polyester resin with a high styrene monomer content and an epoxy EPON 828 resin and diethyl amino propylamine (DEAPA) hardening agent. Plastic overlay studies were made with the polyester resin.

1.4 Application Methods

To achieve maximum master specularity and accuracy, the plastic surface must be void-free and homogeneous. Three application methods, amenable both to small and 20- to 30-foot-diameter collector masters, were used in surfacing the 2-foot experimental masters:

1. Casting
2. Plastic overlay
3. Flow coating

In the casting process, the plastic surface layer is cast between a matched mold consisting of a convex surface (the roughly ground base material of the master) and a concave surface. One 1/4-inch epoxy surface layer was cast using a concave plaster mold. The paraboloidal surface of this concave mold was generated by spin casting the plaster before and during curing. However, the resultant mold was

relatively rough. The plaster surface was coated with several release layers to prevent adhesion to the mold and water contamination of the epoxy by the plaster. The cast surface was relatively rough due to the mold. Eliminating this roughness required considerable grinding time. Also, numerous bubbles and gas pockets in the plastic resulted from water inclusions and other casting defects. These voids caused many surface pits in the final polishing stages and acted as nuclei for stress cracks.

In the plastic overlay technique, a plastic sheet (normally flat) is cast to a uniform thickness and cured. If the plastic casting is made against a highly specular uniform surface, such as polished plate glass, and if the draping is performed with care, the overlay surface forms the finished master without requiring further polishing. An overlay master was made by bonding a cast polyester sheet to the ground epoxy substrate using RTV silicone rubber (room temperature vulcanizing adhesive), RTV primer, and mechanical roughening of the mating bonded surfaces. This method of applying the plastic master surface was superior to the other two alternative methods.

In the flow coating technique, like the casting technique, the plastic coating cures on the master. However, since there is no enclosed mold to restrain the gravity flow of the plastic, the plastic must be quite viscous and must be continuously worked with a squeegee or template until the plastic has cured sufficiently to cease flowing. Several flow-coated epoxy layers were applied but were not completely satisfactory for two reasons:

1. Adhesion of the epoxy to the substrate was poor because the epoxy did not wet the substrate, or the substrate was improperly coated with an adhesion-promoting material. Due to this poor adhesion, a large number of voids resulted.
2. The successive layers of plastic did not blend well. The grinding and polishing of these layers developed numerous transition zones.

The uniformity and bubble problems associated with this method eliminate it as a practical master coating application method.

2. FABRICATION METHODS AND RESULTS

All master fabrication techniques involve the initial fabrication of an approximately paraboloidal shape upon which the final grinding, casting, draping, spinning, or machining operations are performed.

Three methods were experimentally investigated during this program:

1. Cam-template generation
2. Blade grinding and polishing
3. Plastic overlay

2.1 Cam-Template Generation

The initial grinding and polishing work on this program involved the cam-template master generation approach. However, certain geometric and mechanical details of the machine caused periodic grooving and deviation from a paraboloid. Investigation of these difficulties indicated that the existing experimental equipment was inadequate to produce the desired master contour and surface finish. To avoid redundancy, this work was terminated when a template machine was set up on another program for grinding and polishing masters for 10-foot petal mirrors.

Although an entire 2-foot master surface was not polished by the cam-template approach, the polishing of several 2-inch-wide zones indicated that, with sufficient mechanical revision, acceptable master surfaces could be produced. Results of the petal master polishing program verified this assumption.

2.2 Blade Grinding Generation

Figure 4-5 (4150-Final Report, Section 4) shows the blade grinding assembly mounted on a rotary spindle. The machine was fitted with limit switches at the ends of the bearing guide rail to facilitate automatic reversal of the blade motion at the end of travel. The variable-speed spindle drive rotates from 0 to 60 rpm and the variable-speed traverse permits blade traverse rates from 0 to 300 inches per

minute. The spindle rotation is reversible so that the blade wear can be relatively uniform. In practice, the spindle rotates between 10 and 25 rpm and the blade traverses at between 50 and 200 inches per minute, depending on the phase of grinding or polishing.

2.2.1 Blades

The blades used in generating the paraboloidal masters are initially roughly sawed to the approximate parabolic shape desired and filed to remove burrs. Blades have been made from brass, polyvinyl-chloride (PVC), and acrylic plastic.

The quarter-hard brass blades were 25 inches wide by 1/8 inch thick. The rigidized PVC blade was 25 inches wide by 1/2 inch thick and the acrylic blade was 25 inches wide by 3/8 inch thick. In operation, the blades grind into parabolic curves. The edge contour of the blade is such that any plane parallel to the long faces of the blade intersects a portion of the same parabola. In cross section, the blade at any point is convex and symmetrical about the axis of rotation.

Brass blades abraded excessively due both to the hardness of the blade and the tendency of the brass to sliver off the edge. These brass slivers caused excessive scratching of the master surface in fine grinding stages. This initiated use of plastic blades such as PVC and acrylic. The PVC blade ground in quickly, but often tended to leave a residual deposit on the master and apparently abraded in long fibers. Though this blade did not scratch the master surfaces in fine grinding stages, the blade contour was never ideal, possibly because of its fibrous consistency. The low thermal distortion point of PVC may also have tended to cause some of the contour and wear problems.

The acrylic blade worked well under grinding and rough polishing phases. Wear appeared to be quite uniform with a good blade contour. No scratching resulted. In the polishing stages the blade was covered with felt, polishing paper, or vinyl tape, according to the type of polishing agent being used.

2.2.2 Grinding and Polishing Materials

The following grinding and polishing materials were used in generating a polished paraboloidal master:

80-grit silicon carbide

1F silicon carbide

2F silicon carbide

3F silicon carbide

Aluminum oxide

Cesium oxide

Rouge

Meguiar's mirror glaze

Meguiar's plastic cleaner

These grinding and polishing compounds, with the exception of the last two listed, are standard in optical fabrication. The Meguiar's compounds contained a high portion of fatty acid vehicle which gave a false specularity to the plastic master. Because of these waxy finishes, the last experiments were run with the more standard optical polishing agents. The other compounds were used with either a water or a water and glycerine vehicle.

2.2.3 Repairs

Various defects in the epoxy master surfaces necessitated localized repairs. The voids produced in both the casting and flow-coating layers acted as nuclei for stress cracks and reservoirs for grinding and polishing compounds. To insure that no grinding compounds were carried over into the polishing phases, it was necessary to fill the voids. Inadvertently, the thermal shock caused by rapidly evaporating solvent caused one area of the epoxy master to crack. The cracks and other defects were patched with a resin system which had a shorter cure life and greater exotherm than the original casting system. This caused a difference in final patch hardness relative to the original material. During the grinding and polishing

phases, this difference in relative hardness caused ridges on the master which were also visible on the electroformed replica. (A replica is defined as a negative copy of a positive master and is synonymously used for the word "collector".) These ridges demonstrate that although the plastic can be easily patched, the patching material should have the same properties as the material being repaired.

2.2.4 Replication of Blade Finished Masters

The first electroformed replica (collector 2-1) was made from the blade-ground and polished polyester surface, which was the initial master coating. This master was 24 inches in diameter and had about a 60° rim angle. Due to the high sheen provided by the waxy polishing materials used, phonograph type defects, resulting from improper blade material and blade mechanism weight, were not apparent until the master was thoroughly clean. When the master was replicated, the plating temperature was 140°F, which approaches the softening point of the polyester surface. Since the polyester had been initially deposited on a grooved epoxy subsurface, the high temperature plating bath caused the polyester to be stress relieved and to telegraph the grooved epoxy subsurface. The resulting collector looked like a fresnel lens with facets about 1/16 inch wide, the pitch diameter of the screw used to groove the filled epoxy subsurface. This replication was not tested. Subsequent masters made with epoxy and draped polyester surfaces were replicated at a lower temperature.

The next blade grinding and polishing was performed on the cast and flow-coated epoxy layers. These surfaces were easily ground but were difficult to polish using the available blade materials and relative motion of the blade grinder. In standard grinding and polishing techniques, the final polishing is done with a random motion overarm. In the blade grinder, the regular relative motion of the blade and the master produce spiral paths in the grinding and polishing phases. Because the blade machine was not equipped with a polishing overarm, and

since the master weight was more than available, polishing spindles could carry easily, the maximum surface polish attainable with an epoxy surface was not achieved. Also, defects caused by ridges where cracks had been repaired, locally distorted the collector surface. The maximum collector-absorber efficiency for this collector (2-2), using a cold calorimeter and neglecting mirror obscuration, was about 50 percent. Poor silvering of the master due to improper cleaning also decreased the efficiency.

During the fabricating of collector 2-2, the accuracy of the blade grinding process in fine grinding stages was checked by comparing the parabolic curve of the blade with a true parabola. The blade matched the paraboloid contour within 0.001 inch. The deviation of the blade from a true parabola was less than 0.002 inch over a 6-inch radius. This corresponds to a surface error of 1 minute of arc. This general accuracy correlates with the accuracy of the blade-ground 60-inch glass searchlight mirrors made prior to and during World War II.

An additional blade-ground and polished master was made using a polyester plastic overlay-surfaced, 55° rim angle, convex master as a starting point. This master was light enough to finish on a standard optical spindle. Though the finish was much superior to that achieved previously, maximum practical surface specularly was not achieved due to limited time and a polishing tool of marginal quality.

The replica made from this master (collector 2-3) produced encouraging results (see Fig. C-1). The lower curve represents the collector with an improperly applied protective silicone coating. The upper curve represents the efficiency of the collector after stripping this coating. Collector 2-5, discussed below, showed almost no efficiency loss when properly coated with the same silicone. Silver samples properly coated with the silicone showed less than 1 percent reflectance loss after coating, as measured at $5,500\text{\AA}$. Replica 2-3

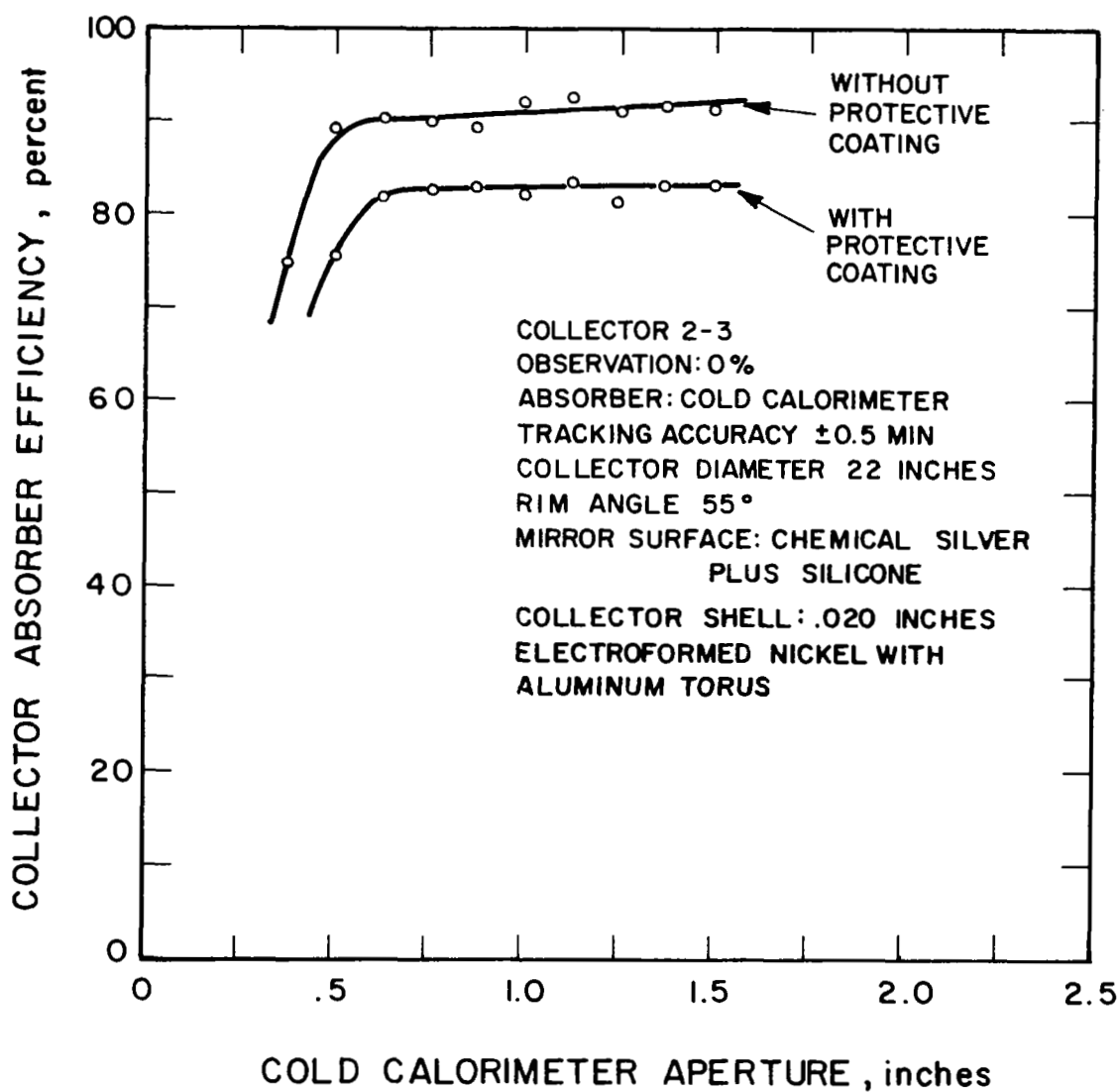


FIG. C-1 COLLECTOR NO. 2-3, EFFICIENCY VS APERTURE DIAMETER

also exhibited a poor silver surface due to improper master cleaning. The resultant darkened silver surface may have decreased the collector-absorber efficiency as much as 5 percent. The maximum efficiency, which is always less than the surface reflectance, exceeds the design reflectance proposed for the Brayton cycle collector by 1 percent. Also, for a concentration ratio approaching that of the 30-foot collector design with an 8-inch cavity aperture diameter, (2025) neglecting obscuration, collector 2-3 meets the efficiency design specifications proposed by EOS. On the basis of these model tests, further improvements are possible in the areas of polishing and chemical silver applications.

Silicone-protected silver samples withstood an ammonium sulfide atmosphere without visible tarnishing, while uncoated samples completely tarnished during the same time. Also, collector 2-3 withstood several months of storage and preliminary testing before the final tests were run.

2.3 Plastic Overlay

2.3.1 Substrate

The blade-ground and polished epoxy 2-foot master was used as an accurate substrate for the first plastic overlay-formed master. In actual practice, one need only carry the grinding operations (by either blade or cam-template) to the fine grinding stage to provide sufficient structural geometry to perform the overlay process.

2.3.2 Technique

A polyester sheet was cast between 2 sheets of optically polished plate glass using a silicone release agent. After the polyester had thoroughly cured, it was stripped from the plate glass and placed over the prepared master substrate. The master surface was formed by stretching the polyester sheet over the convex paraboloidal substrate. Hot water and weights were used to form the plastic. Once the plastic had been formed to shape, RTV adhesive, RTV primer,

and suitable mechanical roughening were used to bond the polyester sheet to the substrate. The composite was then vacuum-bagged while the adhesive cured to achieve maximum adhesion and surface geometry.

2.3.3 Drape Forming Results

The first plastic overlay-formed master produced a highly specular surface with some edge defects which were visible to the naked eye. This master was then used to replicate collector 2-4.

The maximum collector-absorber efficiency for this collector was 60 percent. This low efficiency was due to localized surface distortions in the plastic, edge distortions caused by an undersized master base, and poor collector silvering. This recurrent poor silvering was caused by poor removal of the silicone release agents used in casting the plastic sheet between plate glass sheets.

Most of the above defects were eliminated in the fabrication of the master used to replicate collector 2-5. The maximum collector-absorber efficiency for this silicone-protected, chemical silver-coated collector (93 percent) exceeds any previous collector efficiency measured at EOS or elsewhere. However, at very high concentration ratios associated with thermionic collectors, better efficiencies have been reported than might be expected from extrapolation of Fig. C-2 between a 0-inch diameter and the 3/8-inch diameter aperture (the latter represents an unobstructed concentration ratio of 3,400).

The results of this test indicate that the Brayton cycle design specifications for collector-absorber efficiency can also be met by the plastic overlay-forming technique and the silicone-protected chemical silver reflective layer.

The plastic overlay sheet thickness (1/4 inch) used for the 2-foot master is the same as that proposed for the 30-foot collector. Also, the 2-foot master curvature was over 15 times as great as on a 30-foot master. Surface errors for the 2-foot master, due to the plastic sheet, were probably as great or greater than one might expect for a 30-foot draped master.

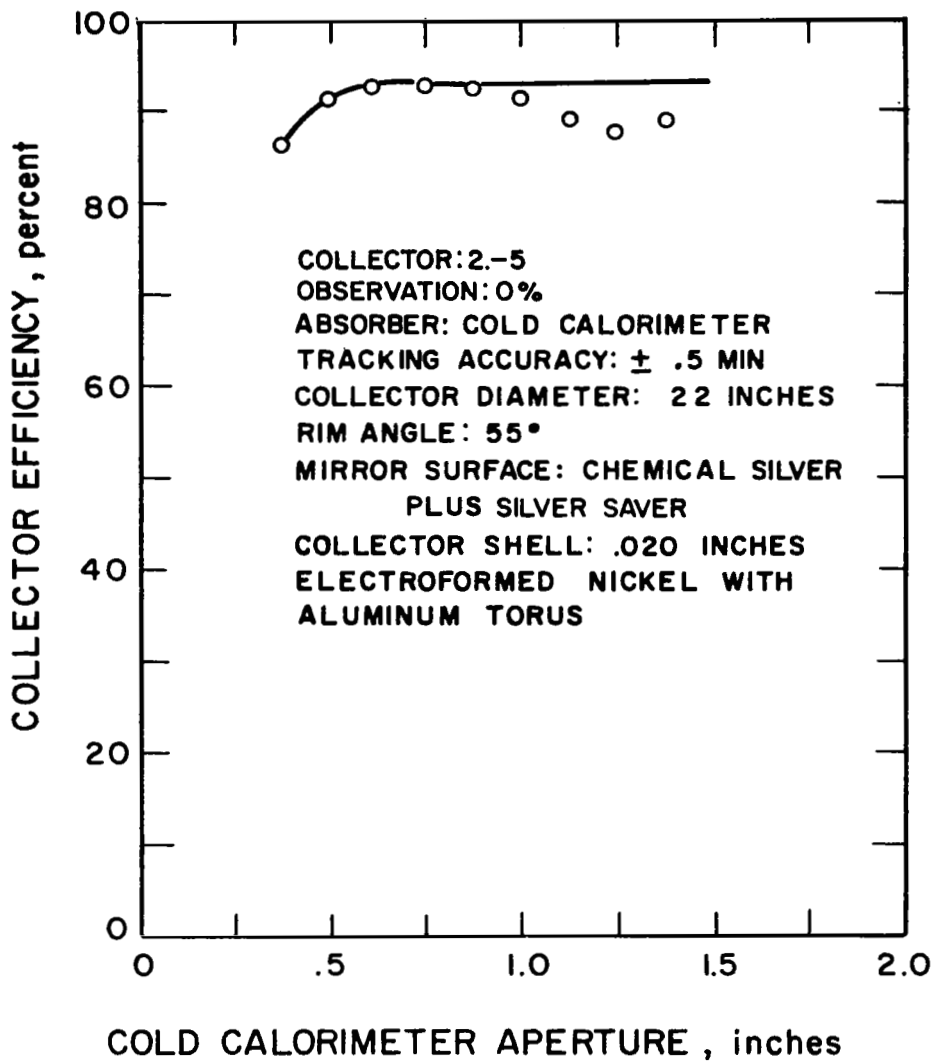


FIG. C-2 COLLECTOR NO. 2-5, EFFICIENCY VS APERTURE DIAMETER

3. CONCLUSIONS

Based on the experimental work which resulted in investigating two hitherto unfunded plastic collector master fabrication techniques and which developed a silicone-protected chemical silver mirror coating, several conclusions can be made.

1. For 2-foot models, either the plastic overlay or blade grinding and polishing technique will achieve the high efficiency goals EOS proposes for the Brayton cycle design. There appear to be no engineering problems which would prevent a 30-foot collector, made by either process, from meeting the specifications.
2. Although only limited time was spent on these two techniques of making collector masters, relative to other master and collector fabricating techniques, the methods offer much promise and probably can be considerably improved with additional support.
3. The drape-forming technique offers greater specularly, uses less costly fabrication machinery, and takes less time than the blade-grinding technique.
4. Protective agents for chemical silver coatings do not reduce reflectance by more than 1 percent when applied correctly. The resultant composite has higher reflectance than any other proposed durable collector coating.